London South Bank University

Development of a Chain Climbing Robot and an Automated Ultrasound Inspection System for Mooring Chain Integrity Assessment

By

D.M. Mahesh Panditha Dissanayake

A thesis submitted to London south Bank University for the degree of
Doctor of Philosophy

October 2018

Abstract

Doctor of Philosophy

By D. M. Mahesh Panditha Dissanayake

Mooring chains used to stabilise offshore floating platforms are often subjected to harsh environmental conditions on a daily basis, *i.e.* high tidal waves, storms etc. Chain breakage can lead to vessel drift and serious damage such as riser rupture, production shutdown and hydrocarbon release. Therefore, integrity assessment of chain links is vital, and regular inspection is mandatory for offshore structures. Currently, structural health monitoring of chain links is conducted using either remotely operated vehicles (ROVs), which are associated with high costs, or by manual means, which increases the risk to human operators. The development of climbing robots for mooring chain applications is still in its infancy due to the operational complexity and geometrical features of the chain. This thesis presents a Cartesian legged magnetic adhesion tracked-wheel crawler robot developed for mooring chain inspection. The crawler robot presented in this study is suitable for mooring chain climbing in air and the technique can be adapted for underwater use. The proposed robot addresses straight mooring chain climbing and a misaligned scenario that is commonly evident in in-situ conditions. The robot can be used as a platform to convey equipment, *i.e.* tools for non-destructive testing/evaluation applications. The application of ultrasound for in-service mooring chain inspection is still in the early stages due to lack of accessibility, in-field operational complexity and the geometrical features of mooring systems. With the advancement of robotic/automated systems (*i.e.* chain-climbing robotic mechanisms), interest in in-situ ultrasound inspection has increased. Currently, ultrasound inspection is confined to the weld area of the chain links. However, according to recent studies on fatigue and residual stresses, ultrasound inspection of the chain crown should be further investigated. A new automated application for ultrasonic phased-array full-matrix capture is discussed in this thesis for investigation of the chain crown. The concept of the chain-climbing robot and the inspection technique are validated with laboratory-based climbing experiments and presented in this thesis.

Declaration of Authorship

I, D.M.M.P Dissanayake, declare that this thesis titled, 'Development of a Mooring Chain Climbing Robot and an Automated Ultrasound Inspection System for Chain Integrity Assessment' and the work presented in it are my own. I confirm that:

- This work was done wholly or mainly while in candidature for a research degree at this University.
- Where any part of this thesis has previously been submitted for a degree or any other qualification at this University or any other institution, this has been clearly stated.
- Where I have consulted the published work of others, this is always clearly attributed.
- Where I have quoted from the work of others, the source is always given. With the exception of such quotations, this thesis is entirely my own work.
- I have acknowledged all main sources of help.
- Where the thesis is based on work done by myself jointly with others, I have made clear exactly what was done by others and what I have contributed myself.

Signed:

Date: October / 2018

Acknowledgement

First of all, I would like to express my appreciation and thanks to academic supervisors Prof. Tariq Pervez Sattar and Dr Jonathan Mark Selig for being tremendous mentors throughout the studentship and help to focus when I was heading off track. I am highly grateful to my industrial supervisors Prof. Tat-Hean Gan and Ivan Pinson for guiding me throughout the studentship to conduct the research. I would also like to thank again Prof. Tariq Sttar, Prof Tat-Han Gan and TWI Ltd, Cambridge for giving me this opportunity.

Then, I would like to thank Dr Shehan Lowe, Dr Michael Corsar, Dr Dave Carswell, Dr Mark Sutcliffe, Dr Channa Nageswara, Dr Philippe Bastid, Dr John Rudlin and Dr Omar Howlader, for the tremendous support during the period of research and publications.

Then I would like to thank my colleagues within London South Bank Innovation Centre (LSBIC), Brunel Innovation Centre (BIC), Non-Destructive Testing (NDT) Smart Material and Joining (SMJ) and Condition and Structural-Health Monitoring (CSM) departments for their support. I would like to thank Mr Marcus young, Mr Udana Ranathunga, NSIRC administrative team and colleagues at InnotecUK, Cambridge for their support and encouragements. A big thank for you all for been there for me and your moral support. Furthermore, our discussions, arguments and debates helped me to improve my knowledge and confidence.

I would like to thank my parents for their love, sacrifices and support which helped me to succeed in life to be the person I am today. Then I would like to thank my brother for his support and love throughout these years. I would like to thank my loving wife Melani Dissanayake for her love, support and more importantly been patient with me throughout these years.

Finally, I would like to thank the School of Engineering London South Bank University, TWI Ltd, Cambridge, National Structural Integrity Research Centre (NSIRC) and InnovateUK grant 102905 RIMCAW for providing the funding for this research.

Contents

List of Figures

List of Tables

Abbreviations

2D	**T**wo-**D**imensional
3D	**T**hree-**D**imensional
AF	**A**ctive **F**ocusing
ASTM	**A**merican **S**ociety for **T**esting and **M**aterials
API	**A**merican **P**etroleum **I**nstitute
CAD	**C**omputer **A**ided **D**esign
CPU	**C**entral **P**rocessing **U**nit
DC	**D**irect **C**urrent
DNV	**D**et **N**orske **V**eritas
DoF	**D**egree **o**f **F**reedom
FE	**F**inite **E**lement
FPSO	**F**loating **P**roduction **S**torage and **O**ffloading
GUI	**G**raphical **U**ser **I**nterface
GPU	**G**raphics **P**rocessing **U**nit
H	**H**eight
FEA	**F**inite **E**lement **A**nalysis
FMC	**F**ull **M**atrix **C**apture
MFNC	**M**agnetic **F**ield **N**o **C**urrent
L	**L**ength
MPI	**M**agnetic **P**article **I**nspection
NDT	**N**on-**D**estructive **T**esting
Op-amp	**O**perational **A**mplifier
PAUT	**P**hased **A**rray **U**ltrasonic **T**esting
PID	**P**roportional– **I**ntegral–**D**erivative
Rx	**R**eception
ROV	**R**emotely **O**perated **V**ehicle
RIMCAW	**R**obotic **I**nspection of **M**ooring **C**hains in **A**ir and **W**ater
Tx	**T**ransmission
TWI	**T**he **W**elding **I**nstitute
UT	**U**ltrasonic **T**esting
W	**W**idth

Publications Arising from the Research

Journal Publication

D1 M. Dissanayake, T. Sattar, G. Tat-Hean, I. Pinson and S. Lowe, "Design and prototype of a magnetic adhesion tracked-wheel robotic platform for mooring chain inspection," *Journal of Systems and Control Engineering: Proceedings of the Institution of Mechanical Engineers, Part I*, vol. 232, no. 8, pp. 1063-1074, 2018.

D2 M. Dissanayake, T. Sattar, S. Lowe, I. Pinson and T.-H. Gan, "Adaptable legged-magnetic adhesion tracked wheel robotic platform for misaligned mooring chain climbing and inspection," *Industrial Robot: An International Journal*, vol. 45, no. 5, pp. 634-646, 2018

D3 M. Dissanayake, D. Carswell, M. Corsar, T. Sattar, S. Lowe and T.-H. Gan, "Automated application of full matrix capture to access the structural integrity of mooring chains," *IEEE Access*, vol. 06, pp. 75560 - 75571, 2018

Conference Publications

D4 M. Dissanayake, T. Sattar, I. Pinson and T.-H. Gan, "Tracked-wheel crawler robot for vertically aligned mooring chain climbing design," in *IEEE International Conference on Industrial and Information Systems (ICIIS)*, Kandy, Sri Lanka, 2017.

D5 M. Dissanayake, O. Howlader, T. Sattar, T.-H. Gan and I. Pinson , "Development of a novel crawler based robot for mooring chain climbing," in *Proc. of 20th International Conference on CLAWAR 2017*, Portugal, 2017.

D6 M. Dissanayake, T. Sattar, T.-H. Gan and I. Pinson , "Mooring chain climbing robot: Design approach," in *NSIRC 2017 Annual Conference*, Cambridge, 2017.

D7 M. Dissanayake, T. Sattar, I. Pinson and T.-H. Gan, "Orthogonally positioned tracked crawler robot for vertically aligned mooring chain climbing," in *NSIRC 2018 Annual Conference*, Cambridge , 2018.

Chapter 1: Introduction

1.1 Introduction to the problem

The history of the mooring chain began in 1808, with advances in the shipping industry, when it became necessary to maintain a floating structure within a given (pre-specified) position. An exponential increase in floating oil and gas production systems has been recorded around the world due to the high demand associated with energy consumption. In total, 277 floating production units (FPU) were recorded by November 2013 and 62% of these were categorised as floating production storage and offloading (FPSO) [1]. Permanent mooring systems were introduced to the floating production units in order to keep them safe and steady during in-service operations, *i.e.* to prevent platform drift due to tidal forces, wind, storms etc. The components of a typical deep-water mooring chain installation are illustrated in Figure 1-1. The shape of a mooring line (*i.e.* catenary curvature) depends on the force applied to the mooring line at the fairland, the unit weight of the mooring line, the length of the suspended mooring line, the operational water depth and the horizontal distance between attachments. This research focuses on the tethering mooring chains; in particular, chain segments that are connected all the way from ≈30m below the surface up through the splash zone to air underneath the turret. This part of the chain segment is likely to be straight. However, misalignments are presented in the mooring line due to in-situ forces.

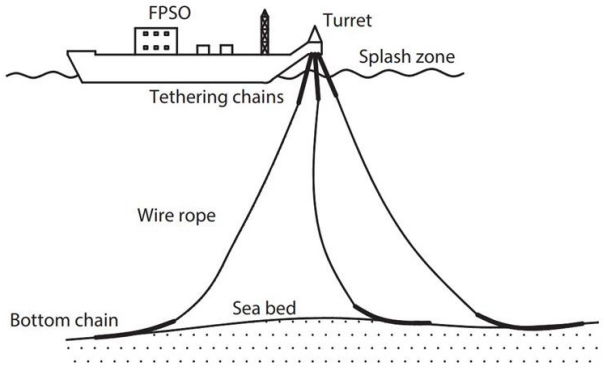

Figure 1-1: Components of a typical deep water mooring installation [150]

The requirement of mandatory structural health assessments raised as a result of the in-situ conditions to which mooring chains are subjected on a regular basis, such as high tidal waves, storms, hurricanes, the effect of salt water and harsh environmental conditions. Chain overload, out-of-plane bending, wear effect between chain links, corrosion and manufacturing defects are the main reasons for mooring breakage. A break in the mooring chains can lead to significant damage such as vessel drift, riser rupture, production

shutdown and hydrocarbon release etc. ***[D5]***. Examples of the possible damage to mooring chain links are illustrated in Figure 1-2. As an example, $1.8 billion had to be spent on the 'Gryphon Alpha' to resume operations after a mooring failure [2]. In the period 2001–2011, 21 accidents were recorded with eight multiple line breakages (system failures) [3]. Modern mooring systems are designed to handle a single breakage, but multiple breakages can easily lead to a catastrophic incident. An in-depth analysis of mooring breakage between 2001–2011 was conducted in [3], and a detailed summary was presented, as illustrated in Figure 1-3.

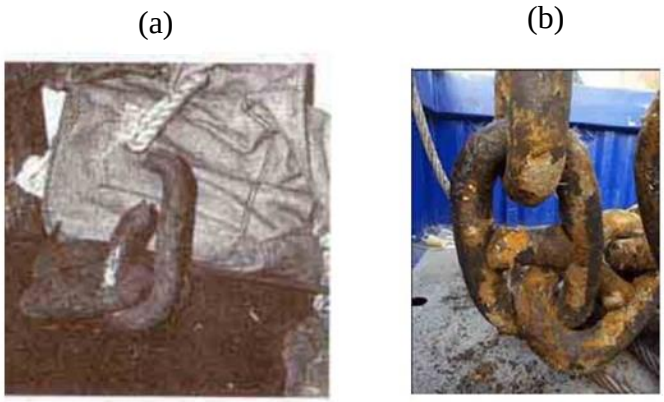

Figure 1-2: (a) Sample of 'North Carr' link failure; (b) General corrosion of a mooring link (after 16-year service) [5]

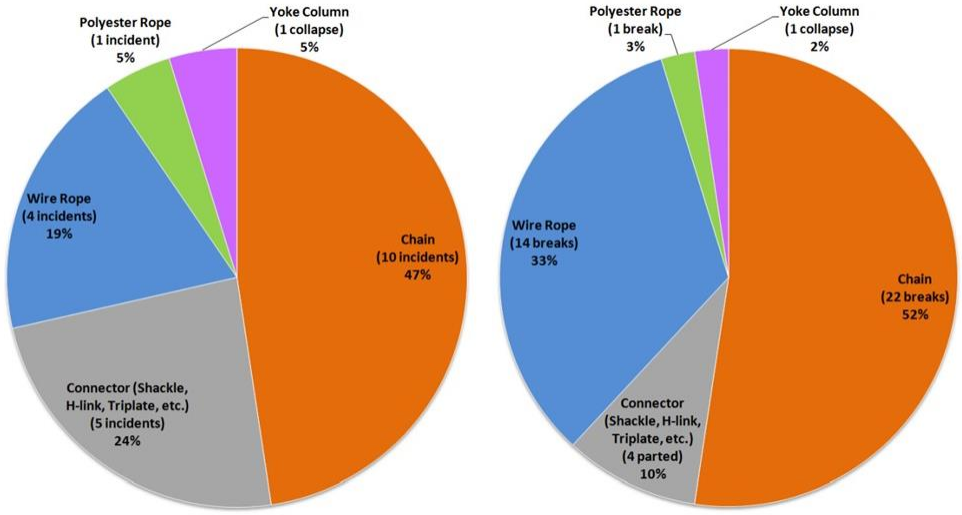

Figure 1-3: Mooring incident analysis (based on reported incidents between 2001–2011) [3]

According to the analysis carried out in Figure 1-3, it is significant that the 'chain' part of a mooring system is vulnerable and mandatory regular inspection is required. According to the reported data from the North Sea (1980–2001), every 4.7 years, a floating production

system has experienced a mooring failure [4]. Approximately £2M–10.5M in losses can occur due to a single mooring failure [5]. After considering the potential damage to humans, as well as the environment, periodic inspection became mandatory for mooring systems [4]. Chain inspection intervals are determined according to service time in the water, *i.e.* a mooring system that has been in operation for 0–3 years should be inspected every 36 months; 4–10-year chain links should be inspected every 24 months; and systems that are over 10 years should be inspected every eight months [6].

1.2 Motivation

1.2.1 Research Gap 1 - automated climbing platform

Mooring chains are not designed to be self-monitoring their condition; therefore, mooring integrity management of FPSO needs to be addressed with a capability to handle in-situ conditions, because most offshore oil production systems cannot be moved for inspection or repair, *i.e.* permanent mooring arrangements. The most common inspection method is manual non-destructive testing (NDT) using trained divers; however, due to health and safety concerns, divers are not permitted to inspect a chain in the splash zone area [4]. Removing and replacing mooring chains for inspection is a costly and unreliable method due to the difficult operational in-situ conditions. Due to the limited access and inspection costs of conventional inspection techniques (*i.e.* ROV inspection, chain removal, divers), in-service applications have been introduced, including climbing and crawling robots. Because of the complicated climbing structures presented by mooring chains, few attempts have been recorded regarding the development of chain-climbing robots; in other words, the chain structure is discontinuous, curved, orthogonal and consists of uneven surfaces. Most of chain climbing robots are research based and unable to extend beyond the initial laboratory experimental stage. Moreover, when considering climbing and crawling robots, chain climbing can be introduced as an area that needs to be developed further. When considering the state-of-the-art chain inspection/climbing mechanisms, development of a new lightweight robotic mechanism/platform that can climb mooring chains both in air and in water is needed.

1.2.1 Research gap 2- automated inspection (Mooring chain crown NDT)

According to the existing literature on chain inspection (*i.e.* mooring chain NDT), only a few attempts have been made to automate the NDT process. Compared to the evolution of automated NDT, chain inspection has not been developed to the level of

commercialisation. The current state-of-the-art automated chain inspection mechanisms are designed to investigate the weld area of a chain link. At TWI Cambridge, a study was carried out to understand stresses between mooring chain links and potential fatigue damage. Residual stresses around the interlink contact zone were analysed during this research and potential fatigue damage around the crown of the chain link was investigated. In the current automated studies, the primary concern was to investigate the weld area of the chain. According to the findings in [7] [8], chain crown investigation was also identified as crucial. The capability of using conventional NDT techniques for crown inspection is limited due to the complex geometrical features, *i.e.* curved, round, overlapping with the orthogonal chain link, rusted etc. Therefore, a novel automated friendly NDT technique that can cope with in-situ conditions is needed.

1.3 Aims and Objectives

The focus of this research is to mitigate the challenges set out by the conventional mooring integrity assessment. The proposed solution will ensure the structural health integrity of FPSO mooring chains by introducing new automated platform and an inspection technique.

The primary aim of this thesis is to design and prototype a new light weight, fast moving, robotic platform which can be applicable for both air and underwater. The design of climbing robots depends on the application field. However, the primary common requirement of all climbing robots is the need to maintain secure and required surface attachment climbing on the given structure.

Design and prototype of a new inspection method for chain crown can be introduced as the second main aim of this research. Inspection of chain crown can be introduced as an emerging NDT requirement. The aim is to establish an automated technique which is capable of chain crown inspections both in air an underwater.

The individual objectives required to achieve the research aims include:

- Investigation of the robotic requirements for chain climbing and chain inspection. Due to the challenging architecture presented by the mooring chains, it is essential to understand the requirements before the development of the robot. Mooring chain crown inspection has not been studied thoroughly. Therefore, an extensive investigation should be carried out to obtain requirements.

- Design and prototype of the chain inspection platform. As it was mentioned previously, only a few attempts have been made in order to establish automated chain climbing techniques. First of all, a study should be carried out to design an orthogonal chain climbing platform. Followed by misalignment climbing / adaptation. Straight mooring chain climbing is considered in this research. However, some misalignments are inevitable.
- Design and prototype of an automated chain crown inspection mechanism. As it was mentioned previously, chain crown inspection has not been studied compared to the chain weld inspection. Therefore, a suitable inspection should be selected and automation capabilities should be investigated.
- Laboratory trials for both chain climbing and inspection should be carried out in order to prove the concepts.

1.4 Contribution to Knowledge

1.4.1 Magnetic Adhesion Tracked-wheel Crawler

An industrial need was identified in the literature for automated mooring chain climbing, *i.e.* a climbing robot. Due to the complex geometry and challenging operational conditions, few studies have been conducted on chain climbing. Few robotic/automated attempts have been studied in the literature on chain climbing. In addition, according to the published literature, a successful technique that is capable of working both in the air and underwater has not been identified. Arm, gripper and slider techniques have been used in past chain climbing attempts, but magnetic adhesion and tracked-wheel principles have not been used. Therefore, an orthogonally positioned magnetic adhesion tracked-wheel robot has been developed. The proposed lightweight, easily deployable robotic climber was tested in air. The demonstrated technique can be adapted for underwater use. The feasibility of using orthogonally placed magnetic adhesion tracked crawler units to climb mooring chains has been established.

1.4.2. Adaptable Climbing Robot for Misaligned Chains

A vertically hanging mooring chain is considered in this research. However, some misalignments are inevitable, *i.e.* chain twist. According to the recorded literature, misalignment climbing has not been considered to date. Therefore, a modification was added to overcome misalignments. A combination of two locomotion mechanisms has

been used to cope with the misalignments. As a result of this study, a robotic platform that can eliminate concerns relating to misaligned mooring chain climbing has been established.

1.4.3. Automated Ultrasound Inspection Technique for Chain Crown Inspection

When considering in-service ultrasound inspection of mooring chains, the crown is not a state-of-the-art inspection procedure due to the operational difficulty. Ultrasound inspection of the chain weld area is mandatory, but the chain crown is also identified as a crucial area for inspection. State-of-the-art ultrasound mooring chain integrity assessments are still at the laboratory stage due to the in-field operational complexities and geometrical features of the chain. As an outcome of this study, a novel application of FMC/phased array for chain crown inspection is suggested as a contribution to the knowledge.

1.5 Overall research methodology used in this study

Moring chain used in this investigation is illustrated in Figure 1-4 and Figure 1-5. Moreover, Figure 1-4 demonstrates the un even, corroded, curved and orthogonal surfaces of the mooring chain. Where Figure 1-5 illustrates the physical dimensions.

First, a comprehensive literature survey was carried out to understand the current state-of-the-art automated chain-climbing techniques. Due to the operation complexity, few attempts have been made to date. A design evaluation of climbing robots was conducted in order to select a suitable locomotion mechanism and an adhesion principle. According to the literature, 'tracked-wheel' locomotion and 'magnetic adhesion' were identified as techniques that have not been used for chain climbing. Therefore, the magnetic adhesion tracked-wheel mechanism is proposed in this study. This work has been presented at the peer-reviewed conference, the 20th International CLAWAR ***[D5]*** and the 2017 NSIRC conference***[D6]***, and is also documented in Chapter 2.

Second, the design phase of the climbing robot was carried out. Permanent magnetic adhesion was investigated in the literature in relation to steel surface climbing, *i.e.* ship hull climbing, wall climbing. However, due to the significant curvature of the mooring chain, a bespoke magnetic adhesion module that can be fitted in the tracked-wheel unit was designed. Finite element analysis (FEA) was used during adhesion module optimisation and robot structural design. The magnetic adhesion results were validated with the use of a test rig. Then, a prototype of the magnetic adhesion tracked-wheel robot

was built and tested on a chain segment. Within this part of the research, the feasibility of using orthogonally placed, magnetic adhesion tracked crawler units to climb mooring chains was established. This contribution to the knowledge was presented at the peer-reviewed IEEE International Conference on Industrial and Information Systems (ICIIS) ***[D4]***, published in the peer-reviewed journal, Proceedings of the Institution of Mechanical Engineers, Part I: Journal of Systems and Control Engineering ***[D1]***, and in Chapter 3-4.

A further investigation was carried out regarding in-situ robotic climbing. The climbing robot described in Chapters 3–4 was designed to climb a vertically aligned mooring chain, *i.e.* laboratory conditions; mooring chain links are orthogonal to each other. According to information from field operators, misalignments occur in the chain during vertical hanging (*i.e.* chain twist and tilt). Therefore, a misalignment adaptation technique was added to the existing design. During the locomotion study in Chapter 2, 'legged' locomotion was identified as a suitable technique to overcome surface discontinuities and abnormalities. Therefore, tracked-wheel locomotion was combined with a Cartesian type legged mechanism to overcome misalignments. The climbing experiments were carried out on a misaligned chain segment. Finally, a feasibility study was conducted to establish a misalignment detection mechanism (*i.e.* ultrasound FEA study and an experimental setup). As a result of this study, the idea of an orthogonally placed Cartesian legged magnetic adhesion tracked-wheel robotic platform that can eliminate concerns related to misaligned mooring chain climbing has been established. This work was presented at the 2018 NSIRC conference***[D7]***, in the peer-reviewed journal, Industrial Robot ***[D2]*** and in Chapter 5.

Finally, an automated chain inspection mechanism was introduced. Ultrasound inspection for the chain weld area is mandatory and is a part of the standard practice. According to recent investigations, the chain crown is also identified as a crucial area for inspection. Mooring chain integrity assessment with phased array is still in its infancy due to in-field operational complexities and the geometrical features of the chain. Therefore, this part of the research was carried out as a feasibility study for a novel NDT application. The full matrix capture (FMC) data acquisition technique was used in the interest of enhancing the quality of the NDT images. Mooring integrity inspection needed to be conducted in both air and underwater. Therefore, a continuous water supply wedge was designed in order to provide a marine coupling environment in the air. A five-axis automated manipulator was designed to simulate the automatic inspection capability. Within this study, a novel application of FMC/phased array is demonstrated for chain crown inspection, and

laboratory experiments were carried out with the use of an automated manipulator. This contribution to the knowledge was presented in the peer-reviewed journal, *IEEE Access**[D3]*** and in Chapter 6.

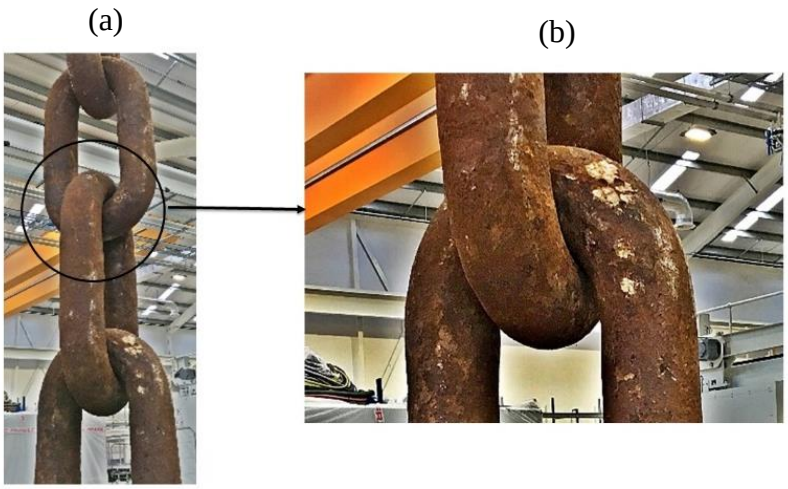

Figure 1-4: (a) Mooring chain sample. (b)Mooring chain's rusted, uneven, curved orthogon chain clinks (sample image)

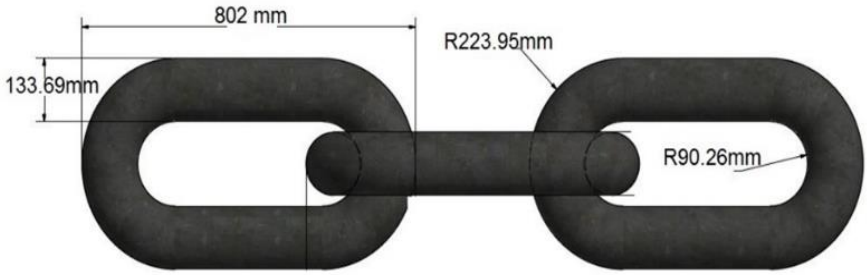

Figure 1-5: Schematic of the chain used in this research

1.6 Thesis Outline

Chapter 2 presents a review of previously published work, *i.e.* literature on automated mooring chain-climbing robotic attempts. Each subsection concludes with an identification of the gaps in the current knowledge and practice. This chapter also includes a review of the commonly used robotic locomotion mechanisms and adhesion techniques.

Next, a design for a novel magnetic adhesion tracked-wheel is proposed and documented in Chapter 3. This consists of the design for a bespoke magnetic adhesion module and a tracked-wheel unit.

The prototype of the novel crawler robot is presented in Chapter 4, *i.e.* the very first approach to using magnetic adhesion and tracked wheels for chain climbing. The FEA used in the adhesion module design (in Chapter 3) is validated in this chapter. The experimental climbing tests are presented at the end of this chapter, *i.e.* vertically aligned mooring chain climbing.

Then, mooring chain misalignments that are commonly evident in vertical hanging are discussed. Required changes to the existing crawler robot are presented, with a mathematical explanation. A modification was added to the robot leg to mitigate misalignments. The proposed robot was prototyped and tested, as discussed in Chapter 5. In order to estimate misalignments, an ultrasound-based feasibility study and laboratory experiments were conducted, and these are presented at the end of the chapter.

Due to the complex geometry and lack of literature, mooring chain crown inspection has not been studied in depth to date. Therefore, a novel automated application of ultrasound full matrix capture for chain crown inspection is presented in Chapter 6. The technique presented in Chapter 6 is the first automated chain crown inspection mechanism that uses an ultrasound phased array along with full matrix capture.

Finally, in Chapter 7, the work presented in the thesis is reviewed and concluded, with recommendations for further work, *i.e.* further development of the robot and NDT robotic manipulator integration.

Chapter 2: Automated chain climbing literature review and climbing robot design review

2.1 Overview

With the significant developments in automation, the connection between industry and robotics has strengthened. A wide range of robotic applications have been introduced in the manufacturing and distribution industry to minimise the physical effort required by humans. With the advancements in the industry and its requirements, robotics applications have become advanced and innovative. When considering structural health monitoring, the involvement of robotics is considerably low due to the complex non-destructive testing (NDT) requirements. Structural health monitoring is often carried out using manual means, which increases downtime and jeopardises the health and safety of NDT operators. Most applications that require structural health monitoring/testing are categorised under operator safety-critical structures. The deployment of human NDT operators involves downtime for reasons of health and safety. Moreover, the cost of an experienced operator is considerably high [9]. Therefore, robots have been introduced as NDT tool carriers (*i.e.* inspection robots are used for ship hulls [10], mooring chains ***[D1]***, long weld lines [11], oil storage tanks [12], wind blades [13], subsea risers [14] etc.). Robotic platforms that can perform structural assessments can negate the effects of hazardous working environments for humans. Due to the in-situ operational quality of robotic platforms, inspection downtime can be minimised.

The primary goal of this chapter is to present the literature survey to find the technical requirements for a chain-climbing robot. Only a few chain-climbing attempts have been recorded in the history of robotics, and each robot is evaluated in this chapter to understand its capabilities and limitations. The selection of the locomotion and adhesion mechanism is vital when it comes to climbing robots. Therefore, commonly used techniques are evaluated with examples. Several design review studies have been carried out in the field of wall climbing (examples can be seen in [15] [16] [9]), but mooring chain climbing is different due to its physical structure. Therefore, this chapter presents a classification of robots with consideration of locomotion and adhesion principles.

2.2 State-of-the-art chain-climbing/inspection approaches

Due to the complexity of the mooring chain structure, only a few attempts have been made to establish a robotic/automated system that can operate both in air and underwater. Most of these are at the research stage and are unable to extend beyond the initial experimental stage; in other words, most of the mechanisms are still at the development stage. Current automated climbing mechanisms are listed below:

'MoorInspect', presented in [17] [18] [19], was a European Commission (EP) framework programme, a collaborative project that began in October 2011. This project aimed to prototype an accurate medium-range ultrasonic testing system that could be used to determine the defects in mooring chains in working conditions [18]. A robot that could climb mooring chains in both air and water was developed in order to deliver the NDT unit to the chain. Two paws were introduced to the robot to simulate a human-like climbing method (see Figure 2-1). Two arms/paws were used to pull the robot up the chain by pushing against the chain's crowns at the same time. The outer structure of the robot was longer than a single link because it was necessary to touch both consecutive chain crowns at the same time for a single movement. The weight of the robot (only) was 450kg in the air [20] Moreover, when considering the weight of the NDT collar, it can be assumed that the net weight of the system was over 600kg [21].

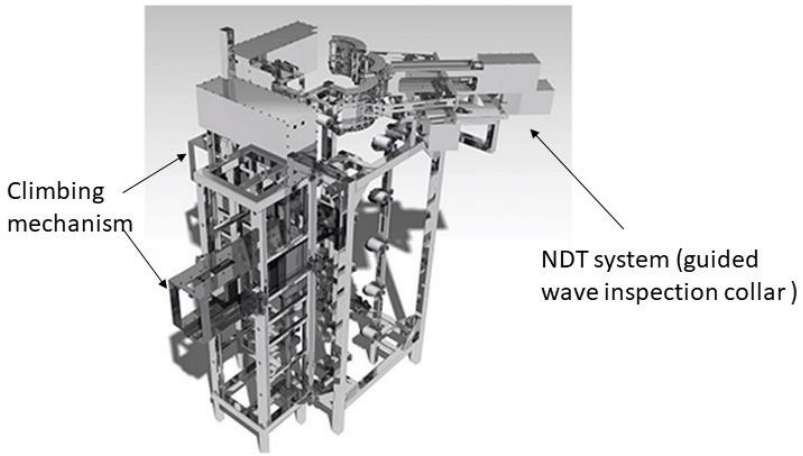

Figure 2-1: MoorInspect climbing robot and guided-wave inspection attachments [17]

The aim of the project presented in [22] was to develop an automated inspection system that could be used to investigate mooring chains in FPSOs (illustrated in Figure 2-2). The chain-climbing robot was developed by CYBERNETICS^{TM} for subsea cleaning and inspection of anchor chains. The climbing method used in this robot was influenced by the human-like climbing method. Two claws were used as the locomotion mechanism (*i.e.* one

claw was used to hold the chain link while the other claw was placed on the next chain link). The control system was powered by hydraulic and electric supplies from an external ROV. The robot was equipped with a vision system and an image-processing unit for NDT. A man–machine interface was introduced to the system. In this way, an additional human inspector was able to be involved in the integrity evaluation process [22].

(a) (b)

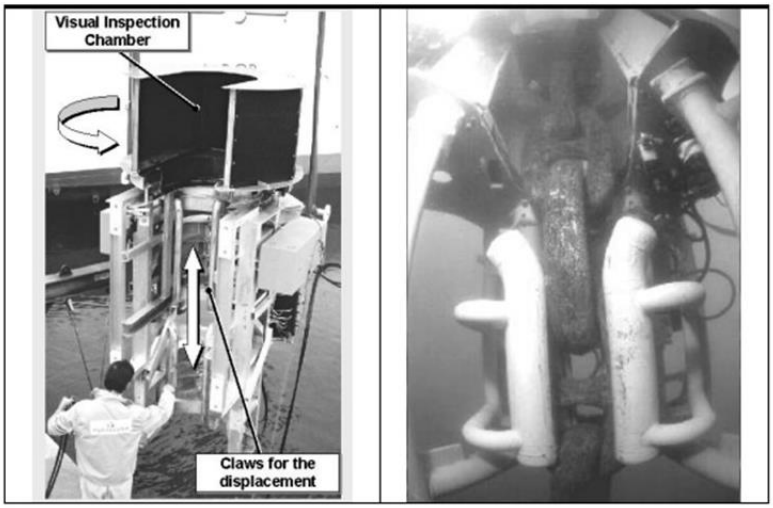

Figure 2-2: The anchor chain-climbing and inspection mechanism [22].(a) robot. (b) testing

(a) (b)

Figure 2-3: Automated weld inspection mechanism [23]. (a) Prototyped version. (b) testing

The automated mechanism presented in [23] was developed (see Figure 2-3) to investigate stud-less mooring chains (111mm to 185mm). During the manufacturing process for the chain links, the 'flash butt welding' method was used to join the bent steel bars. According to the project specifications, welded area investigation was considered the main objective. Establishing an 'in-line' inspection system was introduced as the secondary objective: a system that could be used for ultrasonic inspections without hindering production. This

system was able to detect flaws in the welding zone on both sides and generate visual warnings. Apart from the abovementioned real-time flaw detection, a hard copy of the inspection results was provided to an operator for further investigation. In the interest of detecting inner-plane imperfection, each pair of transducers was configured in both pulse-echo and transmit-receive modes.

The conceptual climbing mechanism illustrated in Figure 2-4 was designed to overcome the limitations of in-situ mooring chain inspection [24]. The main idea was to develop a system that could be operated without bringing the chain on board (removing the chain for inspection is very expensive and can cause production delays). A nozzle that directed a high-pressure water stream was attached to the robot for cleaning/removing marine growth and rust scale [24]. During the first part of the project, a crawling mechanism was developed; however, according to the TWI's analysis of the project, the robot's crawling system was unable to perform as expected. The fundamental motorised climbing mechanism relied on passive friction; however, due to the in-situ condition of the chain surfaces, relying on friction (friction due to a grip) was not suitable. Therefore, the robot's locomotion mechanism was changed to an independently controlled, gravity-assisted cable system.

(a) (b)

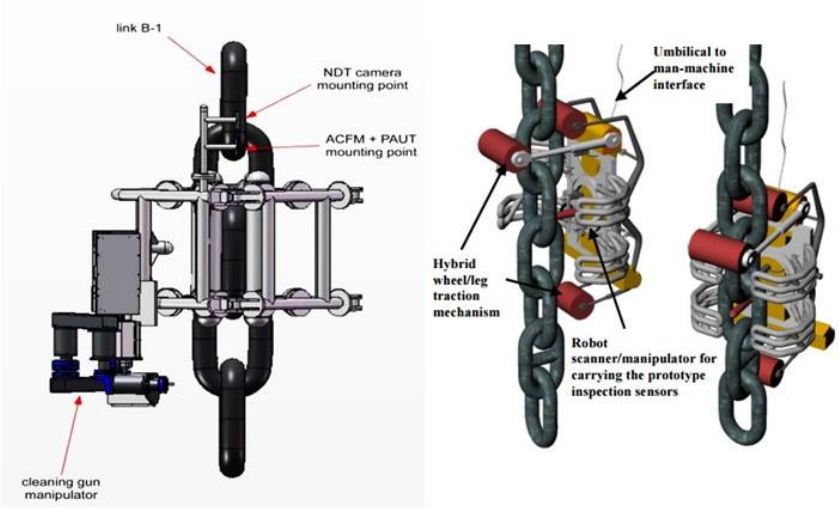

Figure 2-4: Chain test inspection robot [24]. (a) conceptual design 1. (b) conceptual design 2

The 'CIRUS' chain inspection mechanism presented in [25] was designed as a robotic inspection system that could be used at the chain-manufacturing stage (see Figure 2-5). Providing an automated solution to the weld inspection at the manufacturing stage was the primary concern of this project, *i.e.* not an in-situ climbing mechanism. The proposed

system consisted of a chain position mechanism and an ultrasound inspection mechanism. The chain position mechanism was designed in order to place the chain in the inspection module.

(a) (b)

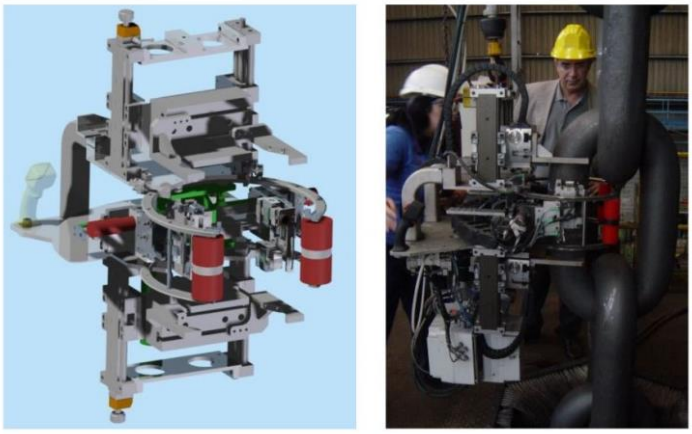

Figure 2-5: The CIRUS manufacturing chain inspection robot (a) CAD design (b) field test [25]

The inchworm – Stewart platform chain-climbing mechanism proposed in [26] [27] was designed as a combination of two locomotion mechanisms (see Figure 2-6). The inchworm locomotion was proposed to climb the chain and the Stewart platform was used to change the orientation of the robot. This teleoperated climbing robot is still at the laboratory prototype stage and should be tested for climbing. Currently, the robot is designed to work underwater; in order to demonstrate in-air usage, the weight of the robot will need to be reduced (*i.e.* the current weight ≈100kg).

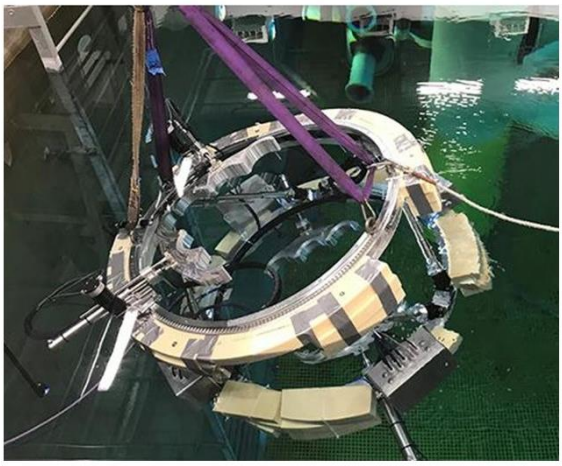

Figure 2-6: RIMCAW chain climbing robot [26]

ROVs are the most commonly used industrial practice when it is necessary to conduct a task in subsea conditions. Most mooring-related ROV assessments are carried out using visual inspection. Visual inspection mechanisms are teleoperated and can be attached to

an ROV that can take the device close to the chain. The Welapetega chain-inspection system (presented in [28] [29]) was designed to measure the dimensions of a mooring chain link when the chain is under working conditions. The system is powered by an ROV and a semi-automated measuring device (see Figure 2-7(a)). Another ROV-assisted chain inspection mechanism is presented in [30]. A gas spring measuring mechanism was designed to record the mooring chain's physical measurements when dragged along the chain surface by an ROV (see Figure 2-7(b)).

(a) (b)

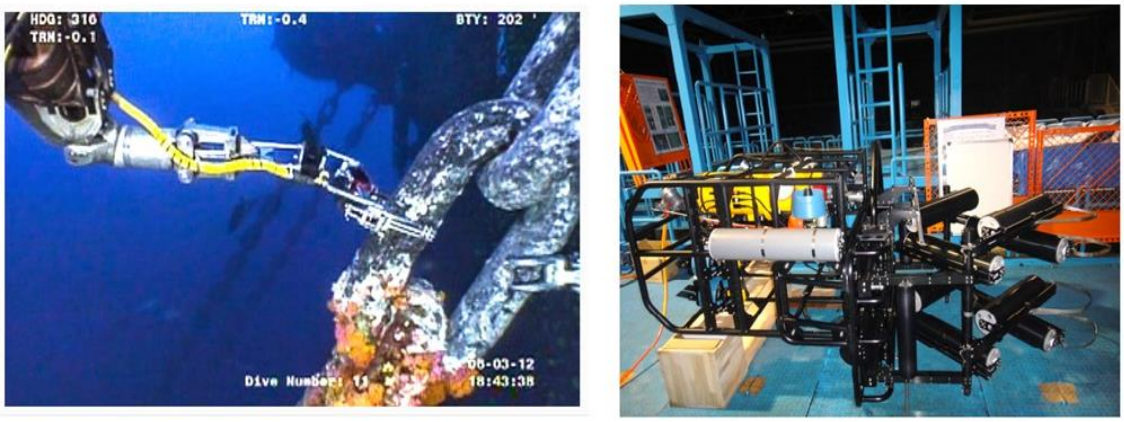

Figure 2-7: (a) Welapetega chain inspection system [28]; (b) gas spring inspection tool [30]

2.3 Other mooring-integrity-related studies

At TWI Cambridge, numerical/experimental analysis was carried out to understand the stresses between mooring chain links and potential fatigue damage. Residual stresses around the interlink contact zone were analysed during the research and potential fatigue damage around the chain crown was investigated [31]. A study was carried out in [32] to reduce the uncertainty of mooring lines by introducing a new technology that can measure mooring line angle and line tensions. A frictionless theory that predicts the resultant torque and 'lifts' in the link is presented in [33]. Safety management in floating platforms (Deepwater stations) is discussed in terms of the design and risk assessment details of mooring systems in [34]. Another study was conducted to determine the rate of wear of mooring chains in [35]. The presented test results are based on various axial loadings and specific angular displacements using dry/wet mooring chains. A method to determine the corrosion loss of low-alloy steel chains is presented in [36] (considering water temperature, salinity, water velocity, and surface roughness). The effects of

microbiologically influenced corrosion (MIC) and pitting corrosion on mooring chains are investigated in [37] .

2.4 General robotics locomotion principles

When considering the mechanical aspects of a robot, locomotion can be viewed as one of the most important concepts because the entire structure of the robot depends on the locomotion. There are several types of locomotion mechanism used in robotics and, in order to select the most suitable mechanism (for a specific task), it is necessary to understand the behaviours (manoeuvrability), pay load, working conditions, adhesion mechanism, and mechanical/electrical/controlling limitations. The shape of the structure and the size of the robot depend highly on the selected locomotion. Therefore, it is vital to consider different locomotion techniques and evaluate these according to the specified task, *i.e.* mooring chain climbing.

2.4.1 Legged-arm locomotion

Legged robots have been used in robotic applications when there is a discontinuous space or discontinuous path to travel. Individual leg manoeuvrability has been used in these types of robot to walk along uneven, discontinuous, non-homogeneous terrains (*i.e.* when the robot has to step over an obstacle). The number of legs is decided according to the complexity of the task and also stability. Several controllable active joints can be introduced to a leg after considering the end effector requirements and the stability of the

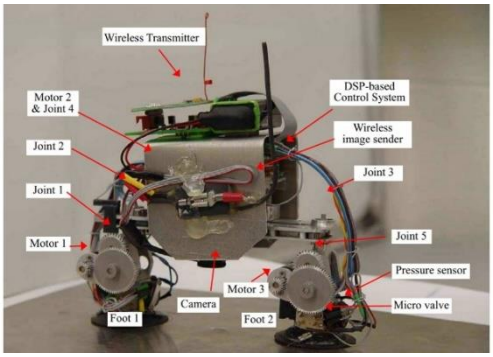

Figure 2-8: Illustration of a micro biped robot with vacuum suction cups for non-destructive structure inspection [39]

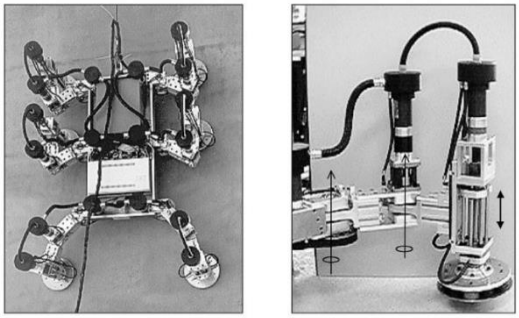

Figure 2-9: Illustration of a six-legged robot with electromagnetic end effector [152]

robot. Additional legs/arms can enhance the payload capacity and the stability, but this also increases the weight of the system [38]. Examples of legged robots include two-legged robots (biped) [39] [40], four-legged robots [41] [42], and six-legged robots [43] [44]. Vacuum suction cups, grasping grippers, or magnetic devices as the end effector of the robot leg are the most common practices in legged climbing robots, *i.e.* the biped robot design for NDT applications illustrated in Figure 2-8 uses vacuum suction cups and the six-legged robot illustrated in Figure 2-9 uses electromagnetic grippers. Planning the gait (pattern of movement of the limbs) can be identified as the most challenging area of legged robot design (*e.g.* the six-legged robot gait planning presented in [45] and the fuzzy multi-sensor data fusion system for a legged robot presented in [46]).

2.4.2 Tracked/wheeled locomotion

Tracked and wheeled locomotion can be seen as the most common locomotion mechanisms in robotics because they involve less mechanical complexity and faster movement (relatively). Tracked robots are often used for maintenance and inspection purposes due to their rigidity, stability, surface adaptation, and payload capacity. Examples of magnetic adhesion tracked robots are presented in [47] [48] [49] [50]. Tracks can be designed according to a given purpose; *e.g.* a robot with four magnetic tracks designed to crawl along curved surfaces is presented in [51] (see Figure 2-10(a)). Triangular tracked robots are very popular when it is necessary to make inner plane transitions (*e.g.* as presented in [49]). Rotation about a point can be performed by driving tracks separately (*i.e.* using a differential drive) and this feature enhances the manoeuvrability of the robot [47] [48].

(a)

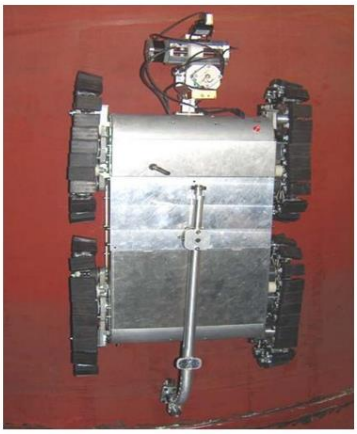

(b)

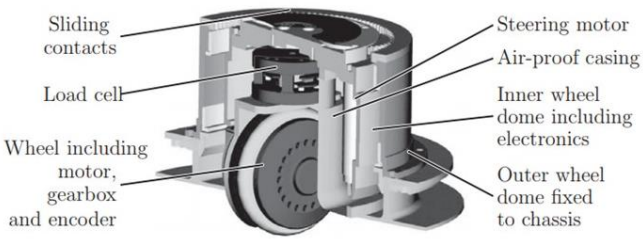

Figure 2-10: (a) Adaptive tracked climbing robot [51]; (b) CROMSCI negative pressure-assisted wheeled robot [59]

Wheeled locomotion is similar to tracked locomotion when considering the degree of freedom, mechanical attachments, motor drivers etc. However, in tracked locomotion, an extended flat traction area between the track and the climbing surface is considered. Therefore, tracked climbing robots are suitable for driving over obstacles and rough uneven surfaces (*i.e.* a mooring chain surface). When considering vertical axis climbing, it is necessary to take into account the traction force. To increase the gripping/traction force of a wheeled robot, the number of wheels can be increased. However, compared to tracks, wheels are more flexible in steering. Some wheeled wall-climbing robots use magnetic wheels as both adhesion and locomotion mechanisms (examples of magnetic wheeled robots are presented in [52] [53] [54] [55] [56] [57]). Some robots use a surface adaptive mechanism for adhesion, such as the six-wheeled robots with adaptable magnet suckers studied in [58]. Vacuum and negative-pressure concepts are also being used with wheeled-type robots (see Figure 2-10(b)) [59] [60].

2.4.3 Sliding frame locomotion

Sliding frame, sliding structure robots (*e.g.* [61] [62] [63] [64]) are another example of a common locomotion mechanism that uses magnetic [65] or pneumatic [66] [67] adhesion. The shape of the sliding structure and the adhesion mechanism are dictated by the application (*e.g.* the robot used to clean the spherical surface of the National Grand Theatre in China, presented in [68] (see Figure 2-11(a)). In this robot, clutches were introduced as grippers). A grit-blasting robot is another example; this robot uses a permanent magnetic adhesion mechanism [69] ((see Figure 2-11(b)) with slider structures. Sliding frame robots are usually constructed with two structures that can make linear or rotational moments relative to each other. Both structures are supplied with their own adhesion mechanisms and by sliding on each other enable the robot to move. To speed up the movement, it is necessary to increase the physical parameters of the structures. Therefore, in most cases, these robots are relatively slow and large.

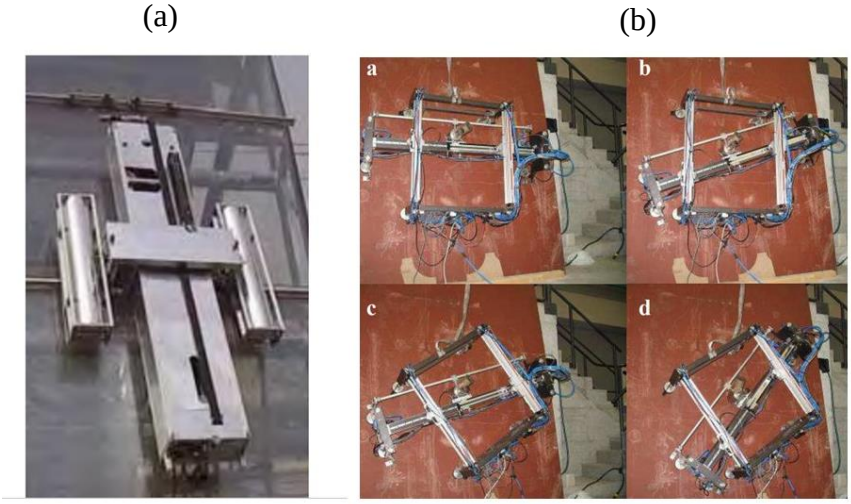

Figure 2-11: (a) Sider robot used to clean spherical surfaces [68]; (b) slider robot for grit blasting [69]

2.4.4 Wire and rail locomotion

Locomotion that involves wires and rails is used mainly for maintenance and cleaning activities due to the straightforward dynamics. The robot schematic illustrated in Figure 2-12(a) is an example of this category [70]. This system uses a conveyor belt that connects ground and roof to move along the surface in order to conduct NDT. Although this type of mechanism allows additional payload capacity and stability in the robot, the overall system is ineffective when considering a complex, taller, or underwater structure (when there is no place to position conveyor belts). More wire-driven applications are studied in [71] [72].

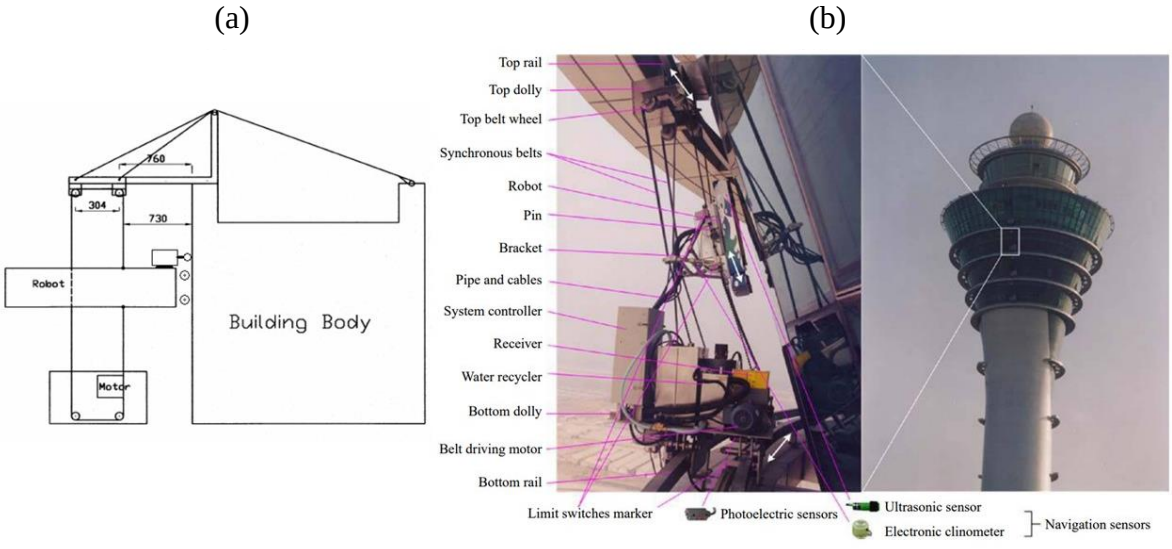

Figure 2-12: (a) Block diagram of the tile-wall robot system [70]; (b) robotic cleaning system for glass facade [71]

2.4.5 Hybrid locomotion

When the terrain/climbing structure is significantly complicated, a combination of techniques is known as hybrid locomotion is used. In most cases, a combination of the previously discussed locomotion techniques is used in this method. Combining multiple locomotive mechanisms to utilise the best qualities of each is the main advantage of this concept. However, it also significantly increases the control complexity. For example, the robot presented in Figure 2-13(a) [73] merges legged locomotion and wheel locomotion to move up and down and overcome disturbances/obstacles of 10–12cm [74]. Before the combination of locomotives, only obstacles under 1cm could be overcome.

(a) (b)

Figure 2-13: (a) Alicia 1 single adhesion modular; (b) Alicia 3's obstacle avoidance procedure [153]

The robotic platform illustrated in Figure 2-13(b) is equipped with three vacuum suction adhesion modules that are connected by a rigid attachment that has a unique rotation joint. In this example, it is clear that a combination of locomotion can enhance the climbing

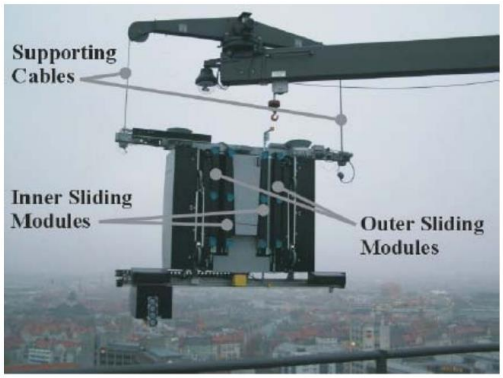

Figure 2-14: Façade-cleaning operation using the SIRIUSc robot and its base station on the roof of a high-rise building [75]

capabilities of the robot. The robot SIRIUSc [75] is another hybrid locomotion mechanism (see Figure 2-14). Previously discussed wire and sliding frame mechanisms are combined to build the facade-cleaning robot.

2.5 Adhesion mechanisms

An adhesion mechanism is the next most crucial mechanical feature that should be considered during the design and planning because the rest of the robot structure needs to be designed accordingly, *i.e.* locomotion and adhesion dictate the structure, weight, control etc., of a climbing robot. However, there is a correlation between the locomotion and adhesion mechanisms. Therefore, it is imperative to consider both locomotion and the relevant adhesion mechanism during the initial stage of the design. Moreover, the required payload, locomotion, environment, manoeuvrability etc., need to be considered in the design of the adhesion mechanism. The following section illustrates the most commonly used adhesion principles.

2.5.1 Vacuum adhesion

Negative pressure suction, commonly known as vacuum adhesion, is often used in wall-climbing robots due to surface adaptability (especially when considering non-ferromagnetic surfaces). Three different methods of implementation can be considered: 1) whole or cavity en-suited with the robot body [76] [77] [78] acts as a suction cup (vortex-type climbing robots); 2) suction cups are attached to the locomotion mechanism (*i.e.* end of the leg) [39] [43] [79]; 3) suction cups are mounted under the chassis of the main body [80]. Similarly, it is possible to categorise negative-pressure developing techniques into seven main categories: 1) suction engine [59] [81]; 2) vacuum generator with pipes [79]; 3) a hydraulic generator connected to the robot by a hose in the tether link [82]; 4) a plunger pump driven by a DC motor [43]; 5) a spinning-motor-driven centrifugal impeller [76] [77] [83] [84]; 6) common passive suction cups [85]; 7) a vibration mechanism to generate adhesion [86]. The vibration mechanism is also known as vibration suction [87] [40] [88] [89].

However, when considering rough surfaces, vacuum adhesion demonstrates poor results because surface quality is very important for suction mechanisms. Moreover, due to air leakage from rough surfaces, the vacuum adhesion method may not be suitable in cases in which there is an uneven surface (*e.g.* the mooring chain surface is rough and uneven).

(a) (b)

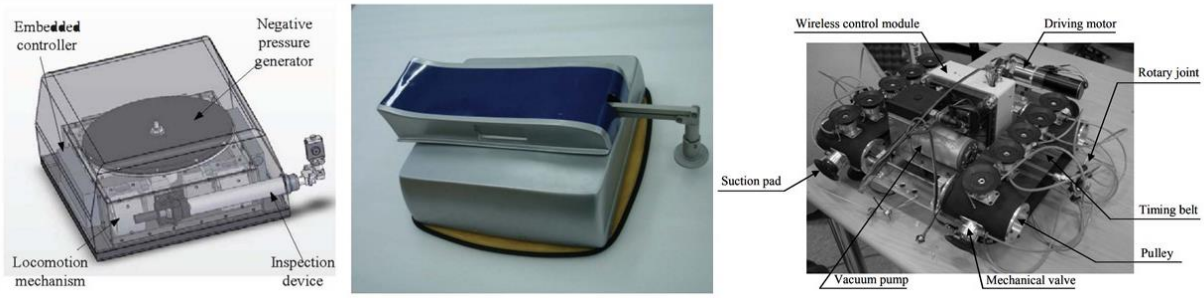

Figure 2-15: (a)Vortex-type suction mechanism assisted robot [77]; (b) suction cups – tracked crawler robot [151]

2.5.2 Magnetic adhesion

Due to the magnetising properties of rare earth magnets, this adhesion mechanism can only be used when the robot operates on a ferromagnetic surface. Both electromagnets and permanent magnets are used in this adhesion mechanism. Due to its high reliability, efficiency, and payload capacity, magnetic adhesion has been adopted in various types of climbing robot. The adhesion of the mechanism can be pre-determined according to the properties of the magnet, the magnet–surface air gap, magnet orientation, and magnet placement. In the studies presented in [90] [91] [92] [93], properties of permanent magnetic adhesion were examined with respect to physical parameters such as the air gap, the thickness of the back iron plate, magnet orientations etc. As an example, to achieve a significant increase in the adhesion force, an iron plate was introduced, and magnets were arranged as a yoke (see Figure 2-16(a)).

Several types of magnetic mechanism are used in practical applications: 1) permanent magnets or electromagnets fixed at the ends of the legs [94] [44]; 2) tracks equipped with multiple integrated magnets [47] [51] [49] [50]; 3) magnetic wheels [95] [96] [54] [97]; 4) magnets installed under the robot body (non-contact) [58] [98]. In general practice, physical parameters such as the size of the magnet, properties of the backplate, magnet–surface airgap, type of magnet, and magnet–magnet gap are changed in order to achieve a given force.

The number of winding turns, the radius of the core, and the amount of current that passes through the winding determine the capacity/adhesion force of an electromagnet; *e.g.* the electromagnetic adhesion legged robot design presented in [99]. When compared to permanent magnets, the usage of an electromagnet in climbing robots is low due to the complexity and uncertainty of power supplies. The requirement of high voltage and large windings makes the electromagnetic adhesion technique less attractive for industrial applications [9].

(a) (b)

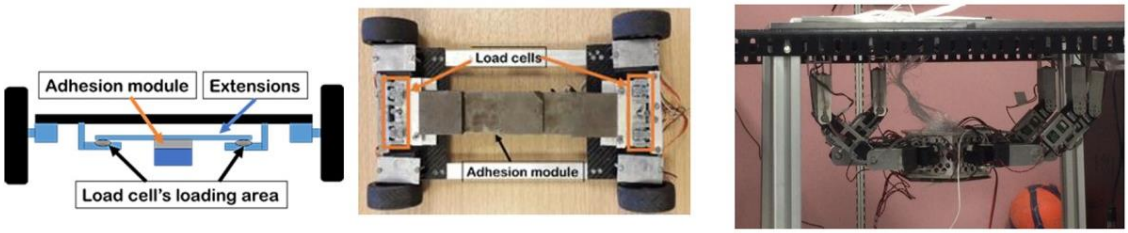

Figure 2-16: (a) Permeant magnet – yoke climbing robot example [9]; (b) electromagnet-assisted climbing robot example [154]

2.5.3 Dry adhesion

Van Der Waals force adhesion, which is commonly known in robotics as the dry adhesion method, is based on the residual attract/repulse forces of molecules. 'Gecko feet' are the main inspiration behind the dry adhesion technique in robotics. Moreover, the Van Der Waals force between a given surface and microscopic fibres is used in most gecko-inspired robots.

Examples of dry adhesion robots are: 1) a gecko-inspired robot with four legs [100] [101] (see Figure 2-17(a)).; 2) a tracked locomotion climbing robot [102]; 3) a tracked robot with a flat, sticky polymer (pressure-sensitive Vytaflex-10 Smooth-on Inc.) on belts [103]; 4) a leg-wheeled robot consisting of four legs and a passive wheel [104]; 5) a multi-spoke structural wheeled-leg locomotion robot with pressure-sensitive adhesive fibres attached to each spoke [105] [106] (see Figure 2-17(b)).; 6) a six-legged robot with polydimethylsiloxane (PDMS) attached under the feet [107].

Robots that are assisted with these types of adhesion mechanism are not designed to carry a payload (considerably large payloads such as ultrasound probes, NDT systems etc.,).

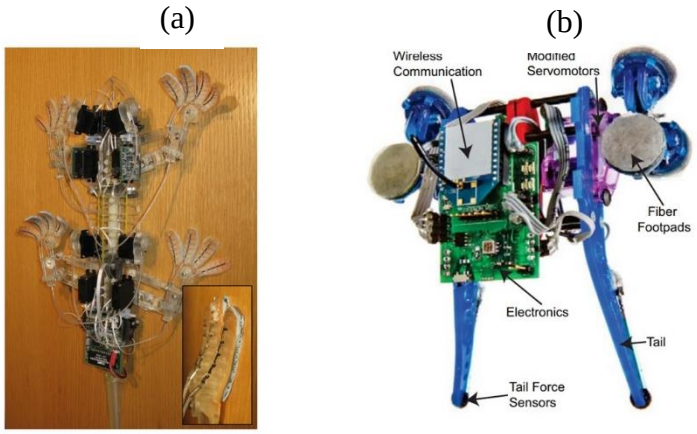

Figure 2-17: (a) Gecko-inspired robot with four legs [101]; (b) adhesive fibres attached climbing robot [105].

2.5.4. Electrostatic adhesion

Compared to other adhesion mechanisms, electrostatic adhesion is a relatively new technique in the field of robotics. The wide range of material compatibility in this technique has attracted robot developers and researchers. The robot must create an electrostatic charge that needs to be the opposite of the surface's charge. The 'opposite charges attract' principle is used to stick the robot structure to a given surface. An example of an electrostatic tracked wall-climbing robot is presented in [108]. It uses lithium batteries to drive two DC motors and excite the electrostatic adhesion force on the compliant interdigital electrode panel. A four-legged robot with a climbing gait similar to a real gecko is presented in [109] (see Figure 2-18). Low noise, low power consumption, lightweight, simplicity, and a less complicated structure are the main advantages of this design. However, in order to carry an industrial inspection payload, the method needs to be developed further. Currently, this technique is not used for underwater activities.

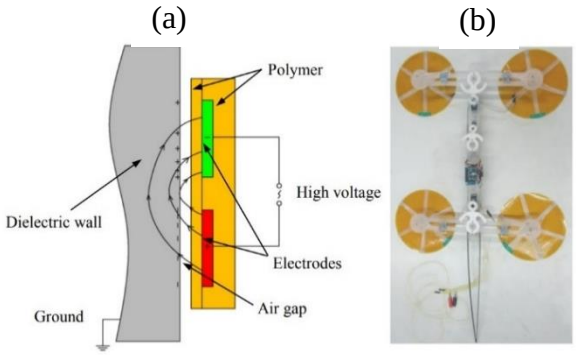

Figure 2-18: (a) Tracked locomotion wall-climbing robot with electrostatic adhesives [108]; (b) four-legged gecko-type robot [109]

2.5.5 Other adhesion mechanisms

Oswald et al. used a hot melt adhesion technique to develop a climbing robot in [110] (see Figure 2-16(b)). A temperature-dependent material was employed as the adhesive and the solid–liquid state transformation in the material was used as the attachment technique. The entire process is temperature dependent, so delays can be expected during this process and surface damage can be observed.

Claw and gripper methods are used in robotics to conduct specific tasks such as tree climbing, rock climbing etc. In common practice, when a robot has to deal with uneven, non-ferromagnetic, and non-electrostatic surfaces, claws and grippers are used. Examples of claws include: the four-legged climbing robot CLIBO has been developed in [111] (see Figure 2-16(b)).. Examples of grippers include: a robot with two grippers fixed at the ends of two arms is presented in [112].

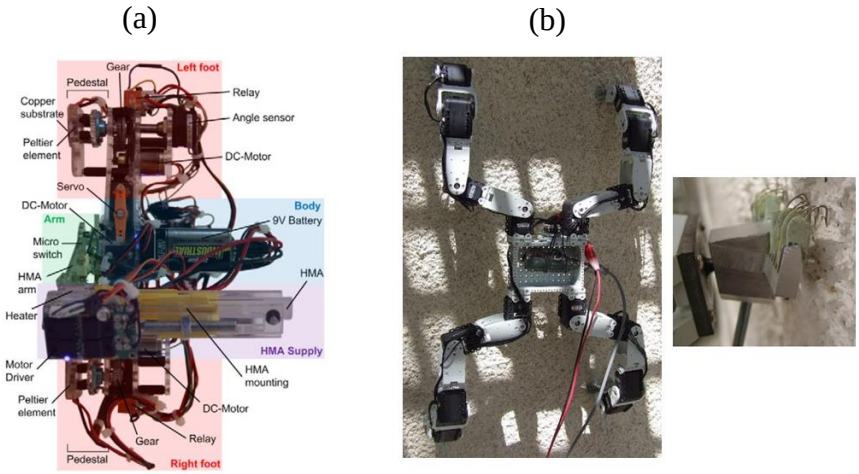

Figure 2-19: (a) Illustration of the hot-melt adhesive robot [110]; (b) climbing robot using claws as adhesives [111]

2.6 Summery of the state-of- the-art

According to the literature, only a few attempts have been made to develop a robotic system that can climb mooring chains due to the complex geometry (*i.e.* orthogonal chain orientations and in-situ chain conditions). Most climbing robots are designed to address single geometric features such as discontinuity, plane changing, underwater climbing, in-air climbing, crawling on a curved surface, moving on a rough terrain etc. However, in the chain-climbing application, all of the abovementioned challenges are involved.

2.6.1 Climbing robots evaluation

The heavy and longer climbing robots discussed above are not easily deployable when considering the offshore environment, catenary curvature and link misalignments. These climbing robots are deployed manually using divers and boats. It is not practically possible to handle a significant weight in a small boat with divers (without lifting equipment). Due to the geometric features of the mooring chain (*i.e.* two curves moveable orthogonal links), it is essential to account for link–link misalignments. FPSO chain links in operating conditions are estimated to experience misalignments in the range of 2–10 degrees. During tidal waves and sudden environmental changes, it is possible for the misalignment to be as much as 24 degrees [113]. When the robot structure is longer than a single chain link, crawling along the catenary curvature is difficult. The gravity-assisted crawling mechanism can cause issues during underwater inspections due to the upward buoyancy forces. Moreover, these systems were tested on ideal chain links, so misalignments were not considered.

2.6.2 Automated manufacturing stage inspection robots evaluation

The abovementioned chain inspection systems can be used to investigate the weld area when the chain links are at the manufacturing stage. However, these automated systems were unable to investigate chain links that were already in use because a climbing or moving method was not introduced in each system. Therefore, handling can be viewed as the main problem with these designs. Moreover, these systems were unable to check the chain crown area, where the integrity can be highly compromised due to residual stress [31].

2.6.3 ROV-assisted inspection robots evaluation

ROVs are unable to access the chain in the air. Therefore, these systems can only be used underwater. Moreover, accessing the splash zone may not be possible with an ROV due to

the limitations associated with underwater ROV manipulation. Measuring the relevant points of the chain may not be practically possible due to marine growth on the chain surface. Moreover, marine growth can profoundly influence the corrosion rate, which can reduce the residual strength by 25% [37]. Microbiologically influenced corrosion can occur under the rust layer. There are different types of mooring chain corrosion due to the variations in water temperature, salinity, pH value, dissolved oxygen, water velocity, and steel composition. These factors can influence the internal corrosion growth rate; therefore, measuring the size of the chain is not suitable to evaluate the integrity of a working chain link. According to the history of mooring chain accidents, ROV inspection cannot be viewed as a reliable method [113].

2.6.4 Summary of the state-of-the-art chain-climbing robots

When considering the literature review, only a few robots have been established for chain climbing. Human-influenced climbing methods/sliding structures [17] [22], cable/gravity-assisted crawling methods [24], ROV-assisted methods [28] [30], and automated inspection techniques [25] [23], are not able to provide a practical approach that can cover the entire chain in working conditions, *i.e.* underwater, in air, misalignments, catenary curvature, in-situ environmental changes etc. The multi-locomotion approach discussed in [26] has not been tested and is still at the laboratory design stage. When considering the necessity of mooring chain inspection, a lightweight, fast, automated, in-situ friendly robotic approach is needed. Studies on the state-of-the-art automated chain climbing techniques were discussed at the beginning of this chapter, along with a critical evaluation. Locomotion and adhesion techniques were discussed with examples to obtain a basic idea of the most commonly used robotic climbing techniques.

The next chapter in this thesis is carried out in order to develop novel mooring chain climbing robot. Specifications of the mooring chain which has been used in this study is illustrated in the Figure 1-4 & Figure 1-5.

Chapter 3: Vertically aligned mooring-chain-climbing robot design

3.1 Chapter overview

As discussed previously, mooring chain or chain climbing is a climbing area that has not been investigated in depth compared to wall climbing. Only a few attempts have been made to establish a robotic/automated system that can operate both in air and underwater. Most are at the research stage and unable to extend beyond the initial laboratory experimental stage. The complicated nature of the mooring chain's physical architecture is the main reason for the lack of investigation. For example, mooring chains are made of two sets of curved iron rings that are kept orthogonal to each other. Therefore, a robot should be able to cope with a link–link discontinuity as well as link orthogonality. Platforms that use mooring chains for stability are often subjected to high tidal waves, storms, and hurricanes on a regular basis. Therefore, the selected robotic mechanism (locomotion, adhesion, and physical structure of the robot) should be able to handle in-situ conditions. Moreover, the locomotion and adhesion mechanism should be able to handle underwater and as well as in air conditions. Due to the orthogonal arrangement of mooring chain links, different types of mooring chain misalignment (discussed in Chapter 5) are presented. This chapter aims to establish a climbing principle for a vertically aligned mooring chain.

As discussed in the literature review, the idea of magnetic adhesion tracked wheels for mooring chain climbing has not been studied. The establishment of a primary climbing/crawling mechanism that can handle the discontinuity and orthogonality is discussed in this chapter, with the use of computer-aided designs (CAD). Magnetic adhesion for wall climbing and steel-plate-type surface climbing has been discussed previously, and the basic principles of magnetic adhesion modules with different orientations have been determined in literature. Due to the unusual structure (curved, rusted etc.) of chain links, a bespoke magnetic adhesion module was designed and optimised with the use of finite element analyse. To understand the structural behaviour against loads (crawler weights and payloads), numerical modelling was carried out and is discussed. Motor requirements were studied after establishing the adhesion module and structure of the robot. The main aim of this chapter is to establish a novel climbing application for vertically aligned mooring chains using magnetic adhesion and tracked-wheel principles. The adhesion technique, motor calculations, structural design, and tracked-wheel design presented in this chapter have been used as design parameters during the prototype of the climbing robot.

3.2 Overall Design requirements / Specifications

According to the available literature, the scientific community has become more interested in the development of climbing robots for industry, *e.g.* ship wall climbing, steel plate climbing etc. Only a few robotic/automated studies have been conducted on chain climbing due to its structural complexity ***[D1] [D4]***. On the other hand, the requirement of chain climbing (mooring chain climbing) is an industry-related task and requirements are based on inspection needs. Mooring chains are made using thick iron rods, which usually hang vertically. Requirements for a climbing robot depend on the application and the method of task execution. Detailed discussion of general climbing robot requirements is presented in [9]. The following points were identified as primary design parameters.

- **Locomotion requirement**: due to the mooring chain's unusual climbing surface, selecting a suitable climbing mechanism is challenging. The ability to change surfaces between orthogonal chain links is considered as a requirement, because mooring chains are discontinuous, being made with two sets of links that are kept orthogonal to each other (see Figure 1-4 and Figure 1-5). Therefore, the crawling/climbing robot needs to cope with this discontinuity. Changing from one plane to another is a highly investigated as well as challenging area in climbing robotics. Due to the orthogonal arrangement of mooring chain links, 3D plane changing is difficult. The chain link shown in Figure 1-4 demonstrates rusted and uneven surfaces as mooring chains are often subjected to extensive environmental change such as tidal waves, wind, and storms. Therefore, the locomotion method should be able to handle the robustness of mooring chains. The adaptability of the locomotion is vital when considering the relative motion of chain links (commonly known as link misalignments). Misalignments are discussed in Chapter 5 and in [19].
- **Adhesion mechanism**: the adhesion mechanism of a climbing robot should be selected according to the application. Mooring chains are made using thick iron rods, and the surface of the chain link is uneven, rough, and corroded due to in-situ conditions. Therefore, the selected adhesion mechanism should be handled/adapted accordingly. When considering in-situ conditions, mooring chains are an amphibious structure, and the adhesion mechanism must be able to work in both underwater as well as in air.

- **Payload capability**: conducting a structural health monitoring assessment is the primary task of a mooring-chain-climbing robot (the real industrial need). Therefore, the robot should be able to provide an appropriate environment for NDT applications, *i.e.* it should be possible to place the NDT device on the robot. Payload capacity and instrument placement on the structure depend on the NDT application, *i.e.* if ultrasound is the selected assessment method, the robot should be able to carry a UT probe and the probe manipulator.
- **Safety mechanism**: this is a non-functional design parameter. The climbing robot needs to be agile and robust (structural hardness) to minimise any damage/impact due to in-situ conditions. Mooring chains are used in the sea; therefore, safety must be taken into account during adhesion mechanism selection, *i.e.* in case of emergency power failure, the robot should be able to maintain its position without creating structural damage by losing grip.
- **Energy consumption**: the energy consumption of a climbing robot determines its efficiency. Locomotion and adhesion mechanisms are the primary energy consumers of a climbing robot. For example, the vacuum suction mechanism has higher energy consumption compared to passive permanent magnetic adhesion. However, the magnetic adhesion mechanism can only be employed on a ferromagnetic surface. Distance power transmission via an umbilical cable can be used for a mooring-chain-climbing robot; however, in order to maximise efficiency, locomotion and adhesion should be selected accordingly.
- **Deployment**: as mentioned previously, mooring chain climbing is an industry-related activity, *i.e.* chain-climbing robots are used as a platform to convey NDT equipment. Therefore, easy deployment ability and retrievability should be considered during the robot frame design phase. A structure/frame that needs to be deployed around a chain link is not practical due to the in-situ mooring chain conditions. The overall weight of the robot should be minimised in order to ease in-situ deployment. As discussed previously, large heavy robot structures are not suitable for in-situ mooring environments. Therefore, deployment and the overall structural specifications should be considered during the initial design stage.

In summery a fast moving (Climbing speed depends on the inspection speed), light weight (should be allow users an easy deployment without using lifting equipment Approx. 50kg or less), easily deployable robotic structure should be developed.

3.3 Selection of locomotion and adhesion mechanism

The Chapter 2 design review considered different capabilities as well as limitations in both the adhesion and locomotion mechanisms that are commonly used in climbing robots. In order to compare the locomotion mechanism with the design parameters, technical properties are tabulated as follows (Table 3-1).

Table 3-1: Comparison summary of commonly used locomotion mechanisms

Compared parameter	**Legged/arm/limb locomotion**	**Sliding frame locomotion**	**Wheel locomotion**	**Tracked locomotion**	**Wire-/rope-assisted locomotion mechanism**
Motion	Not continuous motion	Frame has continuous motion, but adhesion is non-continuous	Smooth and continuous	Smooth and continuous	Continuous
Speed	Slow due to limb movements	Slow	Comparatively fast (depends on the motor speed)	Comparatively fast (depends on the motor speed)	Comparatively fast (depends on the motor speed)
Movement	DOF depends on number of legs (multiple DOF|)	Usually two (planer displacements)	Robot can usually be manipulated in any direction by using differential drive mode	Robot can usually be manipulated in any direction by using differential drive mode	Usually two (planer displacements)
Payload capacity	Low, due to the strength of the limbs/joints	Moderate – usually depends on the adhesion capability	Usually a high payload. Depends on the adhesion capability	Usually a high payload. Depends on the adhesion capability	Very high. Robot is supported by cables
Adaptability	Suitable for rough, uneven and discontinuous surfaces	Mainly used on even surfaces	Suitable for uneven and rough surfaces	Suitable for uneven and rough surfaces	Can be used on any surface but subjected to pulling mechanism placements
Complexity	Highly complex control system due to complex motion/gait planning	Moderate complexity	Less complexity, but can be increased according to the task	Less complexity, but can be increased according to the task	Very simple

The commonly used adhesion mechanisms discussed previously are evaluated in Table 3-2, considering the suitable surface types, payload, and reliability.

Table 3-2: Comparison summary of commonly used adhesion mechanisms

Parameter	**Vacuum chamber (vortex-type model)**	**Suction cups**	**Electromagnets**	**Permanent magnets**	**Adhesion mechanism based on biological models and others**
Suitable surface type	Can be used on non-porous surfaces (any material). Surface must be even and smooth	Can be used on non-porous surfaces such as plane steel, glass. Surface must be even and smooth	Ferromagnetic surface (ferrous surfaces only). Surface quality is not important	Ferromagnetic surface (ferrous surfaces only). Surface quality is not important	Various surfaces according to adhesion properties
Payload	Relatively high but less than suction cups. Adhesion depends on the vacuum	High payload. Depends on the suction capability	These can carry a moderate payload depending on the size of the electromagnet, coil properties, current etc.	Very high, depending on the magnet properties and the thickness of the surface	Usually very low and depends on the mechanical design of the climbing system
Reliability	Moderate. This requires a good seal to avoid air leakage	Good and overall reliability depends on the reliability of suction and surface	The energy consumption of this technique is higher	Reliability is very high due to the passive adhesion quality of magnets	Low when considering industrial structural health monitoring applications

Before selecting adhesion and locomotion mechanisms that are suitable for mooring chain climbing, the following state-of-the-art climbing robot summary was studied. According to the literature on chain-climbing robots, locomotion and adhesion mechanisms can be categorised as follows (refer Table 3-3):

Table 3-3: Summary of state-of-the-art robotic chain-climbing mechanisms

Robot/robots	**Locomotion mechanism**	**Adhesion mechanism**	**Possible issues**
[17] [22] [26]	Sliding frame mechanism	Grippers that can be rested on the chain crown or surface	Due to the sliding frame climbing mechanism, robot must be longer than 2–3 chain links, resulting in increasing the weight of the robot. Robot may not able to achieve the catenary curvature. Entire motion depends on the surface quality/friction
[28] [30]	ROV-assisted method	Springs, automated robot arm/grippers	The entire locomotion mechanism depends on the control capability of the ROV operation. Usually ROVs are expensive and unable to access the splash zone and the in-air part of the chain
[24]	Gravity-assisted crawler – cable mechanism	Gripping mechanism	Gravity cannot be taken as a reliable method of transportation when considering underwater use due to buoyancy forces. The cable-assisted mechanism is unable to provide a practical approach due to the cable attachment near mooring chains

The design review identified and explored numerous locomotion mechanisms and adhesion principles that are used commonly in industry and research. When considering the discussed locomotion requirements (for mooring chain climbing), wheeled, tracked, and legged locomotion techniques seem more suitable. According to the investigation carried out in Table 3-1, the tracked-wheel locomotion mechanism is one of the mechanisms that has not been investigated for mooring chain climbing, *i.e.* sliding frame locomotion and the cable-assisted mechanism have already been studied in the literature and the limitations/capabilities of these mechanisms have been demonstrated. The mechanical and control components needed for wheeled or tracked systems are similar. However, the passive adaptation of tracks provides an additional traction advantage over wheeled mechanisms. Magnetic wheel approach was considered during the selection. However, due to the mechanical complexities it was not selected (*i.e.* Set of wheels should be introduced in order to maintain the balance and it will increase the weight and the

complexity, the adhesion of the wheels cannot be optimised as it is set up during the manufacturing process). As discussed previously, mooring chain surfaces are rough, corroded, slippery, and uneven. Therefore, using a locomotion mechanism that can adapt to an uneven surface is an advantage. However, the tracked locomotion mechanism is unable to overcome significant surface discontinuities (discontinuities that are bigger than the size of the track).

In order to climb mooring chains, the locomotion must be able to handle discontinuities caused by the chain's physical construction, *e.g.* discontinued misaligned and orthogonal chain link pattern. According to the locomotion review above, legged locomotion has been used to climb surfaces with discontinuities. However, when considering mooring chain architecture, a locomotion mechanism that has qualities of both tracked-wheel and legged mechanisms (for adaptation) is needed, *i.e.* a hybrid locomotion or an adaptable tracked-wheel mechanism.

When considering the previously discussed adhesion mechanisms for chain climbing, friction-related mechanisms (used in sliding frames) and arm-related grippers have been studied. Permanent magnetic adhesion, which provides a higher adhesion force by consuming zero energy, has not been studied in relation to chain climbing. Other adhesion mechanisms, such as suction cups, electrostatic adhesion, and hot melt, cannot be used for mooring chain climbing due to the chain's physical conditions (such as amphibious condition and uneven, curved surface). The reliability of electromagnets depends on the power supply. In case of power failure, the robotic system may not be able to recover. Due to the passive adhesion capability of permanent magnets, surface contact is not required. This quality of passive magnetic adhesion can be used against the uneven, curved, rusted, and ferromagnetic surfaces of mooring chains. Moreover, magnetic adhesion is not affected by water or air. Serval studies have been conducted to establish the connection between magnets, magnets orientations, and adhesion forces for wall/steel plate climbing. Even though adhesion between the magnet and the mooring chains is similar to steel plate adhesion, a bespoke study needs to be carried out to understand the feasibility of this technique.

3.4 Conceptual idea for the use of tracked-wheel units

3.4.1 Orthogonal tracked-wheel placement concept

The physical orientation of a mooring chain was considered when establishing the basic idea of climbing. To establish a fundamental climbing/crawling principle, the orientation of a chain was considered as ideal, *i.e.* the face angle of two consecutive chain links is 90 degrees, and the chain is hanging in a vertical plane (no horizontal or vertical moment), as illustrated in Figure 3-1.

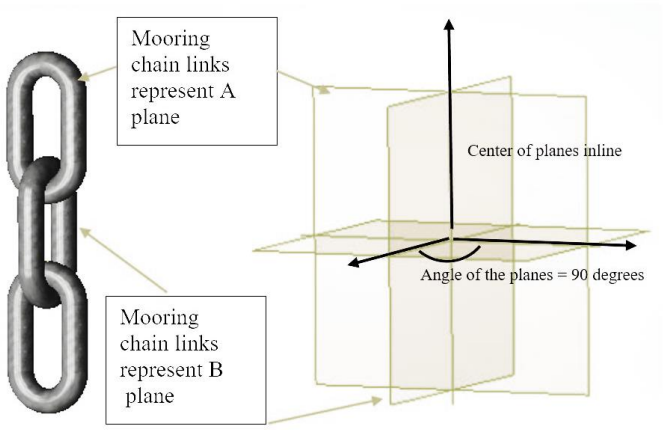

Figure 3-1: Vertically aligned mooring chains and orthogonal chain links

According to the above explained chain link orientation, the basic idea of the mechanism was established. In the literature, magnetic adhesion robots are identified as 'high payload carrying robots', with high stability when considering harsh environmental conditions [9]. Moreover, mooring chains are made of iron; therefore, the use of a magnetic adhesion mechanism for crawling was considered due to the mechanical advantages. The initial idea was established by considering mooring links as iron rods and introducing two tracked-wheel units to represent one plane of chain links, as illustrated in Figure 3-2.

Moreover, in order to travel along the mooring chain, it is necessary to turn the tracked-wheel units 90 degrees at the end of the chain link (to travel along the orthogonal chain link). In the literature search, a number of robots with the facility of changing platforms were investigated. Plane/platform-changing mechanisms are used in complex climbing robots, such as walls, trees, rocks etc. Most of these robots are built from different parts connected by mechanical hinges (modular robots) or complex walking mechanisms (multi-leg climbing robots). Therefore, it is possible to change the current platform by walking/crawling onto the new plane using the front part/legs of the robot, maintaining

balance by keeping the other part/legs on the current platform. Using the abovementioned 'hinge-modular' operation, it is possible to change planes. However, a hinge could not be introduced into this design due to the following practical issues. 1) The centres of the link planes are in line, but the link surfaces (crawling areas) do not coincide with each other. As a result, it is difficult to place a hinge to set up a platform change. 2) At least two tracked-wheel units need to be on the parallel plane to maintain the balance of the robot structure. 3) One of the primary targets of the research is to develop a fast, lightweight, and reliable mooring-chain-climbing mechanism to use for NDT. Therefore, the robot must be able to carry a reasonable payload. Having at least two sets of tracked wheels in contact with the chain enhances the payload capacity and stability. 4) Mooring chains are usually half immersed in seawater and half in air; as such, links are often subjected to bad weather, climate, temperature, and seawater changes. Therefore, the surface of a mooring chain link is not smooth and crawling on it can cause slipping. Using a passive or controllable hinge operation will decrease the structural strength of the robot.

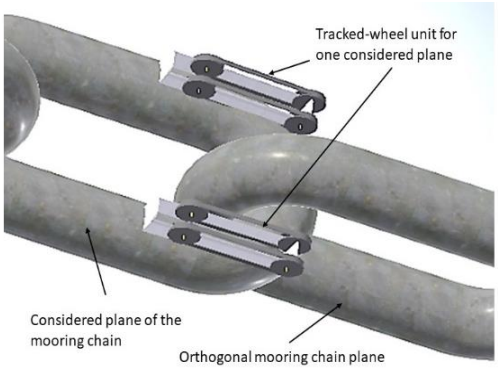

Figure 3-2: Two tracked-wheel units placed on a chain link

After understanding the above concerns, an idea for a set of orthogonal tracked-wheel units was established, rather than changing planes (as illustrated in Figure 3-3). According to this concept, one set of two tracked wheels move on one link while another set moves on an adjacent orthogonal link (see Figure 3-3). Each orthogonal set of tracked-wheel units enables the robot to move along the chain. According to the illustrated tracked-wheel placement, each set of crawlers should be able to support the movement of the robot when it passes the relevant parallel platforms (with respect to each set of crawlers). Due to the

proposed orthogonal placement, it is not necessary to change the planes when it is moving along the chain.

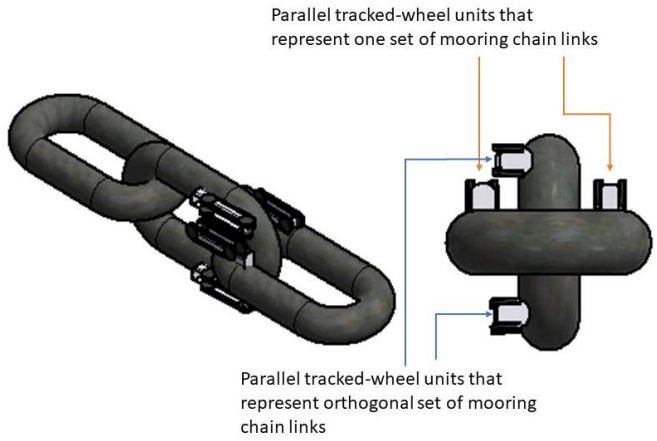

Figure 3-3: Orthogonal tracked-wheel placement on a mooring chain

3.4.2 Tracked-wheel unit placement (tracked-wheel orientation)

A design study was carried out to understand the optimum tracked-wheel position on a chain link while maintaining the proposed orthogonal tracked-wheel concept. The concept illustrated in Figure 3-4(a) satisfies the orthogonal tracked-wheel representation, but it is clear that the gap between the orthogonal tracked wheels is significantly low (see Figure 3-4(b)). When considering the mechanical properties, less space between crawlers is a disadvantage, because the crawlers need to be attached to the main structure and the magnetic adhesion module needs to be attached to the crawlers.

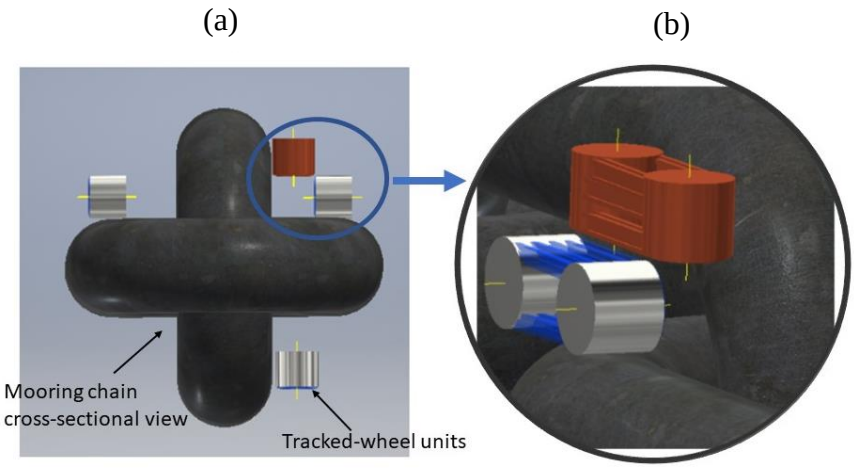

Figure 3-4: (a) Tracked-wheel placement; (b) practical issues of tracked-wheel placement

After considering the design mentioned above, the following orientation was designed (see Figure 3-5). According to Figure 3-5, it is significant that the parallel tracked-wheel concept changed, but the orthogonal placement was still the same. To achieve space between the orthogonal units, one of the parallel tracked wheels was moved to the side of the link. With the new tracked-wheel placement, the space between the orthogonal units increased. It is necessary to ensure there is a reasonable space between the tracked wheels so that collisions do not occur when there is a misalignment in the chain links (chain misalignment is discussed in Chapter 5). Moreover, in this design, there is enough space left on both sides of the tracked-wheel unit to allow for magnet attachment or motor holders.

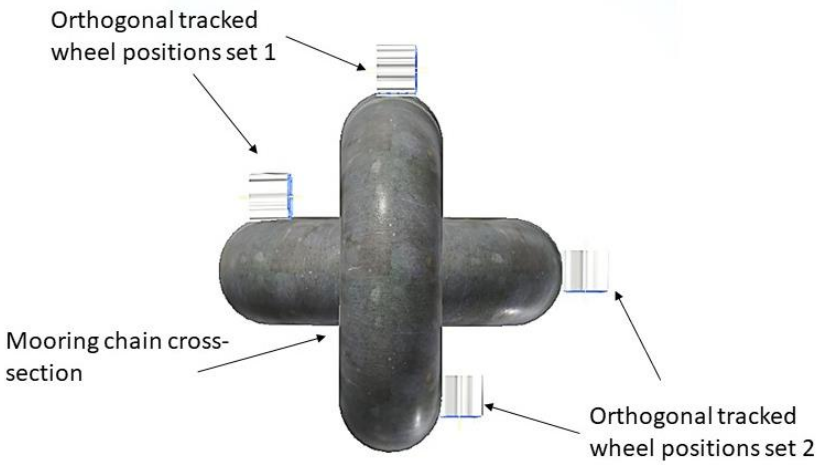

Figure 3-5: Tracked-wheel placement orientation – 02

When considering the disadvantages of the tracked-wheel placement in the above design, it is significant that the parallel tracked-wheel units are not symmetrical and do not rest on the same plane of the link. As determined earlier, magnetic adhesion was selected as an adhesion agent in this study. Magnetic adhesion depends on the ferromagnetic surface area, which is parallel to the adhesion module. Tracked-wheel units placed on the side of the chain links leave the surface earlier, as illustrated in Figure 3-6. This can cause an imbalance in adhesion forces and the crawling pattern, *i.e.* losing grip on one side can cause the entire structure to turn or a change in the crawling pattern.

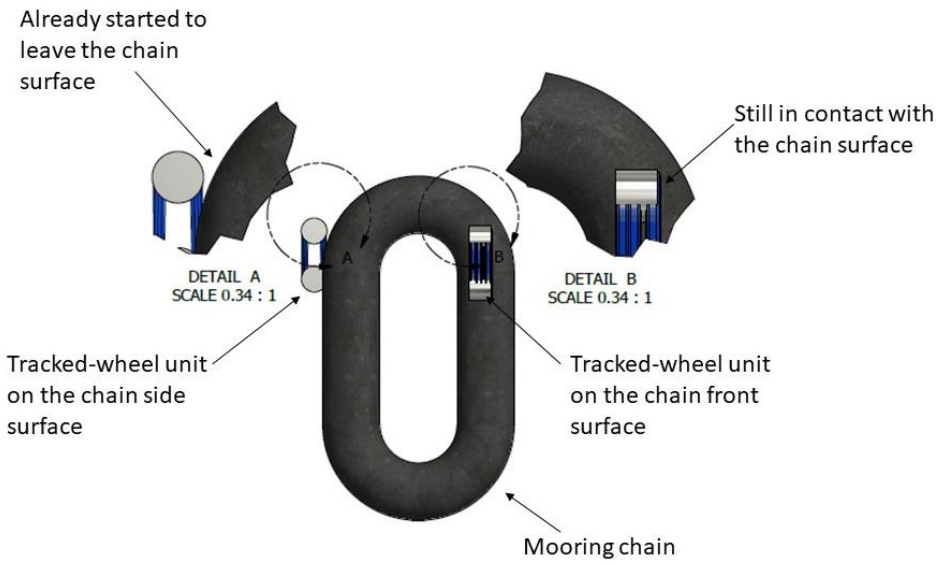

Figure 3-6: Uneven contact time explanation

After considering the above tracked-wheel arrangements, the requirement for a new design with the following capabilities was raised. 1) Arrangement should be able to hold the tracked wheels in an orthogonal position. 2) There should be sufficient space between the tracked wheels. 3) The main frame of the robot should be able to hold tracked-wheel units and should enable easy deployment. The outer frame/deployment design is not discussed at this stage of the study, but it is important to consider during the tracked-wheel placement, *i.e.* placing tracked-wheel units around the mooring chain will not enable smooth deployment. Therefore, at least one side of the chain should remain open (un-enclosed by the structure/tracked wheels). (4) The tracked wheel should be able to provide stable locomotion throughout the climbing. Therefore, a new tracked-wheel orientation was proposed that can fulfil the above requirements. The arrangement presented in Figure3-7 shows four tracked-wheel units (see Figure 3-7(a)), but one orthogonal set is lagging the other. The orthogonal tracked-wheel set in A and B lags when compared to the position of C and D (see Figure 3-7(b–c)). All four tracked-wheel units are placed on the chain according to the orthogonal placement concept and without covering the entire chain cross-section. This will ease the deployment ability of the robot. Therefore, this design was considered as the selected orthogonal placement for the rest of the study.

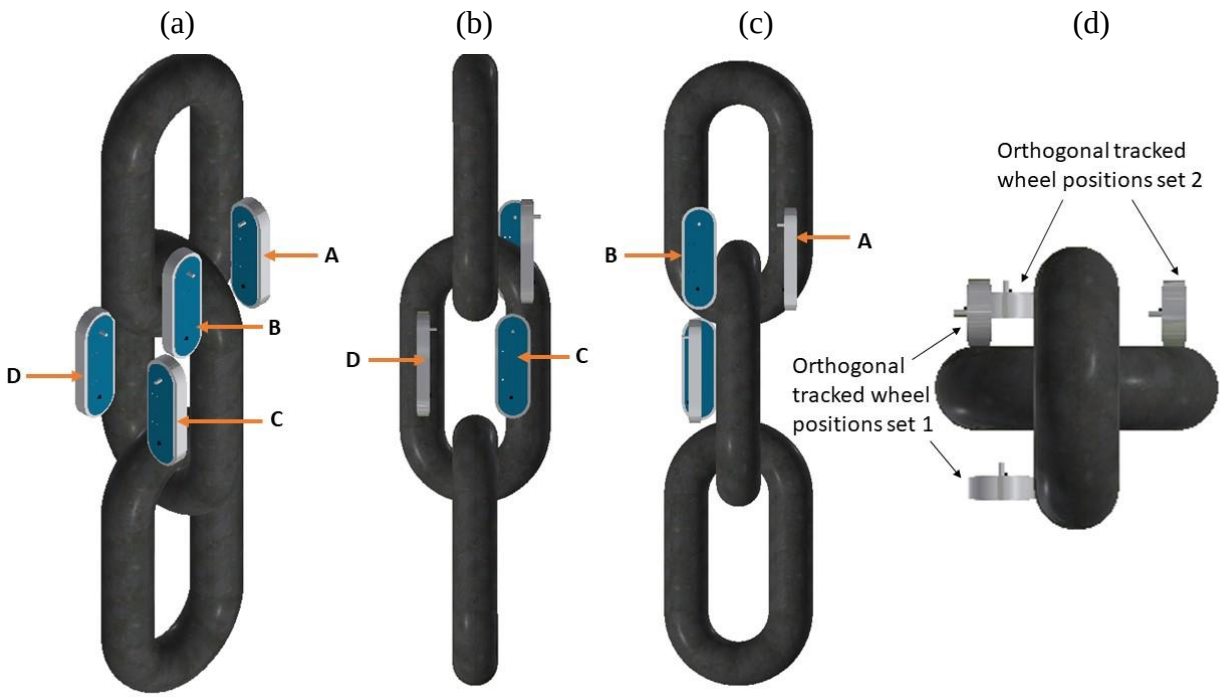

Figure 3-7: (a) Orthogonal tracked-wheel placement – 03; (b) side A – tracked-wheel placement; (b) side B – tracked-wheel placement; (d) tracked-wheel placement cross-section

3.5 Design idea for tracked-wheel unit and adhesion module placement

3.5.1 Basic idea for a tracked-wheel unit

The design of the robot locomotion mechanism and placement of the adhesion mechanism were considered in this study, *i.e.* tracked-wheel locomotion and permanent magnet adhesion. It was necessary to construct or find an available tracked-wheel unit with suitable design specifications. The selected/constructed tracked-wheel unit should be able to carry the adhesion module to generate the required locomotion movement (adhesion and locomotion requirements are discussed later in this study). Initially, the maximum size of the tracked-wheel unit was stated as follows:

1. The tracked-wheel unit should be able to rest comfortably on the curved chain surface. Therefore, the width was selected accordingly, as illustrated in Figure 3-8(a), *i.e.* a wider track provides a higher traction force on a flat surface. However, mooring chains are curved and increasing the width does not provide a traction advantage (due to the curvature of the chain surface). In the illustrated diagram, a 40mm-wide tracked-wheel unit is placed on the curvature of a 133mm-wide mooring chain. A 40mm maximum width was selected after considering the tracked-wheel mechanical components (mechanical design is discussed later in this chapter).

2. In order to avoid disturbances due to small misalignments in the chain links, the length of the tracked-wheel unit was selected as illustrated in Figure 3-8(b). Vertically aligned chain orientation was considered in this study. However, to minimise the impact during a change from one parallel misaligned plane to another parallel plane, the length of the tracked wheel was required to be less than the gap between the planes.

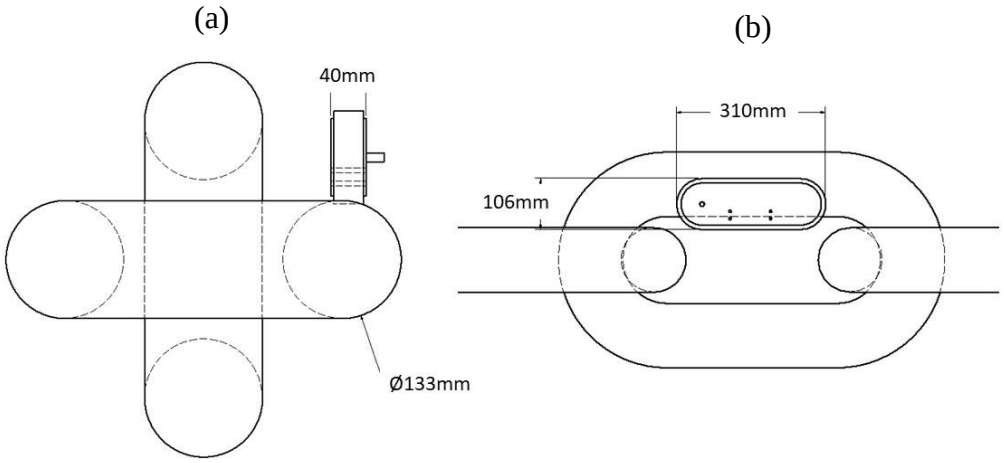

Figure 3-8: Basic tracked-wheel unit dimensions; (a) tracked-wheel unit placement on the chain surface; (b) tracked-wheel unit length with respect to the chain link–link distances

3.5.2 Adhesion module placement according to the tracked-wheel unit

The placement of the adhesion module was considered with the use of the abovementioned maximum tracked-wheel unit sizes. Due to the curvature of the mooring chain, it is necessary to place the adhesion module perpendicular to the tangent surface of the chain link. To understand the behaviour of permanent magnetic adhesion with the chain surface tangent, the following numerical modelling study was conducted. The design of the adhesion module according to the robot's requirements is discussed later in this chapter. This part of the study was conducted to understand the importance of magnet placement on the chain surface. Therefore, magnet arrangement and optimisation techniques are not discussed in this section. The properties of a commercially available magnet were modelled using COMSOL Multiphysics to understand the change in magnetic adhesion force with chain surface–magnet misalignment.

A stationary simulation was conducted in COMSOL Multiphysics with the use of the 'magnet field, no current' (MFNC) module. A free tetrahedral mesh was created with a maximum element size of 10mm and a minimum element size of 0.1mm. The parametric data presented in Table 3-4 were used in the numerical modelling. The CAD layouts

presented in Figure 3-9 (a.1, b.1, and c.1) were used in the FEA study and the corresponding magnetic flux density distribution was plotted as in Figure 3-9 (a.2, b.2, and c.2). Magnetic adhesion forces according to the misaligned distances were recorded, as illustrated in Figure 3-10.

Table 3-4: COMSOL numerical model parameters

Parameter	**Parameter value**
Magnet relative permeability	1.05
Residual flux density (Br)	1.45 T
Magnet size/backplate size	L 40mm, W 20mm, H 5mm/L 100mm, H 15mm, W 35mm
Iron relative permeability	4,000

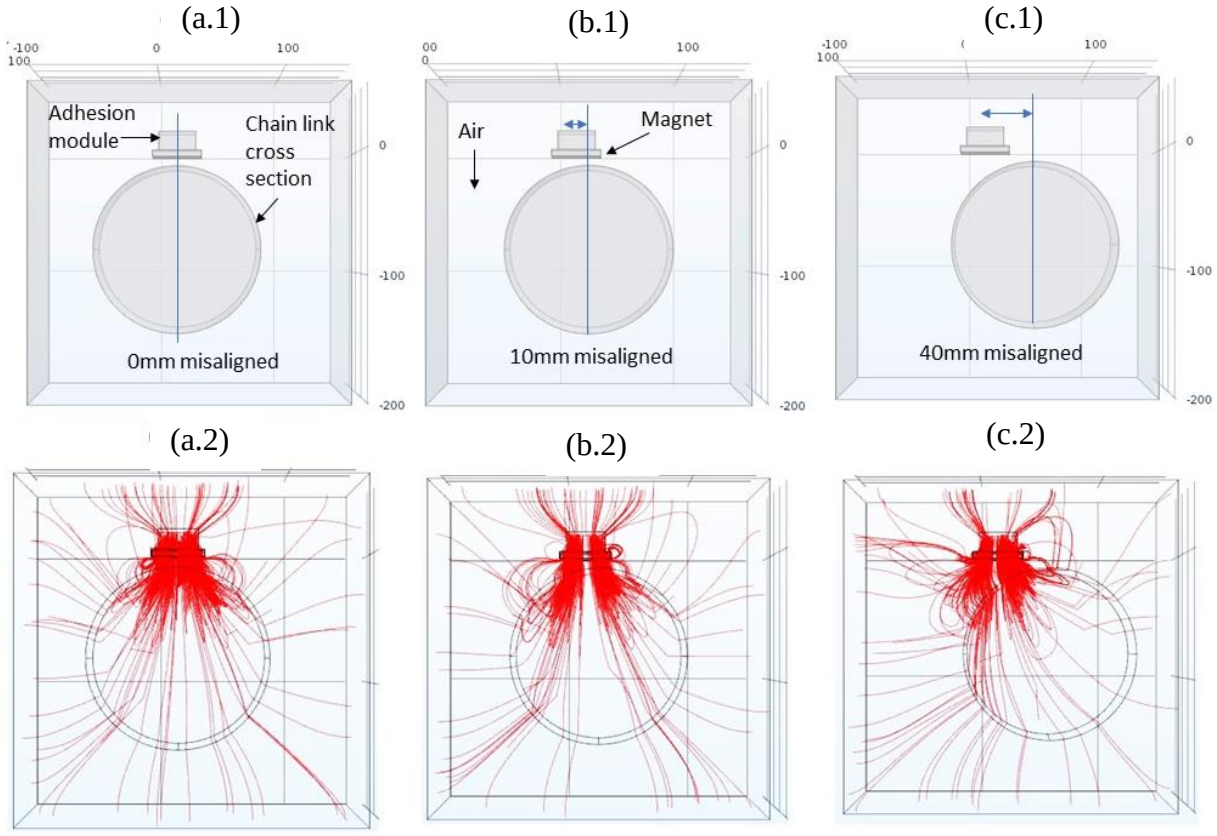

Figure 3-9: Effect of adhesion module-chain surface position; (a.1, b.1, c.1) adhesion module – chain link surface layout; (a.2, b.2, c.2) corresponding magnetic flux density across the chain link

When considering the results in Figure 3-10, a ≈ 9N drop in adhesion force was recorded when the magnet moved 10mm away from the position in Figure 3-9(a.1) and a ≈ 80.6% drop when it moved up to 40mm (see Figure 3-9(c.2)). Similar to the force, a reduction in the magnetic flux density across the chain cross-section can be seen in Figure 3-9(c.2) compared to Figure 3-9(a.2). Therefore, the importance of placing the adhesion module perpendicular to the chain's tangent surface is significant.

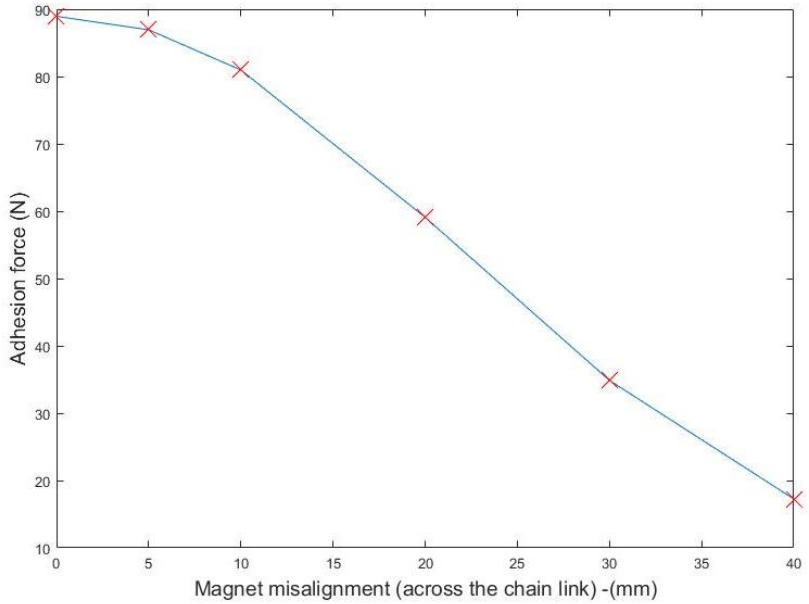

Figure 3-10: Effect of magnetic adhesion force vs magnet misalignment

After considering the above numerical model analysis, the magnet placement/magnet holder design was carried out. The rigidity of the magnet attachment was considered as a serious factor because the tracked wheels needed to be attached to the main frame under vertical gravity force and horizontal magnetic adhesion force. Due to the limited inside space, a magnet holder was designed to be placed on the outside of the locomotion unit. A design for a lightweight and adjustable external holder was needed in order to place the magnet outside the tracked-wheel unit. A conceptual design was proposed, as illustrated in Figure 3-11(a).

(a)

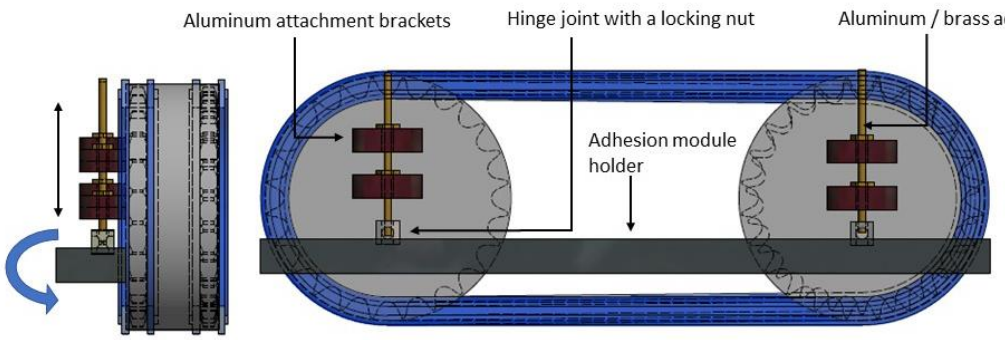

(b)

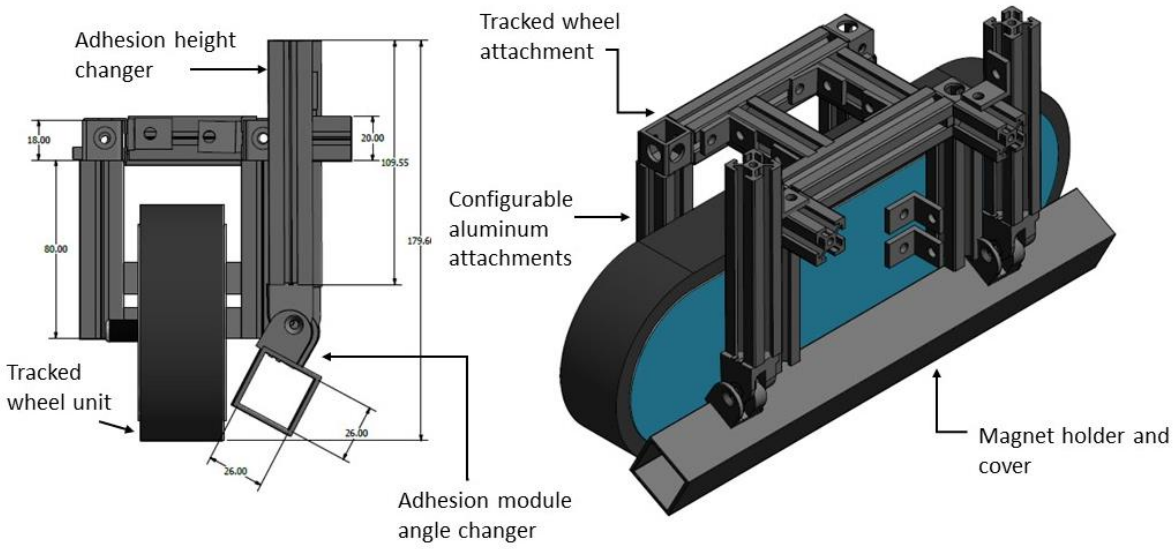

Figure 3-11. (a): Conceptual design of the tracked-wheel unit and adhesion module holder (b): Mechanical design of the tracked-wheel unit with adhesion module holder

According to the above conceptual design, the adhesion module holder/backplate was attached to the tracked wheel with aluminium brackets and adjustable nuts. The adjustable nuts could be used to move the holder up and down. Due to the thin cover plates of the tracked wheels and the lack of space, aluminium welding was proposed as the attachment method between the aluminium brackets and the crawler cover. The above design allowed to change the angle of the adhesion module according to the tangent requirement.

The design in Figure 3-11(b) needed a custom-built aluminium part that was difficult to prototype. Therefore, to reduce the effort of the prototype, the same model was reconstructed with MISUMI configurable aluminium extrusions. During the reconstructions, the size of the magnets was estimated according to the spaces available.

Moreover, in the previous design, the magnets were exposed to the outer environment. According to the specifications of the research, the robot must be able to investigate in working environment conditions. Therefore, an aluminium cover was introduced to the new design to function as a sleeve for the magnets (illustrated in Figure 3-11(b)).

The prototype of the above design is discussed in Chapter 4 (see Chapter 4, Figure 4-1). An evaluation of the above-designed magnet holder (adhesion module holder) was carried out using the prototyped module and the following advantages were identified: 1) the tangent angle and height of the adhesion module could be changed as expected; 2) the adhesion module was placed inside the holder sleeve and was able to create an adhesion force along the entire length of the tracked-wheel unit. However, the issue illustrated in Figure 3-12 caused an imbalance in the tracked-wheel unit during the experiments.

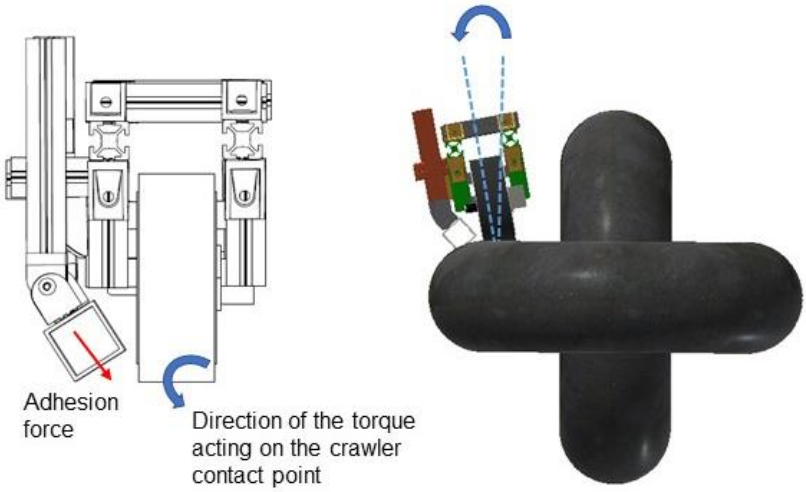

Figure 3-12: External adhesion module placement issue no 1

Balance in each tracked-wheel unit was essential because the balance of the robot structure was based on the individual tracked-wheel units. Therefore, support was added to the prototyped structure using an additional wheelset. The design illustrated in Figure 3-13 was constructed according to the actual sizes of the parts. An A-shaped aluminium attachment was used to create the appropriate angle between the wheel attachment and the support wheel. It was necessary to keep the wheel at an angle to the tracked-wheel unit. Therefore, the side crawler was able to provide additional support while the crawler moved in a straight line along the link surface. To evaluate this idea, a prototype was created and tested. The prototype of the above design is discussed in Chapter 4 (see Chapter 4, Figure 4-3). Introducing more than one support wheel to the structure was necessary because a single support wheel would not be sufficient for some parts of the crawl. For example, the

support wheel was unable to provide the expected support during link transitions, *i.e.* when the tracked wheel was about to enter or leave a chain link. Therefore, the idea of a set of support wheels was considered. The drawback illustrated in Figure 3-13 was observed during the design investigations. The tracked-wheel unit was designed to crawl on the chain link surface; however, it began to share the load with the support wheels and, thus, the orientation began to change during the experiments. The illustrated issue was considered a major concern because it could cause collisions between the tracked wheel and the orthogonal chain link.

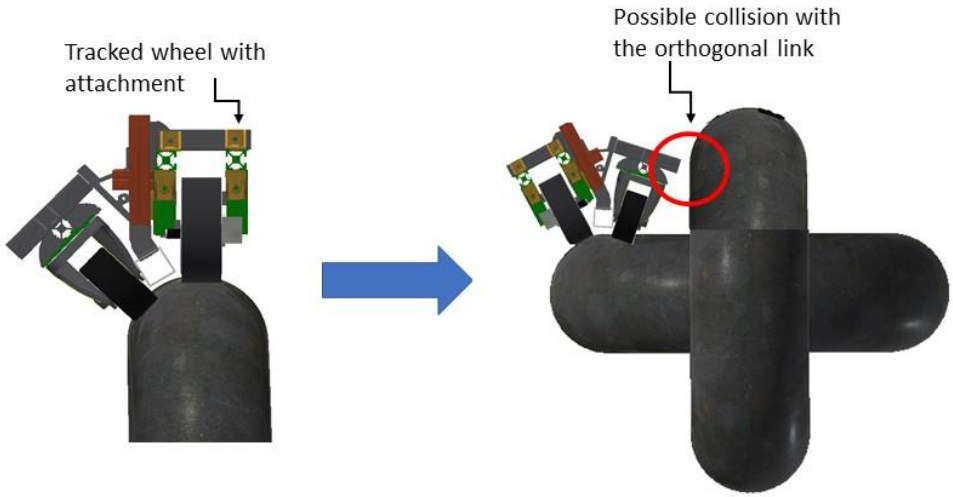

Figure 3-13: External adhesion module placement with the support wheels

3.5.3 Finalising the magnetic adhesion module placement

The previously discussed placements were based on the external adhesion module concept. According to the observations, the idea of an external adhesion module was unable to provide a suitable arrangement. As mentioned at the beginning of this chapter, the external mechanism was considered due to the less-complicated tracked-wheel modifications (when using an off-the-shelf tracked-wheel unit). However, after reviewing the permanent magnet study (see Figure 3-9), the necessity of having a complicated external attachment was raised, *i.e.* height changer and angle changer to make it tangent to the surface. The complicated support attachments made the tracked-wheel unit vulnerable, bigger, and heavier. Therefore, a new allocation arrangement was considered. When considering the studied magnet behaviour, it was important that the centre of the tracked-wheel unit and the magnet arrangement should be in line to extract the maximum adhesion force (see Figure 3-9). Moreover, having an inline adhesion force enhanced the stability of the

tracked-wheel unit. Therefore, embedding the adhesion module into the tracked-wheel unit was considered (see Figure 3-14). The following advantages were gained when the adhesion module was embedded. 1) The height between the magnetic adhesion module and chain surface became a constant (reduction of a variable parameter). 2) The embedded adhesion module was in the middle of the tracked-wheel unit; as such, it was already placed on the tangent surface. Therefore, excess weight due to the external adjustments was avoided. 3) The stability of a single tracked-wheel module was enhanced due to the inline symmetric adhesion force. 4) It is possible to introduce a compact, lightweight, less-complicated tracked-wheel module with adhesion embedded, *i.e.* no additional attachments, wheels.

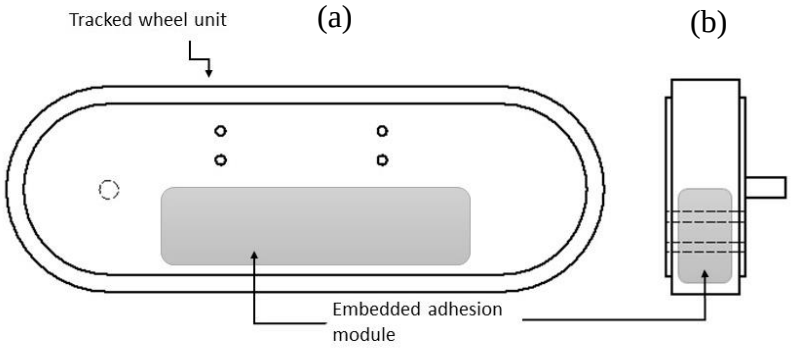

Figure 3-14: Embedded adhesion module placement

3.6 Design of the tracked-wheel unit

The selection of the locomotion method was carried out using the information provided in previous research [9] and Table 2-1 (Chapter 2). Due to the harsh operational conditions (*i.e.* rough, curved, uneven, amphibious nature) of the mooring chains, it was convenient to use a track-wheeled locomotion mechanism ***[D1] [D4]***. The tracked-wheel model was selected because passive track adaptation according to uneven surfaces gives an additional traction advantage, the payload capacity is reasonably high, and the control complexity is comparatively low (discussed in Chapter 2).

The CAD models presented in Figure 3-15 were designed by considering the specifications discussed in the above section, *i.e.* to avoid the effect of parallel misalignments of the chain links, the total length of the track should remain less than the gap between two parallel links, and the width of the tracked-wheel unit should allow the robot to settle on the mooring chain surface with appropriate contact and should also provide an allocated space

for the adhesion module. As mentioned previously, configurable aluminium extrusions were used to design the tracked-wheel unit holder/attachments.

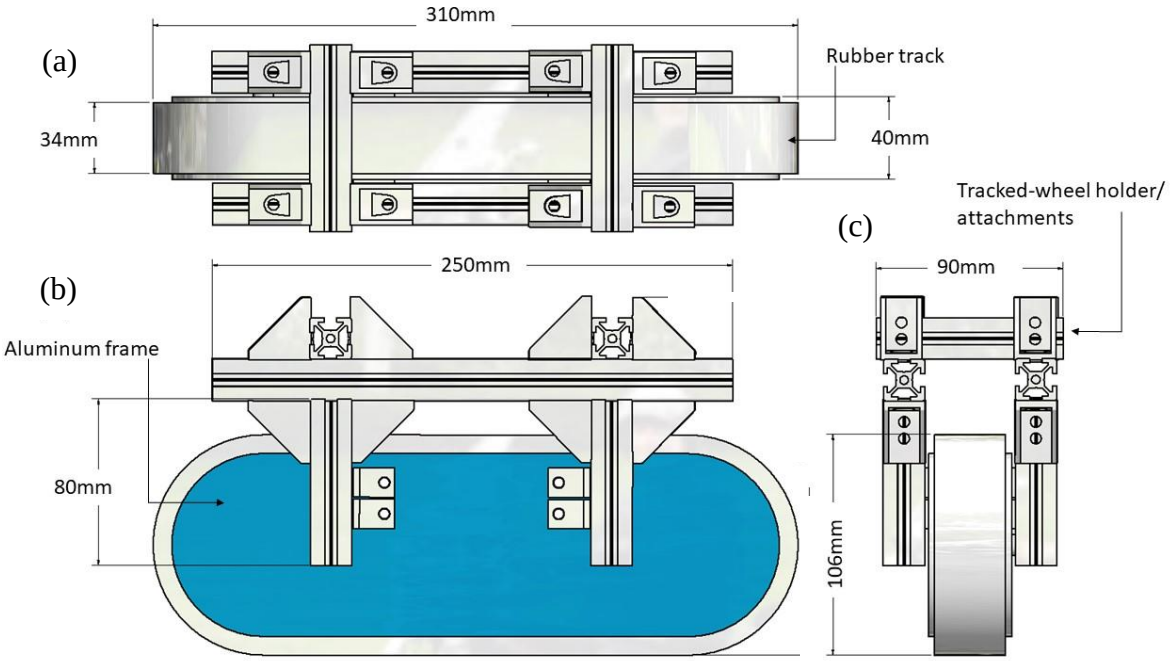

Figure 3-15: CAD models of the proposed tracked-wheel unit

Two large aluminium wheels were introduced to drive the track and a tension wheel was added to the design to keep the rubber track in tension. Introducing two tension wheels to the top and the bottom could enhance the effect of the tension wheels. However, to preserve space for the adhesion module, only one tension wheel was added, as illustrated in Figure 3-16. 'Allocated space for the adhesion module', marked in Figure 3-16(b), was used to place the adhesion module. As mentioned previously, the adhesion module was made with permanent magnets. Therefore, the internal components of the tracked-wheel unit were designed using aluminium because of its non-ferromagnetic nature. If the wheels were made from ferromagnetic materials, motion could be disturbed due to the effect of the permanent magnets.

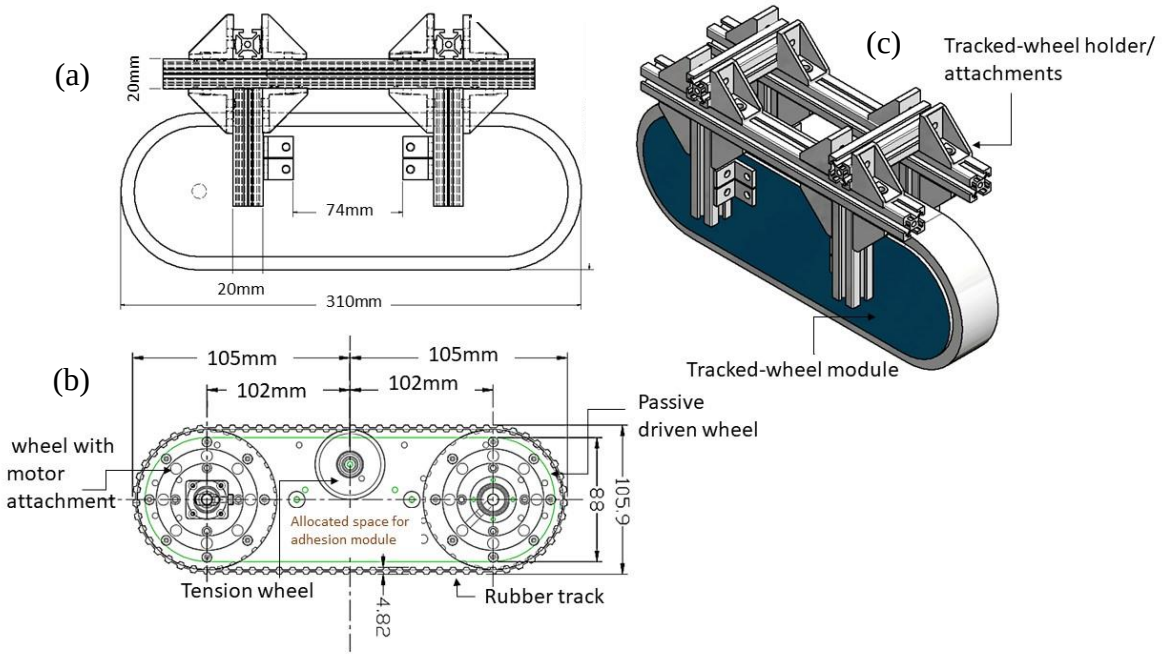

Figure 3-16: Engineering CAD models of the tracked-wheel unit

3.7 Design of the magnetic adhesion module

According to the adhesion principle study and comparison carried out in Chapter 3.3 (Table 3-2), permanent magnets were selected as the adhesion mechanism. The following advantages were identified as the main reason for the selection of magnetic adhesion. 1) Passive adhesion capability – magnetic adhesion does not require input from an external source; therefore, the reliability of the adhesion module is comparatively high. 2) Suitable for application – mooring chains are made using thick iron rods and it is ideal to employ a permanent magnetic adhesion system. In addition to that, this adhesion mechanism is capable of working underwater. 3. Magnetic adhesion is the most suitable adhesion mechanism when the surface is uneven, curved, and ferromagnetic because of its non-contact and passive adhesion qualities.

3.7.1 Background study of magnetic adhesion for climbing robot

The development of a permanent magnetic adhesion module and adhesion force optimisation techniques has been studied in the literature [91] [9] [58]. Previously published studies were conducted in relation to wall climbing, *i.e.* steel walls, steel plates, concrete walls etc. Due to the mooring chain's curved surface and limited adhesion module space, a bespoke adhesion module was designed. In order to establish the basic design

parameters, a background summary of magnetic adhesion force optimisation is discussed here.

The introduction of a high-permeability yoke/backplate to enhance the magnetic adhesion by reducing flux leakage has been studied in the literature in terms of various design parameters, *i.e.* size of the magnet, magnet orientation, number of magnet sets, size of the yoke/backplate, distance between the magnets, material of the yoke etc. The background theory of the design parameters used in this research is discussed below.

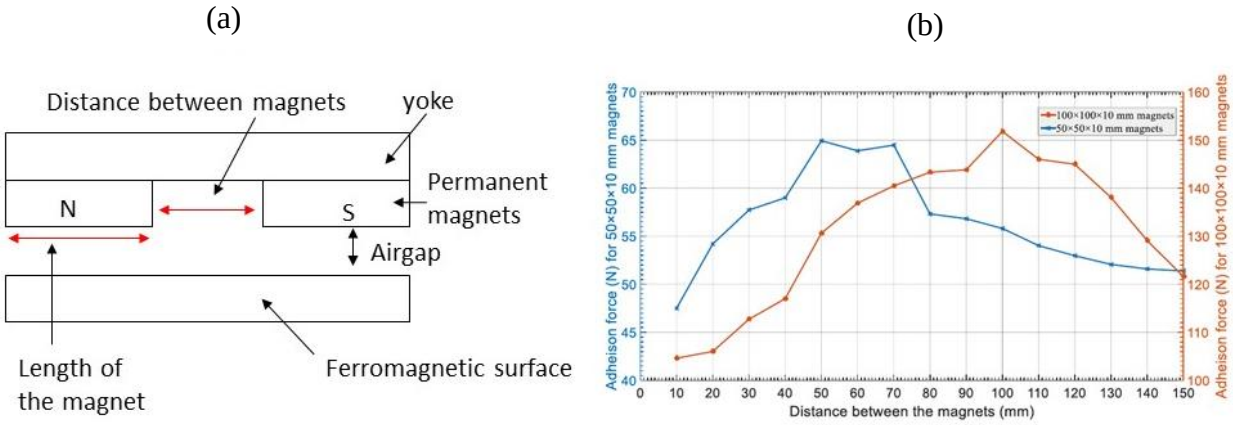

Figure 3-17: Adhesion force vs distance between magnets [9]

The effect of distance between the magnets was studied and the results are illustrated in Figure 3-17. Numerical modelling, as well as experimental data, was recorded to understand the effect. Figure 3-17(b) presents the adhesion results from two different magnet sets. According to the illustrated results, the optimum adhesion force was generated when the length of the magnet was equal to the distance between the magnets. According to the previously published results [9], bringing magnets closer or distant than the magnet length reduced the adhesion force significantly.

Adhesion capability has been studied in the literature to select the most effective physical parameters of a magnet. Comparisons of the adhesion effect has been studied by varying the magnet width and magnet thickness. When considering the previously studied results [9] illustrated in Figure 3-18, these confirm that an increase in the magnet thickness has a greater effect on the adhesion force when compared to an increase in the magnet width. This can be introduced as another key feature used in the adhesion module optimisation, *i.e.* to enhance the adhesion force of a given magnet set, thicker magnets can be introduced. Moreover, an increase in the width causes an increase in the backplate in order to shield

the magnetic flux. Therefore, this increases the net weight of the system but an increase in thickness does not require additional yoke changes.

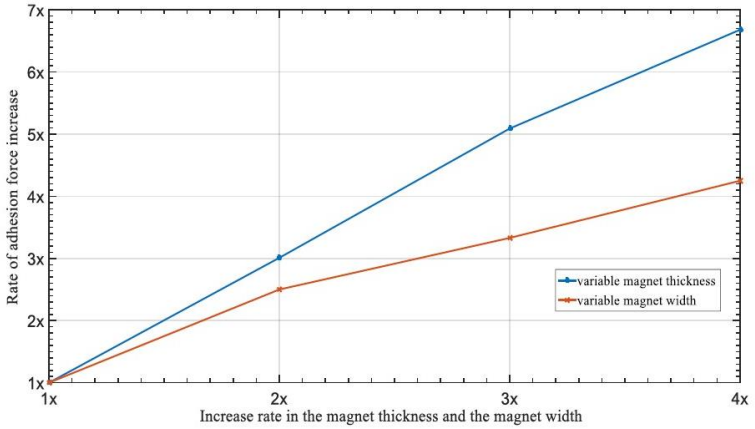

Figure 3-18: Adhesion force vs magnet physical parameters [9]

The use of a high-permeability yoke for adhesion module optimisation has been studied in the literature [9] [90]. An increase in adhesion force with the backplate was studied in the adhesion design module section. The thickness effect of the yoke/backplate with respect to the adhesion force is recorded in the literature (see Figure 3-19). According to the previously published results [9] [90], it is significant that increasing the thickness of the yoke increased the adhesion capability up to a particular value, then began to settle down.

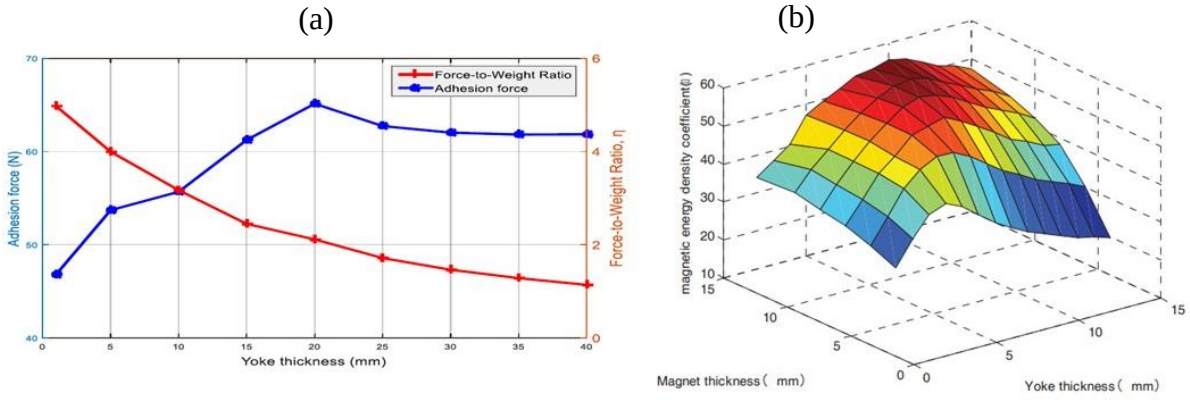

Figure 3-19: Adhesion force vs yoke thickness; (a) study no 1 [9]; (b) study no 2 [90]

Reducing magnetic flux leakage was the primary purpose of the backplate/yoke in the studied adhesion module. Therefore, the use of a high-permeability material for the yoke was essential. The effect of adhesion forces according to various high-permeability ferromagnetic materials were studied and presented in the literature [9], as illustrated in Figure 3-20. Iron was selected as the best material for the yoke. According to the illustrated

figure, it is significant that the adhesion forces generated with commercially available iron also changed with its impurity level, *i.e.* materials with a higher percentage of iron provided a higher effect.

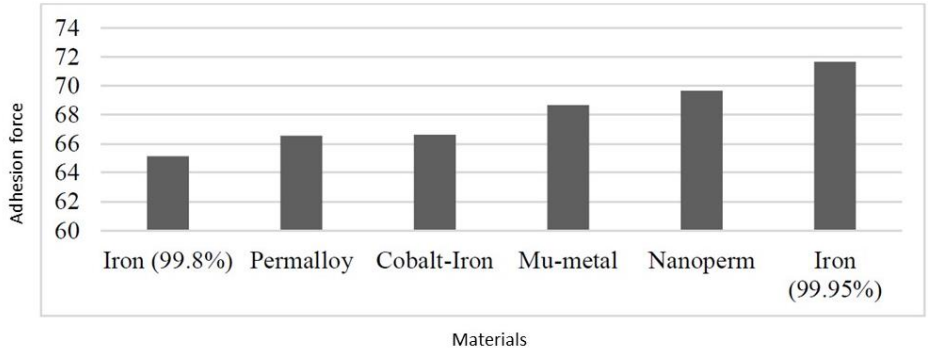

Figure 3-20: Adhesion force vs yoke materials [9]

Magnet arrangement formations have been studied in [90], and the adhesion forces were recorded, as illustrated in Figure 3-21. According to the studied formations, the N-S-N/S-N-S arrangement with a yoke was identified as the most commonly used/suggested magnet arrangement. The magnet arrangement and the size of the yoke depends on the robot's footprint. For example, if the robot has a rectangular narrow footprint, the arrangement in Figure 3-21(a) is suitable, and the arrangement in (c) can be used for a wider square-type footprint. Therefore, the magnet arrangement must be able to cope with the design of the robot's magnetic adhesion footprint. In addition, it is essential to consider the effect of the air gap during the adhesion module design. According to the previously mentioned permanent magnet adhesion module studies, there is a significant drop in forces when the air gap is higher than the 1–5mm region. The results/parametric studies presented in the abovementioned studies were used to develop a bespoke mooring-chain-climbing adhesion module, *i.e.* backplate, magnet arrangement, air gap, distance between magnets, and yoke materials.

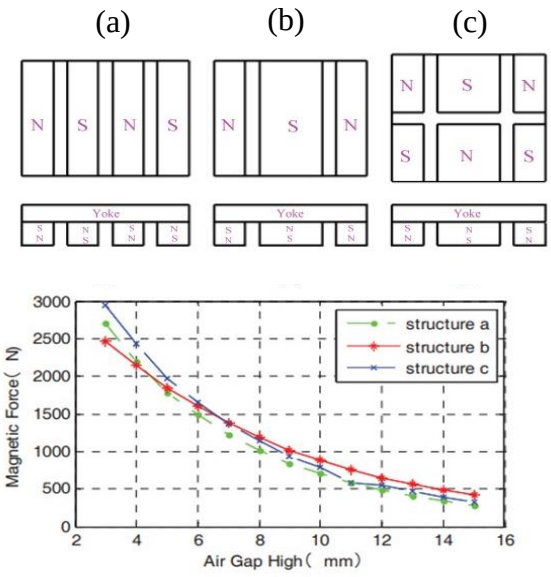

Figure 3-21: Adhesion force vs magnet arrangements [90]

3.7.2 Design of the magnetic adhesion module

Designing the best adhesion module according to the adhesion force requirements is the most common practice in robot design. In this study, force requirements, as well as available space, were considered as design parameters. The available space for the adhesion module was considered as the primary design constraint. As discussed previously, the adhesion module should be able to fit inside the tracked-wheel module. *i.e.* Space constraints were studied before selecting magnets, backplate etc. The allocated space for the adhesion module was recognised as illustrated in Figure 3-22, and 35mm, 100mm, and 40mm cuboid-shaped spaces were considered for the adhesion module placement.

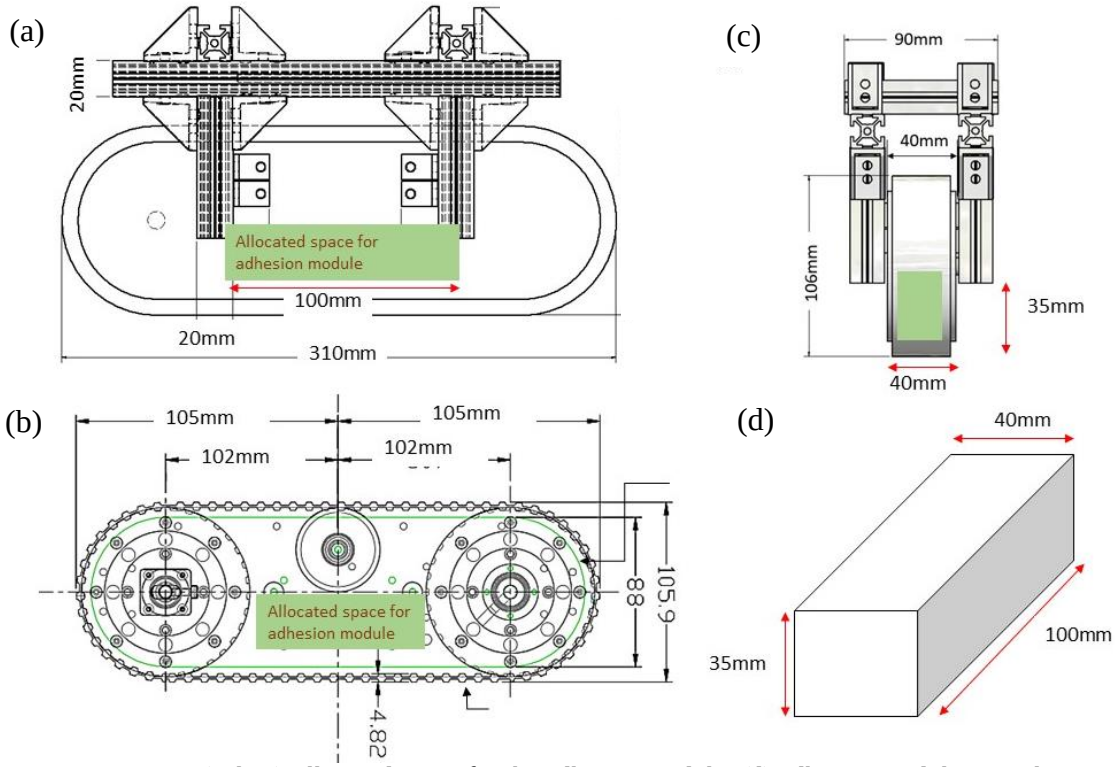

Figure 3-22: (a, b, c) Allocated space for the adhesion module; (d) adhesion module space limits

A backplate/yoke has been used in climbing robots as an adhesion force enhancement technique. Optimising an adhesion module to achieve a given force using a given space was considered as a main design task in this part of the study. Initially, a backplate was introduced to the design. The yoke/backplate was introduced after considering the following advantages: 1) optimisation of the adhesion module; 2) the use of the same backplate to hold and keep the magnets in place; 3) the same yoke/backplate can be used to cluster the body plates of the tracked-wheel unit. According to the previously published studies [9] [90], 10-20mm thickness of the backplates was used. The backplate thickness was set to 15mm because it was used to hold the magnets and used as the attachment of the tracked-wheel frame. *i.e.* To ease the attachment of the tracked-wheel unit and the backplate, 15mm was selected as the thickness. A width of 40mm was chosen for the magnetic adhesion unit; however, due to the mechanical clearances/attachments, a width of 30mm was considered for the backplate design, as illustrated in Figure 3-23. Hereafter, the dimensions and space illustrated in Figure 3-23 are used when referring to the adhesion module.

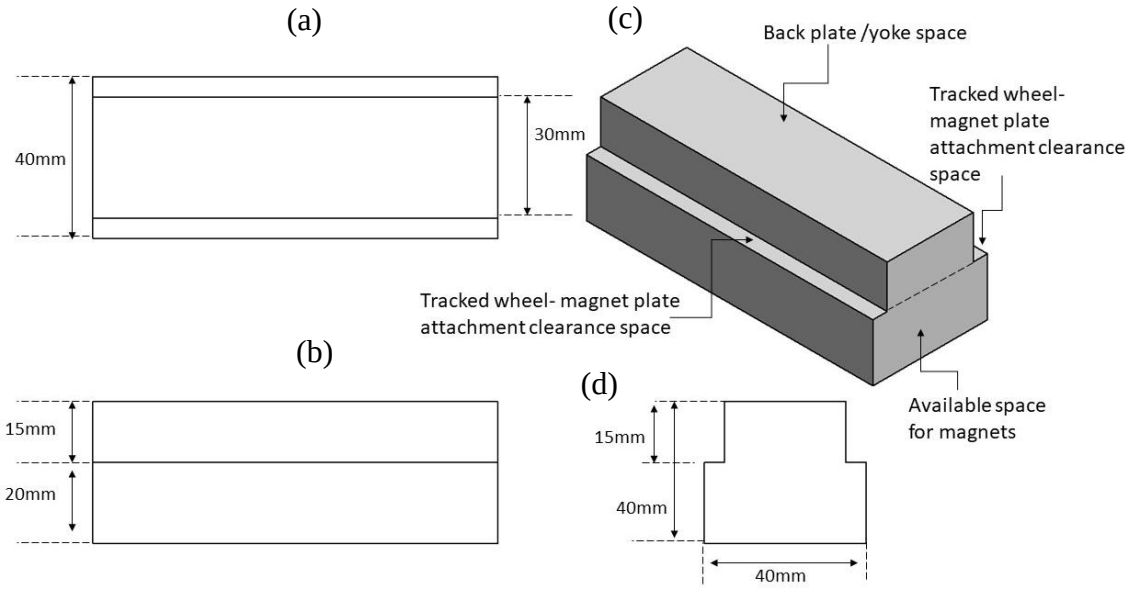

Figure 3-23: Adhesion module space limits

3.7.3 Adhesion module requirement study

Before the parametric design of the adhesion module, it was necessary to calculate/estimate the required adhesion force that should be provided by each tracked-wheel module. The required adhesion force was calculated in the literature [9] for a wall-climbing robot, and this was adopted for this study. Vertical chain climbing was considered in this chapter; therefore, the adhesion calculation was conducted by

considering a single tracked-wheel unit and a plane, as illustrated in Figure 3-24. Although vertical climbing is discussed in this study, an inclination was introduced to the climbing surface to generalise the formula.

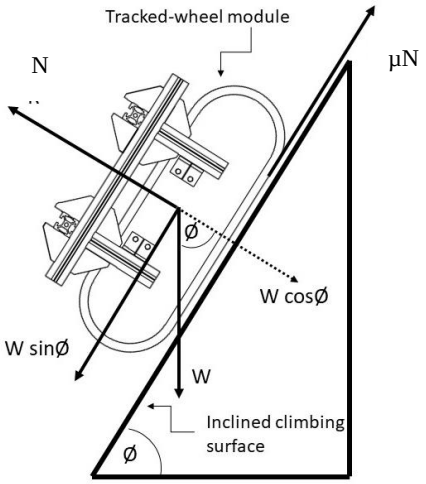

Figure 3-24: Adhesion requirement force diagram

The main force/parameters used for the calculations were the weight of the robot (W), the inclination angle of the climbing surface (Ø), the coefficient of friction between the track and the climbing surface (μ), as well as the reaction force from normal to the surface (R), and the required adhesion force for slide avoidance (F_a).

Considering the equilibrium (parallel to the plane) of the tracked-wheel unit, the following can be obtained:

$$\sum F_x = W\ sin\emptyset - \ \mu N = 0 \qquad \textit{Eq 3-1}$$

Therefore, the reaction force (N) can be derived as follows:

$$N = \frac{W \sin \emptyset}{\mu} \qquad \textit{Eq 3-2}$$

Considering the equilibrium (perpendicular to the plane) of the tracked-wheel unit:

$$\sum F_y = W\ cos\emptyset + F_a - N = 0 \qquad \textit{Eq 3-3}$$

Therefore, the reaction force (N) can be derived as follows:

$$N = W\ cos\emptyset + \ F_a \qquad \textit{Eq 3-4}$$

Considering Eq 3-3 and Eq 3-4:

$$\frac{W\ sin\emptyset}{\mu} = w\ cos\emptyset + F_a \qquad \textit{Eq 3-5}$$

Therefore, rearranging Eq3-5, the generalise adhesion force requirement equation can be formed:

$$F_a \geq \frac{W\ sin\emptyset}{\mu} - w\ cos\emptyset \qquad \textit{Eq 3-6}$$

Vertical climbing was considered in this study; therefore, the inclination angle Ø =90. The general adhesion force equation can be re-simplified as:

$$F_a \geq \frac{W}{\mu} \qquad \textit{Eq 3-7}$$

To calculate the required adhesion force, Eq 3-7 can be used. In order to use Eq 3-7, the weight of the robot should be a known parameter. The weight of the full robot structure was discussed in the prototype chapter (see Chapter 4, Figure 4-17). The Calculation is as follows;

$$F_a = \frac{191.23(N)\sin(90^{\circ})}{0.5} - 191.23\ cos\left(90^{\circ}\right) = 382.46N \qquad \textit{Eq 3-8}$$

According to Eq 3-8, the required minimum total adhesion force was calculated as 382.46N when the weight of the robot was considered as ≈ 19.5kg. (Downward force due to weight = 19.5 × 9.81 = 191.229 ≈ 191.23N (gravitation acceleration was considered as 9.81m/s-2)). The friction coefficient (μ) between the rubber track surface was considered as 0.5 (0.5 was extracted from the manufactures data sheet). Therefore, the minimum total adhesion force (Fa) was calculated as Eq 3-8:

According to the proposed orthogonal tracked-wheel locomotion mechanism, at least two tracked-wheel units support the movement; therefore, each tracked-wheel unit's minimum adhesion requirement can be calculated as follows:

$$F_{a(per\ each\ tracked-wheel)} = \frac{F_a}{x} \qquad \textit{Eq 3-9}$$

Where, x is the minimum number of tracked-wheel units in contact with the surface at a given location. According to Eq 3-9, each tracked-wheel unit should be able to provide a minimum adhesion force of 191.23N. The tracked-wheel contact with respect to the adhesion force was studied in the permanent magnet FEA section (*i.e.* later in this chapter).

3.7.4 Permanent magnet adhesion numerical modelling studies

The challenge in this study was to design an adhesion module to obtain a given adhesion force within a limited space. Therefore, the quality of the magnet was considered, and a study was carried out to find commercially available magnet materials that are suitable for heavy-duty purposes. Neodymium magnet (NdFeB, NIB, or Neo magnet) were considered as rare-earth magnets are widely used in industry due to their adhesion capability. The tetragonal crystalline structures of neodymium (Nd), iron (Fe), and boron (B) are used for this alloy and these magnets are the strongest commercially available magnets. The magnetic properties of a rare-earth magnet can vary with the working temperature and their maximum energy product (magnetic flux output per unit volume). Therefore, different types of neodymium magnet are available; i.e. N35-N52, N33M-N48M, N30H-N45H, N30SH-N42SH, N30UH-N35UH, N28EH-N35EH. The numerical value (e.g. 40, 42, 45) stands for the maximum energy product of the magnet (in MGOe) and the letters (e.g. N, M, H, SH, UH EH) indicate the maximum working temperature, such as 80°C, 100°C, 120°C, 150°C, 180°C or 200°C. For example, N35M can produce 35MGOes and is capable of working at 100°C. The N52 magnet range (works up to 80°C) was selected for this study because it is the strongest commercially available magnet grade. A higher-grade magnet can generate a considerably higher adhesion force compared to a lower-grade magnet of the same size (due to the higher magnetic flux output per unit volume).

To design a magnetic adhesion module 'available space for magnet' named area in Figure 3-22(b) was considered. As discussed in detail in the literature, the effect of the backplate was studied. The effect of adhesion force was studied using two magnets setups: 1) setup without the backplate (see Figure 3-25); 2) setup with the backplate (see Figure 3-26). Figure 3-25(c) shows the FEA layout used in COMSOL to study the 'no backplate model', and it illustrates the magnet orientation, sizes of magnets, and polarity. Figure 3-26 (c) illustrates the FEA layout used to study the 'backplate model'. Magnet, air, and chain surface parameters were kept the same in both simulations. Magnet layouts in the models were designed according to the previously mentioned studies. The length of the adhesion module was 100mm, as determined in Figure 3-22(d). According to the previous studies [9], the space between the magnets should be same as the length of the magnet. Moreover, N-S-N-type or S-N-S-type polarity have been studied in the literature for better adhesion. Therefore, at least three sets of magnets should be placed within the 100mm length and the space between them should be equal to the length. Three magnets consume two spaces

between them. This leads to a division of the 100mm space into five equal parts of 20mm. Therefore, the length of the magnet was set to 20mm. In addition, the commercial availability of permanent magnets was also considered. A 9mm air gap was introduced between the magnet–chain surface due to the mechanical clearance of the tracked-wheel unit (this will be discussed in Chapter 4).

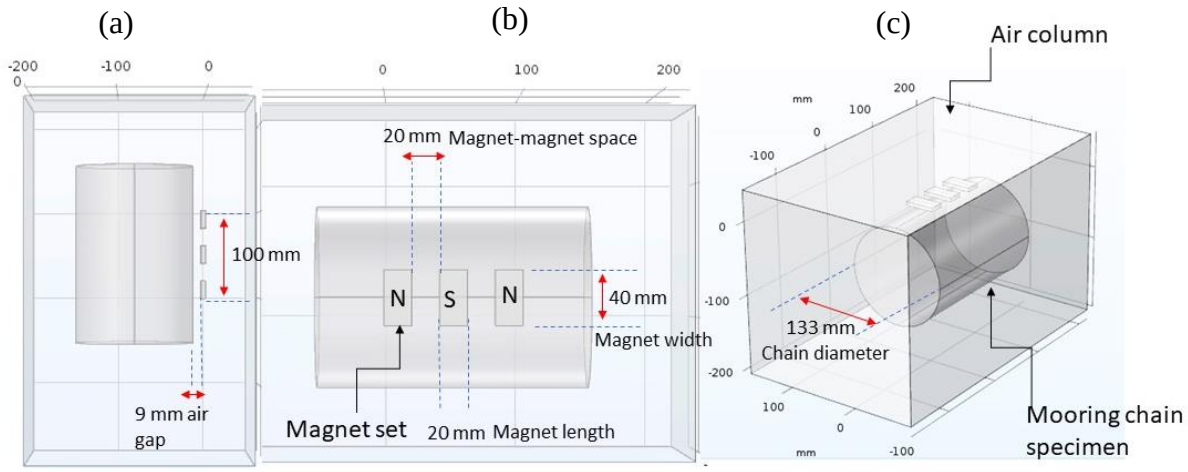

Figure 3-25: Adhesion module study 01 – no backplate FEA layout

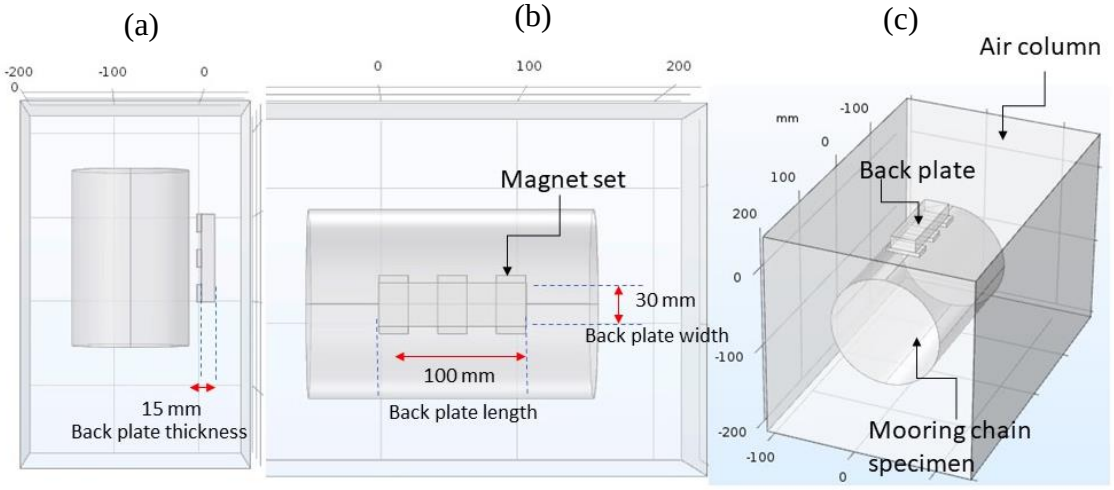

Figure 3-26: Adhesion module study 02 – with backplate FEA layout

The model layouts illustrated in Figure 3-25 and Figure 3-26 were designed using CAD software SolidWorks, then imported to FEA software COMSOL for numerical modelling. A stationary simulation was conducted in COMSOL Multiphysics with the use of the MFNC module. The free tetrahedral mesh was created using the mesh data from Table 3-2. The data presented in Table 3-3 was used for numerical modelling.

Table 3-2 Mesh Data use for numerical modelling

Parameter	Value
Mesh type	Free tetrahedral mesh
Max element size	10mm
Minimum element size	0.6mm
Maximum element growth rate	1.35
Curvature factor	0.3
Resolution of narrow regions	0.85

The adhesion force generated on the mooring chain specimen was recorded during the simulation studies. To visualise the effect of the backplate, magnetic flux density/flux lines were plotted, as illustrated in Figure 3-27.

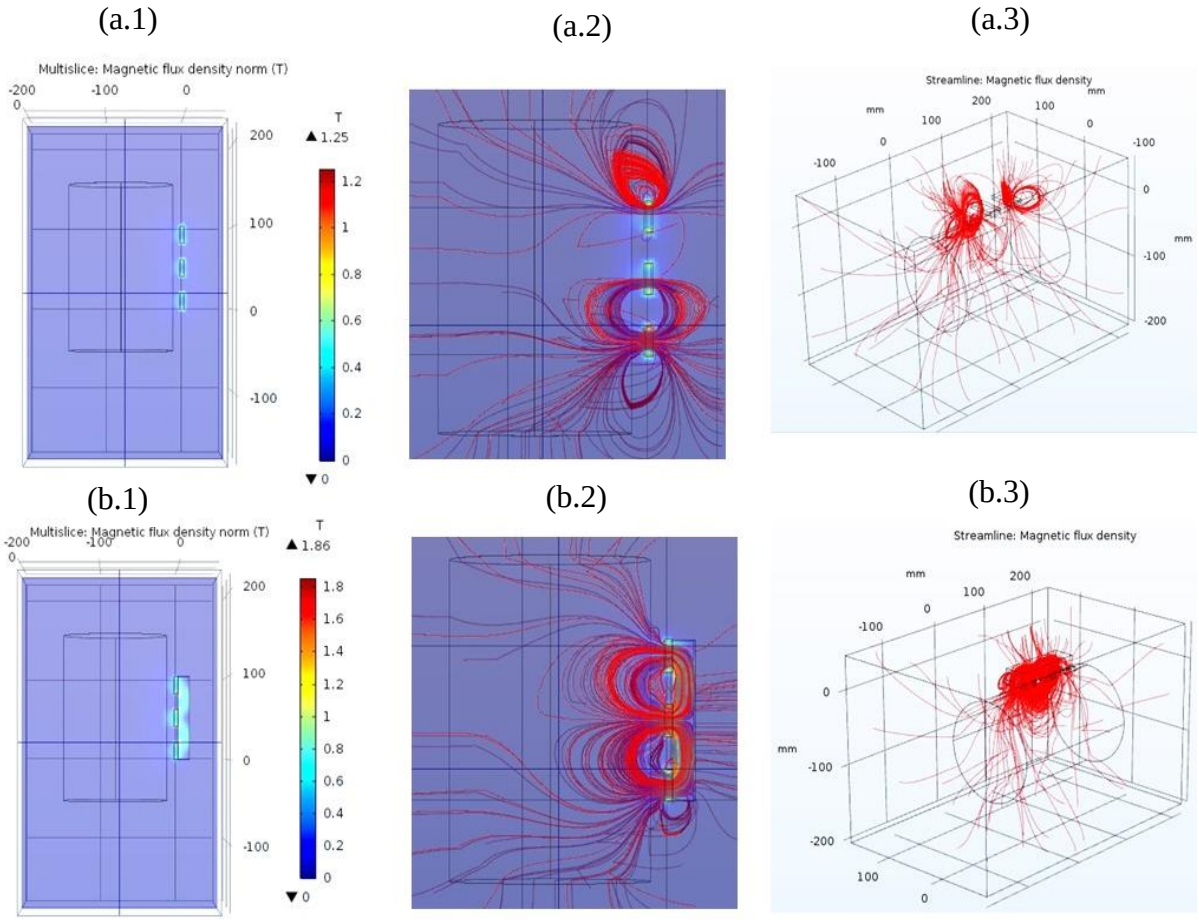

Figure 3-27: Adhesion module study results comparison: (a.1) no backplate magnetic flux density; (a.2) no backplate magnetic flux distribution 2D; (a.3) no backplate magnetic flux density distribution 3D; (b.1) backplate magnetic flux density; (b.2) backplate magnetic flux distribution 2D; (b.3) plate magnetic flux density distribution 3D

Table 3-3: COMSOL numerical module parameters

Parameter	Value
1. Magnet type	N52 [114]
2. Residual flux density (Br)	14.3–14.8KGs .14.5 was used in the FEA
3. Coercive force (Hcb) of magnet	≥796kA/m
4. Intrinsic coercive force (Hcj)	≥876kA/m
5. Maximum energy product (BH) max	398–422MGOe
6. Max operating temperature	80°C
Magnet relative permeability	1.05
Magnet size/backplate size	L 40mm, W 20mm, H 5mm / L 100mm, H 15mm, W 30mm
Iron relative permeability	4,000

A 28.698N force was recorded between the chain surface and the magnet during the simulation with no backplate. This adhesion force was increased to 88.94N by introducing the backplate. From Figure 3-27 (a.2) and (b.2), it can be seen that it is significant that the backplate was able to reduce magnetic flux leakage by shielding the back of the magnet. The backplate was able to work as a closed circuit at the back of the magnet set; therefore, the density of magnetic flux towards the chain surface is higher in Figure 3-27 (b.3) compared to (a.3). This shielding effect raised the adhesion force by ≈ 60N. Therefore, the setup with the backplate was selected as the adhesion module design base. The abovementioned adhesion module base was able to enhance the force significantly, but the required 191.23N (design requirement) was not achieved. Therefore, previously published [9] magnet thickness increase technique was used to obtain the required force. According to the literature [9], an increase in magnet thickness has a more significant impact on adhesion force compared to an increase in width. An N52 commercially available super-strength magnet with a thickness of 5mm was used in the abovementioned base FEA experiment. Therefore, adding layers of magnets to increase the thickness was considered, as illustrated in Figure 3-28.

The magnet-backplate combination illustrated in Figure 3-28 (a) was tested previously in order to understand the need for the backplate. Numerical modelling studies were carried out according to the schematic illustrated in Figure 3-28(b), (c), and (d). The generated adhesion forces were recorded as in Figure 3-29.

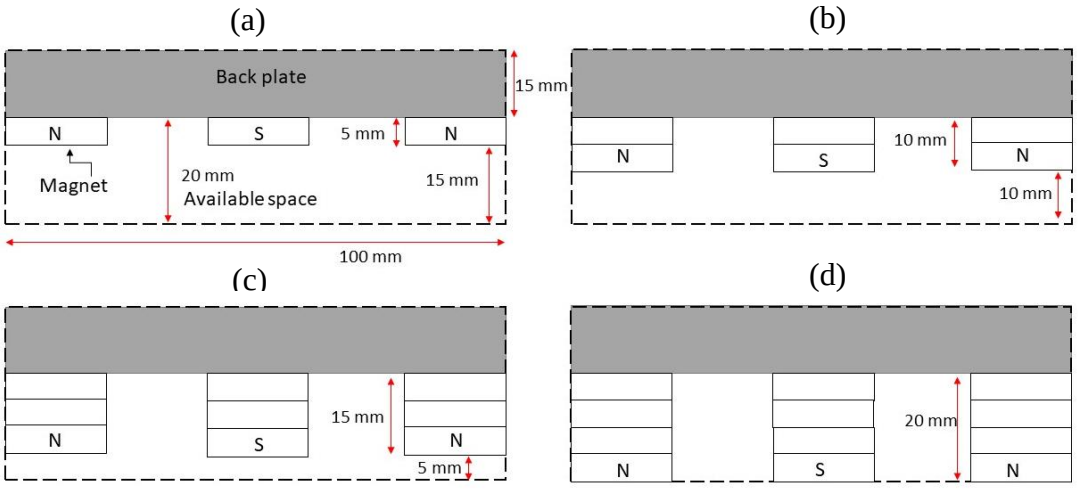

Figure 3-28: Thickness increase magnet layouts; (a) 5mm thickness; (b) 10 mm thickness; (c) 15mm thickness; (d) 20mm

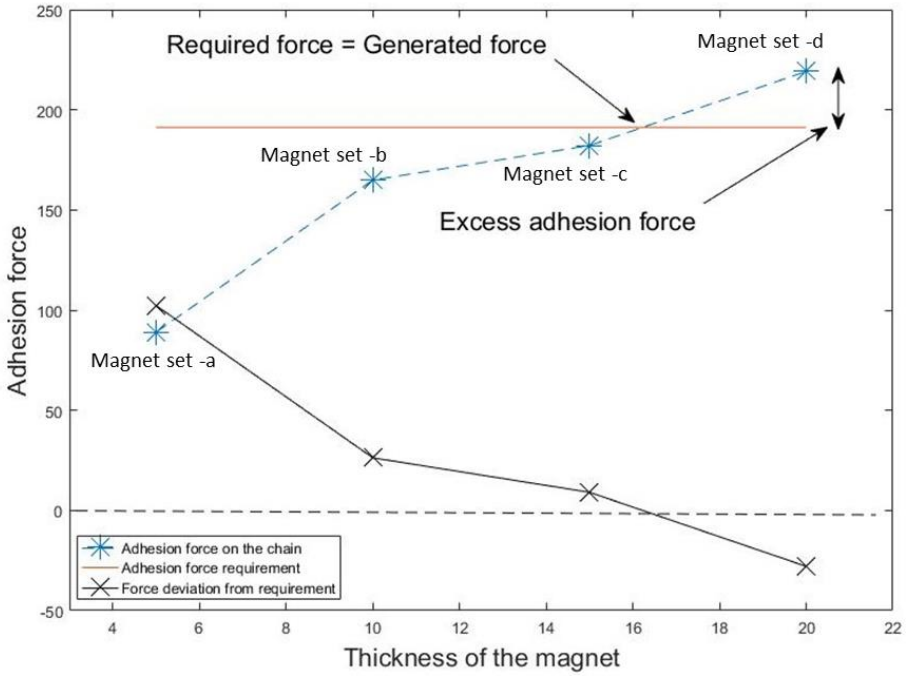

Figure 3-29: Thickness increase magnet layouts vs obtained adhesion forcers

Considering the above-recorded adhesion forces, magnet set (d) (see Figure 3-28) was able to generate an adhesion force of 219.16, which was slightly above the requirement (estimated adhesion requirement). Moreover, the thickness of this setup complied with the allowable space mentioned earlier. Therefore, this magnet-backplate combination was selected as the adhesion module for this study. Figure 3-30 illustrates the COMSOL FEA layout and the magnetic flux density of the selected magnet set. As mentioned previously, a 9mm air gap was introduced to the simulation due to the mechanical clearance between the bottom of the tracked-wheel unit and the chain contact surface. The parameters presented in Table 3-2 and Table 3-3 were used in the numerical modelling. Aluminium

was suggested for the outer structure during the design of the tracked-wheel unit and this is also a nonferromagnetic material. Therefore, aluminium parts in the tracked-wheel unit did not interfere with the adhesion forces, *i.e.* the relative permeability of aluminium is closer to the relative permeability of air, which is ≈ 1. Therefore, in order to simplify, only the chain surface and the adhesion module were considered in the FEA studies.

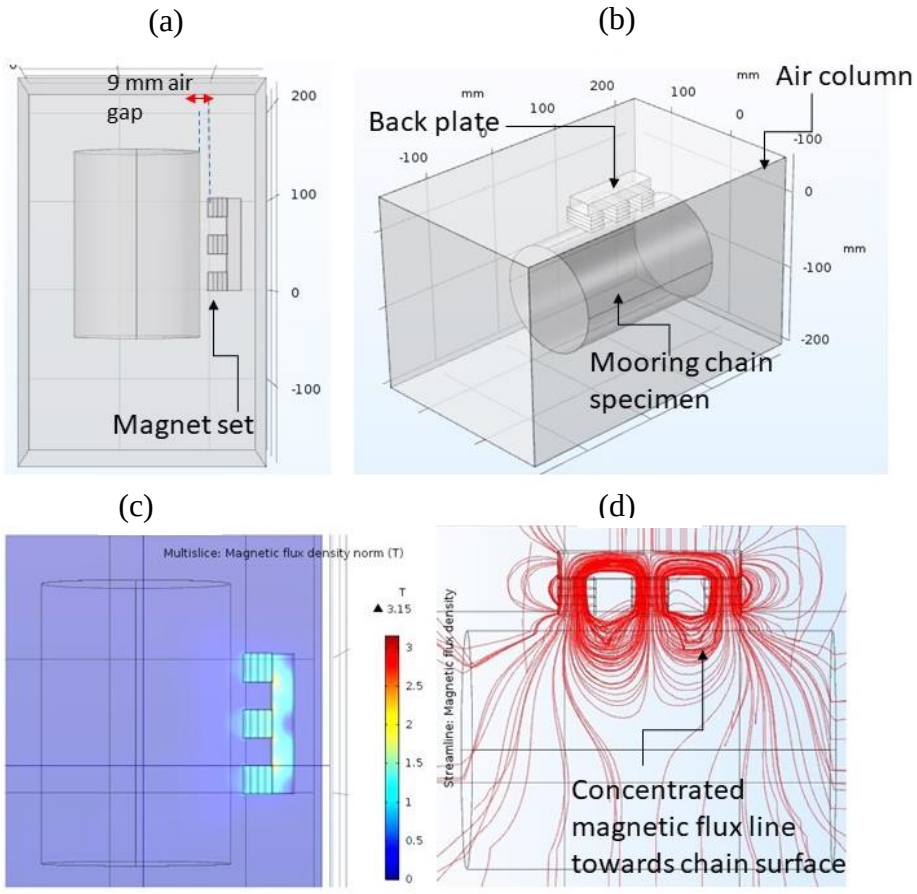

Figure 3-30: Selected magnet – back place model; (a) and (b) FEA layouts; (c) and (d) results

3.7.5 Magnetic adhesion during climbing – numerical modelling

The numerical modelling studies were conducted by considering a chain link specimen, which is similar to a thick iron rod. The physical geometry of the mooring chain is complicated compared to a rod due to the curved surfaces at the end of the links and the orthogonal link placement (as explained in Figure 3-31). Therefore, it was essential to study the variations in adhesion forces generated from each tracked-wheel module, *i.e.* tracked-wheel modules were placed in different orthogonal positions because contact time with the chain changes during climbing. To understand the adhesion behaviour, a numerical modelling study was conducted with all four tracked-wheel units. A mooring chain segment with three links was modelled in CAD, and the magnetic adhesion modules were placed in orthogonal positions (as proposed earlier), as illustrated in Figure 3-32. Adhesion module placement, as well as the distance between each adhesion module set was kept precisely the same as the tracked-wheel design proposed previously. In order to simulate the adhesion forces during chain transitions, three link chain segments were selected, *i.e.* three links consist of two link-to-link transitions. For the simulation, the parameters listed in Table 3-3 and the mesh data presented in Table 3-2 were used. The designed CAD files were imported to the COMSOL stationary simulation of the MFNC module for FEA analysis. A variable distance parameter P1 was declared (see Figure 3-32(b)) and magnetic adhesion simulation was carried out by varying the adhesion module positions along the chain links. Adhesion modules were placed orthogonal to each other and the forces were recorded according to the directions, *i.e.* adhesion modules were kept

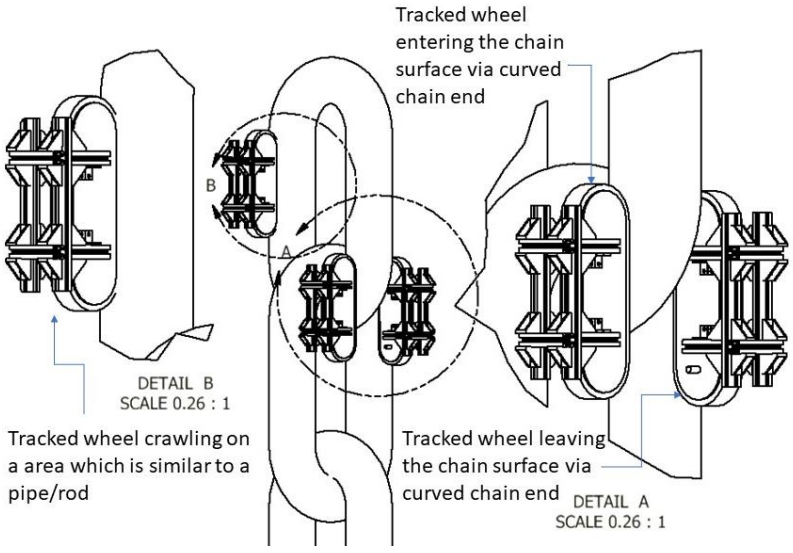

Figure 3-31: Complex, curved, and orthogonal behaviour of mooring chain surface

in y and z directions, so the forces were recorded considering the same directions (see Figure 3-33). Forces acting on the chain due to the magnetic adhesion were considered and the results were plotted against the corresponding positions on the chain surface. The start position, labelled in Figure 3-32(b), was set as the 0 position and the distances were measured from that point.

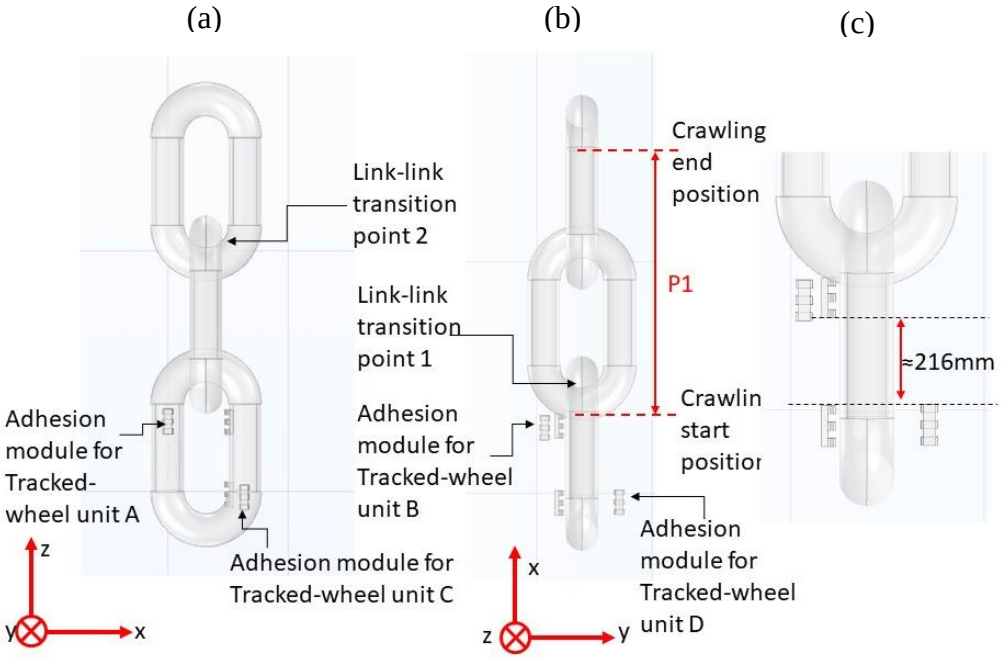

Figure 3-32: CAD model layout of the climbing adhesion simulation

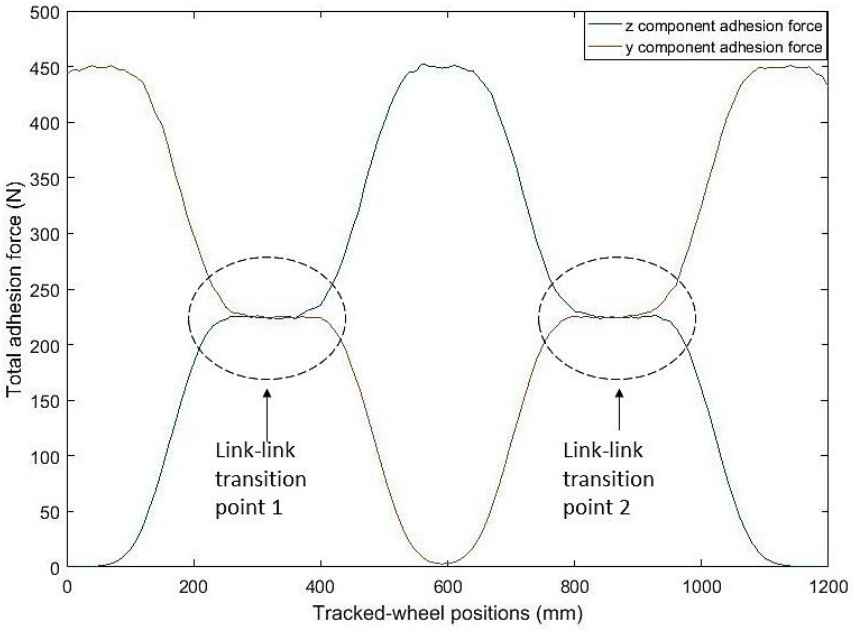

Figure 3-33: Directional adhesion forces vs tracked-wheel position on the chain

According to the recorded results, it is significant that the adhesion force began to drop when a tracked-wheel unit entered/left a chain link but that, simultaneously, the corresponding orthogonal adhesion module started to gain the adhesion force. In order to understand the abovementioned effect, the total adhesion force was plotted against the tracked-wheel position on the chain (see Figure 3-34).

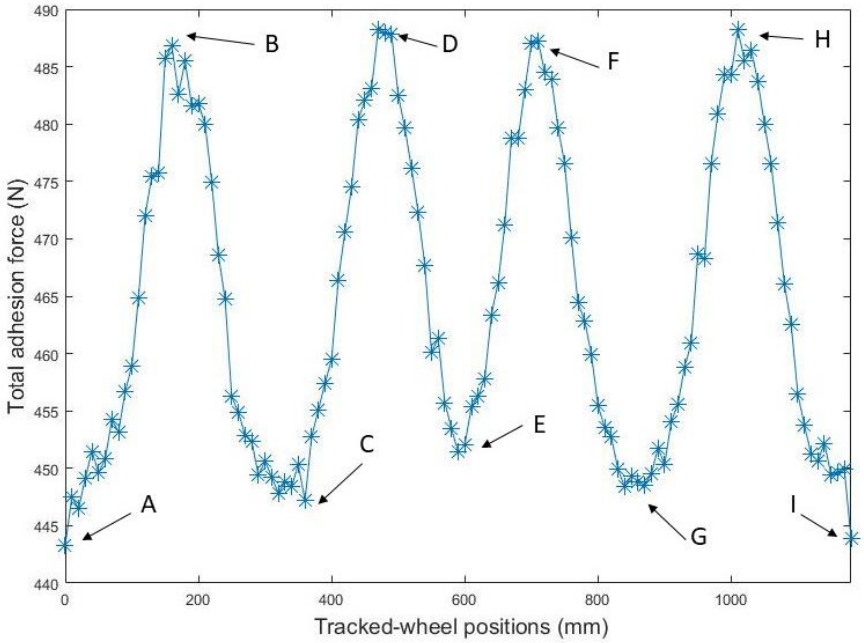

Figure 3-34: Total adhesion forces vs tracked-wheel position on the chain

According to the above total adhesion force study, an adhesion force of a minimum of ≈ 443N and a maximum of ≈488N was generated during climbing. Moreover, the required adhesion force was ≈ 382.46N and it is significant that the proposed mechanism was capable of delivering the required force throughout the climb. When considering the total adhesion force graph in Figure 3-34, significant force variations can be seen. In order to understand the reasons for the variation, the physical placement of the adhesion module on the chain were studied. In Figure 3-35, A, B, C… illustrates the physical positions of the adhesion module, which are mentioned in Figure 3-34. The B, D, F, and G positions in Figure 3-34 are the recorded peak adhesion values. When considering the physical positions of B, D, F, and G in Figure 3-35, it is significant that the contribution of more than two adhesion modules helped the system. The A, C, E, G, and I points were marked as low adhesion points compared to others (but the adhesion force was higher than the requirement). When considering the physical conditions in Figure 3-35, it is significant

that only two adhesion modules were in contact with the chain surface. Therefore, the net adhesion force was recorded at a low value.

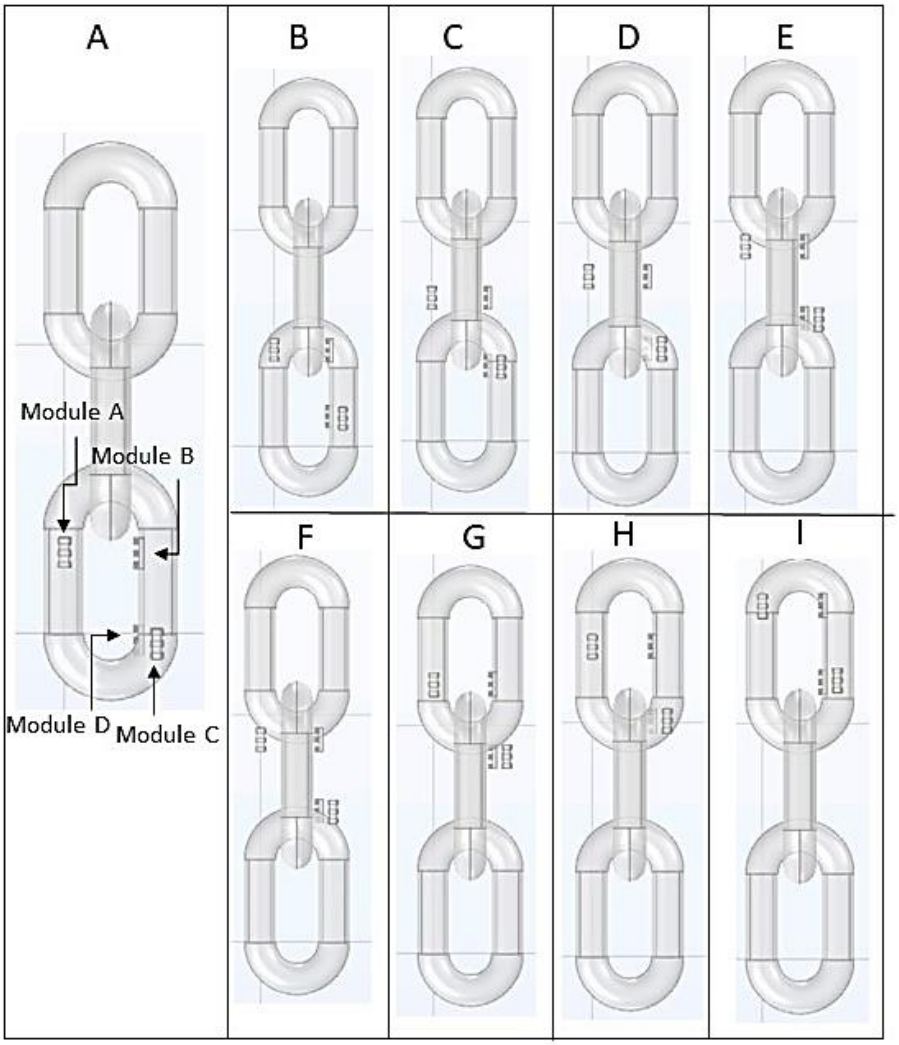

Figure 3-35: Corresponding tracked-wheel places of Figure 3-34

The abovementioned numerical modelling results were based on the adhesion module geometry illustrated in the Figure 3-32(c). The distance between the two adhesion module sets was considered as ≈ 216mm.

Therefore, another study was conducted to understand the behaviour of the adhesion forces and distance between the two modules. For this, the adhesion modules were placed closer than in the previous test, as illustrated in the layout (see Figure 3-36). Similarly, parameter p1 was varied, as before, and the adhesion forces were recorded as presented in Figure 3-37.

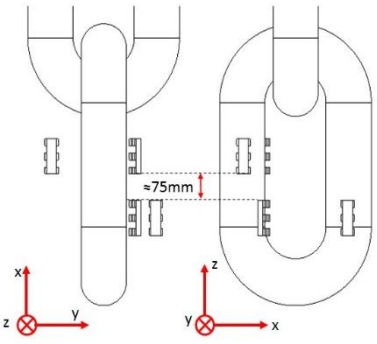

Figure 3-36: Distance between orthogamy adhesion modules

(a)

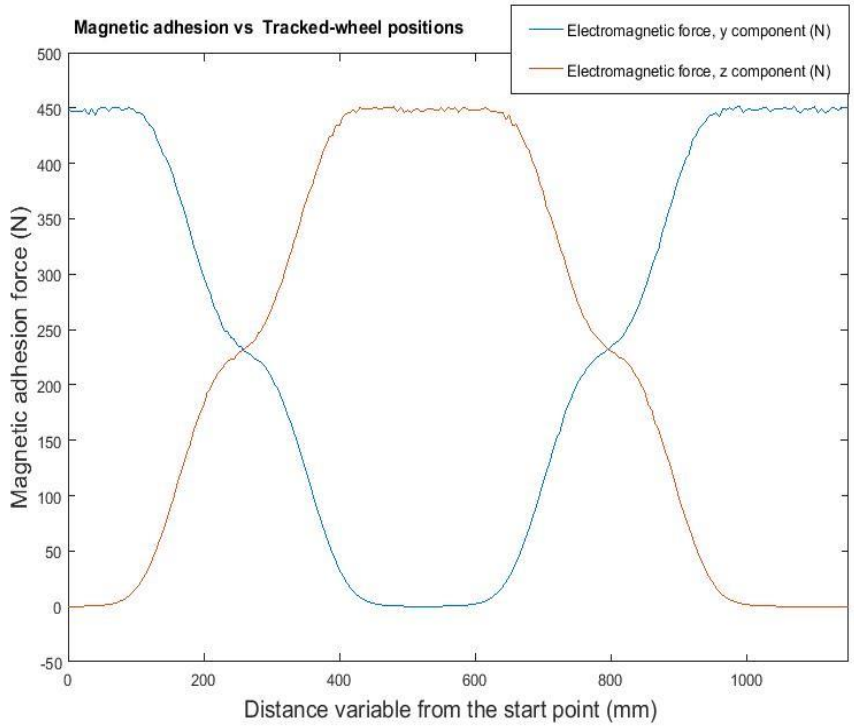

(b)

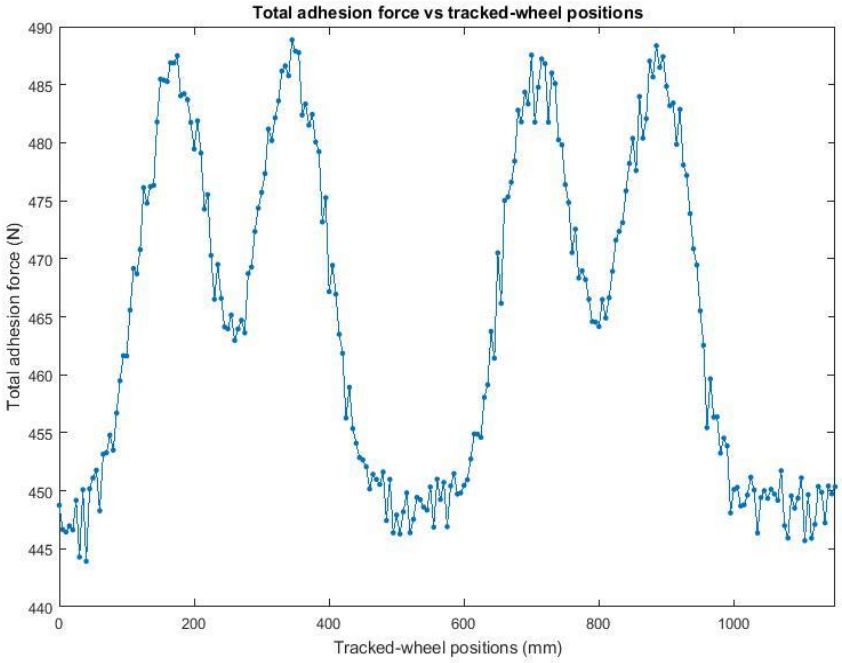

Figure 3-37: (a) Directional adhesion force; (b) total adhesion force

When considering the results presented in Figure 3-37(a), a similar curve shape of adhesion force variation (directional component) was obtained. When considering the total adhesion force in Figure 3-37(b), this demonstrates a peak adhesion of 487.89N and a minimum adhesion of 433.17N, which is higher than the requirement. From this study, it was possible to conclude that the distance between orthogonal adhesion module sets did not impact the overall adhesion force. To simplify the prototype procedure, the distance between the orthogonal adhesion modules were maintained at 216mm (for this study). If the value increased more than this, the overall length of the tracked-wheel crawler robot increased, which would cause manoeuvrability and deployment difficulties.

3.8 Motor requirement calculations

As discussed previously, the tracked-wheel locomotion mechanism was selected for this study. The designed/proposed tracked-wheel system needed to be externally driven by a motor. The motor torque calculation for magnetic adhesion climbing robots has been studied in the literature [9] , the torque is calculated as follows,

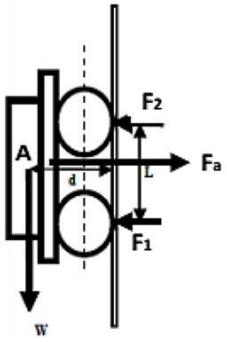

Figure 3-38: Torque calculation force diagram (used in [91] [9])

$$\tau = W\ d + \ \mu\ F_m\ r \qquad \textit{Eq 3-10}$$

The main parameters required for the torque to drive the robot (τ) are the robot's weight – surface distance (d), the wheel – surface coefficient of friction (μ), robot weight (w), and magnetic adhesion force (F_m). The previously published equation, Eq 3-10, was adapted according to the physical quantities of the tracked-wheel unit as follows (refer figure 3-39). To simplify, a single tracked-wheel unit was considered with the full structural weight.

$$d = (r_1 - r_2)\frac{w - w_c}{w_c + w_t} + r_2 \qquad \textit{Eq 3-11}$$

$$\tau = w\left[(r_1 - r_2)\frac{w - w_c}{w_c + w_t} + r_2\right] + \mu F_m R \qquad \textit{Eq 3-12}$$

Eq 3-12 was adopted according to Figure 3-39. The distance (d) in Eq 3-10 (the weight of the robot to the surface) was calculated by considering the equilibrium position of the weight (refer Eq 3-11). Therefore, the required motor torque equation can be expressed Eq 3-12. Where F_m is the magnetic adhesion force generated by the adhesion module (calculated in section 3.5.3) and R is the effective radius of the tracked-wheel unit. The required speed of the robotic platform can be calculated as follows:

$$S = S_{RPM} \times 2\pi R \qquad \textit{Eq 3-13}$$

where S_{RPM} is the rounds per minutes of the gearbox + motor combination, R is the effective radius of the tracked wheel, and S is the net speed (per minute) of the robot. According to the orthogonal tracked-wheel concept of climbing, at least two sets of tracked-wheel units contribute to the motion at a given point. Therefore, each crawler should be capable of delivering half of the torque, which is calculated in Eq 3-12. The speed of the robot and the motor torque were calculated in the prototype section (Chapter 4). The inspection methods were not presented at this stage of the research, but the speed of the robot needed to be allocated according to NDT inspection requirements.

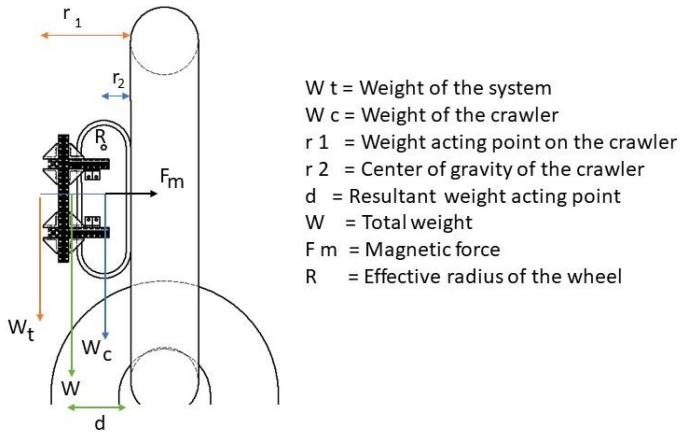

Figure 3-39: Motor torque valuation force diagram

3.9 Structural analysis of the strength of the frame

As the final design parameter of the tracked-wheel climbing robot, the robot's outer structure was designed. A numerical modelling study was carried out to understand the behaviour of the structure when the tracked-wheel units were in place. The importance of deployment was discussed as a requirement in Chapter 2. Therefore, easy deployment ability and retrievability were considered during the robot frame design phase. A structure/frame that needed to be deployed around a chain link was not practical due to the in-situ mooring chain conditions. Therefore, a lightweight L-shaped frame that could be

placed easily on the chain link was considered. The CAD design presented in Figure 3-40 was designed to hold the orthogonal crawlers that could fit on the specified chain link (for chain link dimensions, see Figure 2-21). The un-enclosed characteristic of the L-shaped design allows robot operators to easily deploy/retrieve the robot on/off the chain, as illustrated in Figure 3-40 (b, c, and d).

According to the climbing concept, at a given point, two tracked-wheel units are attached to the chain while the other two are suspended in air. It was necessary to understand the

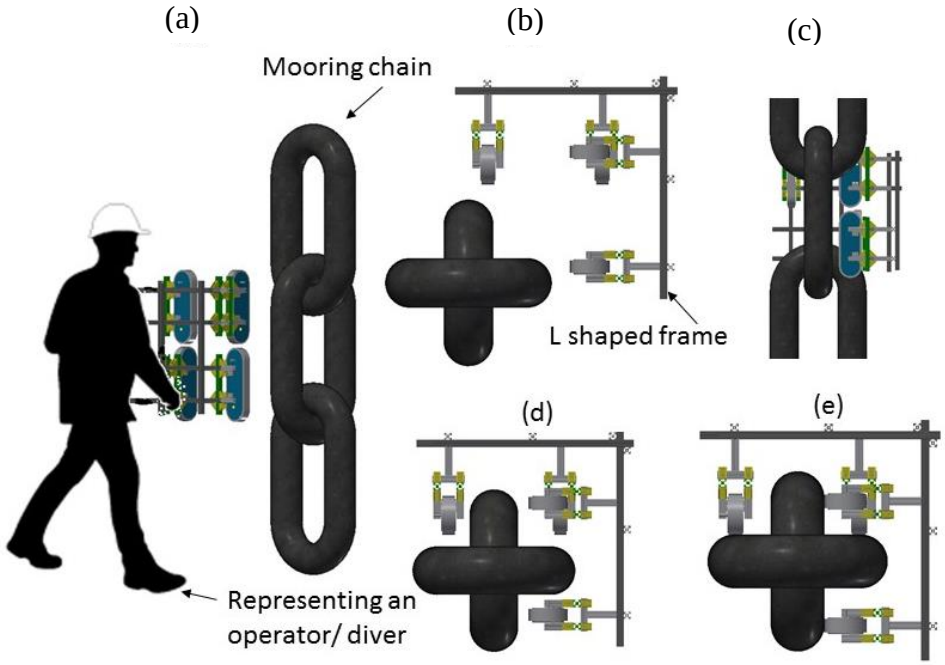

Figure 3-40: Main frame of the robot and deployment; (a) deployment using an operator/diver; (b) deployment step 1; (c) deployment step 3; (d) deployment step 4

displacement behaviour of the unattached tracked-wheel units in 3D space. If the displacement of the unattached units was significant (which could disturb the linear trajectory of motion), vertical climbing could be disturbed because they needed to be placed on the next chain surface. Therefore, FEA was conducted to understand the displacement behaviour of the unattached tracked-wheel units. In order to conduct the numerical modelling, an L-shaped frame was designed using SolidWorks CAD software, and the solid model was imported into the FEA Static structural module in the ANSYS workbench. The study was carried out with a mesh of a maximum element size of 20mm and a minimum element size of 0.1mm. The material properties assumed for the study are

presented in Table 3-4. The layout presented in Figure 3-41(a) was used in the study under gravity forces. The tracked-wheel displacements in 3D space are presented in Figure 3-41.

Table 3-4: Frame design/modelling parameters

Parameter	**Parameter value**
Material	EN AC-51400 cast aluminium
Density	2.7g/cm^3
Young's modulus	70GPa
Tensile strength: Ultimate	200MPa
Tensile strength: Yield	120Mpa
Poisson's ratio	0.33

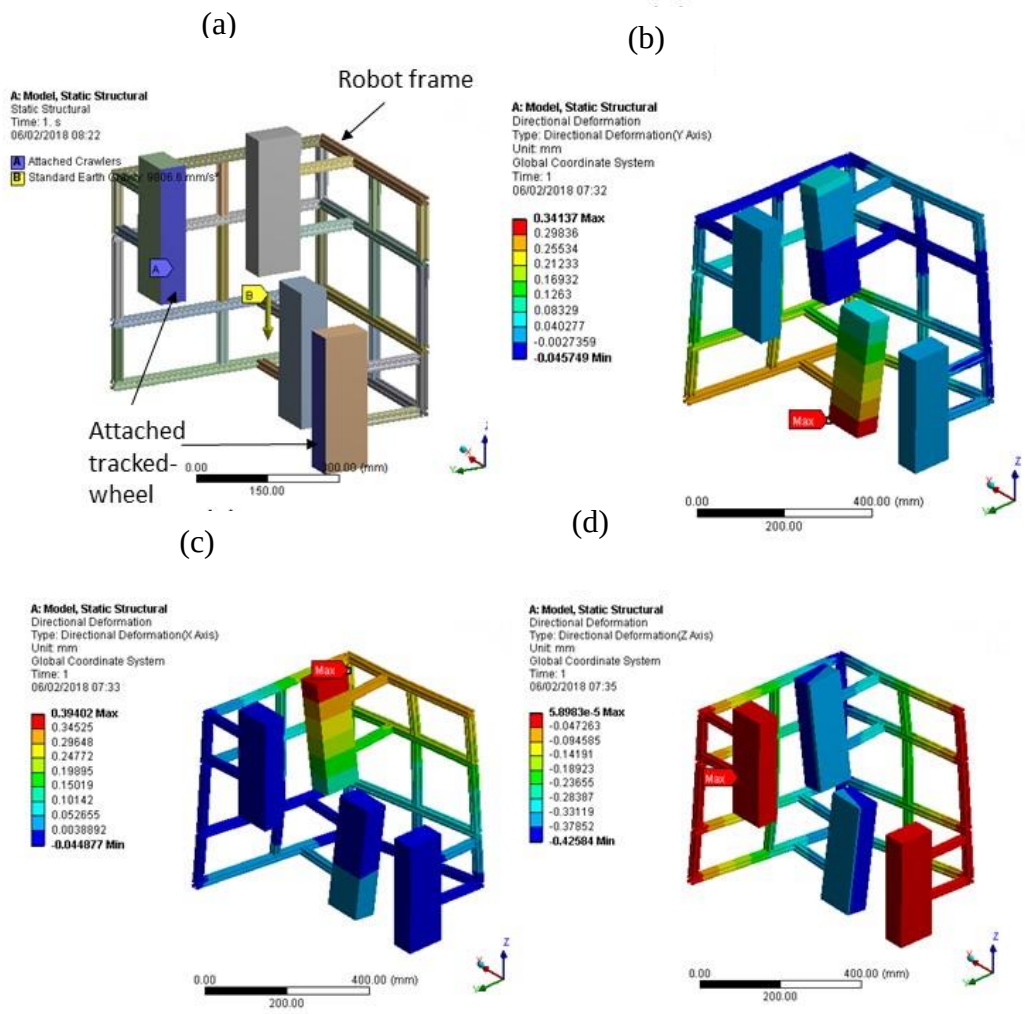

Figure 3-41: Structural deformation analysis 1: no payload; (a) model layout; (b) y axis deformation; (c) x axis deformation; (d) z axis deformation

The displacements in 3D space were recorded as illustrated in Figure 3-41(b, c, and d). According to the study, maximum displacement occurred along the x axis (see Figure 3-41(c)), which was 0.394mm and was relatively low when compared to the width of the chain link (≈ 133mm).

Structural health monitoring of mooring chains was the primary objective of this robotic platform. Therefore, it was vital to understand the behaviour of the frame when carrying a payload. The payload was assumed to be the weight of the NDT instrumentation, such as the ultrasonic probe/probe manipulator, camera etc. A payload of 100N was equally distributed and added to both sides of the frame (see Figure 3-42(a): layout of the model). The static structural module in the ANSYS workbench was used in this study. The material properties assumed for the study are presented in Table 3-4. The layout presented in Figure 3-42(a) was used in the study. The tracked-wheel displacements in 3D space were recorded

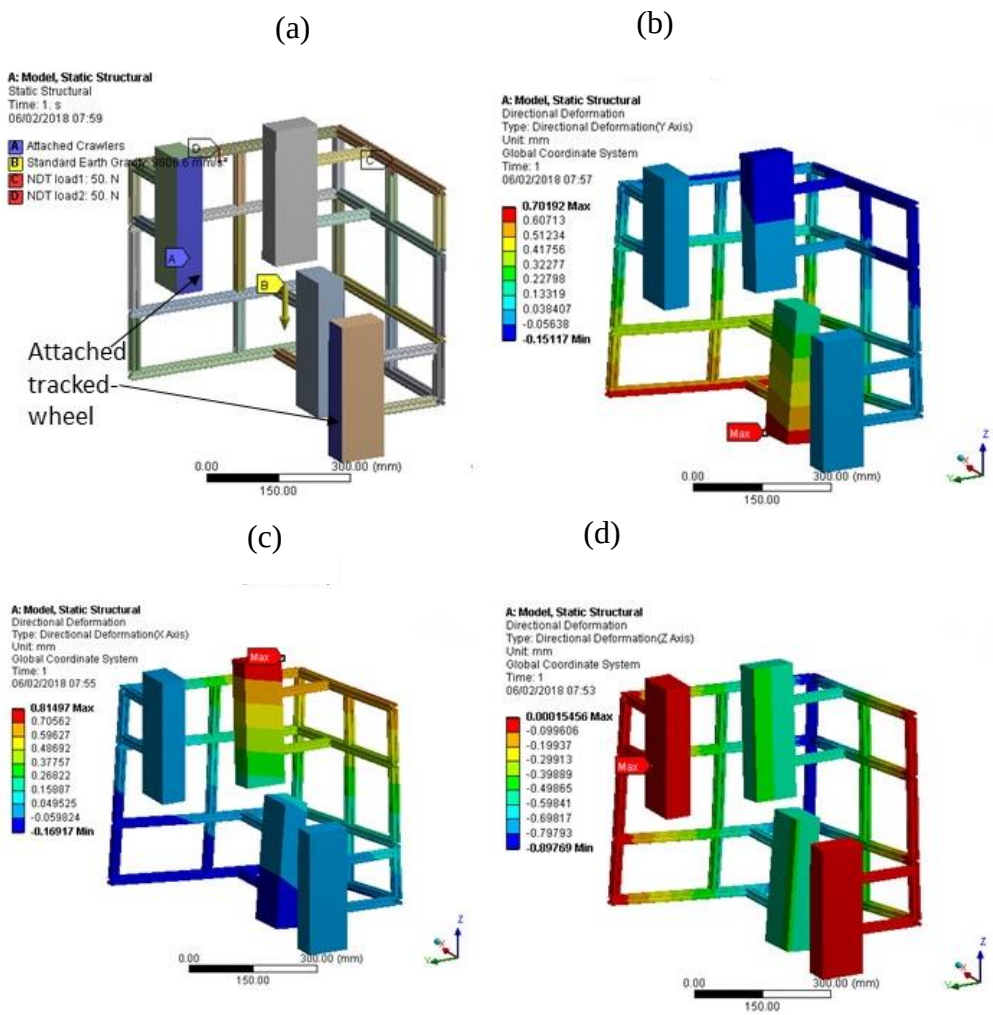

Figure 3-42: Structural deformation analysis 2: with 100N payload; (a) model layout; (b) y axis deformation; (c) x axis deformation; (d) z axis deformation

and are presented in Figure 3-42(b, c, and d). According to the study, maximum displacement occurred along the x axis (see Figure 3-42(c)).

The displacement recorded was 0.814 mm, which was still a relatively low value when compared to the width of the chain link (≈ 133mm). Therefore, it is possible to conclude that the proposed L-shaped frame/tracked-wheel unit displacements were significantly low and the impact of tracked-wheel orientation due to the structural displacement was negligible.

According to the design of the locomotion, the robot should be attached to the chain surface with a minimum of two tracked-wheel units. The following structural deformation study was extended by considering following variations (see Figures 3-41, 3-42, 3-43, 3-

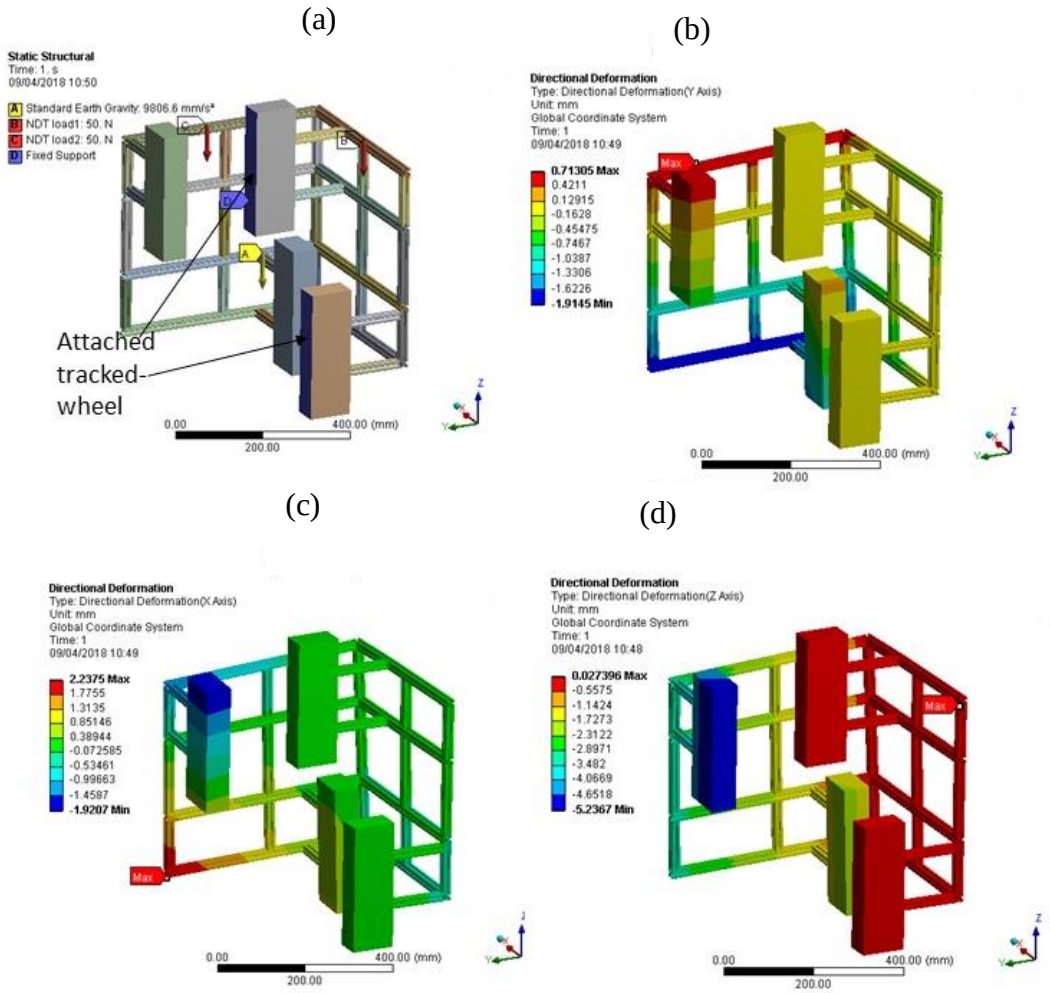

Figure 3-43: Structural deformation analysis 3: with 100N payload; (a) model layout; (b) y axis deformation; (c) x axis deformation; (d) z axis deformation

44, 3-45, and 3-46); *i.e.* contact tracked-wheel pairs were varied and corresponding numerical modelling studies were carried out.

When considering all of the layouts and the FEA results, the maximum deformation observed was ≈ 5.2mm on the z axis, as shown in Figure 3-43(d) (with a payload of 100N). When considering the length of the structure and the chain surface, ≈ 2.2mm on x axis was negligible (chain link sizes are illustrated in Chapter 2, Figure 2-21).

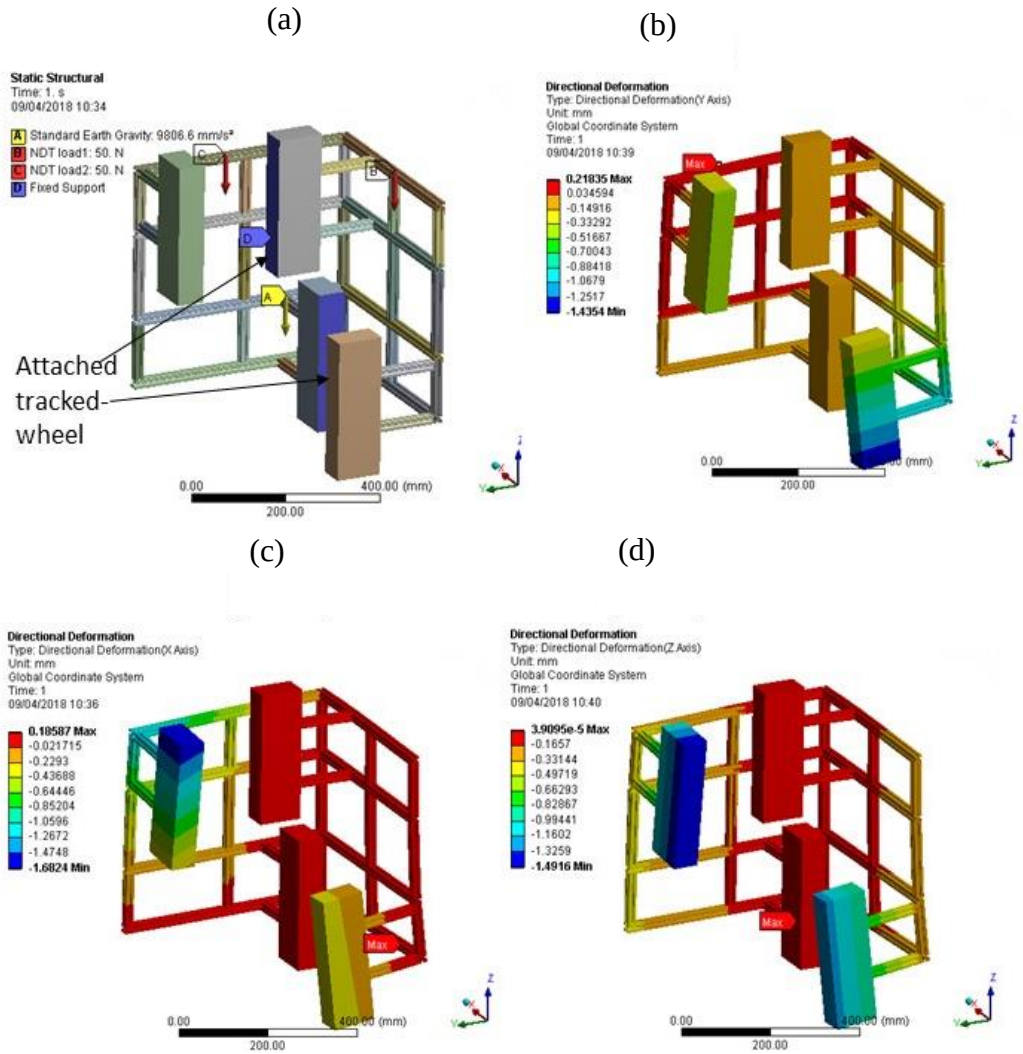

Figure 3-44: Structural deformation analysis 3: with 100N payload; (a) model layout; (b) y axis deformation; (c) x axis deformation; (d) z axis deformation

(a) (b)

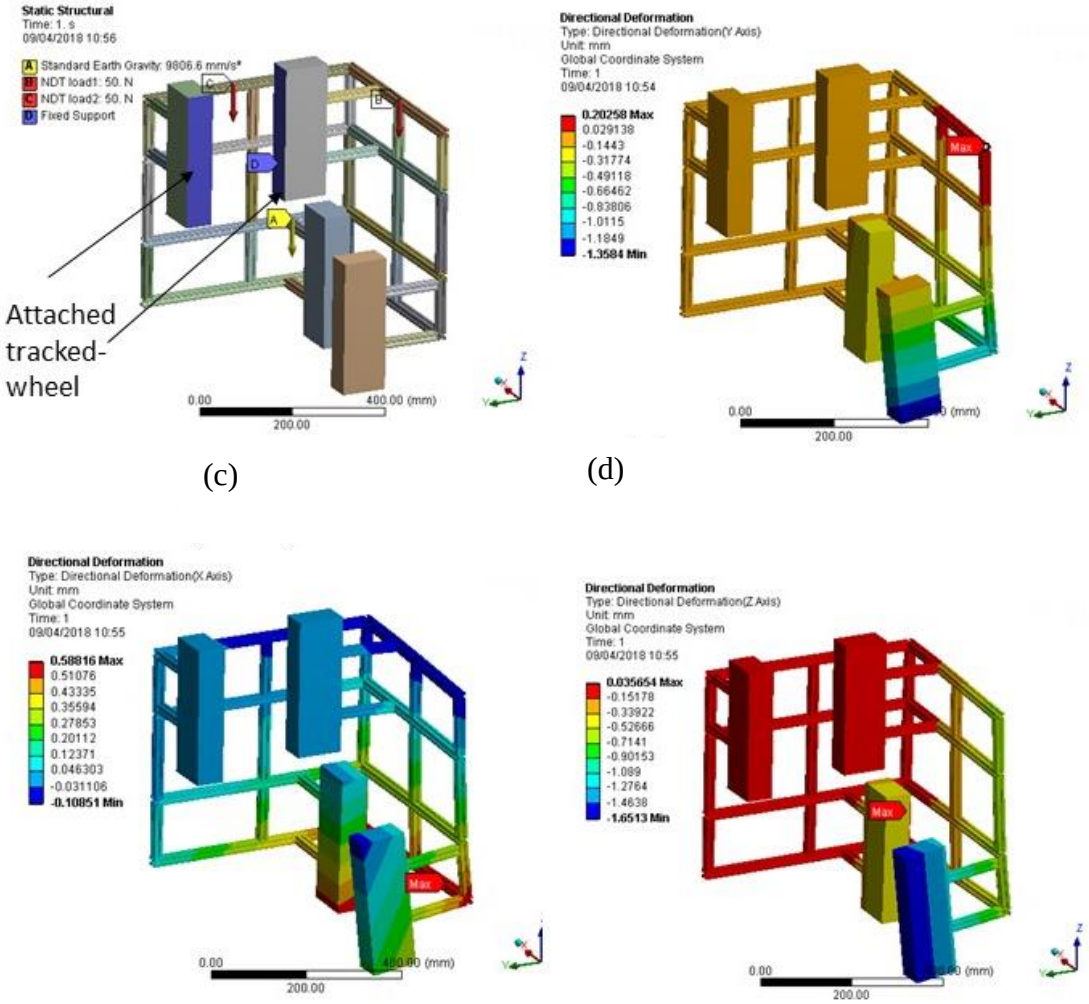

Figure 3-45: Structural deformation analysis 5: with 100N payload; (a) model layout; (b) y axis deformation; (c) x axis deformation; (d) z axis deformation

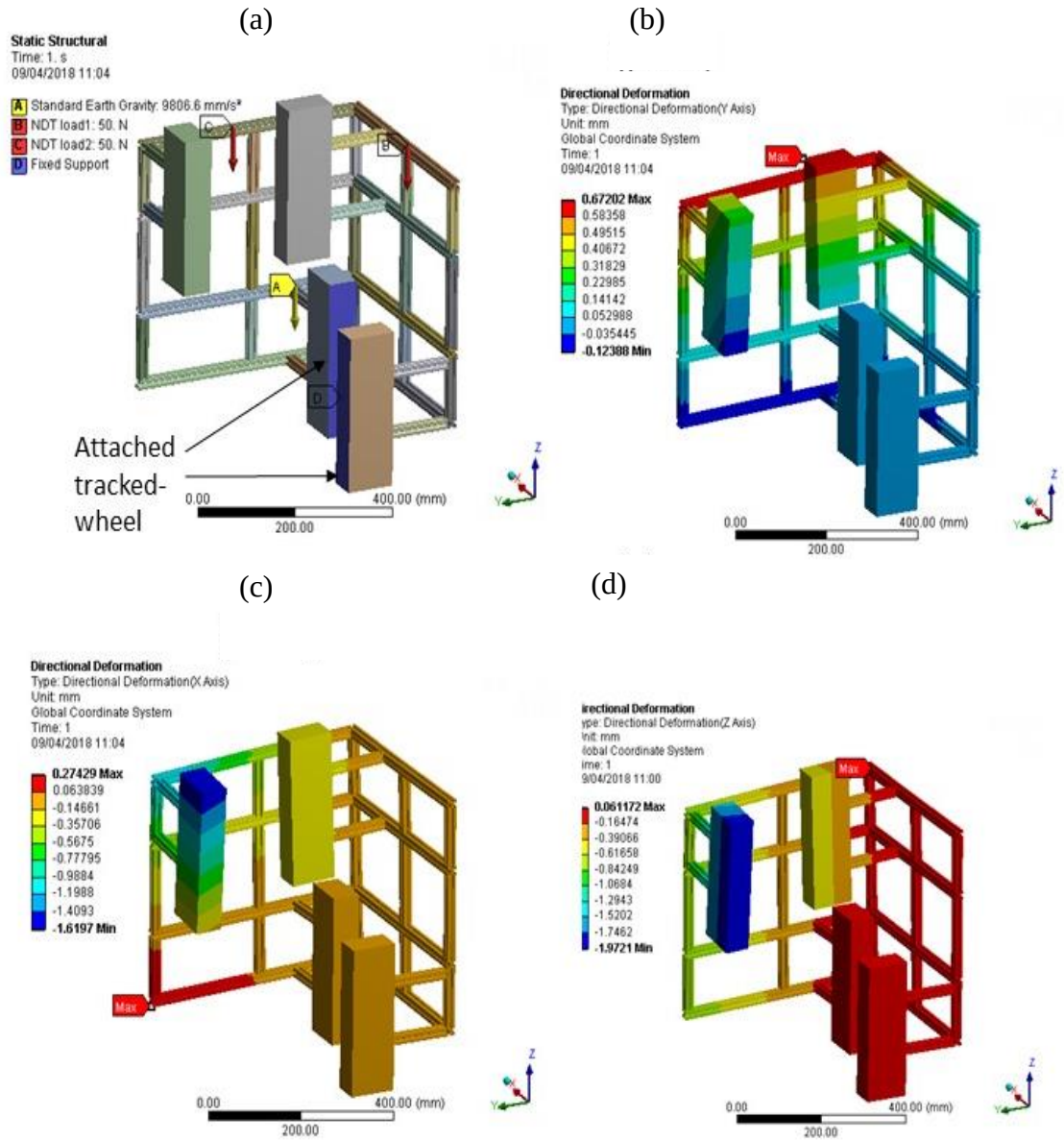

Figure 3-46: Structural deformation analysis 6: with 100N payload; (a) model layout; (b) y axis deformation; (c) x axis deformation; (d) z axis deformation

3.10 Chapter summary and proposed design

3.10.1 Summary of the design

The locomotion idea was to use two sets of tracked-wheel units maintained in an orthogonal position to match the orthogonal links of a mooring chain (see Figure 3-47). One tracked-wheel unit moves on one chain link while the other moves onto an adjacent orthogonal chain link. Therefore, each orthogonal set of tracked-wheel units enables the robot to move continuously along the chain. Units A and D (see Figure 3-48(a)) represent parallel wheels that move on parallel tracks of a link on one side, while units B and C

represent parallel wheels that move on parallel tracks on the orthogonal links. During the climbing process, A–D and B–C tracked-wheel units engage with the relevant chain surfaces to support the motion, as illustrated in Figure 3-48(b). Permanent magnets were considered due to their zero-energy consumption and the amphibious nature of mooring chains. The positioning of the adhesion module on uncertain surfaces was minimised due

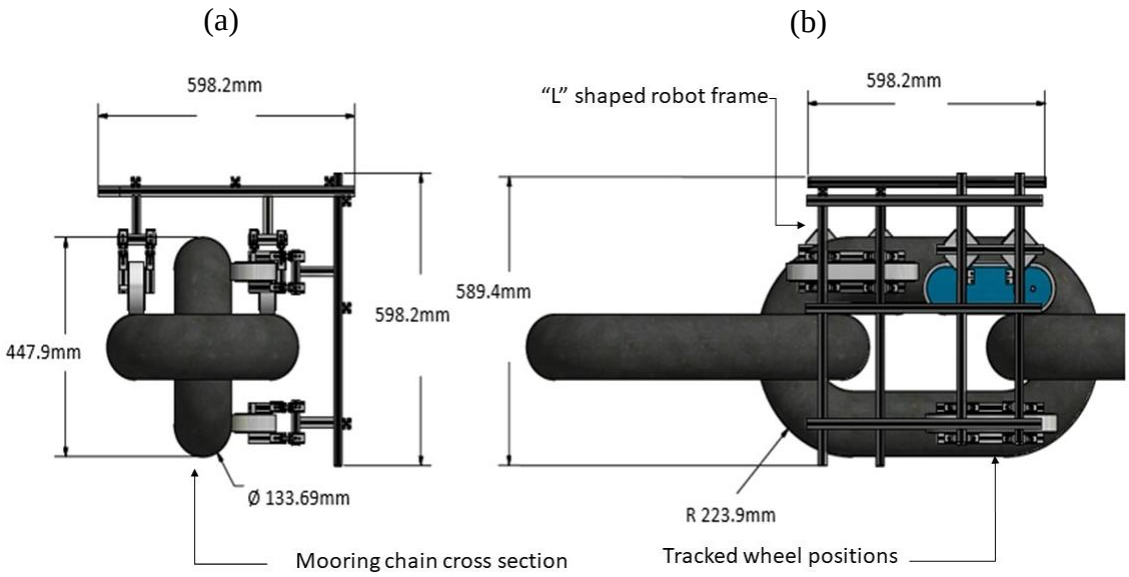

Figure 3-47: Tracked-wheel robot design and placement on the chain; (a) cross-section view; (b) side view of the design

to the passive adhesion quality of the permanent magnets.

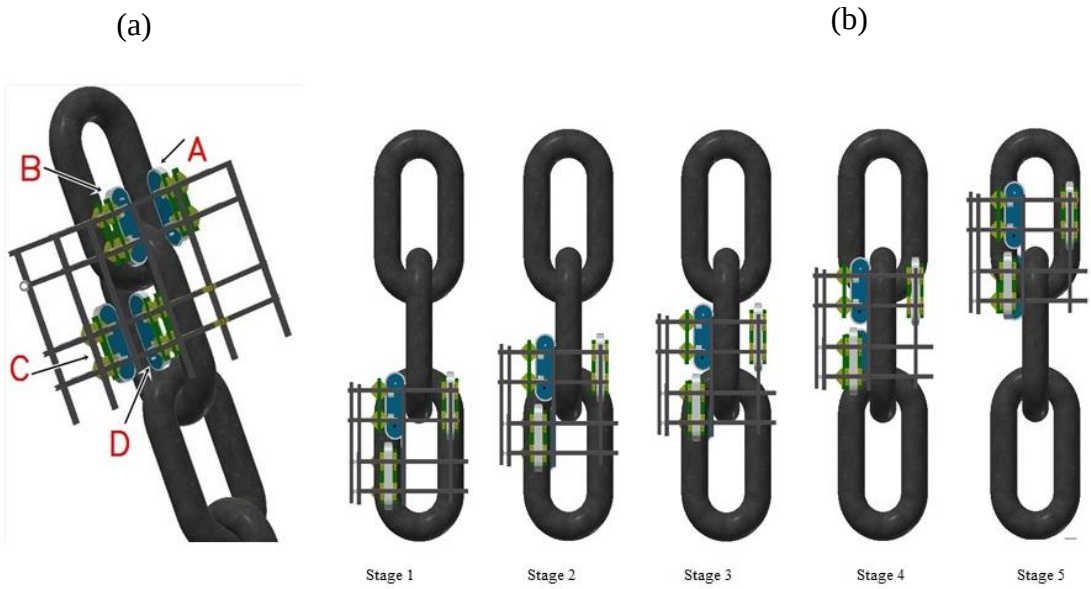

Figure 3-48: Robot crawling explanation; (a) tracked-wheel placement; (b) climbing sequence

3.10.2 Overall summary of the chapter

The physical nature of the mooring chain and the in-situ environmental conditions create a significant requirement for an automated robotic system that has high structural tolerance. Mooring chains are often subjected to significant environmental changes such as tidal waves, wind, storms etc. The chain link shown in Figure 1-4 demonstrates rusted and uneven surfaces. Therefore, the robustness of the climbing robot needs to be ensured. Due to the harsh offshore conditions in which the robot operates, easy robot deployment was identified as one of the primary design requirements. Deployment of a large and heavy robot is much more difficult in offshore environments. In addition, a robot structure that encloses the chain is more laborious to deploy. The ability to change surfaces between orthogonal chain links was considered as the second requirement because mooring chains are discontinuous, being made with two sets of links that are kept orthogonal to each other. Therefore, the crawling/climbing robot needs to cope with the discontinuity. An amphibious adhesion module and suitable locomotion were also identified as the areas that needed to be addressed in the design. The adhesion module and locomotion mechanism were selected according to the mooring chain's physical nature, *i.e.* curved, rusted, ferromagnetic, amphibious, and uneven. The design aimed to achieve a maximum target weight of 35kg to ease off-shore deployment with a maximum of two human operators. Mooring chain link size can vary according to the location, application, load capacity etc. This chapter aimed to describe the design of a lightweight, permanent magnetic adhesion, wheeled robot that could be used as a platform to convey NDT equipment along the mooring chain to perform NDT in air and also be adapted for underwater operation. In this chapter, the mechanical design of a mooring-chain-climbing robot, its structural strength analysis, motor drive and magnetic adhesion systems, and the optimisation of a permanent magnetic adhesion module were discussed. The designs and models proposed in this chapter were used as the prototype aid, as discussed in Chapter 4.

Chapter 4: Prototype of the vertically aligned mooring-chain-climbing robot

4.1 Chapter overview

The magnetic adhesion tracked-wheel approach for mooring chain climbing has not been studied in the literature. Therefore, a study was carried out, as discussed in Chapter 3, to propose a suitable tracked-wheel orientation and tracked-wheel specifications. The required adhesion and torque calculations were added to the study as a design aid. Moreover, a bespoke permanent magnetic adhesion module was designed, and a parametric study was carried out with the use of numerical modelling. An L-shaped lightweight aluminium structure was designed and analysed in terms of its structural behaviours.

This chapter discusses the prototyping and testing of the principles and designs established in the previous chapter. Previously published (*i.e.* in the literature) magnetic adhesion modules were discussed in Chapter 3 in terms of the process of the adhesion module design. Previously published adhesion module design parameters were used in the design process, but a bespoke adhesion module was designed in order to comply with the tracked-wheel unit. A number of numerical modelling studies were carried out during the design of the adhesion module with the use of COMSOL Multiphysics. Validation of the numerical modelling was carried out using a test rig, and a comparison of the results was presented in this chapter. A tracked-wheel unit prototype was presented in the chapter according to the proposed design architecture. Finally, the validation of the tracked-wheel locomotion and the permanent magnetic adhesion principles was carried out by prototyping and testing.

The novel approach of using tracked wheels and permanent magnets to climb vertically aligned mooring chains was tested in this chapter under laboratory conditions. Three link mooring chain segments were used for testing, and climbing experiments were conducted to observe the chain link–link transitions.

4.2 Prototype of the early-stage design

Before the establishment of the proposed magnetic adhesion orthogonal tracked-wheel concept, a few attempts were made during the initial stage of the research. The tracked wheel and external magnet attachment design presented in Chapter 3, Figure 3-12, was prototyped using MISUMI configurable aluminium extrusions (see Figure 4-1). The prototype of the tracked-wheel unit are discussed in this chapter.

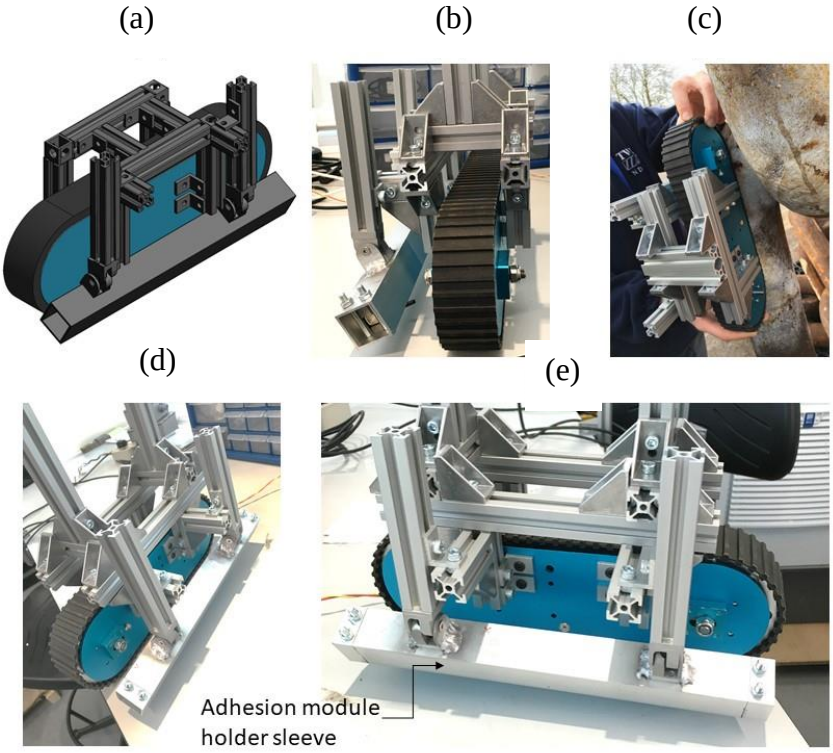

Figure 4-1: Prototype of the tracked-wheel adhesion module attachment attempt 01

The prototyped tracked-wheel adhesion configuration illustrated in Figure 4-1 is a low-cost configurable design. In the above design, a lightweight, rigid aluminium tube was introduced to hold and protect the magnets and the backplate. Moreover, the same tube's outer surface was used to attach a hinge joint. To attach the hinge joint to the magnet holder (aluminium tube), a TIG welding procedure was used (*i.e.* tungsten inert gas arc welding procedure), as shown in Figure 4-2(a). Both the hinge and tubes were made using aluminium. Therefore, welding was proposed for the attachment. In the above-illustrated design, a rigid frame was introduced to hold and attach the crawler to the main frame of the robot. When the prototype was ready, the tracked-wheel unit was tested on a mooring

chain for performance analysis (as illustrated in Figure 4-2(b)). This design was unable to maintain its balance, as explained in Chapter 3 (see Figure 3-12).

(a) (b)

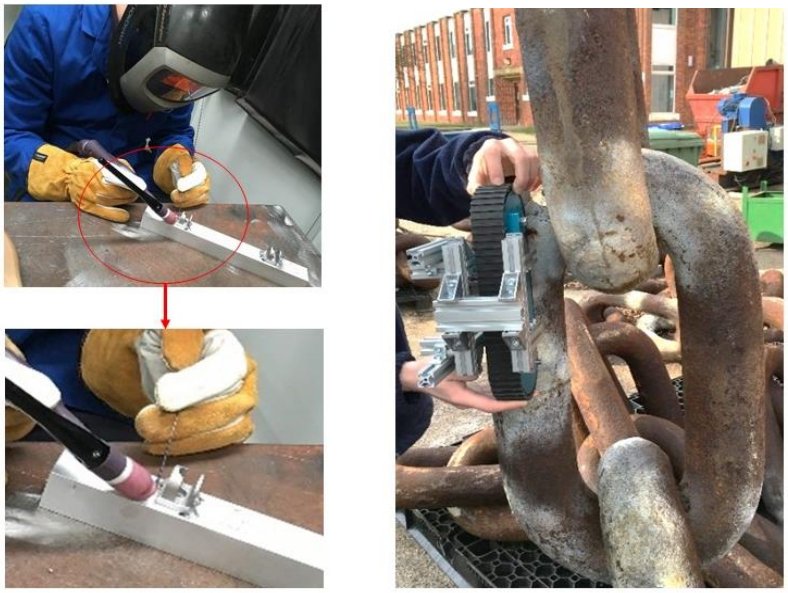

Figure 4-2: (a) TIG welding procedure for attachment; (b) tracked-wheel testing on the chain surface

The idea of a support wheel/wheelset to counter the imbalance forces was prototyped, as proposed in Chapter 3, Figure 3-13 (for the prototyped image see Figure 4-3). An additional wheelset was introduced to the Figure 4-1 tracked-wheel setup in order to maintain balance. The prototyped attachment was tested to check the reliability of the system, but it was unable to behave as expected, *i.e.* the tracked-wheel unit started to share the load with the support wheels, which led to the issue described in Figure 3-13. Moreover, the attachment led to a considerable increase in weight (approximately 1.5kg).

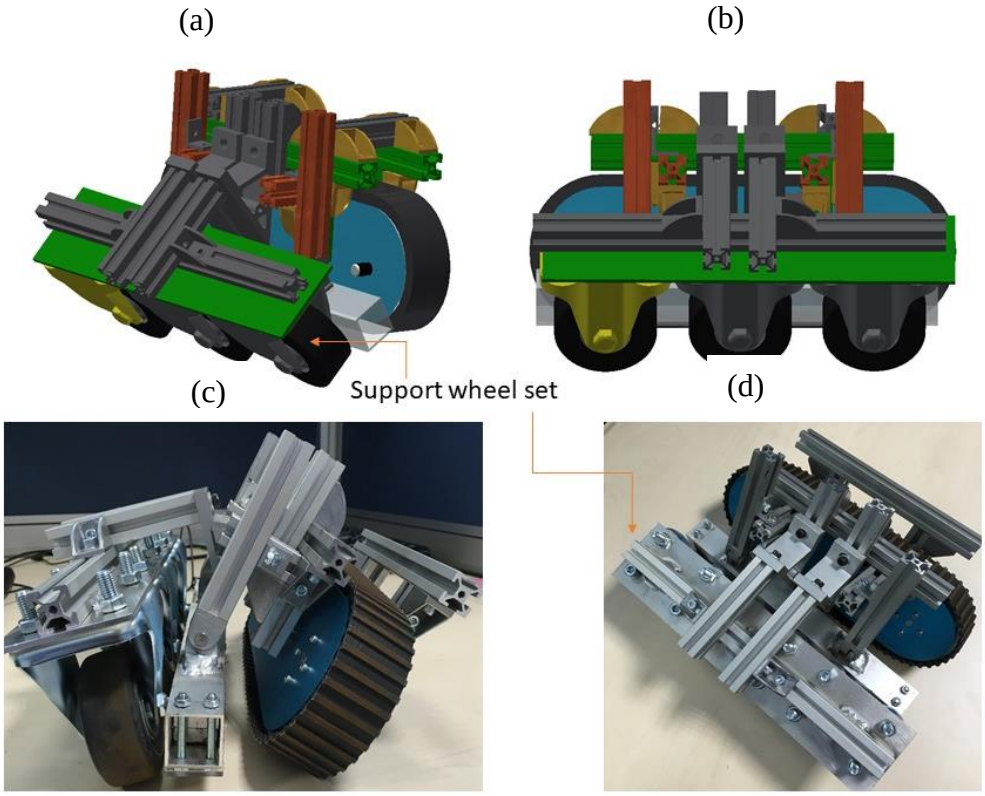

Figure 4-3: (a) and (b) design of the support wheel; (c) and (d) prototype of the design

4.3 Tracked- wheel unit prototype

As explained in the design section of Chapter 3, a prototype of the proposed tracked wheel was constructed (see Figure 4-4). A rubber tracked wheel was introduced to drive two aluminium wheels, and a support wheel was introduced to maintain the tension of the track. As proposed in Chapter 3, permanent magnets were considered for adhesion. Therefore, non-ferromagnetic materials were selected for the tracked wheel to avoid magnetic interferences. If the critical parts of the tracked-wheel unit (*i.e.* aluminium wheel, bearings) were affected by magnetic interference, locomotion could be disturbed. In the design stage for the adhesion module, a high-permeability backplate was proposed to shield/minimise magnetic flux leakage. However, as seen in Figure 3-30(d), some flux leakage was observed. One aluminium wheel was the driving wheel, which was connected to a motor, and the other was passively driven by the track mechanism.

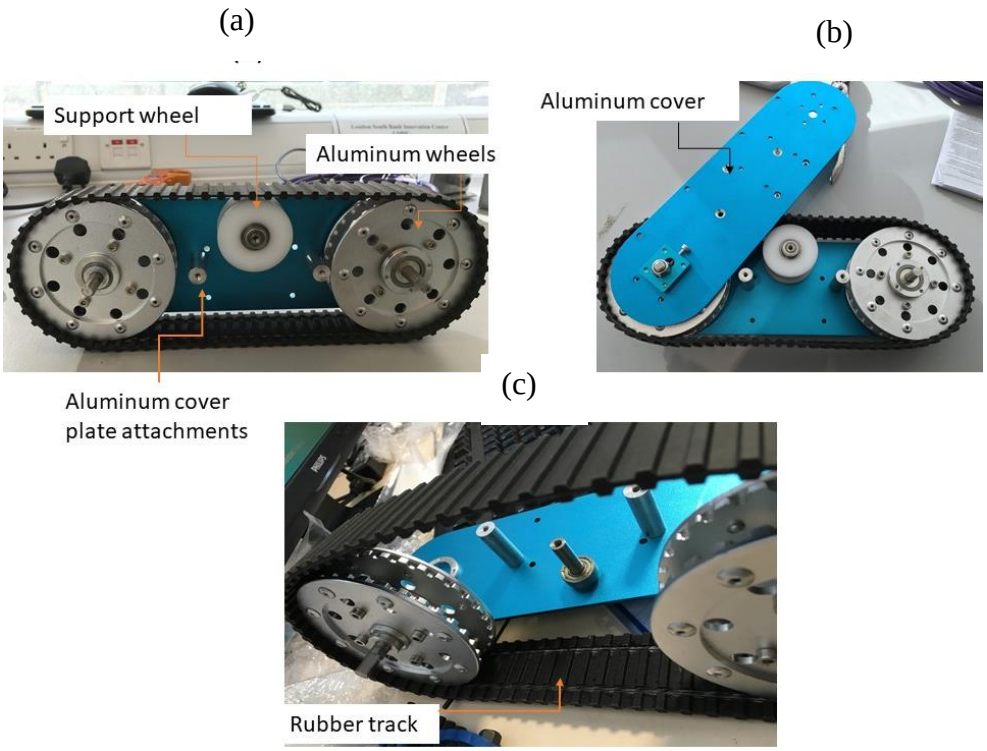

Figure 4-4: (a) and (b) prototyped tracked wheel unit; (c) rubber tracked-wheel set

The dimensions proposed in the tracked-wheel design were considered for the prototype, as illustrated in Figure 4-5(a-b). As discussed previously, 310mm was selected to avoid link–link misalignments. A 40mm internal width was selected to ensure the tracked-wheel unit was able to rest comfortably on the 133mm diameter chain link. The tracked-wheel unit was tested on a chain link, as illustrated in Figure 4-5(c-d). The adhesion module was not included in this test; therefore, the chain link was placed on the floor and testing was carried out. Once the outer structure of the tracked-wheel unit had been prototyped, the adhesion module was investigated.

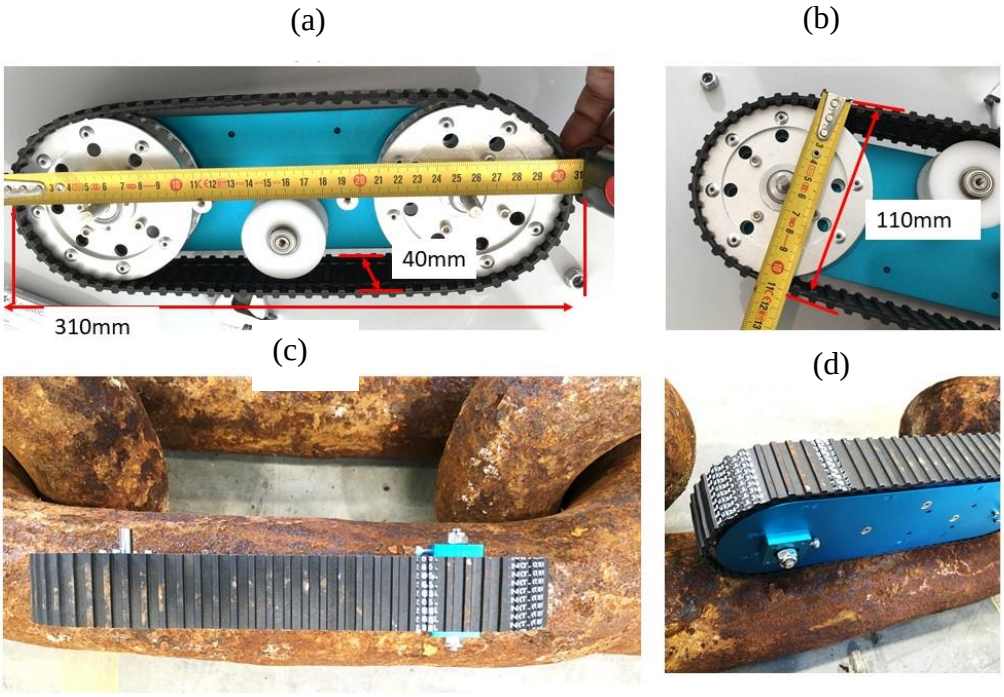

Figure 4-5: (a) and (b) dimensions of the prototyped tracked-wheel unit; (c) and (d) tracked-wheel set testing on the chain surface

4.4 Magnetic adhesion module validation

4.4.1 Validation test rig

In the FEA studies carried out in Chapter 3, a bespoke magnetic adhesion module was designed. It was necessary to develop the adhesion module according to the space provided in the tracked-wheel unit. Therefore, a number of numerical modelling studies were carried out to understand the adhesion properties and magnetic flux density behaviours. It was necessary to validate the results generated in the numerical modelling studies. The test rig in Figure 4-6 was used to validate the magnetic adhesion results simulated in the FEA study. The frame and magnet holding plates were made using (3–5mm) carbon fibre and aluminium plates (see Figure 4-6(c)). Magnets were attached to an aluminium plate with free movement in the direction of the magnetic forces, and the plate was kept on a set of four load cells (see Figure 4-6(b)). Aluminium spacers were introduced to maintain the same air gap as in the FEA simulation (see Figure 4-6(a)). Four strain-gauge-based load cells were introduced to the test rig, and these were capable of measuring up to 1500N. The bottom ends of the load cells were attached to the structure, while the top ends rested on the plate holding the magnets. This setup enabled to measure the changes in plate deflections due to the adhesion force between the magnet and the chain surface. However,

the output of the load cells was relatively weak, *i.e.* millivoltage was obtained compared to the applied load/force. An operation amplifier (op-amp), HX 711, was introduced to the output signal and an AVR microcontroller (with a 10bit digital–analogue module) was used to convert the signal. To enhance the accuracy of the reading, the load cells were configured as a Wheatstone bridge.

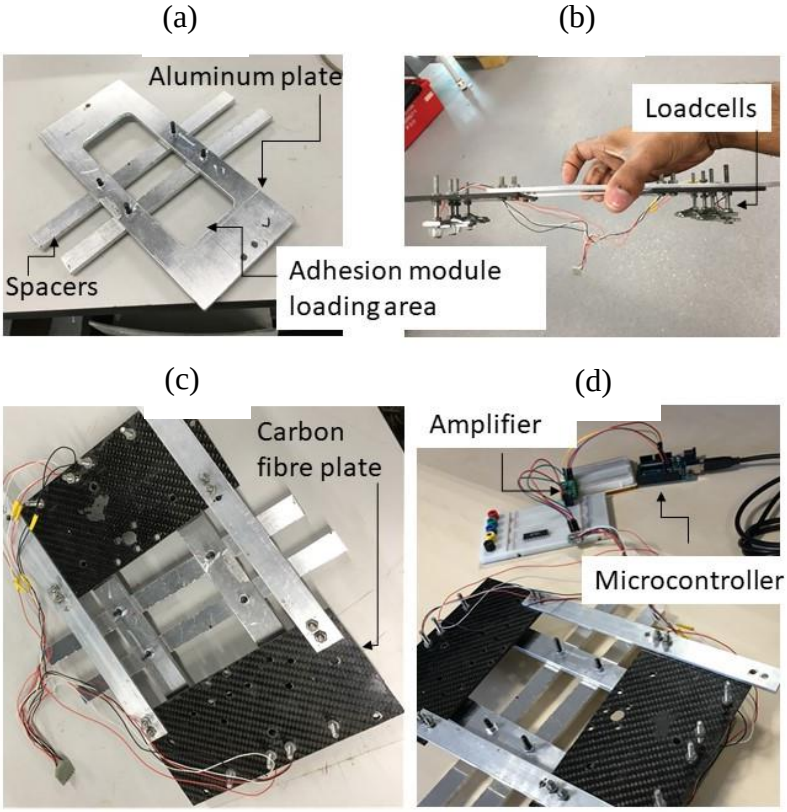

Figure 4-6: Adhesion force validation test rig; (a) free-moving aluminium plate and spacers; (b) load cell arrangements; (c) carbon fibre plate; (d) test rig – amplifier – microcontroller

After prototyping the validation test rig, it was necessary to calibrate the force reading (*i.e.* the digital reading obtained from the microcontroller). A known (pre-calibrated) weight set was used for the test rig calibration. 4N–70N calibration weights were used during the calibration (see Figure 4-7(a)) and the digital reading was plotted to establish the pattern of the force-reading curve (see Figure 4.7(b)). Parts of the test rig that were affecting the load cells were measured independently and deducted from the reading. To enhance the accuracy of the reading, an average of 10 readings was taken for each calibration wright.

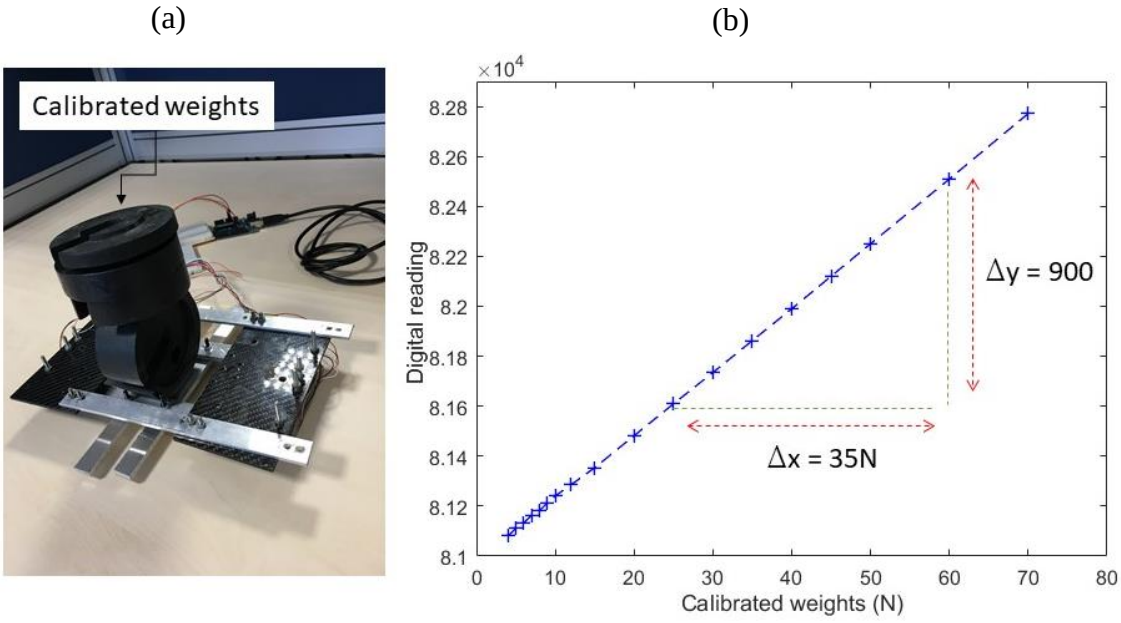

Figure 4-7: (a) Calibration with known weights; (b) calibration curve (known weight vs digital reading)

According to the known weight and the corresponding digital reading curve plotted in Figure 4-7(b), the relationship between the digital reading and the weight was established. By considering the y = mx + c type curve, and can be written as;

$$y = \frac{\Delta y}{\Delta x} x + 80893.90 \qquad \textit{Eq 4-1}$$

Where y is the digital reading and x is the force reading. Therefore, the above equation can be rearranged to obtain the true adhesion force:

$$Force = \left\{(Digital\ reading - 80893.90)/\frac{\Delta y}{\Delta x}\right\} - external\ weight(N) \qquad \textit{Eq 4- 2}$$

According to the adhesion module placement studies, inside the tracked-wheel unit was selected as the best option for the magnets. Figure 4-6 illustrates the space availability as proposed in Chapter 3, Figure 3-22. The experimental test rig illustrated in Figure 4-8 was used to validate the modelling results. The mooring chain was kept in the upright position during the following experiment. Therefore, the external weight subtraction in Eq4-2 was avoided. The base plate was introduced between the test rig and the chain surface to maintain enough surface contact (see Figure 4-8(b and c). To ease the test rig placement

on the chain surface, the base plate was used because the width of the test rig was greater than the width of the chain.

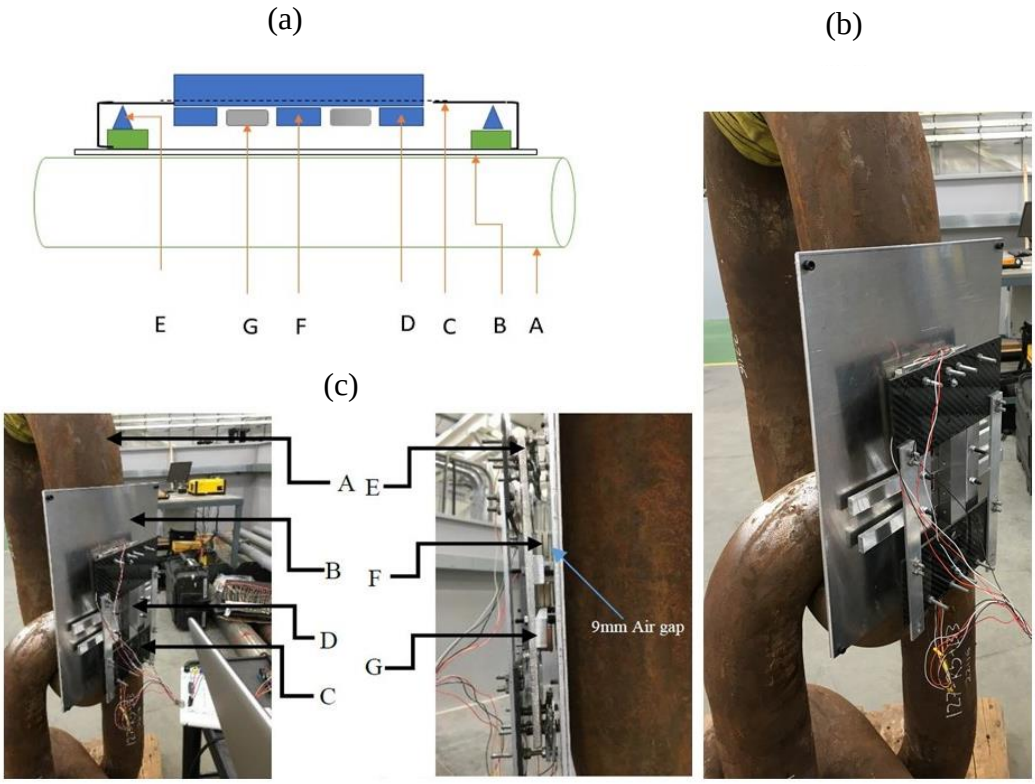

A – mooring chain; B – base plate; C – carbon fibre test rig; D – iron backplate and magnets; E – load cells; F – magnets; G – spacers

Figure 4-8: (a) Experiment schematics; (b) and (c) experimental setup

The experimental magnet sets in Figure 4-9 were tested in the test rig (Figure 4-8) and the forces are recorded in Table 4-1. The 9mm airgap used in the FEA design was kept the same in the experiment by adjusting the height between the magnet–chain surface. The error between the recorded experimental adhesion results and the FEA results are within the acceptable range (*i.e* less than 10%). The maximum variation / error recorded was 6.07 %. A change in air gap distances (± 0.5mm) while setting up the test rig and the sensitivity of the load cells (0.2% manufacturing error in the sensor) were possible factors affecting the error between the FEA and experimental results. Based on the results, it was possible to accept the validity of the FEA study and force calculations.

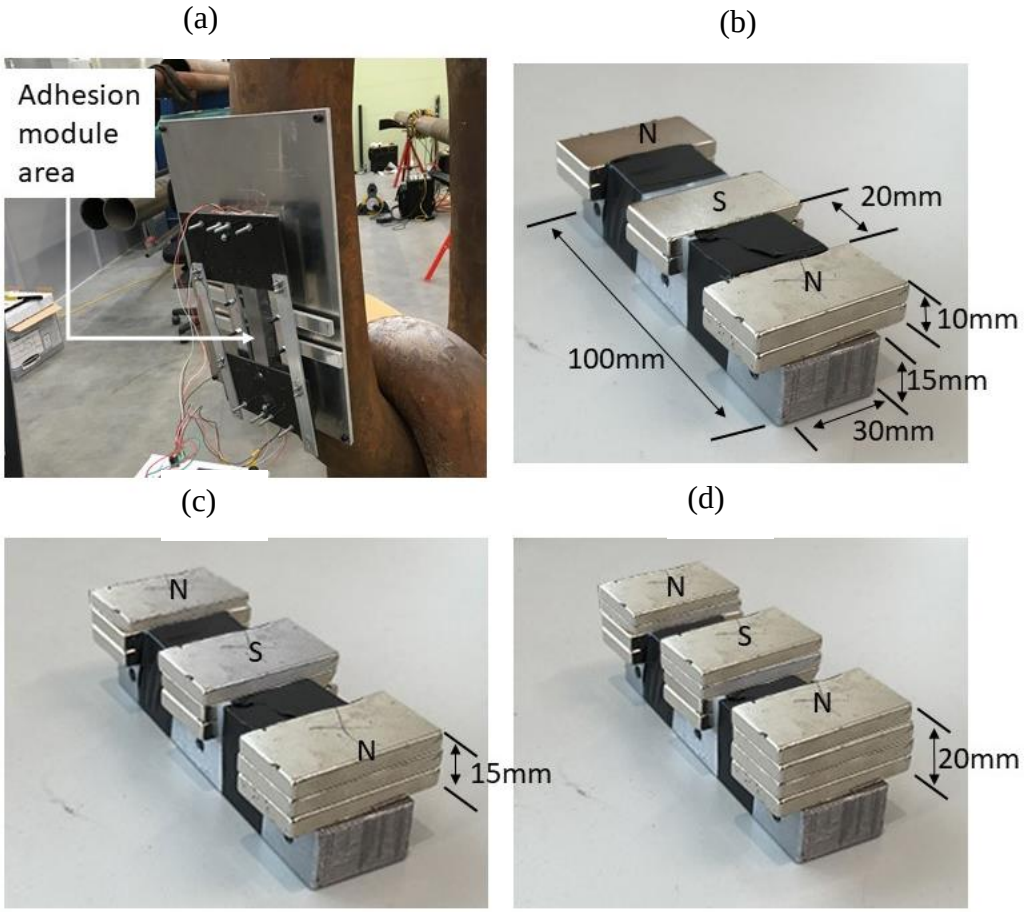

Figure 4-9: (a) Experiment setup; (b) 10mm thickness setup; (c) 15mm thickness setup; (d) 20mm thickness setup

Table 4-1: Simulation vs experimental results

Studied magnet arrangement	**Numerical modelling results**	**Experimental results**	***Error %**
B	164.95N	155.504N	-6.07%
C	182.17N	185.35N	1.72%
D	219.16N	216.60N	-1.18%

* Error calculation = [(Experimental – Numerical)/Experimental] x 100.

4.5 Adhesion module placement

As discussed in Chapter 3, Figure 3-22, the adhesion module was placed inside the unit after testing the prototype, *i.e.* the adhesion module was inserted (see Figure 4-10(b)). There were small changes in the air gap between the magnet–chain surface (due to the uneven surface of the mooring chains). This led to a sudden increase/decrease in adhesion force. Therefore, small support wheels were introduced between the magnets to maintain the steadiness of the air gap during the entire motion (see Figure 4-10(b)). The support wheel and crawler were made using aluminium to avoid any interference with the magnets. Small cuts were introduced to the crawler to keep the magnets in place, as illustrated in Figure 4-10(a) (it was essential to maintain a constant air gap between the two magnets). Once the addition module was placed inside the tracked-wheel unit, it was tested on a mooring chain, as illustrated in Figure 4-10(c). Only the adhesion (ability to stick to the chain) capability was tested at this stage because the motor attachments had not been added. During the experiment, adhesion capability, support wheel behaviours, and tracked-wheel behaviours were observed.

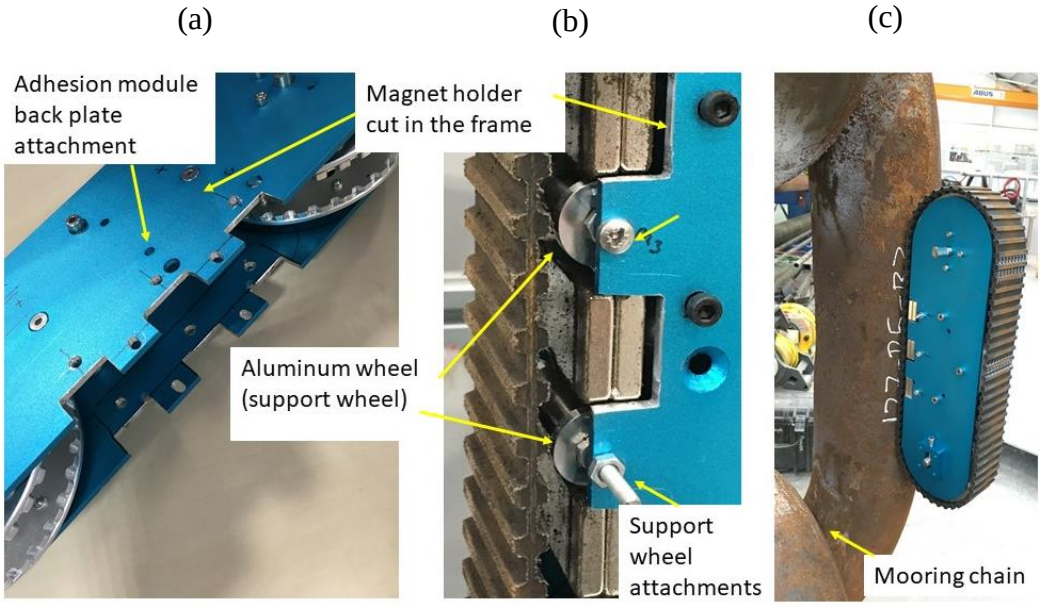

Figure 4-10: (a) Cuts introduced to the tracked wheel; (b) aluminium support wheel; (c) tracked-wheel unit testing on a mooring chain

4.6 Motor attachment and motor control

According to the orthogonal tracked-wheel concept of climbing, at least two sets of tracked-wheel units contribute to the motion at a given point. Therefore, each crawler should be capable of delivering half the torque, which was calculated in Chapter 3, Eq 3-12 (approximately 14Nm). Each crawler unit was equipped with a brushless DC motor (24V/16Nm DC brushless, 8mm diameter output shaft), and a suitable worm gearbox to supply the calculated torque (631:1 gear ratio with an output speed of 4rpm). The speed of the robot was calculated at 42cm/min according to Eq 3-14. To save space between the orthogonal chain links and the crawlers, each motor was attached with a 90˚ attachment (see Figure 4-11).

(a) (b)

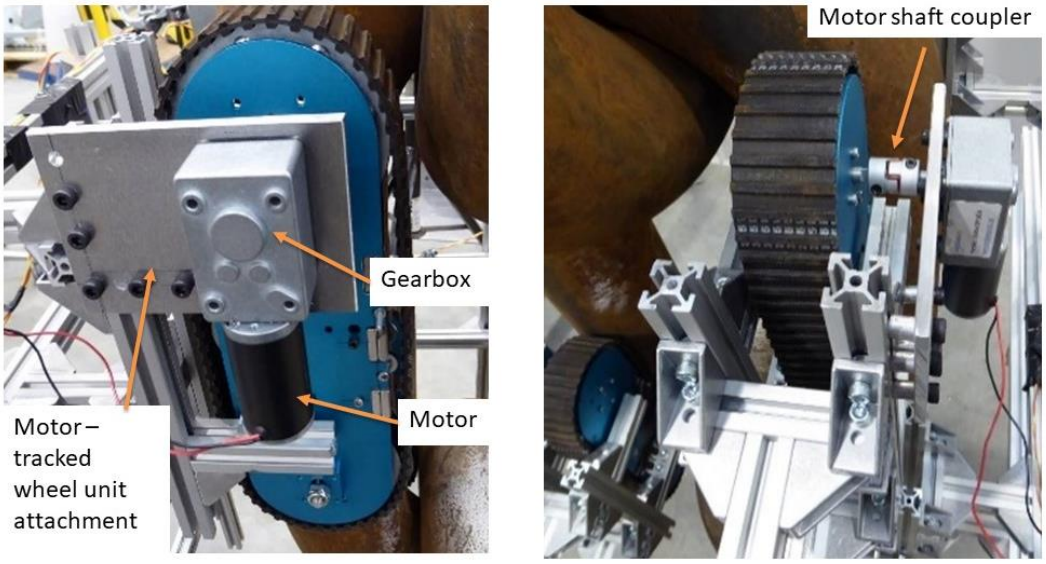

Figure 4-11: Motor and gearbox attachment and placement on the robot

As mentioned at the beginning of this chapter, this study aimed to establish a fundamental principle for a fast, lightweight tracked-wheel-based robot solution for chain climbing. Therefore, the basic flow chart operation described in Figure 4-12 was used to drive the robot platform along the mooring chain. To drive the motors along the mooring chain, each set of motors was attached to an H-bridge module, and the relevant H-bridge signals were generated using a microcontroller with an input signal from a joystick.

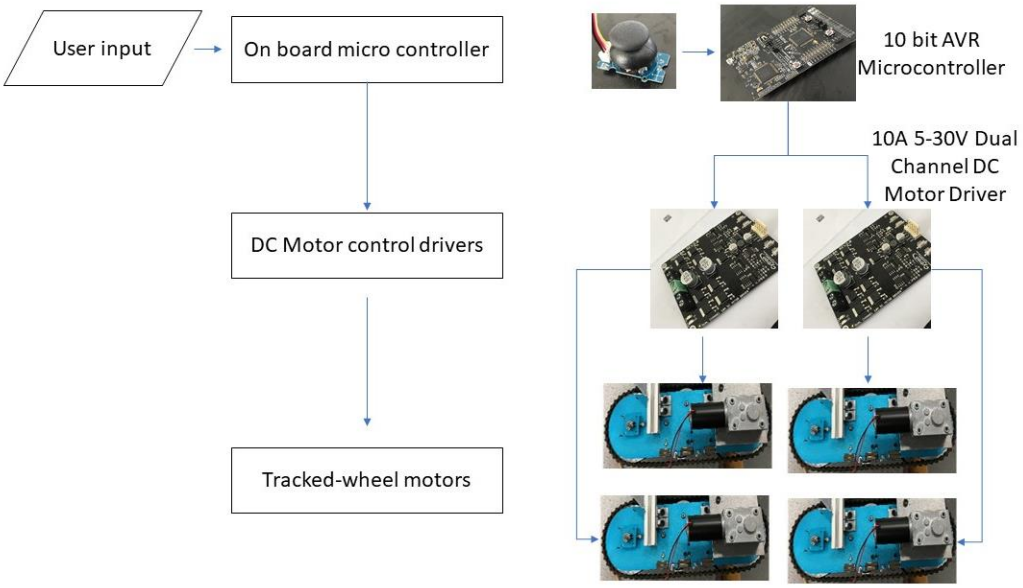

Figure 4-12: Tracked-wheel motor control

4.7 L-shaped frame design and adhesion test

Using the previously discussed simulations and CAD designs, the prototype of the tracked-wheel units and the L frame were built. Aluminium extrusions were used to prototype the L-shaped main frame and the four crawler units (tracked-wheel) were attached to the frame (see Figure 4-13). Additional 10cm lengths of aluminium extrusions were used during the prototyping for further mechanical changes. At this stage of the research, the mooring chain inspection mechanism was not included; therefore, the following climbing tests were carried out with the robot's own weight. A stability check was performed with external payloads (see Figure 4-14) to check the adhesion capability of the design. According to the experimental results, the robot stayed attached to the chain link surface with up to 50N of external force (all safety cables were released during the stability test experiment).

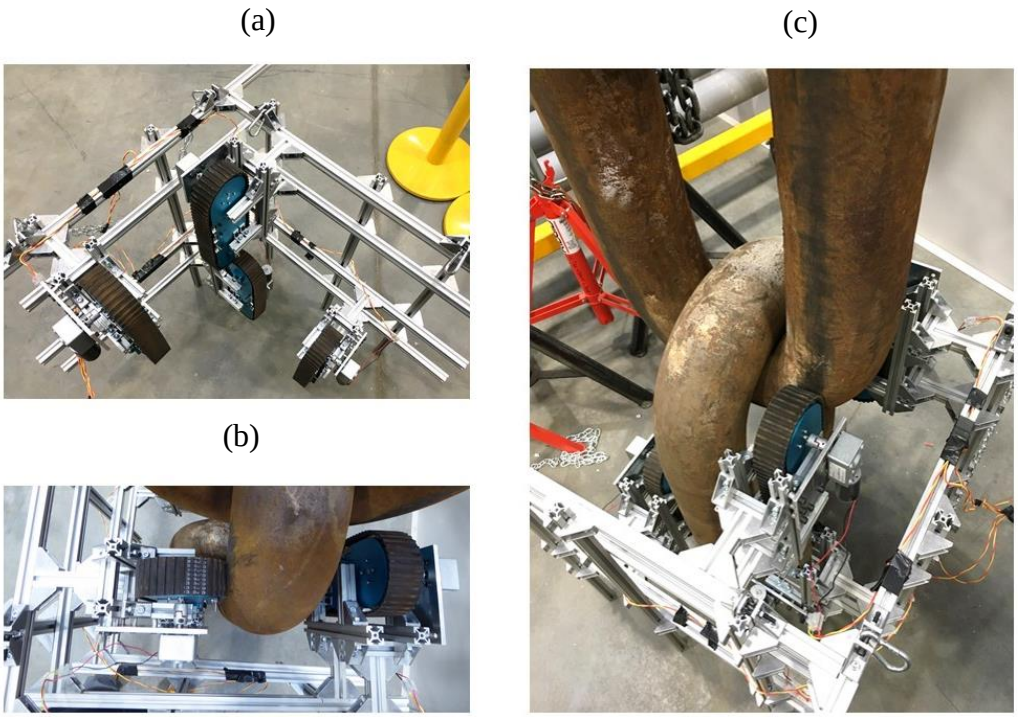

Figure 4-13: (a) L-shaped robot main frame and tracked-wheel units; (b) example of orthogonal tracked-wheel placement; (c) L-shaped frame deployment onto the mooring chain

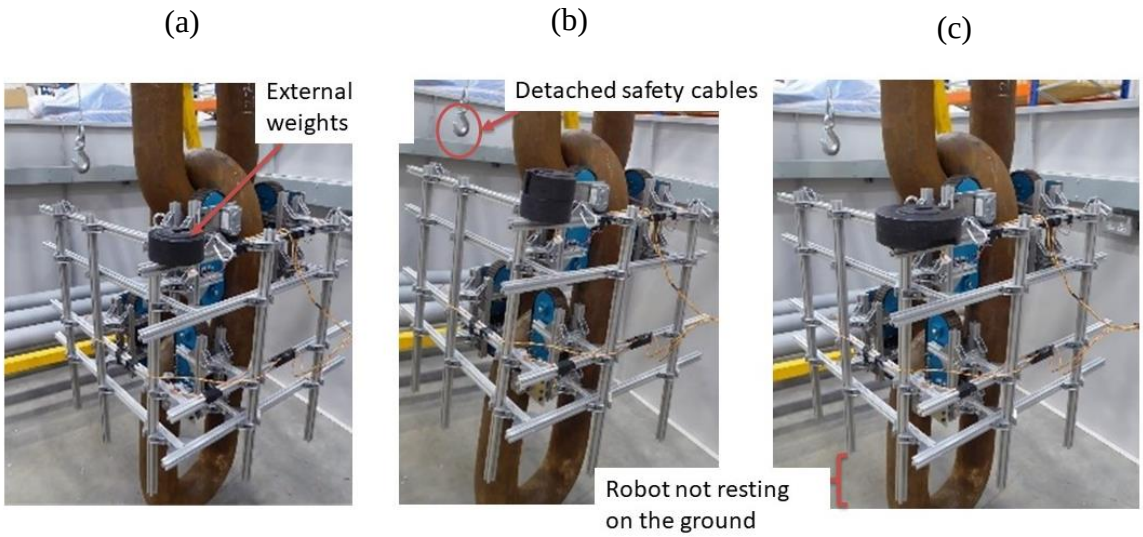

Figure 4-14: Robot on chain stability check; (a) with 20N load; (b) with 40N load; (c) with 50N load

4.8 Laboratory climbing sequence test

The climbing sequence illustrated in Figure 4-16 was recorded during the laboratory experiment trial. The crawler robot was placed on a mooring chain segment (see Figure 4-15) comprising three links and the up/down movement was tested (see Figure 4-16). The experimental trial was conducted in an industrial environment. Therefore, an additional cable (*i.e.* safety cable) was used to enhance safety (internal laboratory safety regulation). The robot was able to attach and climb the mooring chain by making transitions between the chain links.

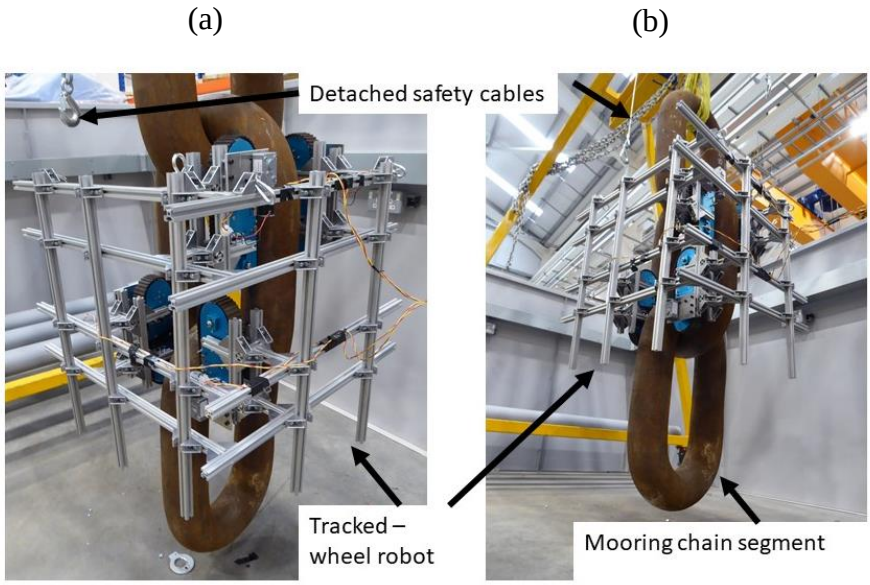

Figure 4-15: Laboratory climbing sequence – robot placement on the chain

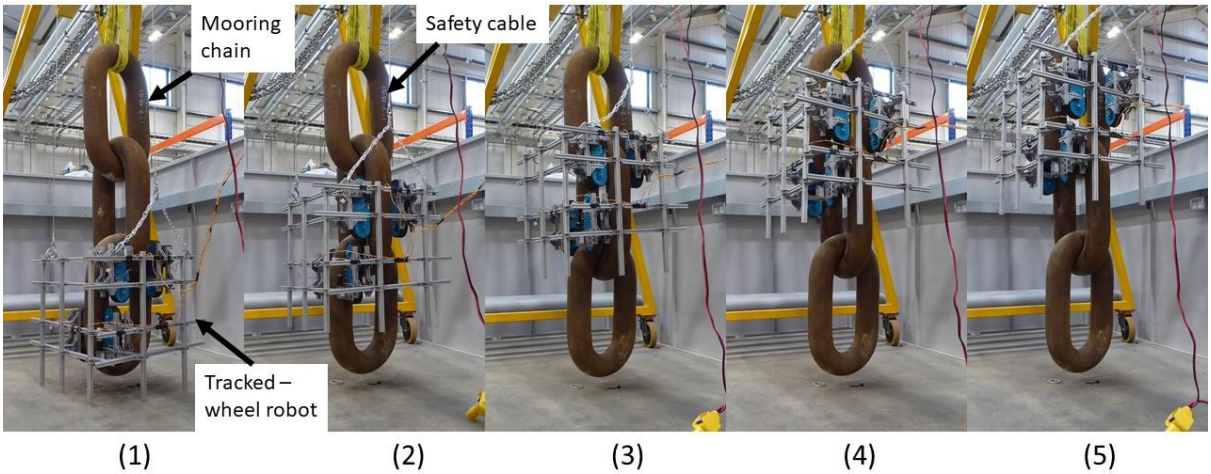

Figure 4-16: Laboratory climbing sequence test

At the fundamental design stage for the robot (in Chapter 3), the net weight was estimated at 19.5kg. The weight of the prototype of the robot was recorded at 19.48kg. The robot was placed on a laboratory scale and the weight was measured, as illustrated in Figure 4-17.

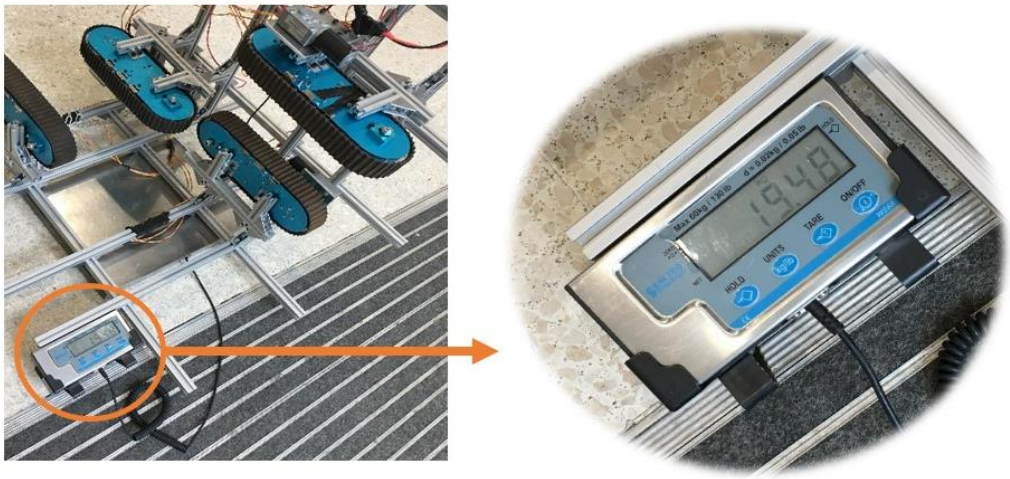

Figure 4-17: Weight of the robot

4.9 Overall summary of the chapter

Compared to other climbing terrains, mooring chain climbing or chain climbing with robots has not been significantly investigated in the literature. Sliding structures with arms/grippers, ROV-assisted, and cable-assisted locomotion mechanisms were discussed in the literature for climbing. However, magnetic adhesion tracked-wheel climbing has not been studied previously in relation to chain climbing. Therefore, the use of tracked wheels for chain climbing was investigated in this research.

In Chapter 3, a fundamental robotic approach was proposed for mooring chain climbing using orthogonally positioned tracked-wheel units and magnetic adhesion. The primary aim of Chapter 4 was to prototype the proposed concept and test this on a chain. In this chapter, a lightweight, fast-moving mooring-chain-climbing robot system that could be quickly deployed and retrieved was prototyped. Moreover, validation of the neodymium permanent magnet adhesion system was conducted. Finally, the robot system was tested in a laboratory on a three-link chain segment to study its climbing capability and stability. In conclusion, the feasibility of using a crawler with an orthogonal arrangement of tracked wheels to climb vertically aligned mooring chains was established.

Chapter 5: Design and prototype of the chain misalignment adaptation mechanism

5.1 Chapter overview

The magnetic adhesion tracked-wheel mechanism for mooring chain climbing was discussed in Chapters 3 and 4. An ideal (straight) mooring chain configuration was considered in the study mentioned above. According to the observations, a straight mooring chain can be used in laboratory conditions, but misalignments are present in chain links during normal conditions. The robotic platform discussed in the previous chapter was able to climb on strictly straight mooring chains due to the rigid attachments. This chapter presents a Cartesian-legged, tracked-wheel crawler robot developed for mooring chain inspection. The proposed robot addresses the misalignment condition of mooring chains that is commonly evident in in-situ conditions. The primary purpose of the presented robotic platform is to convey NDT equipment along the chain to perform an inspection. Therefore, in-situ chain misalignment adaptation is essential. The preliminary design (basic climbing robot) of the proposed robotic platform was discussed in the previous chapters and in ***[D1] [D4]***. This chapter describes an upgraded version of the robotic platform that solves the climbing problem posed by link misalignment in mooring chains. The previously presented magnetic adhesion robotic platform was able to climb orthogonal chain links that were in a uniformly straight, but it was unable to adapt to chain curvature and chain link misalignment due to relative twists between the links. This chapter presents a brief description of the previously studied robot. The mooring chain misalignment was investigated mathematically and used as a design parameter for the proposed robot. This is followed by the design of the proposed misalignment adaptation mechanism. The final section of the chapter describes the prototyping and validation of the climbing technique. The robot was validated using laboratory-based climbing experiments. The presented robot can be used as a platform to convey equipment, *i.e.* tools for NDT/evaluation applications. The robot presented in this chapter was teleoperated and a feasibility study was added in order to identify chain misalignments.

5.2 Comparison of robotic manipulator configurations

As discussed in the Appendix (please see the appendix), several robotic manipulators have been used in industry/research studies. The selection of the manipulators was conduct according to the requirements, *i.e.* space constraints, end effector workspace/reachability, complexity, durability, payload capacity etc. A comparison of the commonly used manipulators is discussed below, which was used to select the manipulator operation that could cope with the selected misalignments. The comparison was carried out considering

the mooring chain misalignments (misalignment and misalignment workspaces are discussed later in this chapter).

Table 5-1: Comparison of commonly used industrial manipulators

Manipulator	**Joints**	**Advantages/disadvantages**
Cartesian	Three prismatic joints	Advantages 1. Three simple linear motions that can cover three dimensions 2. Rigid structure (compared to others) 3. Simple kinematic model Disadvantages 1. Smaller work space compared to the robot's dimensions 2. Unable to achieve complex geometries (*i.e.* under objects) 3. Gliding surfaces/space required for prismatic joints
Cylindrical	Revolute (waist) Prismatic (shoulder) Prismatic (elbow)	Advantages 1. Can be driven with a simple kinematic model 2. Easy access to areas such as cavities 3. Suitable for operation that requires 360° movement (round shape access) Disadvantages 1. Restricted work space 2. Work volume can be overlapped (back of the robot)
Spherical	Revolute (waist) Revolute (shoulder) Prismatic (elbow)	Advantages 1. Able to reach a considerably large space from the central support 2. Suitable for operation requiring spherical access Disadvantages 1. Complex kinematics model 2. Spherical reachability is not important for this case
Articulated	Revolute (waist) Revolute (shoulder) Revolute (elbow)	Advantages 1. Maximum flexibility compared to any other 2. Comparatively large workspace Disadvantages 1. Complex kinematic operations are required 2. Low rigidity when the manipulator is at full reach mode

The mooring chain misalignments discussed in this research can be achieved by manipulating in a 2D Cartesian plane (discussed later). The rigidity of the manipulator is a vital parameter when considering a climbing robot. Moreover, the leg/arm that will cope with the misalignments should be able to handle the weight of the robot and the adhesion force (*e.g.* a manipulator with many vulnerable joints is not suitable for this type of operation). Moreover, the selected manipulator should be able to attach to the L frame. Therefore, adaptability was also considered during the selection. A simple kinematics model can be introduced as an advantage in this situation due to the complex climbing (*i.e.* climbing under operational conditions). When considering the above selection criteria, a Cartesian manipulator with a suitable wrist/end effector was considered for research in this chapter.

5.3 Misalignment problem during vertical climbing

The first part of this research was conducted by considering strictly orthogonal chain links in laboratory conditions. Introducing a new chain-climbing mechanism to the literature was the primary purpose of the abovementioned study. When considering the industrial application of the proposed robot, it should be capable of working as a platform to convey the tools required to conduct in-service activities, *i.e.* structural health monitoring. As discussed in the introduction chapter, mooring chains cannot be moved for inspection or repair. Therefore, any proposed robotic solution should be capable of climbing along a real chain surface. According to the literature, there are three main types of misalignment presented in an in-situ mooring chain: chain curvature due to the effect of gravity and distance between both ends of the chain; chain curvature due to out-of-plane bending and chain link–link misalignment due to external forces; and chain curvature due to gravity (also known as catenary curvature), which depends highly on the physical attachments of each mooring system (see Figure 5-1(a and b)). Moreover, chains with a shorter distance between ends (*i.e.* attachment between FPSO and floor) have a steep/significant curvature, but the curvature of the first 30m is negligible for longer chain attachments. The chain segment within the straight (upright) range was considered in this study. Misalignment between two successive links is evident in any conditions (including laboratory conditions) (see Figure 5-1(d)). Ideally, the angle between two successive links should be 90°; however, due to external forces, ± 8° variations can occur [19].

Most significant and inevitable misalignments between two successive chain links were considered (common misalignments when the chain was hanging vertically) in this chapter and misalignment adaptation was studied (see Figure 5-1(c and d).

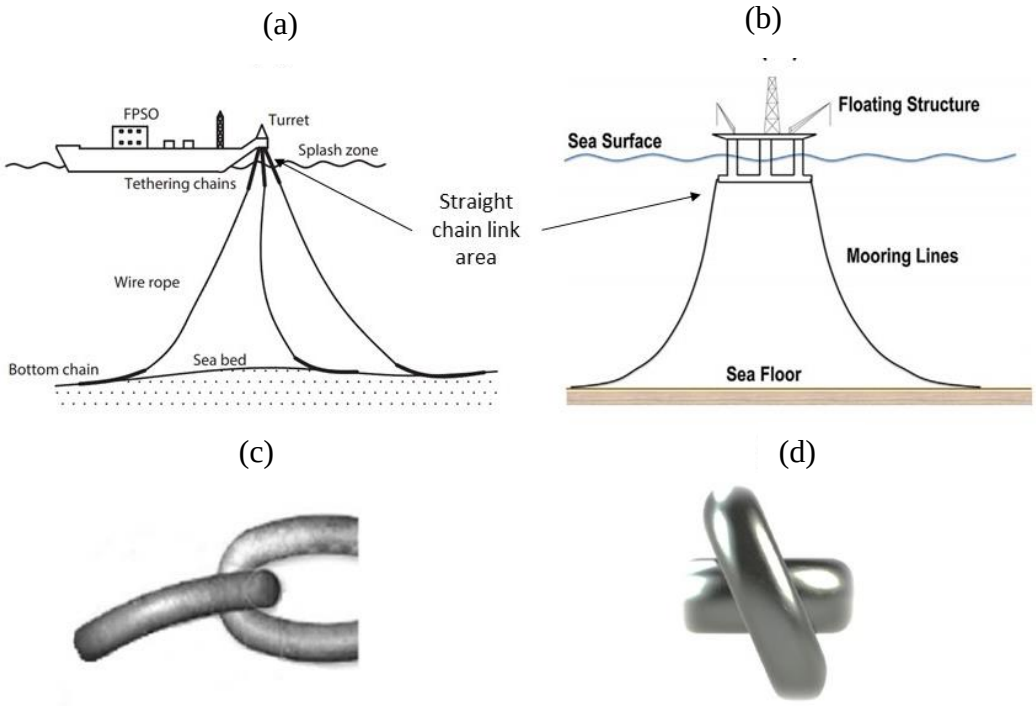

Figure 5-1: (a) and (b) Catenary curvature and mooring attachments [150] [156]; (c) link bending [19]; (d) misalignment between successive chain links [19]

5.4 Understanding of misalignments and tracked-wheel orientations

An orthogonally positioned, magnetic adhesion tracked-wheel robotic approach (see Figure 5-2) was used at the beginning of this research. The tracked-wheel units were rigidly attached to the main body of the robot and research was conducted to test the robot's climbing capability when chain links were strictly orthogonal to each other (ideal laboratory condition).

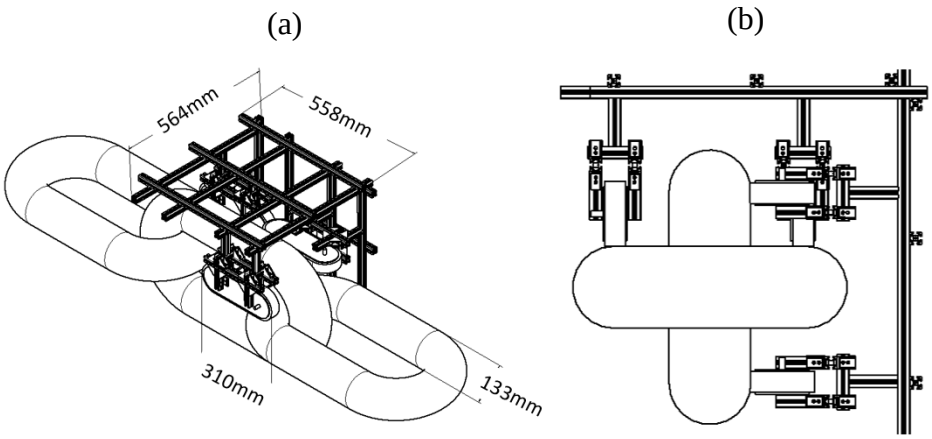

Figure 5-2: Orthogonally positioned magnetic adhesion tracked-wheel climbing robot; (a) climbing robot design; (b) orthogonal tracked-wheel placement concept

Due to in-situ environmental forces, chain links are not always orthogonal to each other [19]. The magnetic adhesion tracked-wheel crawler robot requires sufficient surface contact to generate sufficient friction force for climbing ***[D1]***. In the earlier study, when there was a misalignment in the chain link orientation, the robot was unable to adapt its orientation due to the rigid body attachments. Further investigations were conducted to understand the behaviour of the tracked-wheel module with respect to selected misalignments. Two types of chain misalignment were considered in this study (common misalignments when the chain was hanging vertically). Figure 5-3 illustrates an ideal (non-misaligned) chain link. To aid visualisation, the chain surface in Figure 5-3(a) is plotted as a planar surface. Due to the curvature of the mooring chain links, the centre of the chain link was selected as the optimum crawling path, as illustrated in Figure 5-3(a). To place the tracked-wheel unit on the optimum crawling path, a pure translation needed to be applied (see Eq 5-1 and Figure 5-3(b)), *i.e.* PP joint operation to tracked-wheel unit.

$$P\ (ideal\ ) = P\ (home) + \begin{pmatrix} d1 \\ -d2 \\ 0 \end{pmatrix} \qquad \textit{Eq 5-1}$$

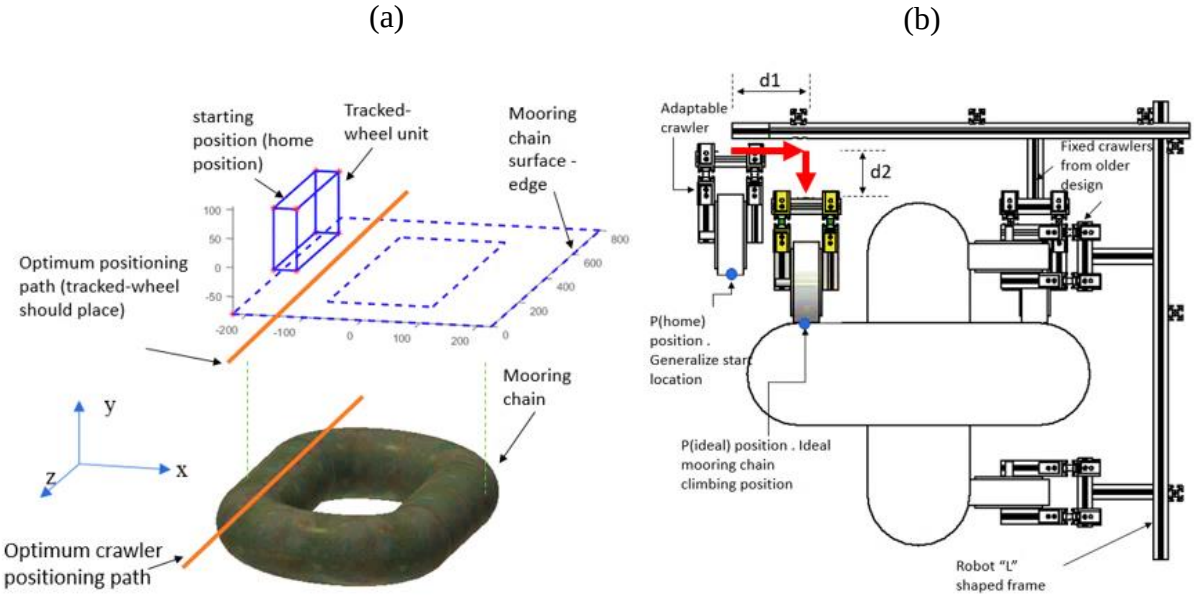

Figure 5-3:(a) Model of a chain link without misalignments; (b) placement distances

where P (ideal) represents the optimum crawling position when the chain links are in ideal conditions (see Eq 5-1). In order to generalise the tracked-wheel positions, the ideal path was not taken as the home position. *d1* and *d2* are the directional distances (see Figure 5-3(b)) from a given home position (home is considered to be the edge of the frame in this case).

The first misalignment is explained in Figure 5-4(a). A chain link was rotated around its z axis at angle α (angle measured with respect to the x axis). To place the crawler on the chain in the same way as the ideal scenario, the wheel unit should be translated onto the new point in the x–y plane (see Figure 5-4(b)). Due to the tangential placement of the wheel unit, as illustrated in Figure 5-5, it was not necessary to rotate the wheel unit (rotation to cope with the twist angle) when there was a twist-type misalignment. If this feature is not considered, another DOF has to be added to the system, *i.e.* rotation around the wheel unit's z axis. Therefore, $p(twist_z)$ can be written as follows.

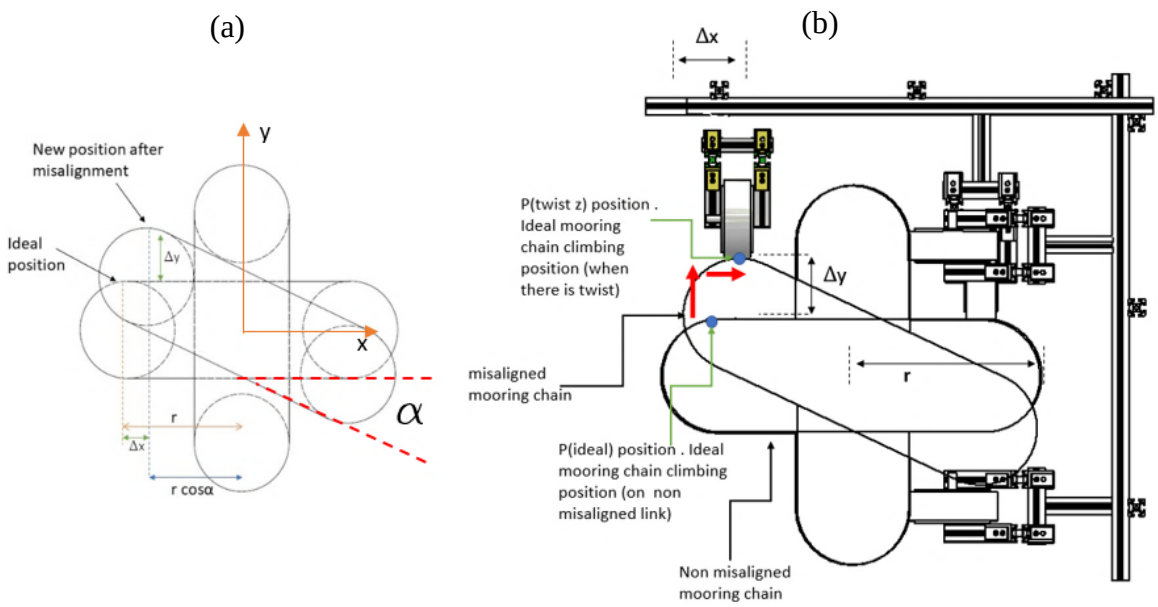

Figure 5-4: Misalignment case 01: (a) schematic of chain link rotated around the z axis; (b) tracked-wheel unit placement after introducing the translation

$$P\ (twist_z) = P\ (ideal) + \begin{pmatrix} \Delta x \\ \Delta y \\ 0 \end{pmatrix} \qquad \text{Eq 5-2}$$

where P (twist $_z$) is the optimum crawling position when the chain link is in a misaligned condition (rotate around the chain link's z axis). Δx and Δy are directional distances (see Figure 5-6(b)) that the tracked wheel should move in order to cope with the misalignment.

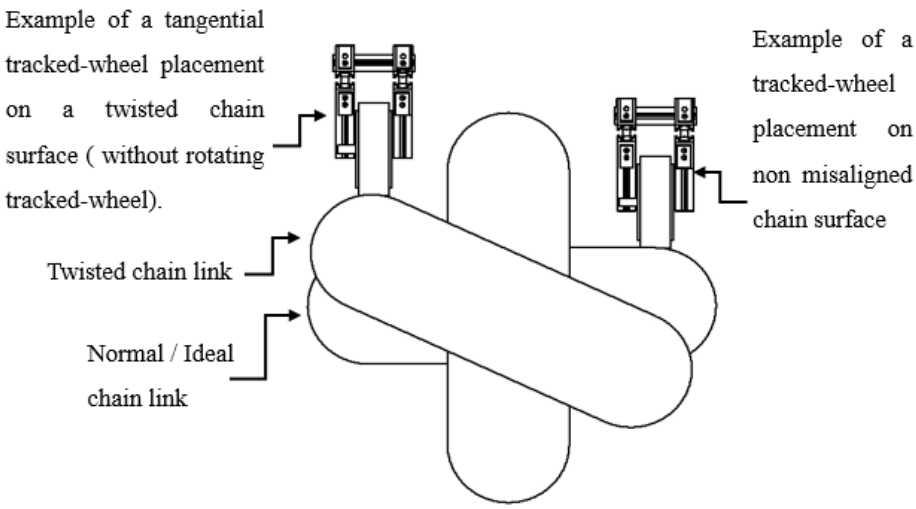

Figure 5-5: Tracked-wheel unit placement during misalignment

In the second misalignment, illustrated in Figure 5-6, a chain link was rotated along the x axis. To place the tracked-wheel unit on the chain surface, it was necessary to introduce a pure rotation to the x axis of the wheel unit. After applying the rotation, it was possible to create the appropriate angle that would allow better surface contact (see Figure 5-6(b)). In this case, the tracked-wheel unit was already aligned on the optimum working axis (because of climbing). Therefore, no translation was needed. The robot's vertical climbing motion would be smoother after achieving this rotation. The required rotation can be modelled by Eq 5-3, where β is the misaligned angle (see Figure 5-6):

$$P\ (twist_x) = \begin{pmatrix} 1 & 0 & 0 \\ 0 & cos\beta & -\sin\beta \\ 0 & \sin\beta & \cos\beta \end{pmatrix} \times\ P\ (ideal) \qquad \textit{Eq 5-3}$$

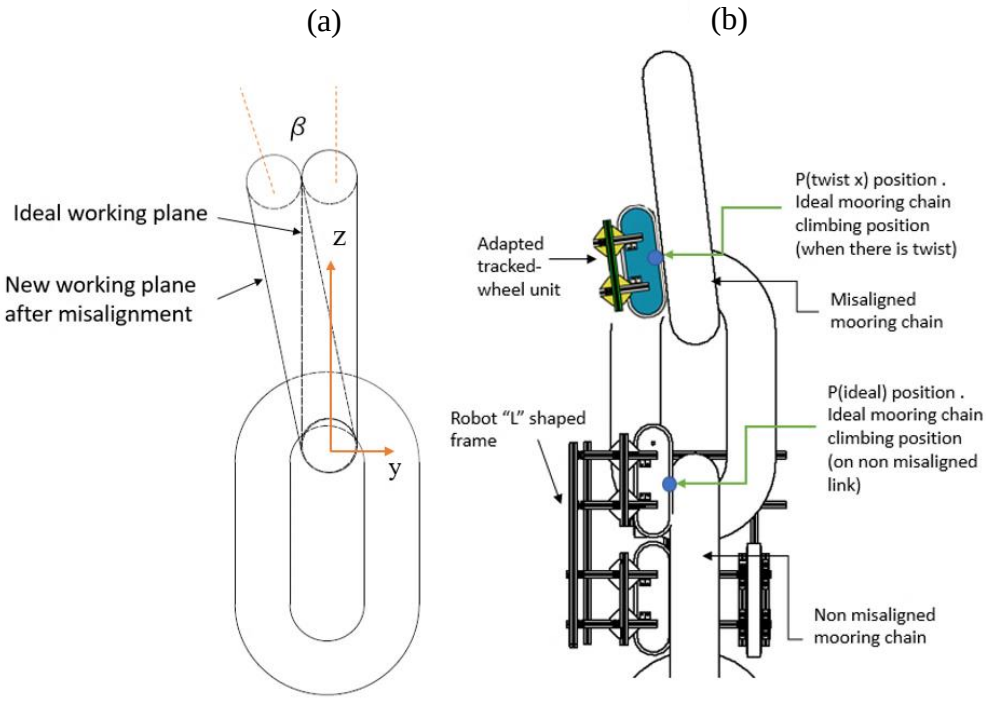

Figure 5-6: Misalignment case 02: (a) schematic of chain link rotating around x axis; (b) tracked-wheel unit placement after introducing the rotation

When observing the above three cases (ideal alignment, chain twist, and tilt misalignments), where α(twist angle) and β (tilt angle) can be identified as the only variables that are required for wheel manipulation. The remaining variables were calculated with the help of angle variations (discussed later in this chapter). According to

Eqs 5-1 – 5-3, two translations and a rotation can be observed. Therefore, by introducing 3DOF to the existing tracked-wheel crawler, adaptations could be made to achieve the abovementioned misalignments.

5.5 Robotic manipulator design

5.5.1 Design of 3DOF

The 3DOF mentioned in the above section can be categorised as two translations (along the x and y axes) and a rotation around the x axis (*i.e.* PPR type). The above description relates to an operation of a planar Cartesian arm/leg with a revolute joint as an end effector. The modification capability of the existing structure was also considered during the conceptual design. Moreover, two translations were modelled with prismatic joints, and the rotation was modelled with a revolute joint (see Figure 5-7). In the conceptual manipulator diagram (Figure 5-7), L_1 and L_2 are the link lengths due to possible mechanical attachment clearances. L_3 is the distance between the crawler attachment and the revolute joint. The variable parameters of two linear motions (prismatic joints) and the revolute joint are d_1, d_2, and Ø, respectively. Therefore, an active transformation of the end effector (see point P in Figure 5-7(c)) from its home position (Figure 5-9(a and b)) to its current position (with the given joint variables) can be modelled as follows:

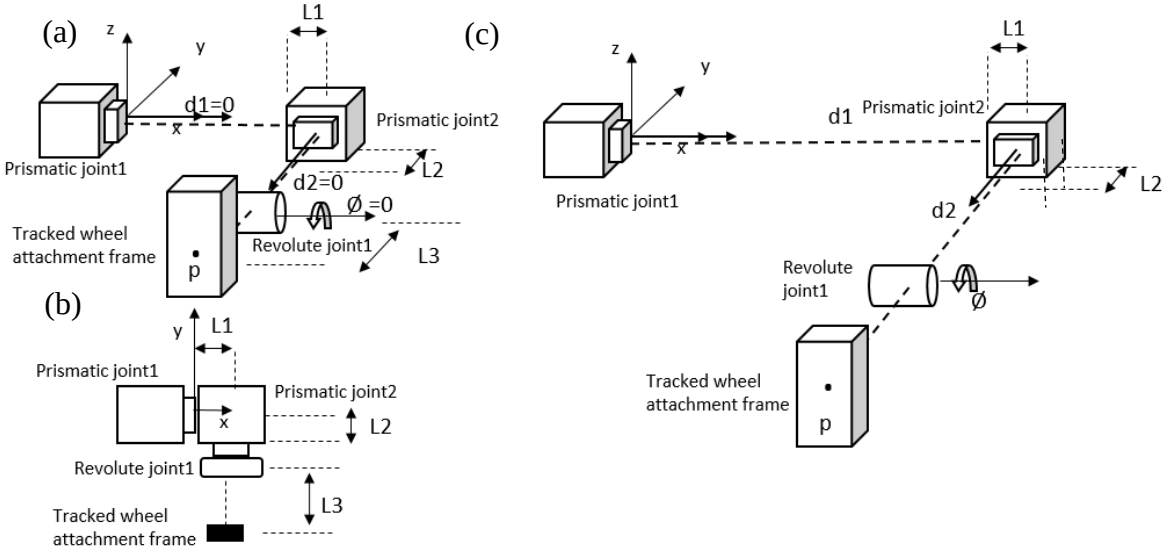

Figure 5-7: Conceptual design of the robotic manipulator (schematic); (a) home configuration explanation; (b) home configuration; (c) active transformation

Considering the prismatic joint translation along the x axis with a d_1 extension:

$$\text{Prismatic joint 1} = A_1(d_1) = \begin{pmatrix} 1 & 0 & 0 & d_1 \\ 0 & 1 & 0 & 0 \\ 0 & 0 & 1 & 0 \\ 0 & 0 & 0 & 1 \end{pmatrix} \qquad \textit{Eq5-4}$$

Considering the prismatic joint translation along the y axis with a d_2 extension:

$$\text{Prismatic joint 2} = A_2(d_2) = \begin{pmatrix} 1 & 0 & 0 & 0 \\ 0 & 1 & 0 & (-d_2 \\ 0 & 0 & 1 & 0 \\ 0 & 0 & 0 & 1 \end{pmatrix} \qquad \textit{Eq 5-5}$$

When considering the $A_3(Ø)$ revolute joint transformation (rotation around x axis with L_1 and L_2 bias distances), the joint transformation matrix (expressed in Eq 5-6) was obtained according to the theory explained in Appendix:

$$[\,\mathrm{I} - R_x(Ø)\,]\,\mathrm{p} = \left\{ \begin{pmatrix} 1 & 0 & 0 \\ 0 & 1 & 0 \\ 0 & 0 & 1 \end{pmatrix} - \begin{pmatrix} 1 & 0 & 0 \\ 0 & cos\,Ø & -sinØ \\ 0 & sinØ & cosØ \end{pmatrix} \right\} \begin{pmatrix} L_1 \\ -L_2 \\ 0 \end{pmatrix} \qquad \textit{Eq 5-6}$$

After simplification, $A_3(Ø)$ can be written as follows:

$$A_3(Ø) = \begin{pmatrix} 1 & 0 & 0 & 0 \\ 0 & cosØ & -sinØ & -L_2(1 - cosØ) \\ 0 & sinØ & cosØ & L_2 * sinØ \\ 0 & 0 & 0 & 1 \end{pmatrix} \qquad \textit{Eq 5-7}$$

Therefore, the active transformation of the end effector from home to its current position when the joint variables are d_1, d_2, and Ø can be obtained as:

$$A_1(d_1)\,A_2(d_2)\,A_3(Ø) = \begin{pmatrix} 1 & 0 & 0 & L_1 + d_1 \\ 0 & cosØ & -sinØ & -d_2 - L_2 * (1 - cosØ) \\ 0 & sinØ & cosØ & L_2 * sinØ \\ 0 & 0 & 0 & 1 \end{pmatrix} \qquad \textit{Eq 5-8}$$

When considering the home position of the tool frame, assuming that it is parallel to the world frame but translated by $(L_1; L_2, L_3; 0)^T$. So, the active transformation from the world frame to the tool frame (B) is expressed as follows:

$$B = \begin{pmatrix} 1 & 0 & 0 & L_1 \\ 0 & 1 & 0 & -L_3 - L_2 \\ 0 & 0 & 1 & 0 \\ 0 & 0 & 0 & 1 \end{pmatrix} \qquad \textit{Eq 5-9}$$

Active transformation from the world frame to the tool frame when the joint variables are d_1, d_2, and Ø is given by matrix multifaction of $A_1(d_1)*A_2(d_2)*A_3(Ø)*B$:

$$AA_1(d_1)\,A_2(d_2)\,A_3(Ø)\,B = \begin{pmatrix} 1 & 0 & 0 & L_1 + d_1 \\ 0 & cosØ & -sinØ & -d_2 - L_2 - L_3 * cosØ \\ 0 & sinØ & cosØ & -L_3 * sin(Ø) \\ 0 & 0 & 0 & 1 \end{pmatrix} \qquad \textit{Eq 5-10}$$

Finally, for the tracked-wheel unit, active transformation to adapt according to the selected misalignments in 3D space can be expressed as:

$$(p)_{\,Active\ transformation} = \begin{pmatrix} 1 & 0 & 0 & L_1 + d_1 \\ 0 & cosØ & -sinØ & -d_2 - L_2 - L_3 * cosØ \\ 0 & sinØ & cosØ & -L_3 * sin(Ø) \\ 0 & 0 & 0 & 1 \end{pmatrix} \qquad \textit{Eq5-11}$$

5.5.2 Robotic leg design for proposed kinematic motion

The rigidity of the leg design/mechanism was vital due to the mooring chain's rough and robust nature. Moreover, the load/weight acting along the axis was considered during the design of the above mechanism. To create a linear movement along the axis, DC geared actuators were used. The possibility of introducing a slider actuator was considered; however, due to the load capacity and rigidity, a low-friction, dry-coupled glider was introduced to the system with actuators, as illustrated in Figure 5-8. Two linear actuators were introduced to the system to ensure the tracked-wheel attachment remained rigid and stable. A dual actuator design with a pin-type joint was introduced to achieve the pitch action (rotate along the x axis) of the wheel unit. The system strength could be enhanced by replacing the rotary axis with two actuators that create a pitch angle by changing the distance of each actuator. Both y-axis actuators were mounted on a linear glider. The bodies of 'b' actuators in Figure 5-8 were mounted on a linear glider 'c', and both actuators were connected by a rigid attachment 'f'. The rigid attachment 'f' was connected to the end of the actuator stroke 'a'. The magnetic adhesion tracked-wheel unit 'e' was attached to the actuator end by using a pin-type joint 'd'. Movement along the x axis was achieved by manipulating the actuator 'a' and y axis movement could be made using the actuator 'b'. By introducing a differential motion to the 'b' actuators, rotation along the x axis could be made. This actuator-assisted robotic leg was mounted on the L-shaped main frame of the robot.

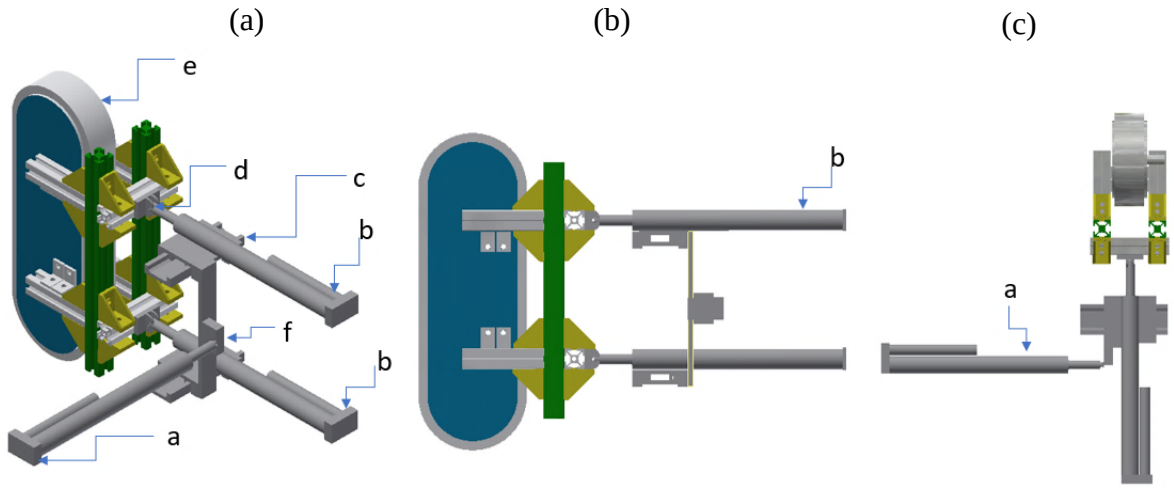

Figure 5-8: Design of the robotic manipulator; (a) design; (b) planner mode; (c) Cartesian mode

5.5.3 Kinematics of the actuator's assisted robot leg

To understand the kinematics of the design, the entire motion of the leg can be separated into two main motions: planar manipulator (Figure 5-8(b)) and Cartesian manipulator (Figure 5-8(c)). The Cartesian manipulator operates as discussed in the previous section. For the Cartesian manipulator, actuator 'a' represents the x axis and both 'b' actuators represent the y axis without any differential motions, as illustrated in Figure 5-9. Therefore, the active transformation of the wheel units (see point P in Figure 5-9(c)) in the 3D plane relative to the home configuration (Figure 5-9 (a and b)) can be expressed as follows, where L_1, L_2, and L_3 are attachment distances and d_1 and d_2 are variable actuator stroke lengths. It is possible to find the new translation point along the XY plane (see Figure 5-9) with respect to the chain misalignment angle and the known parameters of the chain link (see Figure 5-4). 'r' (r in Figure 5-4(b)) is the distance between the optimum working path to the centre of the chain link. For a given chain, r will always be a known parameter. If the chain twist along the z axis is α, $\Delta x = r - r\cos(\alpha)$ and $\Delta y = r\sin(\alpha)$. Where Δx and Δy are the differences in actuator lengths from the ideal position.

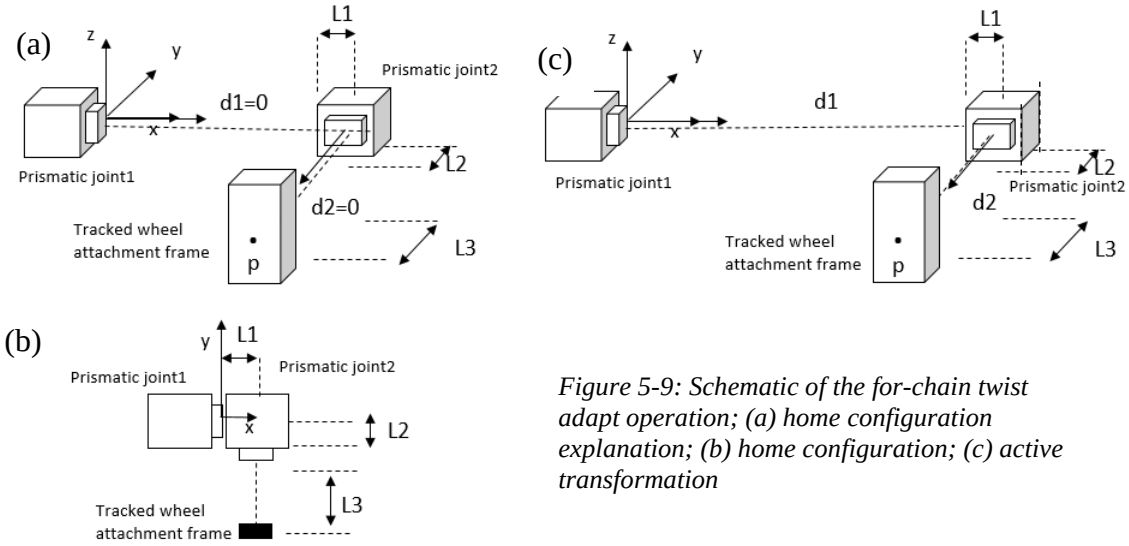

Figure 5-9: Schematic of the for-chain twist adapt operation; (a) home configuration explanation; (b) home configuration; (c) active transformation

Considering the prismatic joint translation along the x axis with a d_1 extension:

$$\text{Prismatic joint 1} = A_1(d_1) = \begin{pmatrix} 1 & 0 & 0 & d_1 \\ 0 & 1 & 0 & 0 \\ 0 & 0 & 1 & 0 \\ 0 & 0 & 0 & 1 \end{pmatrix} \qquad \textit{Eq 5-12}$$

Considering the prismatic joint translation along the y axis with a d_2 extension:

$$\text{Prismatic joint 2} = A_2(d_2) = \begin{pmatrix} 1 & 0 & 0 & 0 \\ 0 & 1 & 0 & (-d_2) \\ 0 & 0 & 1 & 0 \\ 0 & 0 & 0 & 1 \end{pmatrix} \qquad \textit{Eq 5-13}$$

Therefore, the active transformation of the end effector from home to its position when the joint variables are d1 and d2 can be expressed as follows:

$$A_1(d_1)\,A_2(d_2) = \begin{pmatrix} 1 & 0 & 0 & d_1 \\ 0 & 1 & 0 & -d_2 \\ 0 & 0 & 1 & 0 \\ 0 & 0 & 0 & 1 \end{pmatrix} \qquad \textit{Eq 5-14}$$

When considering the home position of the tool frame, assume that it is parallel to the world frame but translated by $(L_1; L_2, L_3; 0)^T$. So, the active transformation from the world frame to the tool frame (B) is expressed as follows:

$$B = \begin{pmatrix} 1 & 0 & 0 & L_1 \\ 0 & 1 & 0 & -L_3 - L_2 \\ 0 & 0 & 1 & 0 \\ 0 & 0 & 0 & 1 \end{pmatrix} \quad \textit{Eq 5-15}$$

Active transformation from the world frame to the tool frame when the joint variables are d_1 and d_2 is given by:

$$A_1(d_1)\, A_2(d_2)B \;=\; \begin{pmatrix} 1 & 0 & 0 & L_1 + d_1 \\ 0 & 1 & 0 & -d_2 - L_2 - L_3 \\ 0 & 0 & 1 & 0 \\ 0 & 0 & 0 & 1 \end{pmatrix} \quad \textit{Eq 5-16}$$

Finally, for the tracked-wheel units, active transformation to adapt according to the selected misalignments in 3D space can be expressed as:

$$(p)_{Active\ transformation} \;=\; \begin{pmatrix} 1 & 0 & 0 & L_1 + d_1 \\ 0 & 1 & 0 & -d_2 - L_2 - L_3 \\ 0 & 0 & 1 & 0 \\ 0 & 0 & 0 & 1 \end{pmatrix} \quad \textit{Eq 5-17}$$

To understand the behaviour of the planar part of the robot leg, the differential motion of the 'b' actuators was considered (see Figure 5-10). $d_{2\text{-}1}$ and $d_{2\text{-}2}$ represent the variable stroke distances of the 'b' actuators. L_2 and L_3 were considered as fixed offset distances due to the mechanical design of linear actuators. D is the fixed vertical distance between two actuators:

$$(\Delta \mathrm{d})\ \text{differential distance} \;=\; \text{distance}(d_{2-2}) - distance(d_{2-1}) \quad \textit{Eq 5-18}$$

$$(\Delta \mathrm{d}) = \frac{D}{\tan(\emptyset)} \quad \textit{Eq 5-19}$$

Eq 5-18 and Eq 5-19 were used to calculate the appropriate actuator stroke distances. The sign of the angle was used to identify the associated actuator. For example, if the angle is (+ve), the $d_{2\text{-}2}$ actuator was extended by Δd and the $d_{2\text{-}1}$ actuator remained the same.

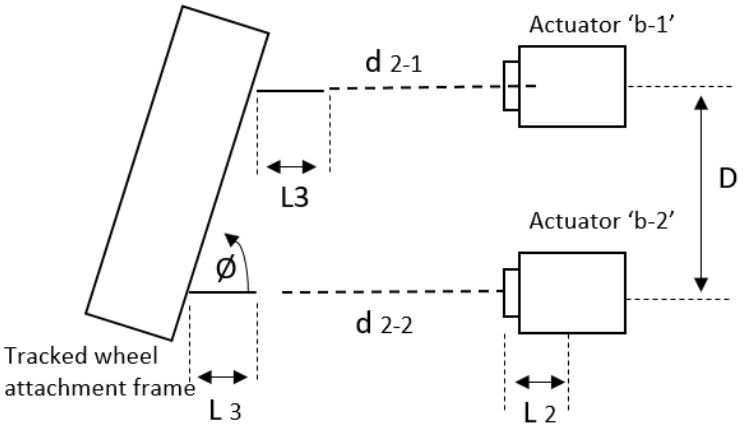

Figure 5-10: Schematic of the for-chain tilt adapt operation

5.5.4 Mitigating the misalignment

The previously discussed legged magnetic adhesion tracked-wheel module was used to replace the rigid attachment (see Figure 5-11) to deal with the misalignment. Some unmodified legs of the robot are shown in Figure 5-11(a) to distinguish the modifications in the other figures. Potential NDT attachment places are marked in Figure 5-11(a and d), but the NDT system/s are not reported in this part of the study. The performance of the upgraded design was tested using CAD models of chain twist and chain tilt misalignment scenarios (see Figure 5-12).

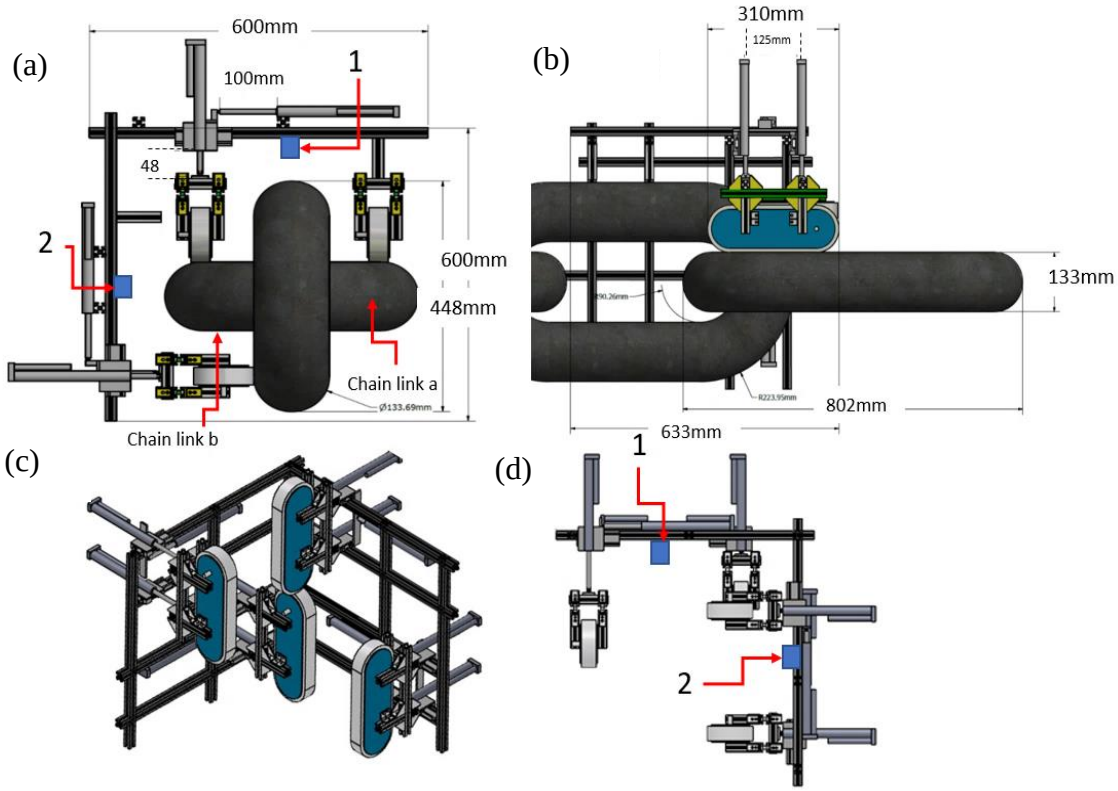

1,2 Potential places to attach a NDT equipment i.e., Camera , UT manipulator etc.,. 1 is to inspect chain link-a. 2 is to inspect chain link-b

Figure 5-11: Robot (a) and (b) design schematics; (c) and (d) full design

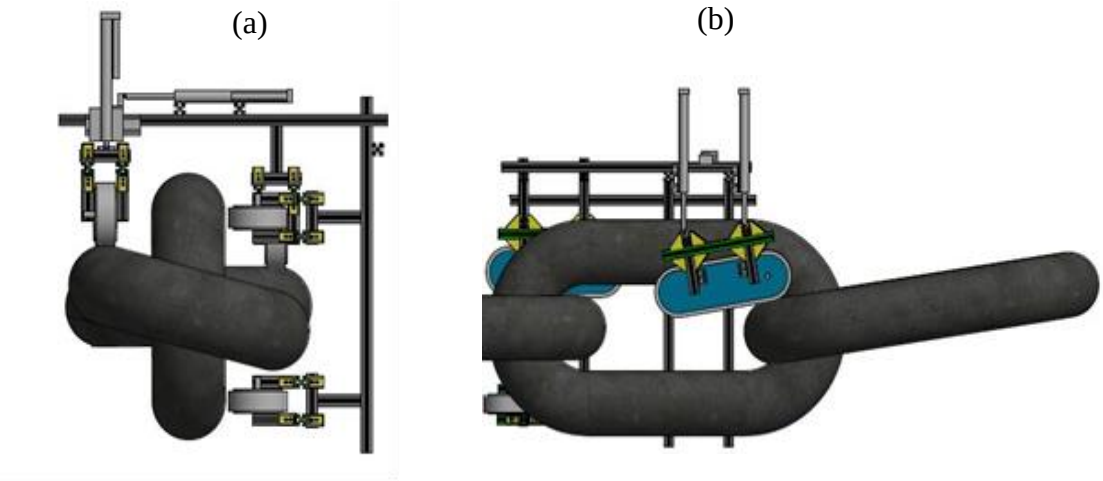

Figure 5-12: CAD compatibility of design; (a) twist adaptation; (b) tilt adaptation

5.6. Prototype and testing

5.6.1 3DOF Cartesian leg

A prototype of the Cartesian leg mechanism was developed to the design specifications provided in the previous section, as illustrated in Figure 5-13(a). The prototyped system in Figure 5-13 was attached to the robot's mainframe (L frame, discussed in Chapters 3 and 4) and a third linear actuator was added, as illustrated in Figure 5-13(b). Actuators were attached to the system using a linear slider plate. The motion of the legged system was tested to observe the 3DOF movement, as explained in the design process (Eq 5-11). To test the 3DoF (3-degree of freedom), the proposed movements were observed, as illustrated in Figure 5-14, without attaching the robot to a chain. During the development of the prototype, 5–8mm clearance was introduced to the pin joint for mechanical advantage during the tilt motion (to help the system cope with the vertical distance increase during the rotation of the tracked-wheel unit).

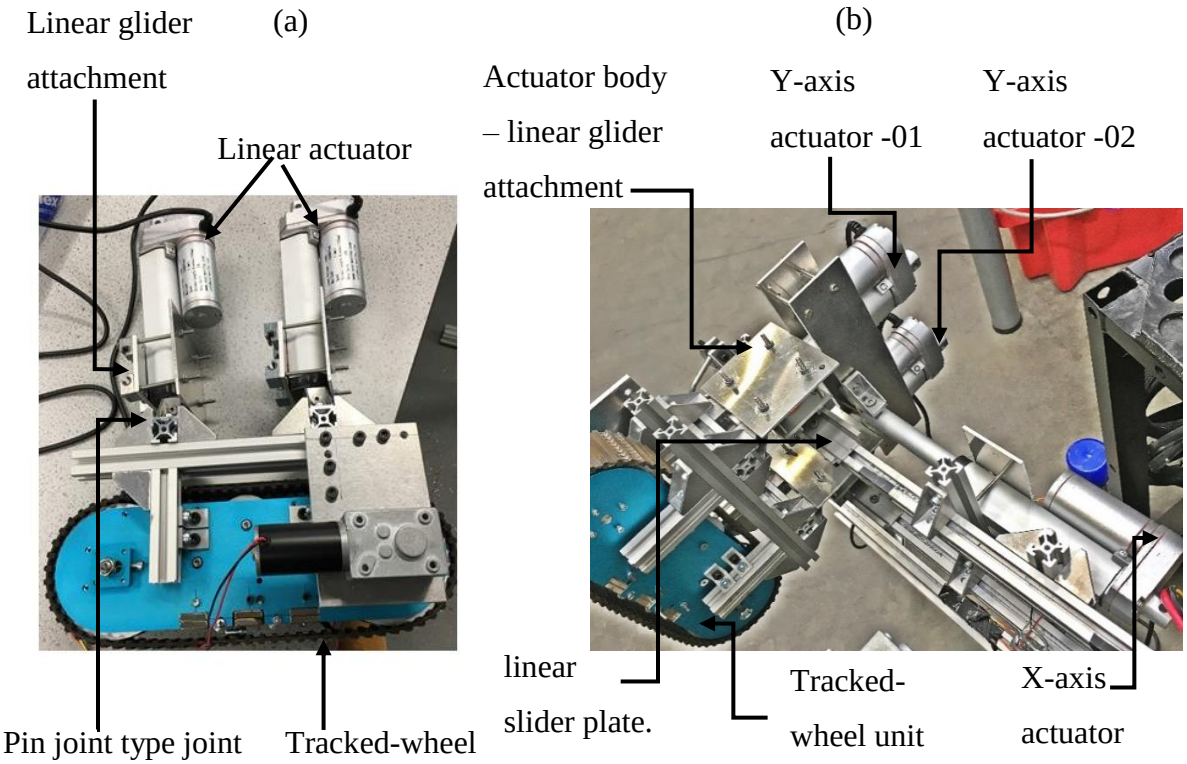

Figure 5-13: Prototyped Cartesian legged tracked-wheel unit; (a) prototyped robot leg with two actuators; (b) robot leg mounted on the robot with the third actuator

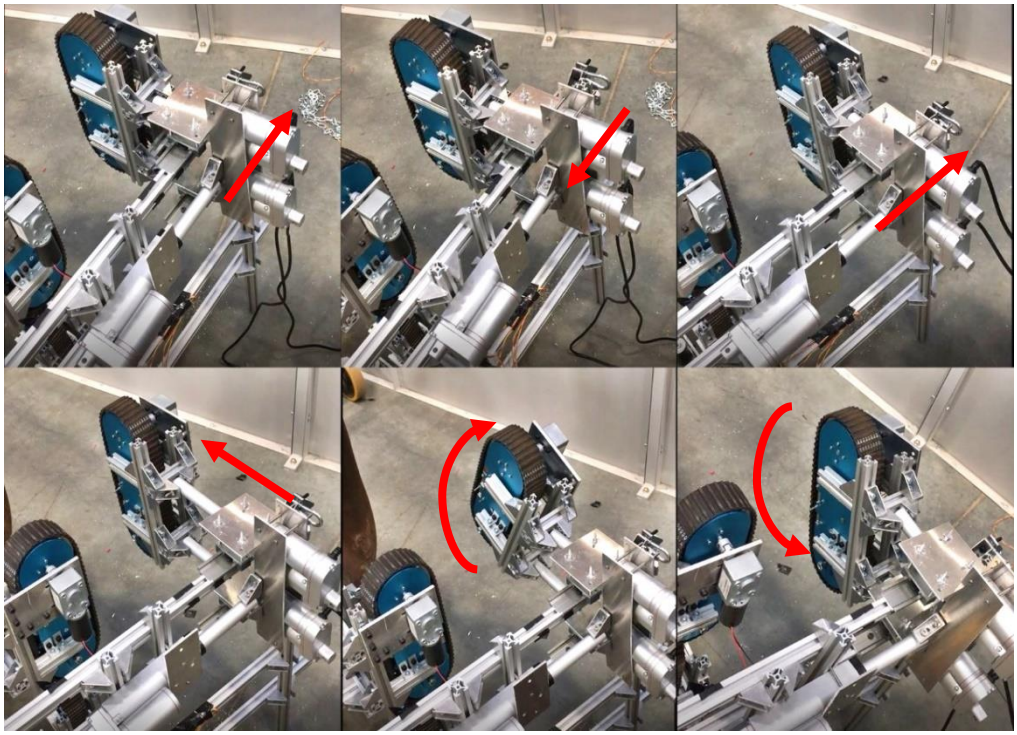

Figure 5-14: Prototyped Cartesian legged 3DOF testing

5.6.2 Climbing test

To test the Cartesian legged motion of the robot, link tilt and link twist misalignments were introduced to a three-link chain segment, as illustrated in Figure 5-15, and climbing capability was tested. To create the mooring chain twist misalignment, a series of wooden wedges were inserted between the first and second links. A tensioned strap was used, as illustrated in Figure 5-15, to create tilt misalignment.

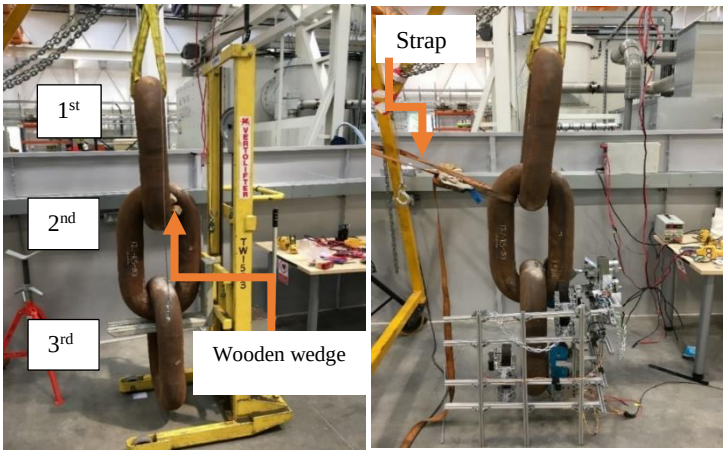

Figure 5-15: Robot climbing sequence testing test rig (misalignment test rig)

Chain twist misalignment was introduced to the first link, as illustrated in the above experimental setup, and climbing capability was tested, as illustrated in Figure 5-16. The robot was able to adapt to the misalignment of the chain link and climb along the chain. The robot was also able to adapt and climb when a tilt misalignment was introduced to link 1, as illustrated in Figure 5-17. A stability check was performed without safety cables (see Figure 5-18). According to the experimental results, the robot stayed attached to the misaligned chain link surface with its own weight (all safety cables were released during the stability test experiment).

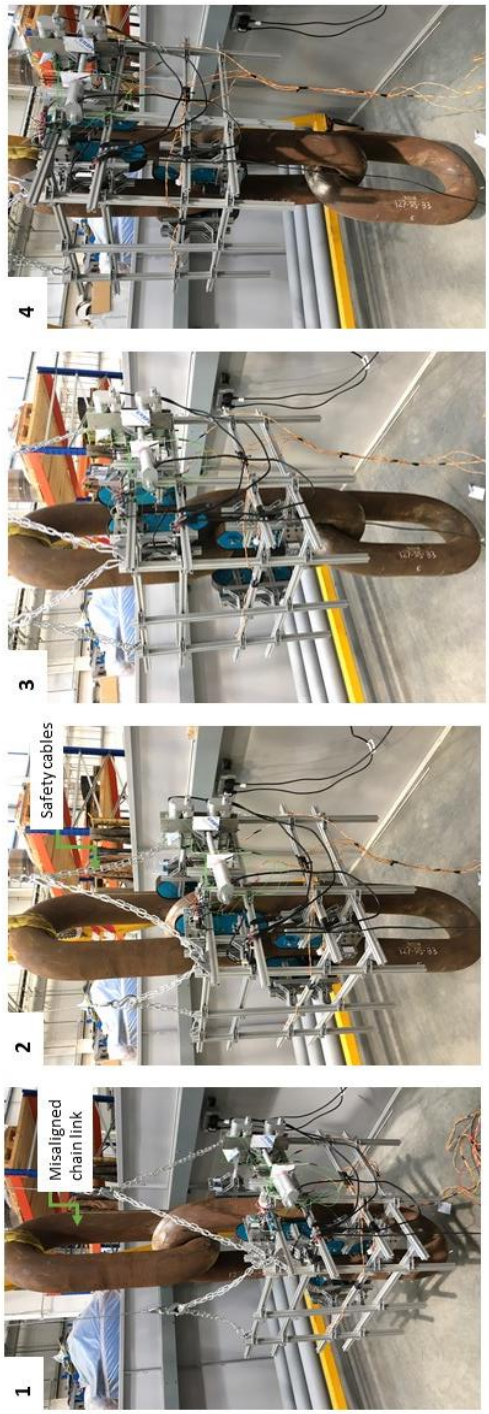

Figure 5-16 : Robot climbing sequence testing for 10-degree twist misalignment

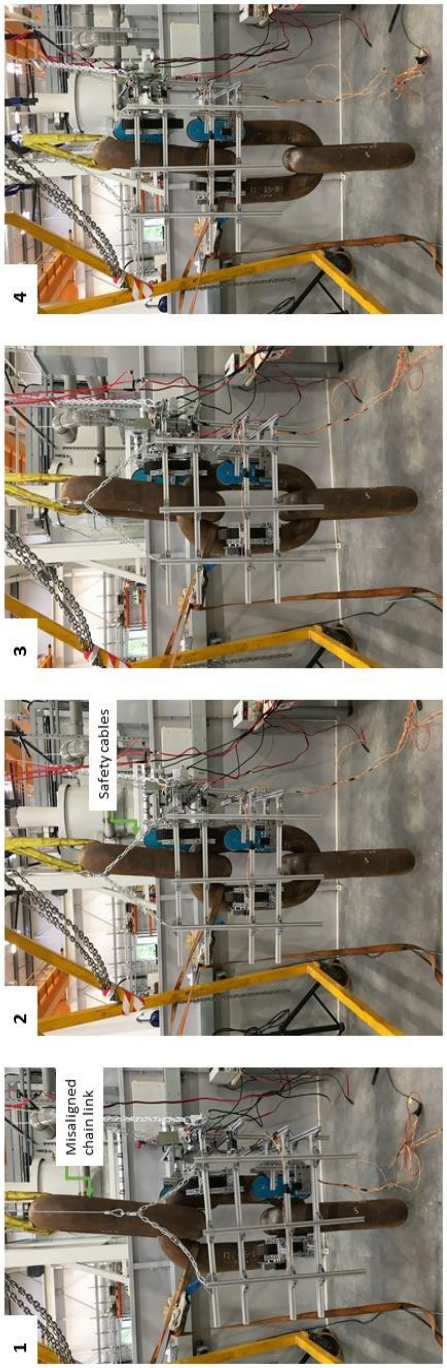

Figure 5-17 : Robot climbing sequence testing for 5-degree tilt misalignment

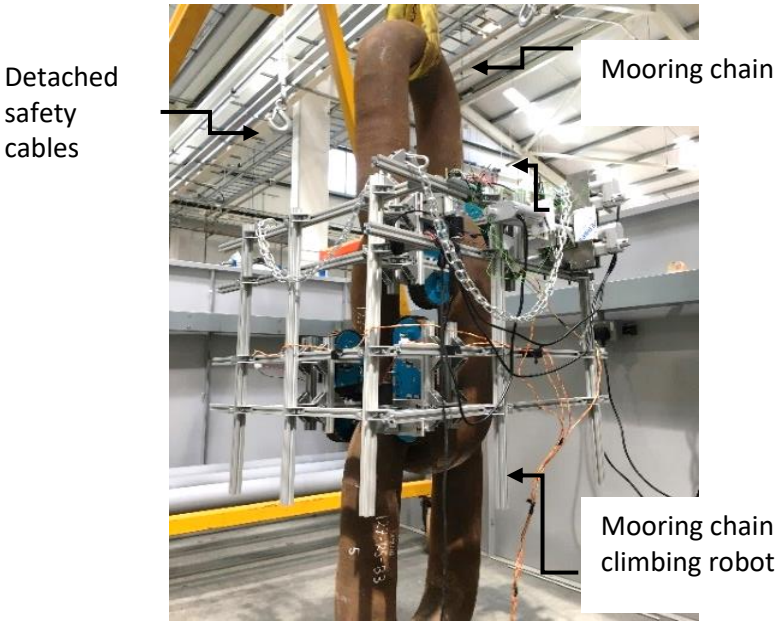

Figure 5-18: Robot climbing stability check without safety cables

Actuator distances were recorded during the misalignment climbing and checked against the distances measured during the CAD study (see Figure 5-20). Comparison between CAD distances and the experimental readings are illustrated in the Figure 5-20. The control architecture presented in Figure 5-19 was used in this study for robot control. Automated detection of misalignment angles was not established within this part of the study. Therefore, misalignment angles and control commands were added to the system as an input from the robot control graphical user interface (GUI) (LabVIEW), *i.e.* the commands 'climb up' and 'climb down' and the misalignment angles. The GUI was connected to the microcontroller (on the robot) via serial communication.

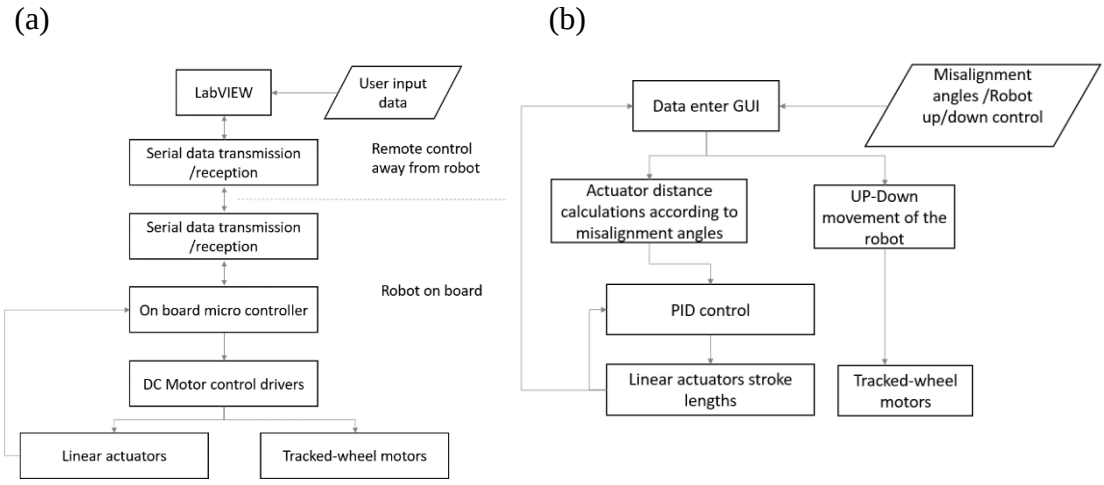

Figure 5-19: (a) hardware architecture diagram; (b) control flow chart

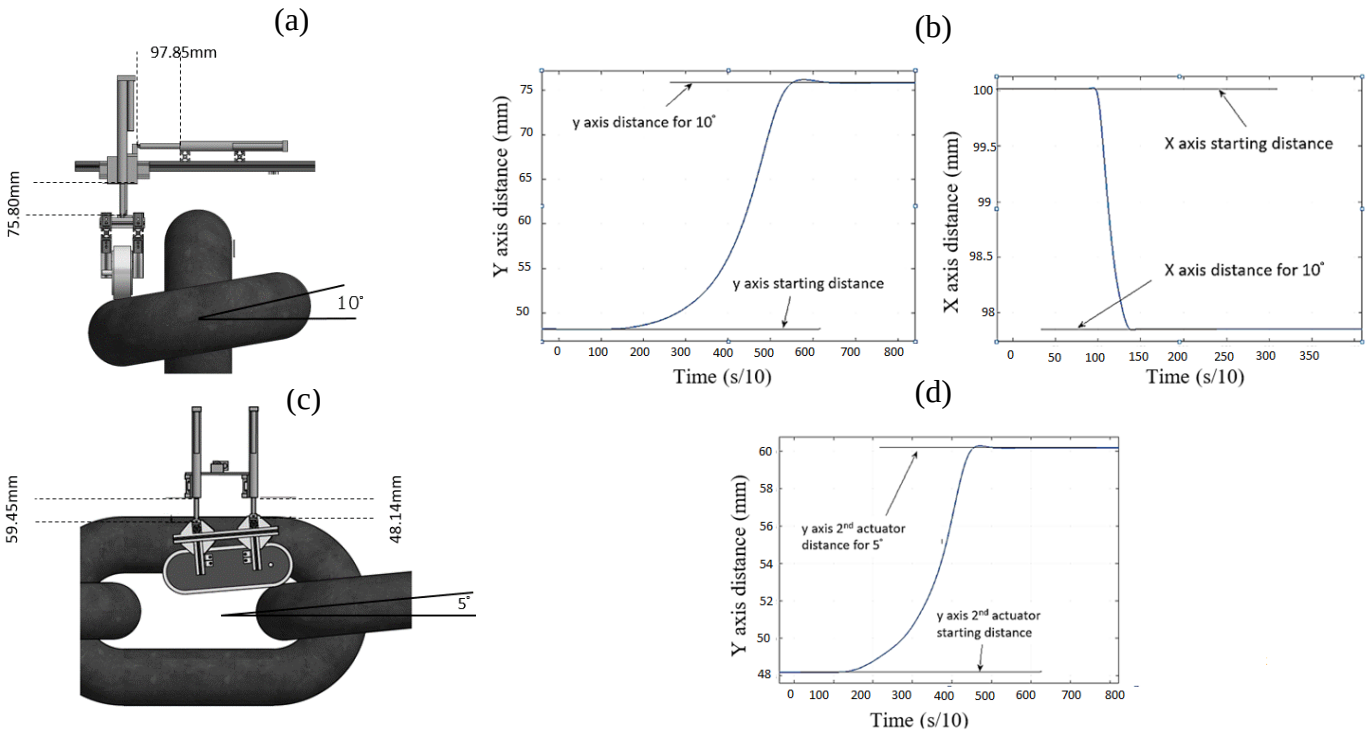

Figure 5-20: Actuator distance check; (a) 10-degree twist misalignment CAD distances; (b) 10 degrees recorded actuator distances; (c) 5-degree twist misalignment CAD distances; (d) 5 degrees recorded actuator distances

5.7 Chain misalignment detection feasibility study

5.7.1 Numerical modelling and design

The misalignment detection of the proposed robot was conducted by manual measurement and a numerical feasibility study was conducted to improve the robot with autonomous misalignment detection capabilities. Sample misalignment angles (as discussed in the previous section) were introduced to a CAD file, and an FEA study was carried out using COMSOL numerical modelling. The FEA study was carried out by considering air and solid objects. COMSOL pressure acoustics and solid mechanics modules were incorporated to detect the misalignment using ultrasonic distance measurement transducers. The boundary load force on the transducer point was used as the excitation.

The parameters considered in the FEA are presented in Table 5-2 and the model layout is shown in Figure 5-21.

Table 5-2: Parametric data used in the numerical modelling

Parameter / expression	**Value**
Frequency (f)	40 khz
Number of cycles (n)	5
Angular frequency (w)	2.5133e5hz
Speed of sound in air (c)	343m/s
Density of air (app at sea level)	1.225 kgm^{-3}
Density of iron	7700 kgm^{-3}
Speed of sound in iron	5130 m/s
Maximum element size	8.5750e-4 m
Sampling frequency	2.5e-5 s
Maximum element size	0.8mm
Minimum element size	0.015mm
Mesh type	Free triangular mesh

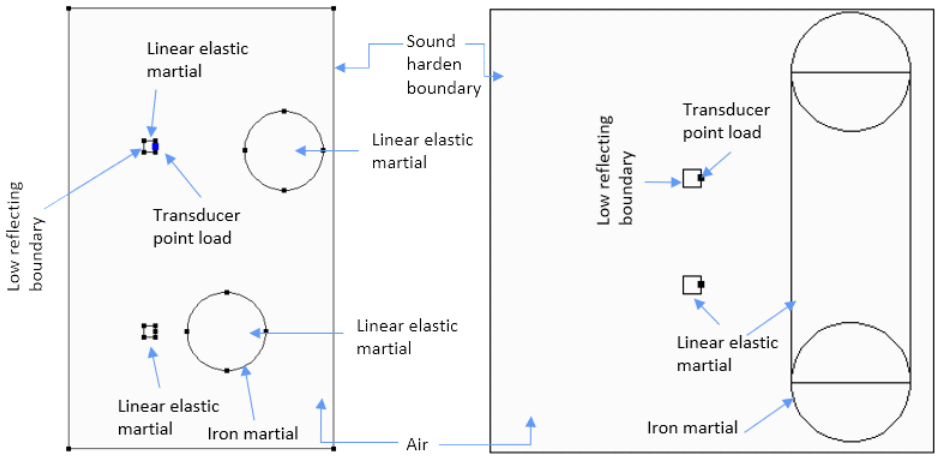

Figure 5-21: COMSOL FEA model layout and boundaries

A study of chain twist misalignment detection was carried out, as illustrated in Figure 5-22. Two ultrasound detectors were used to measure the distances, as illustrated in Figure 5-22(a). Ultrasound detectors were placed perpendicular to the chain surface during the ideal condition. Then, a 17° misalignment was introduced to the chain while the transducers were kept in the same place. Transmit and receive signals, illustrated in Figure 5-23, were obtained from the wave patterns illustrated in Figure 5-24. To minimise the disturbances, ultrasound transducers were fired one after another, *i.e.* noise could be added to the signal if the waves began to interfere with each other.

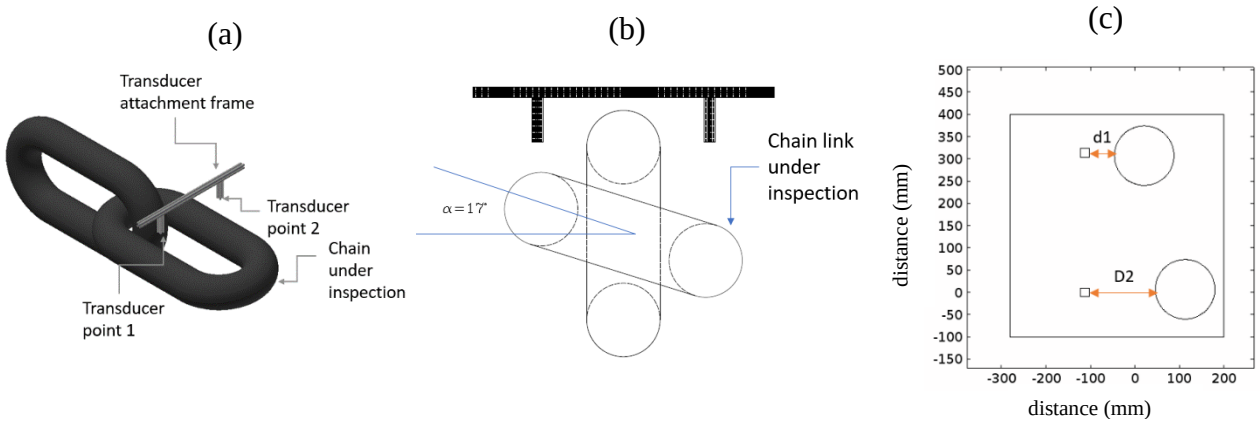

Figure 5-22: FEA case 1; (a) 3D CAD design; (b) misaligned angle cross section; (c) simplified CAD layout for FEA

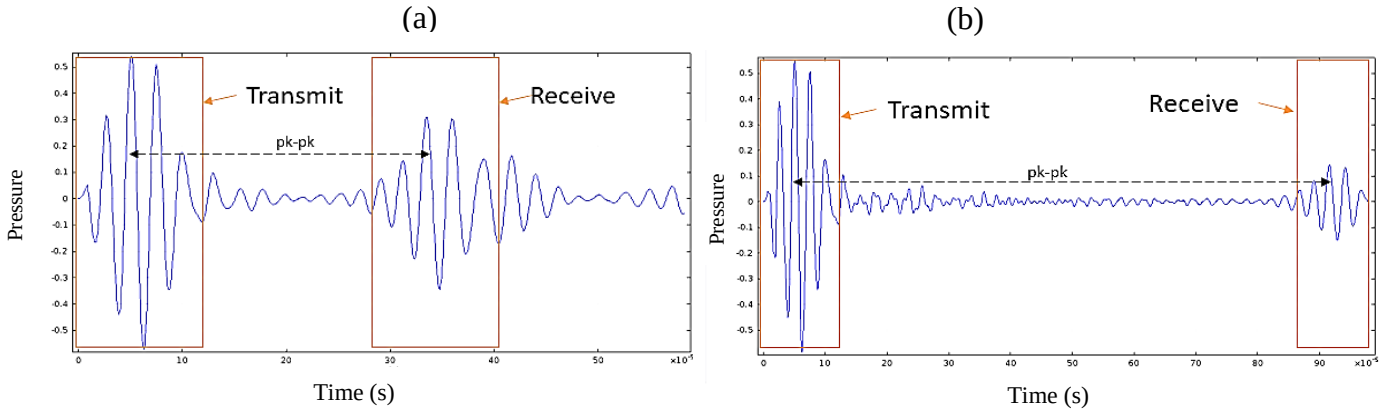

Figure 5-23: Time-of-flight signals; (a) from d1; (b) from d2

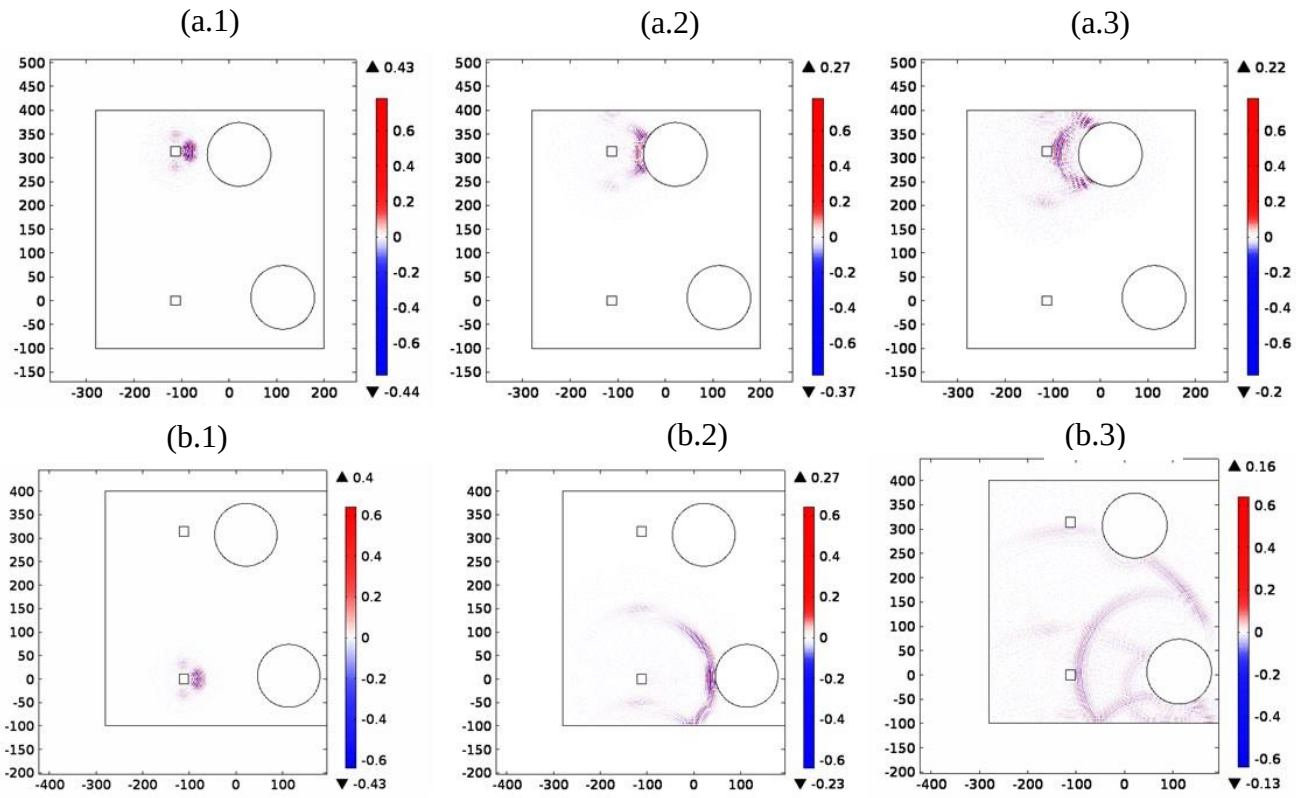

Figure 5-24: Wave pattern; (a.1) d1 wave start; (a.2) d1 wave hits the chain surface; (a.3) d1 return to the transducer; (b.1) d2 wave start; (b.2) d2 wave hits the chain surface; (b.3) d2 return to the transducer

Output signals monitored in FEA case 1 are illustrated in Figure 5-23 (d1– Figure 5-23(a), d2 – Figure 5-23(b)). Distances d_1 and d_2 were calculated by considering the peak-to-peak time of arrival. d1 was calculated as 48.96mm and d2 was calculated as 148.09mm. Therefore, the misaligned angle was calculated by considering the trigonometry between the transducer positions and the d1 and d2 distances. The calculated misaligned angle is as follows:

$$\alpha = \tan^{-1}\left\{\frac{d2-d1}{La}\right] = \left\{\frac{148.09-48.96}{314.2}\right] = 17.51^{\circ} \qquad \textit{Eq 5-20}$$

where L_a is the known (fixed) distance between the transducers. The sign of the angle could be used to determine the clockwise and anti-clockwise misalignment directions.

A study of the chain tilt misalignment detection was carried out, as illustrated in Figure 5-25. Two ultrasound detectors were used to measure the distances, as illustrated in Figure 5-25(a). Ultrasound detectors were placed perpendicular to the chain surface during the ideal condition (both were placed on the same side of the link, separated by a known

distance). Then, a 5° misalignment was introduced to the chain while transducers were kept in the same place. Transmit and receive signals, illustrated in Figure 5-26, were obtained from the wave patterns, illustrated in Figure 5-27. In order to minimise the disturbances, ultrasound transducers were fired one after another, *i.e.* noise could be added to the signal if the waves began to interfere with each other.

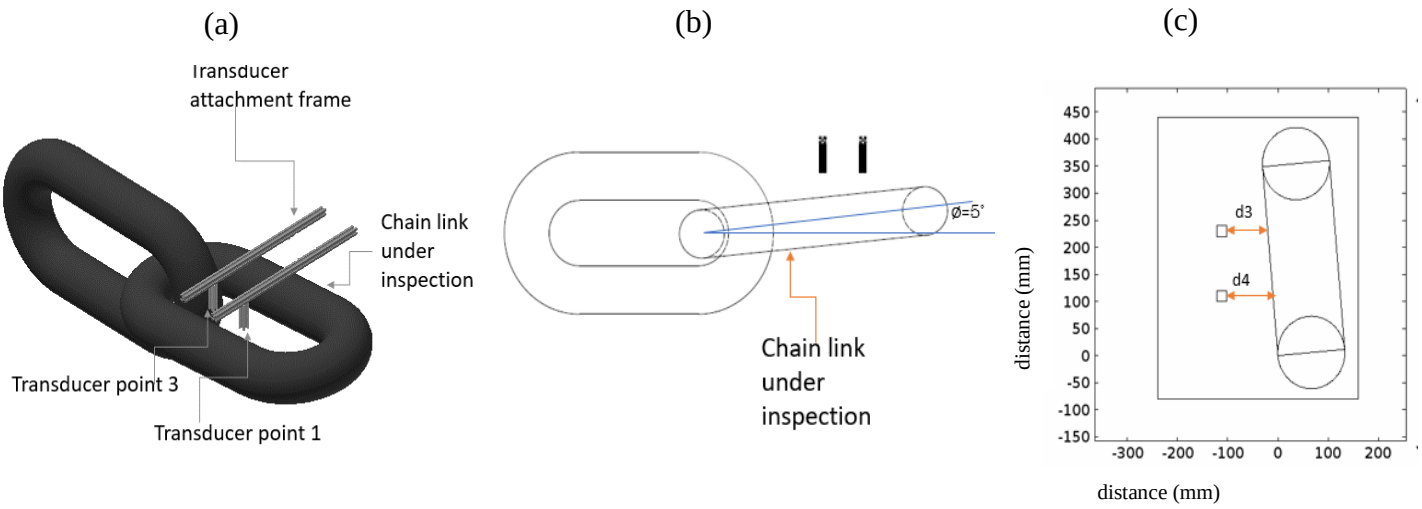

Figure 5-25: FEA case 2; (a) 3D CAD design; (b) misaligned angle cross-section; (c) simplified CAD layout for FEA

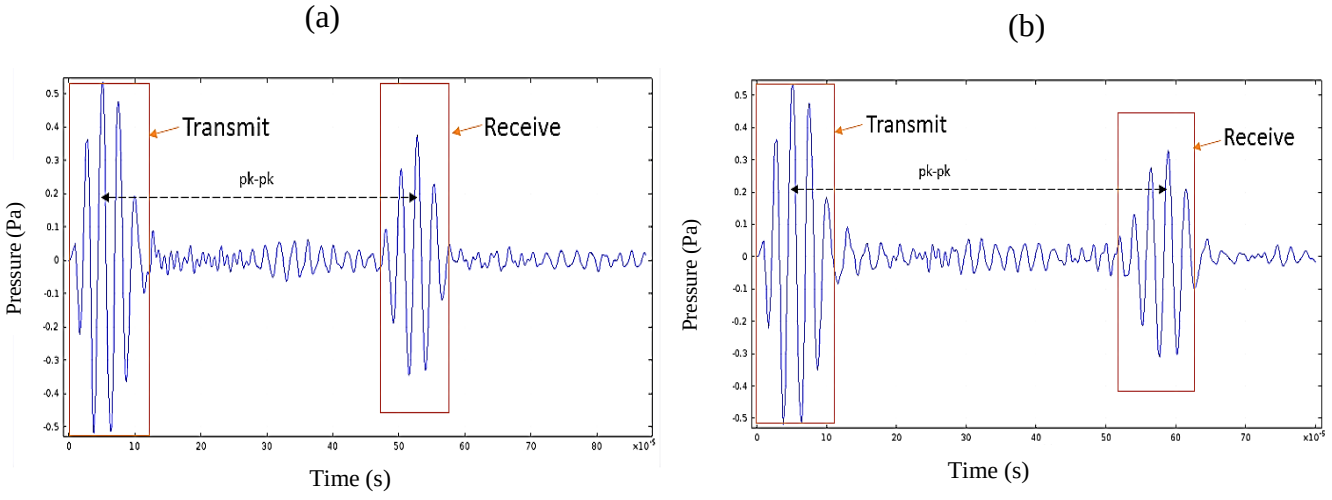

Figure 5-26: Time-of-flight signals; (a) from d3; (b) from d4

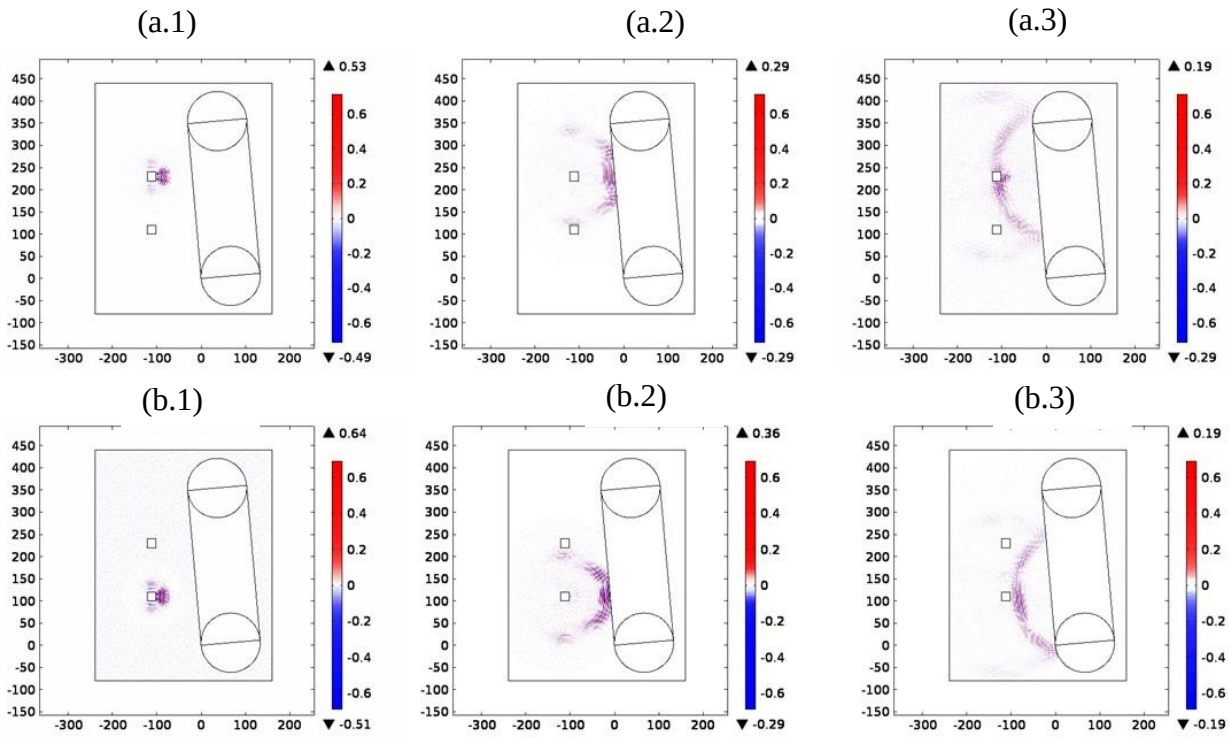

Figure 5-27: Wave pattern; (a.1) d3 wave start; (a.2) d3 wave hits the chain surface; (a.3) d3 return to the transducer; (b.1) d4 wave start; (b.2) d4 wave hits the chain surface; (b.3) d4 return to the transducer

Output signals monitored in FEA case 2 are illustrated in Figure 5-26 (d3 – Figure 5-28(a), d4 – Figure 5-26(b)). Distances d3 and d4 were calculated by considering the peak-to-peak time (see Figure 5-26). d_3 was calculated as 47.55mm and d_4 was calculated as 92.18mm. Therefore, the misaligned angle was calculated by considering the trigonometry between the transducer positions and the d_3 and d_4 distances. The misaligned angle is as follows:

$$\emptyset = \tan^{-1}\left\{\frac{d4-d3}{Lb}\right] = \left\{\frac{92.18-47.55}{120}\right] = 5.06^{\circ} \qquad \textit{Eq 5-21}$$

where L_b is the known (fixed) distance between the transducers. The sign of the angle could be used to determine the clockwise and anti-clockwise directions of the misalignments.

According to the above examples, it was possible to use the ultrasound distance measurement to estimate the misalignment angle of the chain links.

5.7.2 Ultrasound misalignment detecting experimental test

After the misalignment detection feasibility study, which was carried out using ultrasound, a test rig was built to test the idea. At this stage of the research, autonomous climbing was not established, but it was necessary to understand the misalignment of the chain surface (link's climbing surface) for future upgrades. The test rig illustrated in Figure 5-28(b) was constructed according to the specifications provided in the Figure 5-28(a) schematic. A transducer with the specifications provided in Table 5-3 was used in this experiment, *i.e.* the frequency of the transducer was the same as in the FEA studies. At the beginning of the experiment, the prototyped test rig remained parallel to the chain, as illustrated in Figure 5-28(c). Then, misalignments were introduced. A scale/pointer was used in this experiment to indicate the reference angle (see Figure 5-28(d)).

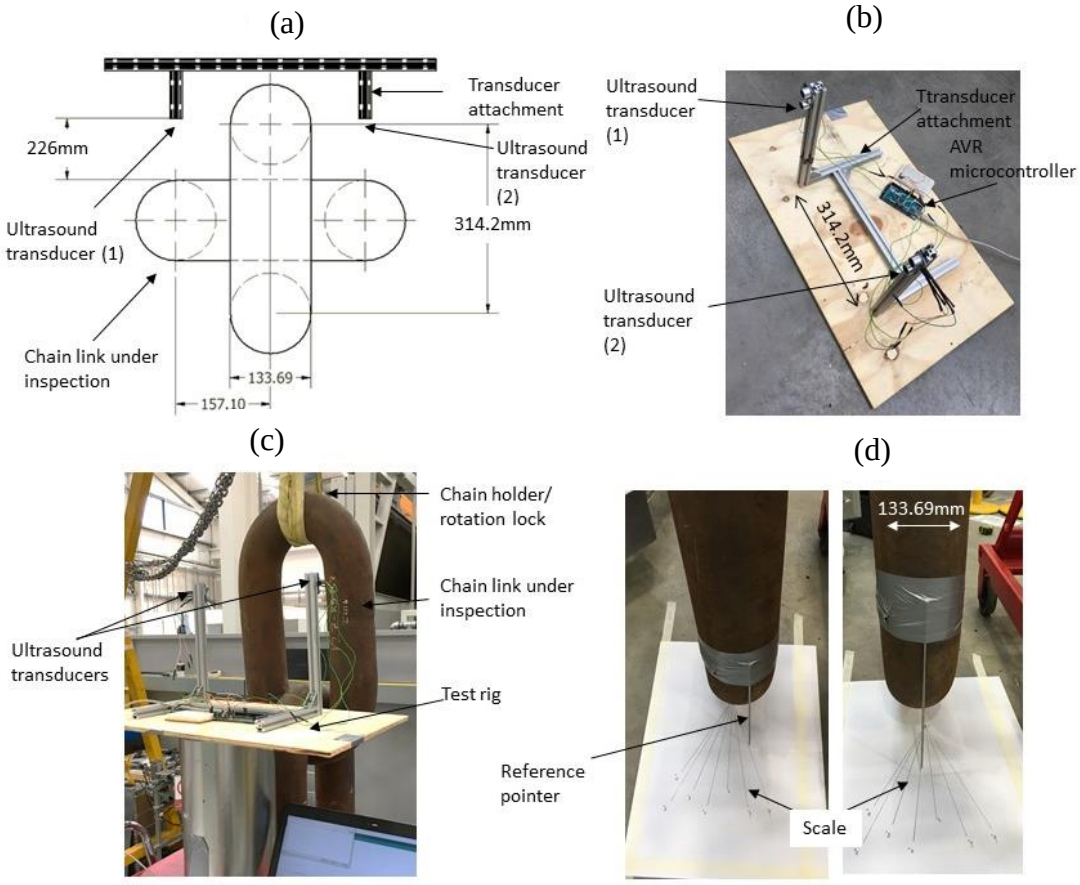

Figure 5-28: Ultrasound test rig for twist misalignment detection; (a) test rig schematic; (b) prototyped test rig; (c) test rig placement with the chain surface; (d) pointer/scale used as reference

Table 5-3: Transducer specifications

Transducer Parameter	**Specification**
Working Frequency (During Experiment)	40khz
Working Voltage (Input Voltage)	Dc 5v
Working Current (Input Current)	15mA
Max Range	4m
Min Range	2cm
Measuring Angle	15 Degrees
Trigger Input Signal	10µs Ttl Pulse

The measurement of the angle was conducted by introducing misalignments to the chain link under inspection. The misalignment angle was measured as explained in the FEA (*i.e.* by using two distances measured using ultrasound), and the distance between the transducers and the corresponding reference angle was measured by the scale. Both the ultrasound angles and reference angles were recorded (an average reading was taken from ten recorded values for each reading), then the results were plotted for evaluation, as illustrated in Figure 5-29. The error between the reference measurements and the experimental readings were not significant. The maximum error between the reference and measured results was 1.97°, *i.e.* the angle measured – 18.03°, the reference angle – 20°. According to the experimental results, the error between the readings was less than ± 0.8° when the misalignment was ± 17°. In this method of angle measurement, the transducers were not perpendicular to the chain surface when there was a twist. However, the surface was still within the ultrasound measuring range, as illustrated in Figure 5-30. This can be seen as the main reason for the error when the misalignment was greater than 17°. According to previously published studies, twist misalignments can be ± 8° [19]. Therefore, it was possible to use ultrasound distance measurement to estimate the misalignment angle of the chain links.

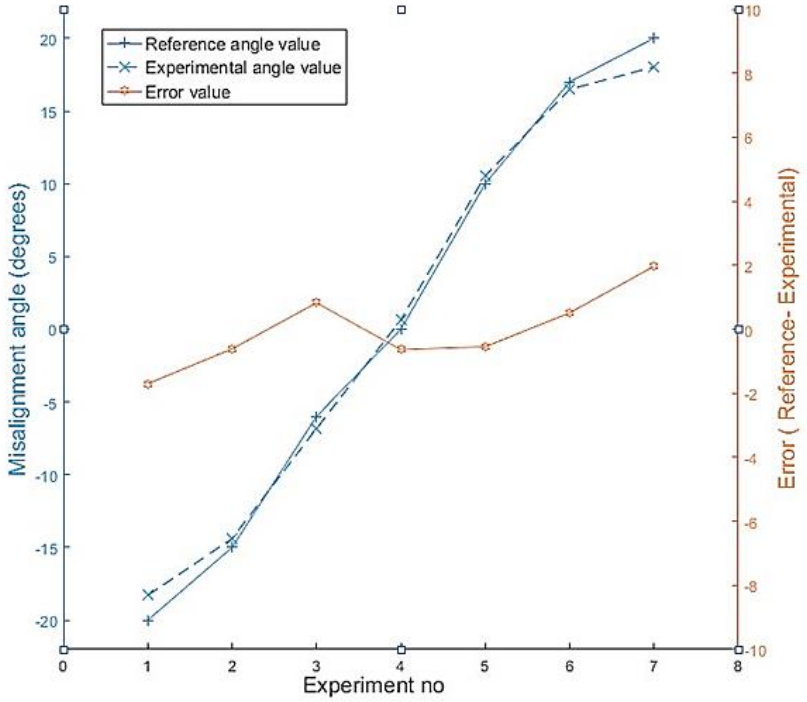

Figure 5-29: Twist misalignment angle measuring experimental results vs reference values

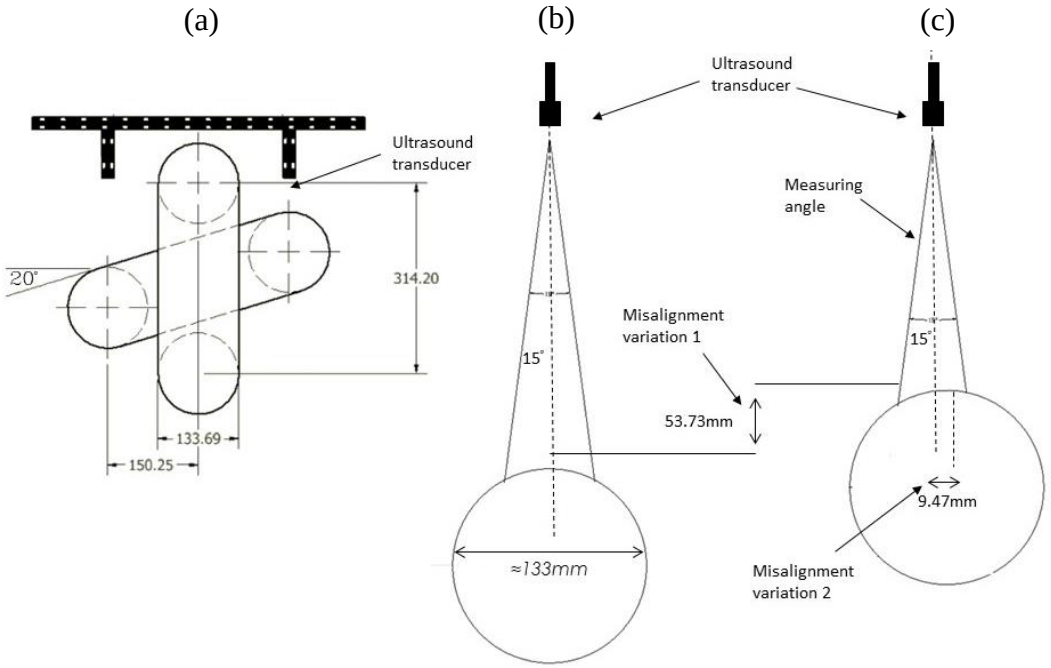

Figure 5-30: Chain link vs ultrasound measuring range (example of 20-degree misalignment); (a) misalignment schematic; (b) ultrasound beam and the chain link when there is no misalignment; (c) ultrasound beam and the chain link when there is a 20-degree misalignment (chain surface still covering the beam width)

The test rig illustrated in Figure 5-31(b) was constructed according to the specifications provided in the Figure 5-31(a) schematic. A transducer with the specifications provided in Table 5-3 was used in this experiment, *i.e.* the frequency of the transducer was the same as in the FEA studies. At the beginning of the experiment, the prototyped test rig remained parallel to the chain, as illustrated in Figure 5-31(c). Then, misalignments were introduced (see Figure 5-31(d)).

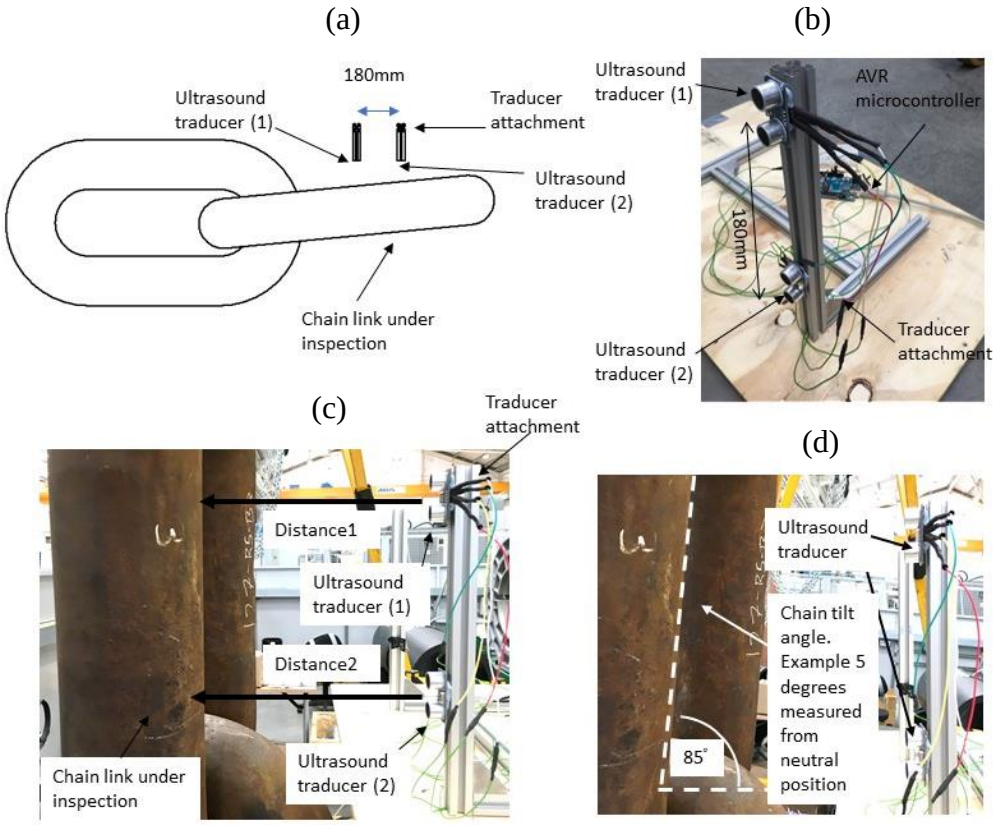

Figure 5-31: Ultrasound test rig for tilt misalignment detection; (a) test rig schematic; (b) prototyped test rig; (c) test rig placement with the chain surface; (d) sample measurement position

Angle measuring was conducted by introducing misalignments to the chain link under inspection. The misalignment angle was measured as explained in the FEA, *i.e.* using two distances measured using ultrasound and the distance between the transducers. The corresponding reference angle was measured by a scale. Both the ultrasound angles and reference angles were recorded (an average reading was taken from ten recorded values for each reading), then the results were plotted for evaluation, as illustrated in Figure 5-32. The error between the reference measurements and the experimental readings were not significant. The maximum error between the reference and measured results was 0.89°,

i.e. the angle measured – 9.89°, the reference angle – 9°. In this method of angle measurement, the transducers were not perpendicular to the chain surface when there was a tilt. However, the surface was still within the ultrasound measuring range, as illustrated in Figure 5-30. This can be seen as the main reason for the error. When considering the experimental data in Figure 5-29 and Figure 5-32, it was possible to use the ultrasound distance measurement to estimate the misalignment of the chain links when they were ± 17° (for the tilt) and ± 8° (for the twist).

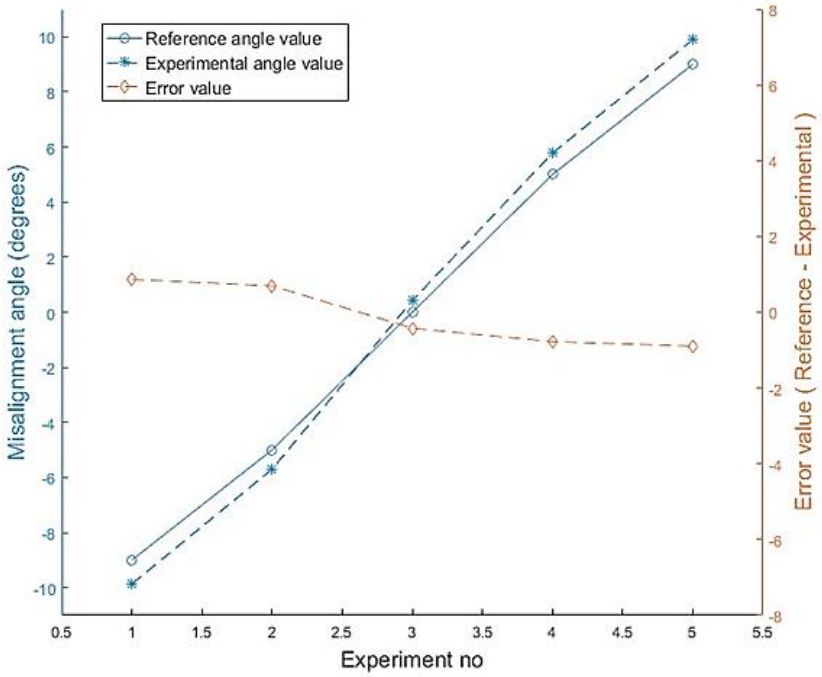

Figure 5-32: Tilt misalignment angle measuring experimental results vs reference values

5.8. Chapter summary

This chapter discussed the results that showed that it was possible to upgrade a previously designed magnetic adhesion tracked-wheel mooring-chain-climbing robot to address the misalignment issues of operational mooring chains. The results and findings in the chapter were added to the literature in ***[D2].*** The previous version of the climbing robot was unable to demonstrate climbing when there was a misalignment presented in the chain. Two types of misalignment (chain twist and chain tilt) were studied and a mathematical model of a robot leg was proposed. Then, the proposed model was modified according to the mechanical needs of the climbing robot. The prototyped robot leg was introduced to a single tracked-wheel module of the previous robot and experimental studies were carried

out. The complete robot system was tested on a three-link mooring chain segment to study the climbing capability. For this study, 5–17° link twist and 1–5° link tilt misalignments were introduced to the chain link and the robot was able to adapt the tracked-wheel unit by using the newly added Cartesian robot leg. During the climbing experiment, misalignment angles were added to the system manually. Therefore, a feasibility study was conducted using ultrasound in order to establish a misalignment detection concept. The concept was designed using ultrasound FEA, then an experiment was conducted. As a result of the study in this chapter, the idea of an orthogonally placed, Cartesian-legged magnetic adhesion tracked-wheel robotic platform that could eliminate concerns relating to the misaligned mooring chain climbing was established.

Chapter 6: Feasibility study of automated mooring chain inspection

6.1 Chapter overview

Chain climbing is a highly industry-related activity due to its application, *i.e.* for the use of FPSO mooring chain integrity management. Only a few automated attempts have been tested in the history of chain integrity management due to the inspection complexity and lack of reachability, *i.e.* due to the mooring chain's curved, round, complex geometry and because most automated robotic platforms are still at the laboratory stage. Therefore, integrity assessment of mooring chains is carried out using manual methods such as visual inspection, hammer testing, mechanical measurements etc.

The development of a chain-climbing robot that is capable of working as a platform was investigated in Chapters 2–5. In the interest of robotic improvements, chain climbing is an area that requires further exploration. Therefore, in the first part of the thesis, a magnetic adhesion tracked-wheel robot was proposed. As mentioned previously, the primary concern of mooring chain climbing is to conduct an in-situ integrity investigation. Therefore, a feasibility study was carried out in this chapter to investigate a suitable method of inspection that could be used both in air as well as underwater. Moreover, the capability of automation was considered as a primary aspect because the idea presented in this chapter was to propose a technique that could be used with a climbing platform. Inspection of the chain crown area was considered as the primary concern in this chapter. It is imported to evaluate the crown of a link and the interlink contact zone due to the heavy residual stress and wear effects. In previous automated studies, the primary concern was to investigate the weld area of the chain. According to the findings in [8] [7], chain crown investigation was also considered as priority. The capability of using conventional NDT techniques for crown inspection are limited due to the complex geometrical features of the chain crown, *i.e.* curved, round, overlapping with the orthogonal chain link, rusted etc.

State-of-the-art mooring chain inspection techniques were discussed at the beginning of this chapter. Commonly used NDT techniques were investigated in order to select a suitable technique. The background theory of the selected techniques was also presented. Finally, the design and testing of the selected technique were presented, as well as a feasibility conclusion, *i.e.* phased-array/FMC ultrasound inspection.

6.2 State-of-the-art chain inspection mechanisms

6.2.1 Automated mechanisms

When considering the literature on chain inspection, only a few attempts have been made to automate the process. Compared to the evolution of automated NDT, chain inspection is still in its infancy. Long-range, guided-wave inspection was used in the 'Moorinspect' project [19] [115]. A collar with guided-wave transducers was introduced around a chain link with the use of a pneumatic actuator arm and NDT inspection was carried out (see Figure 6-1). According to the internal project reports, ensuring the mobility of the system became more difficult with the extra weight of the pneumatic collar. This system aimed to access the chain from a single point and inspect the entire chain.

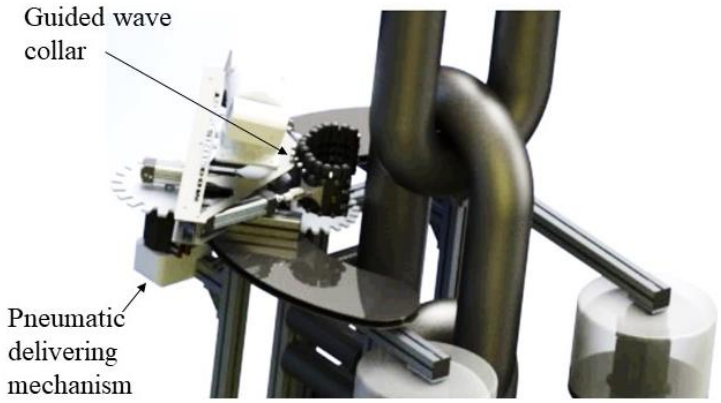

Figure 6-1: Guided wave inspection collar and attachments [115]

A visual inspection system was designed in [22], as illustrated in Figure 6-2(a). An inspection chamber was designed for this mechanism that could rotate in order to inspect orthogonal chain links. An image-processing mechanism was added to the system to measure the distortions of the structure (see Figure 6-2(b)).

(a) (b)

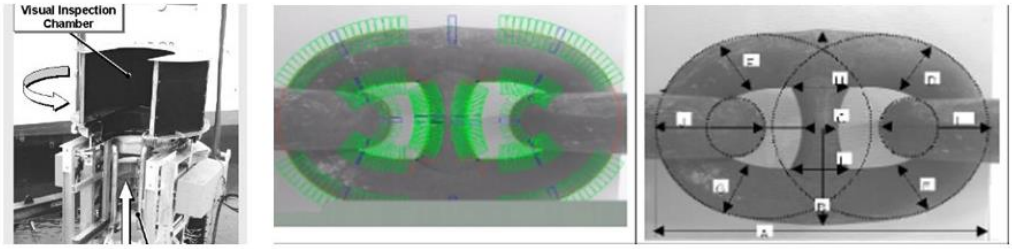

Figure 6-2: ICARE anchor chain inspection mechanism; (a) visual inspection chamber; (b) image-processing sample [22]

The automated inspection system presented in [116] was designed for use in the chain-manufacturing process (see Figure 6-3). The system was designed to investigate manufacturing flaws in the soldered area using ultrasound transducers. Angle probes were used in this system and the results were obtained by considering the entire curvature of the welded surface. Since this was designed to work at the manufacturing stage, chain links needed to be placed in the system in order to conduct the inspection.

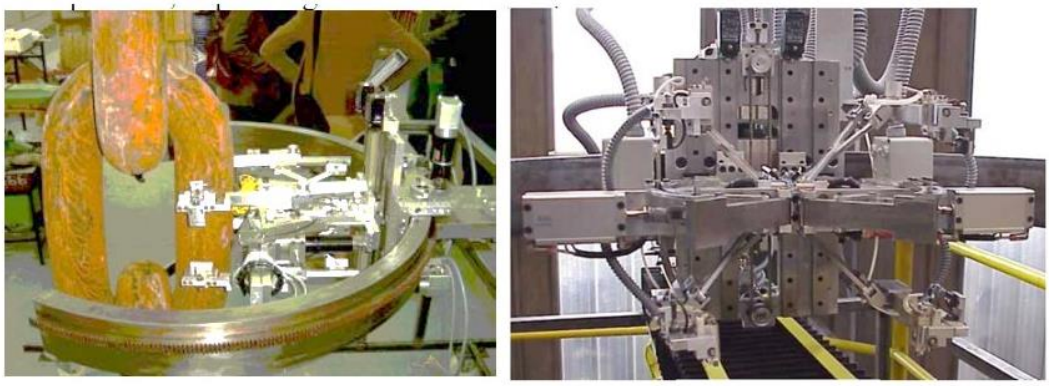

Figure 6-3: Ultrasound welding inspection automated system [116]

A conceptual NDT system was proposed in [117], as illustrated in Figure 6-4. Phased-array NDT and visual inspection were considered in this project ('chain test'). A phased-array system with a robotic manipulator was proposed in order to investigate the welding joint area.

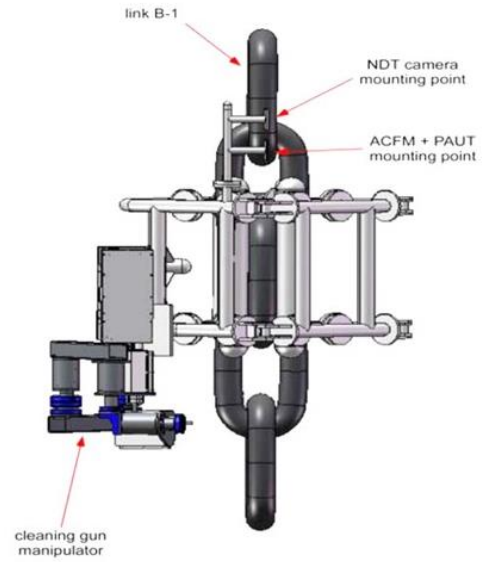

Figure 6-4: 'Chain test' PAUT inspection mechanism [117]

For industrial subsea inspection, ROVs are the most common industrial practice. Most ROV inspections are carried out using visual inspection, *i.e.* a camera system or a 3D laser surface detection mechanism [118]. Most of these visual inspection mechanisms are teleoperated and can be attached to an ROV, which can take the device close to the chain. The visual inspection is based on images/measurement readings/3D models of the chain surface. Few ROV-assisted attempts with automated measuring have been recorded in the literature. The system illustrated in Figure 6-5 (a) consists of an automated robotic manipulator designed to take measurements of the chain links [28] [29]. Figure 6-5(b) illustrates a gas spring measuring mechanism that was designed to record the mooring chain's physical measurements when dragged along the chain surface by an ROV [30].

(a) (b)

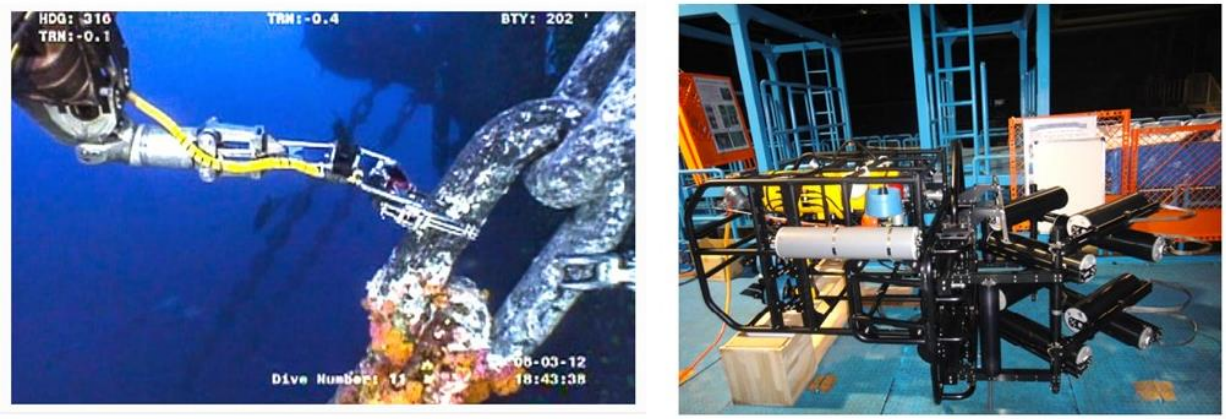

Figure 6-5: ROV-assisted inspection mechanism; (a) Welaptega mooring measuring system [155]; (b) gas spring mooring measuring system [30]

Employing divers or NDT operators (hanging in air from the top side) to investigate mooring chains is another common inspection mechanism. The device illustrated in Figure 6-6 was designed to investigate the crown of a pre-specified chain link [119]. In this device, a set of single-degree UT probes were attached to a rigid mould that could be fitted onto a chain crown.

Figure 6-6: TWI's handheld chain crown inspection device [119]

6.2.2 Mooring chain inspection standards and related studies

As discussed in the introduction chapter, a break in a mooring system can lead to catastrophic events, *i.e.* riser rapture, vessel drift etc. Therefore, standards and codes of practice have been introduced to mooring systems. Standards have been discussed from the manufacturing stage to in-situ inspection because it is vital to maintain integrity throughout the process.

According to the DNV offshore standards [120], mooring chain links should be inspected both visually and using NDT. Moreover, inspection of the welding area should be carried out using ultrasound inspection (inspection should be according to ASTM E587 standards). According to API standards [121], a diameter reduction that indicates less than 95% (nominal diameter) must be considered a rejected link. Chain inspection intervals are determined according to service time in the water, *i.e.* a mooring system that has been in operation for 0–3 years should be inspected every 36 months, 4–10-year chain links should be inspected every 24 months, and systems that have over ten years of service should be inspected every eight months [121]. When considering both API and DNV standards, visual inspection can be identified as a common and vital NDT inspection. According to API standards, offshore mooring chain inspection should be carried out using visual inspection, magnetic particle inspection (MPI), diameter calliper inspection, measuring gauge inspection (go-no-go gauge), and the hammer test.

At TWI Cambridge, a study was carried out to understand the stresses between mooring chain links and potential fatigue damage. Residual stresses around the interlink contact zone were analysed in this research and potential fatigue damage around the crown of the chain link was investigated. Moreover, in the above-mentioned research, the fatigue sensitivity of the Kt point (approximately the region of the intrados where the shank and the crown intersect (see Figure 6-7)) was also investigated [8]. A comprehensive historical review of the permanent mooring system was presented in [3]. In the review, accidents and incidents relating to the integrity of mooring systems between 2001 and 2011 are discussed and integrity failures of different parts of mooring systems are presented according to the accident percentage. A study was conducted to determine the rate of wear of a mooring chain's interlink contact zones in [35]. The presented test results are based on various axial loadings and specific angular displacements using dry/wet mooring chains.

6.3 Selection of NDT technique

6.3.1 Comparison of NDT techniques

Table 6-1 presents a brief comparison of the NDT techniques that are commonly used in the industry. A detailed comparison of NDT techniques is presented in [122] [123].

Table 6-1: Common NDT techniques

NDT technique	Characteristic observed	Usage	Technical limitation
Ultrasound inspection	Indication of acoustic impedance change caused by defects	Able to penetrate via thick solid materials. Resolution of defect detection is comparatively high. Automation capability	Good surface contact/coupling requirement
Visual inception	Observation of surface characteristics	Easy to set up. Can be automated with controllable cameras. Works with any surface	Inspection is only for the surface. Internal defects cannot be observed
Radiography	Density changes in materials, material variations, voids, inclusions etc.	Applicable to a wide range of materials. Different thicknesses can be measured according to the power of the radiography	Radiation safety must be considered. Detection of cracks depends on the perpendicularity
Liquid penetrant	Openings of the surface, cracks, defects, porosity	Sensitive to surface defects. Easy to use. Portable. Inexpensive	Defect must be open to the surface. Not useful for rough materials
Magnetic particles	Leakage of magnetic flux caused by a defect	Sensitive to surface and near-surface defects. Easy to use. Portable. Inexpensive	Lack of surface penetration. Limited to ferromagnetic surfaces
Eddy current	Electrical conductivity changes due to material defects	Sensitive to surface and near-surface defects. Easy to use. Portable	Limited to electrically conducted surfaces. Limited surface penetration

6.3.2 Selection of NDT technique for mooring chain inspection

When considering the NDT techniques listed in Table 6-1, a liquid penetrant cannot be used for mooring chain crown inspection because this technique does not penetrate the surface. Magnetic particle inspection and eddy current techniques are difficult to establish in underwater mooring environments, and surface penetration is unable to look through the diameter of the chain, *i.e.* the chain diameter used in this research was ≈ 133mm). Radiography is a useful technique, but underwater inspection capabilities are limited and placing source and the detector in order to inspect the crown is not practical. Visual inspection is vital to understand the physical nature of the material, but it is unable to provide a greater evaluation other than the surface quality. However, according to the standards, a visual inspection should be included. In the findings in [8] [7], inspection of the chain crown and interlink contact zone was suggested as vital to the structural health monitoring of mooring systems. In order to evaluate the structural health condition of a chain system, it is imported to investigate the crown as well as the weld area for possible defects such as cracks, corrosion, manufacturing defects etc. To investigate the crown and interlink contact zone, a surface penetration method such as ultrasound is needed.

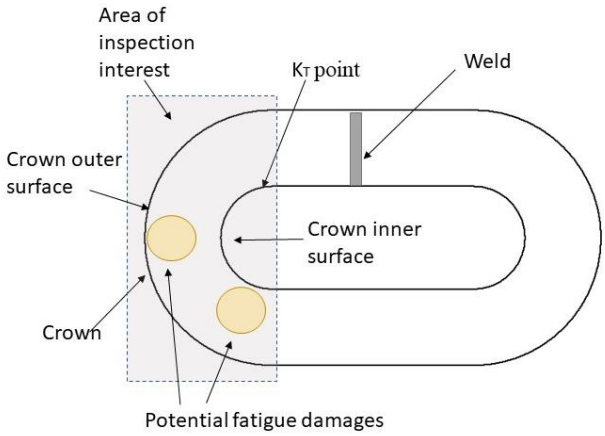

Figure 6-7: NDT inspection focused areas due to high stress that can cause fatigue cracking [7] [8]

The current state-of-the-art automated mechanisms are designed to investigate the weld area of a chain link using ultrasound. Due to the geometry, inspection of a chain weld is similar to inspection of a weld in a pipe. However, inspection of the chain crown requires further study due to the lack of investigation in the literature, *i.e.* initially, mooring chain inspection focused on the welding, but the importance of the chain crown has been identified recently. Moreover, single-degree probe ultrasound inspection of the chain crown was studied in [119], and an NDT handle was designed to be operated by divers;

however, automation capability was not considered. To conduct an automated ultrasound inspection of a chain crown, the following aspects were considered: 1) placing – the inspection probe must be kept on the outside of the chain crown and should provide a detailed image of the cross-section, *i.e.* access via the inner crown surface is restricted due to the orthogonal chain link; 2) defect identification – the system should provide clear identification of the defects such as cracks, backwall loss etc; and 3) automation capability – the mechanism should be able to provide automation capability.

As mentioned previously, a single-degree probe (conventional ultrasound inspection) was considered in the literature [119]. In automated ultrasound inspection, the use of ultrasound arrays is common practice compared to single crystal transducers because arrays are capable of electronically focused steer and sweep without physically moving the transducer, *i.e.* they provide the ability to inspect an area with a single transducer placement. The reduction of mechanical movements provides an advantage when considering a robotic/automation inspection, *i.e.* with the reduction of physical probe manipulation, automation path planning can be discreet and less complicated. Full matrix capture (FMC) is a well-known ultrasound data accusation technique which has been used in the industry/ research to capture the complete time domain signals for each transmit-receive element of an array. This technique has been studied and used in [124] [125] [126]. FMC phased array data acquisition technique is capable of providing a higher resolution entirely focused images and better sensitivity to small defects compared to the conventional phased array as illustrated in the Figure 6-8. In the conventional phased array inspection, an area can be covered, but the resolution of the image is comparatively low due to the unfocused points/defects (see Figure 6-8(a)). Due to the multiple A scan capability of FMC, every point on the scan is focused with higher quality and resolution

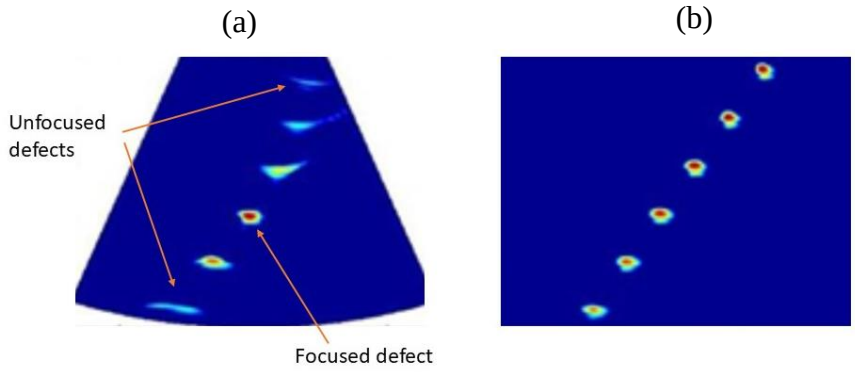

Figure 6-8: (a) sample image of a conventional phased array inspection; (b) sample image of an FMC phased array inspection [137]

(see Figure 6-8(b)). In conclusion, Ultrasound phased array inspection with full matrix capture was selected.

6.4 Basic background theories in propagation of sound waves

Prior to the experimental approach of the ultrasound chain inspection, a fundamental understanding of how sound waves propagate in a medium is useful. Detailed studies of wave propagation have been presented in many textbooks, *i.e.* Ultrasonic testing of materials [127], Ultrasonic waves in solid media [128], NDT fundamentals [129] and is merely briefly outlined here. Navier's equation [128] of motion for an isotropic elastic unbounded media is,

$$(\lambda + \mu)\nabla\nabla.u + \mu\nabla^2 u = \rho\frac{\partial^2 u}{\partial t^2} \quad \textit{Eq 6-1}$$

Where λ and μ are Lamé constants, three-dimensional displacement vector (u), the three-dimensional Laplace operator (∇^2), material density ρ. Helmholtz decomposition can be used to write u as a sum of the compressional scalar potential (Ø), and an equivoluminal vector potential (ϕ),

$$u = \nabla\emptyset + \nabla x\Phi \quad \textit{Eq 6-2}$$

With

$$\nabla\Phi = 0 \quad \textit{Eq 6-3}$$

$$\frac{\partial^2\phi}{\partial t^2} = c_l^2\nabla^2\phi \quad \textit{Eq 6-4}$$

$$\frac{\partial^2\Phi}{\partial t^2} = c_s^2\nabla^2\Phi \quad \textit{Eq 6-5}$$

By substituting the potentials of Helmholtz decomposition (Eq 6-2) in to Navier's equation (Eq 6-1) of motion, generate two separate equations for the unknown potentials which govern longitudinal waves (Eq 6-4) and shear waves (Eq 6-5).

where, c_l and c_s are the velocities of longitudinal and shear waves and they can be expressed as bellow,

$$c_{l=} \sqrt{\frac{\lambda+2\mu}{\rho}} \qquad \textit{Eq 6-5}$$

$$c_{s=} \sqrt{\frac{\mu}{\rho}} \qquad \textit{Eq 6-6}$$

Comprehensive background theory of ultrasonic inspection, i.e. Fundamentals, properties of sound waves and phased array has been discussed in [129] [130] [131] [132].

The method of FMC is an ultrasonic data collection process that uses phased-array probes to record A-scans for each pair of transmitting and receiving elements. Therefore, for an n element phased-array probe, the number of A-scans is in the order of n^2 [133]. Prior to using the technical approach of FMC, a fundamental understanding of the principle is useful. Detailed studies of FMC are presented in [125] [134] [135] and are briefly outlined here. The FMC algorithm was introduced to the non-destructive inspection by the University of Bristol in 2005 [135]. The basic mathematical explanation of the algorithm is expressed as:

$$I_{(x,z)} = \left| \sum h_{tx,rx} \left(\frac{\sqrt{(x_{tx}-x)^2+z^2} + \sqrt{(x_{rx}-x)^2+z^2}}{cl} \right) \right| \qquad \textit{Eq 6-7}$$

This expresses a grid of pixels that represents a cross-sectional area of the specimen of interest for inspection. The pixel intensities (I) are dependent on the time of flight, which can be calculated using both tx and rx, *i.e.* transmit and receive, where h is the Hilbert transform that converts the acquired data from the time domain to the frequency domain. By calculating the complex signal, this can create the signal magnitude envelope. Each pixel in the image, $I(x,z)$, is determined by Eq 6-7. Previous work presented in [125] shows how the parallel processing capabilities of modern graphics cards could be utilised to accelerate the processing of the algorithm.

$$\frac{\sin(\phi_i)}{c_i} = \frac{\sin(\phi_R)}{c} \qquad \textit{Eq 6-8}$$

The well-known Snell's law was used to establish the direction of a sound beam between two points separated by two mediums that have acoustic velocities *ci* and *c*. When the angle of incident is $Ø_i$ and the angle of diffraction is $Ø_R$, the relationship between them can be written as Eq 6-8.

$$time = \frac{\sqrt{px^2 + pz^2}}{c_i} + \frac{\sqrt{qx^2 + qz^2}}{c} \qquad \textit{Eq 6-9}$$

Snell's law can be derived using Fermat's principle to express the shortest time between the P and Q points in Figure 6-9(a), *i.e.* Eq 6-9, where point P is located with *px,py* and Q is located with *qx,qy*.

$$I_{(x,z)} = \left| \sum h_{tx,rx} \left(\frac{\sqrt{(x_{tx} - x_{txi})^2 + {z_{txi}}^2} + \sqrt{(x_{rx} - x_{rxi})^2 + {z_{rxi}}^2}}{cl} + \frac{\sqrt{(x_{txi} - x)^2 + (z - z_{txi})^2} + \sqrt{(x_{rxi} - x)^2 + (z - z_{rxi})^2}}{c} \right) \right| \qquad \textit{Eq 6-10}$$

Modification of the basic FMC equation (Eq 6-7) was studied in [126] to focus the sound beam through dual media, *i.e.* when the probe was placed on the water surface and inspection was carried out inside a metal. Eq 6-10 was developed according the above dual media refraction illustrated in Figure 6-9(b), where the intensity value of the pixel located at' *x*, *z* is *I*, which is determined by each *tx* (transmit) and *rx* (receive) pair to the pixel region of interest (*x,z*), via the point at which the ultrasonic energy passes through the refractive interface (x_{txi}, z_{txi} for transmit and x_{rxi}, z_{rxi} for receive) to the pixel location. The velocity in the medium is c and the velocity though the interface material is c_i. Detail discussion of Eq 6-8, Eq 6-9, and Eq 6-10 is presented in [126] [136].

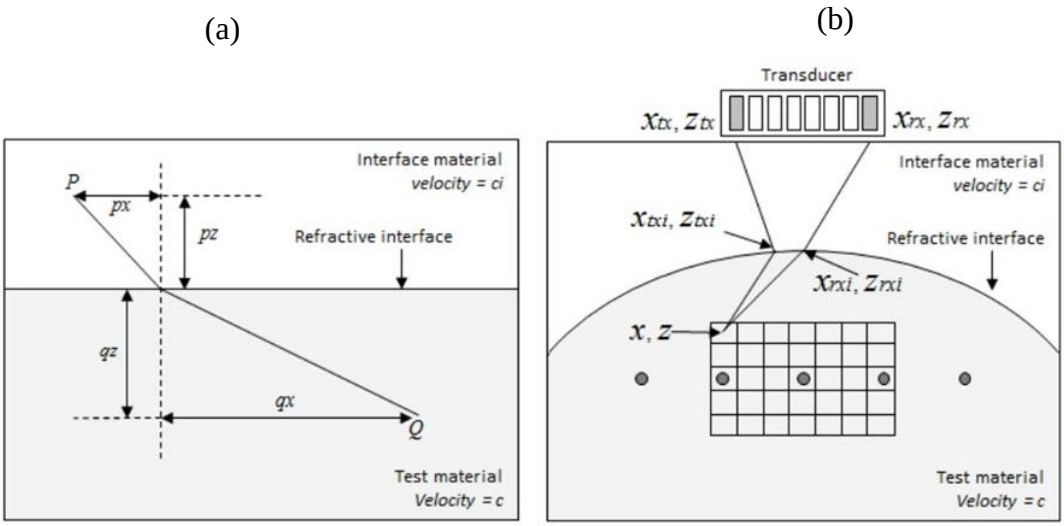

Figure 6-9: (a) Demonstration of Fermat's principal; (b) fully focused FMC data – focusing through dual media explanation [126]

6.5 Requirements of the FMC algorithm and surface adaptation

The FMC algorithm and the GUI used in this study were developed by TWI Ltd. [137], in its internal project deliverable report [138], for the InnovateUK project RIMCAW [27]. Inspection of the chain (*i.e.* phased-array inspection discussed in this chapter) was conducted as a novel application of the previously establish FMC concept [136].

6.5.1 Algorithm adaptation requirement

For inspections carried out with a static wedge, the ultrasonic transmission paths can be computed once before any signal processing commences. However, for chain inspection, the probe is separated from a curved surface of unknown geometry (*i.e.* curved geometry of the chain) by a water path of approximately 35–40mm, *i.e.* the requirement of the water path and the height are discussed later in this chapter). This presents additional problems: 1) the surface must be mapped, then 2) the ultrasonic transmission paths must be recalculated based on this surface. Therefore, the adaptations mentioned below were added to the existing algorithm.

A number of algorithms for surface mapping were evaluated to determine the most optimum algorithm for the geometry considered here, *i.e.* the mooring chain's curved surface. The front wall is typically of little interest, so it is usual for responses from this region to be saturated in favour of acquiring clear signals in the region of interest (which tends to be deeper inside the material). Conversely, when surface mapping, the ultrasonic

signal from the front wall is of critical interest and a saturated front wall signal will lead to inaccuracies in the estimation of the front wall position. For this reason, the imaging algorithm at each transducer position was sub-divided into two acquisitions: 1) surface-mapping acquisition performed at lower gain, so as not to saturate the front wall response; and 2) an imaging acquisition with a higher gain in order to maximise the signal-to-noise ratio of the FMC dataset.

Three surface-mapping algorithms were assessed:

1. Vertical projection
2. Dipping reflectors
3. Point-like reflectors

6.5.2 Vertical projection

In this algorithm, each element was fired separately in pulse-echo mode and the distance to the front wall was derived from the water velocity and the time to the first response. A typical front wall response is illustrated in Figure 6-10(a). As the location of each transducer was known, the surface could be constructed by positioning the surface point directly below it. An example plot of this algorithm is shown in Figure 6-10(b).

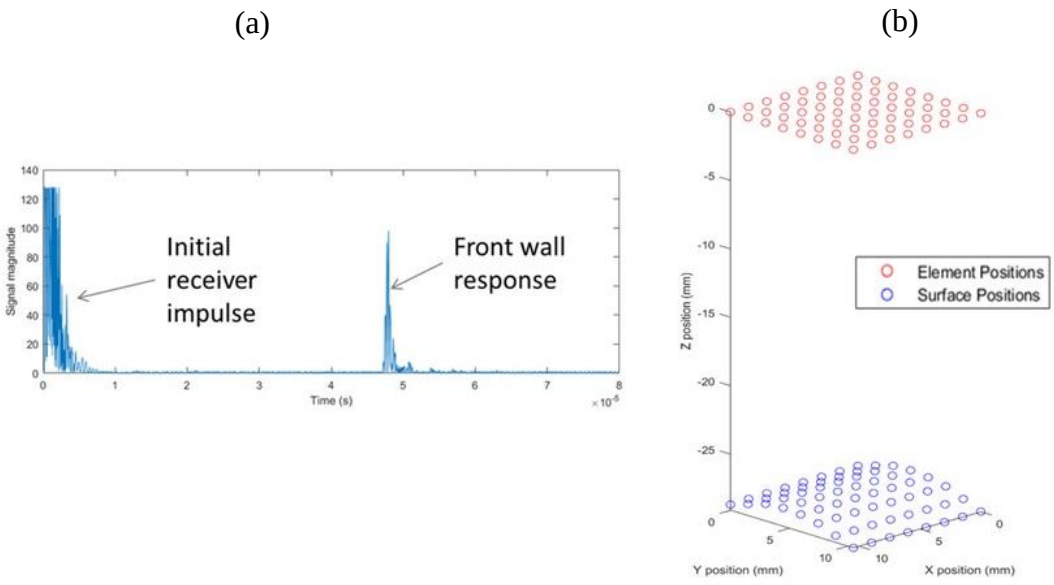

Figure 6-10: (a) Sample ultrasonic response with the initial receiver impulse and the front wall response; (b) example output of the vertical project algorithm showing transducer positions (red) and surface positions (blue)

6.5.3 Dipping reflectors

The studies conducted in [139] show that, unless the surface is flat and parallel to the plane in which the transducer elements lie, vertical projection mis-plots the position of the surface. However, if the surface can be assumed to be flat between adjacent pairs of transducer elements, then the dipping reflector algorithm can be used.

$$\Delta z = \frac{d_2}{\sqrt{1 + \frac{(d_2 - d_1)^2}{s^2}}}$$

Eq 6-11

$$\Delta \mathrm{x} = \Delta z \frac{(d_2 - d_1)}{s}$$

Eq 6-12

Each transducer emits a spherically spreading wave that bounces off the front wall and returns to the element. The ray paths are orthogonal to the front wall in each case; therefore, the angle of incidence and angle of reflection must be equal. Differences between the lengths of the two paths are used to calculate the shifts in the horizontal (Δx) and vertical (Δz) directions, where s is the element pitch (see Figure 6-11(a), Eq 6-11, and Eq 6-12).

On a 3D surface, groups of four neighbouring elements are considered where the front wall is assumed to be planar between the responses from each group of four. An average gradient is computed in the passive and active directions of the probe, as shown in Figure 6-11(b and c). The final position of the point on the surface generating the signal for each element can then be calculated as a combination of two shifts, a vertical shift parallel to the z axis and a shift in the x–y plane.

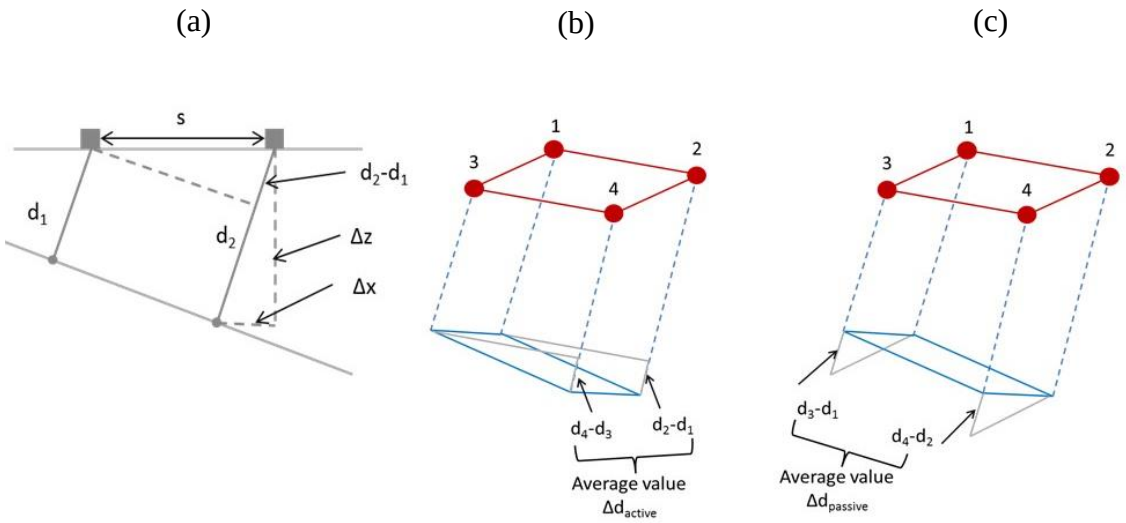

Figure 6-11: (a) Calculation of the shift in x and z from the transducer location using the difference in paths d1 and d2; (b) and (c) calculation of the average gradient in the active x and passive y array directions

6.5.4 Point-like reflectors

The point-like reflector algorithm assumes that the response received by two adjacent transducer elements originates from the same point on the surface. For linear phased-array probes, a detailed methodology of this algorithm is given in [136]. Adapting this algorithm for 2D probes involves locating the intersection point of three neighbouring transducers. Graphically, the fundamental principle of this technique is presented in Figure 6-12.

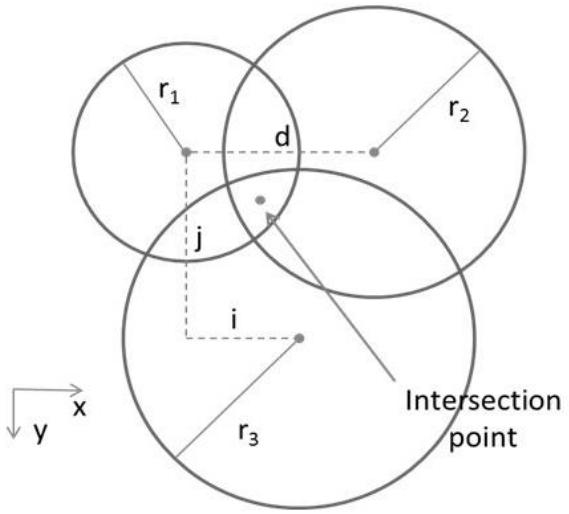

Figure 6-12: (a) Calculation of the inspection point of three spheres

The x, y, and z locations of the intersection point of these three spheres relative to the centre of sphere 1 are given as follows;

$$\mathrm{x} = \frac{r_1^2 - r_2^2 + d^2}{2d} \qquad \textit{Eq 6-13}$$

$$y = \frac{r_1^2 - r_3^2 + j^2 + i^2}{2j} - \frac{i}{j}\,x \qquad \textit{Eq 6-14}$$

$$\mathrm{z} = \pm\sqrt{r_1^2 - x^2 - y^2} \qquad \textit{Eq 6-15}$$

6.6 Experimental testing – surface mapping

After considering the above projection/reflating methods, a laboratory experiment was carried out in order to select a suitable technique (discussed previously) for chain inspection. An experiment was set up as illustrated in Figure 6-13 and responses from the focusing techniques were analysed. Selecting a suitable mapping technique was the primary concern of the experiment. Specifications of the ultrasound probe are discussed later in this chapter. A 3D printed probe holder, illustrated in Figure 6-13(a), was constructed in order to place the probe on the chain surface (see Figure 6-13(b)). The holder was capable of changing the probe's angle and chain-probe height. Moreover, permanent magnetic adhesion attachments were proposed to keep the probe steady on the chain surface. The probe was placed on the chain surface, as illustrated in Figure 6-13(b), with the use of magnet adhesion. Then, the air gap between the probe and the chain surface was filled with water (see Figure 6-13(c)). The gap between the probe and the chain surface (water path) was calculated as ≈ 40mm in order to avoid front wall reflections (see Eq 6-16), where the maximum inspection depth was ≈ 134mm, the speed of sound in the material was 5130m/s, and speed of sound in water was 1,482m/s. A reduction of the front wall reflection was needed in order to examine the material inside.

$$\frac{Maximum\ inspection\ depth}{Speed\ of\ sound\ in\ material} < \frac{Height\ of\ the\ water\ path}{Speed\ of\ sound\ in\ water} \qquad \textit{Eq 6-16}$$

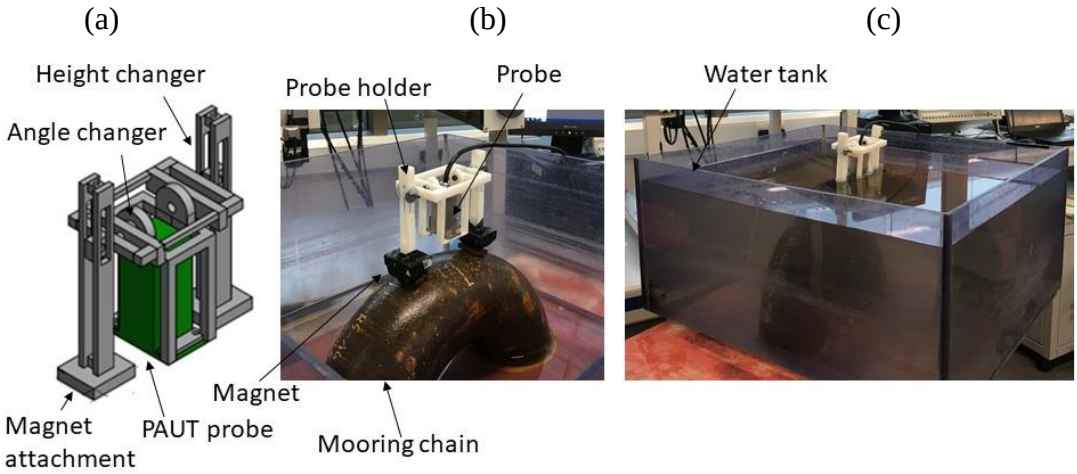

Figure 6-13: (a) CAD model of the probe holder; (b) experimental setup; (c) full experimental setup with the water path

A water path was introduced to the system as a couplant due to the mooring chain in-situ conditions, *i.e.* sea condition. Understanding the automation feasibility is the primary concern of this chapter, and continuous water supply was used previously during NDT automation in [140] [141]. After the abovementioned experimental setup, comparisons between the vertical projection, dipping reflectors, and the point-like reflector algorithms were studied, as in Figure 6-14, Figure 6-15, and Figure 6-16, respectively.

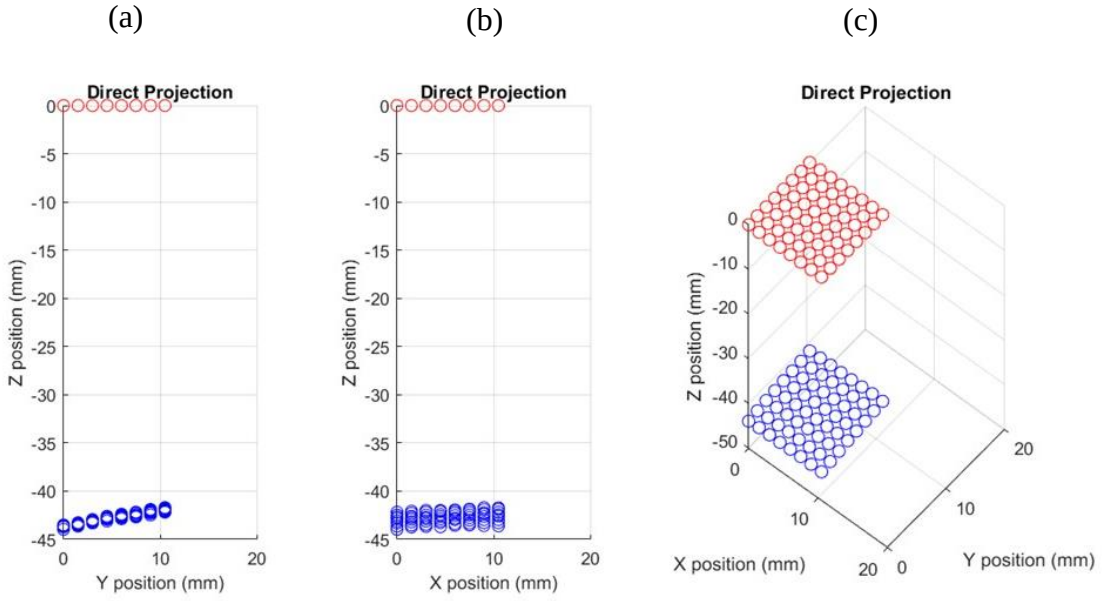

Figure 6-14: Example surface mapping results for the direct projection algorithm; (a) y-z mapping; (b) x-z mapping; (c) x-y-z surface mapping sample

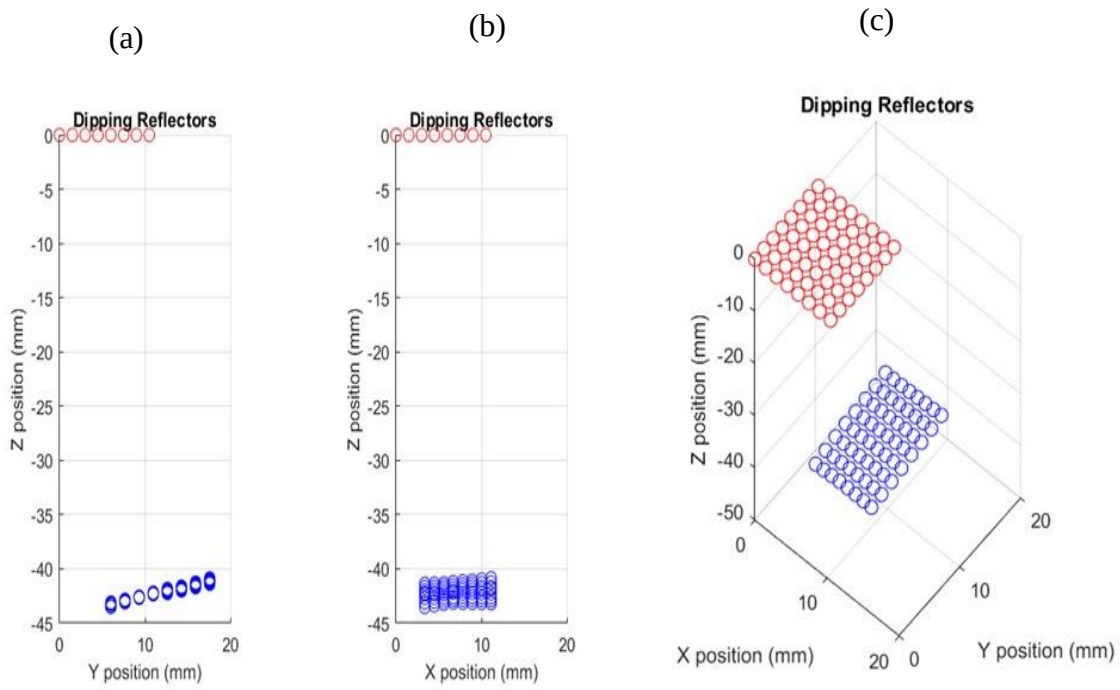

Figure 6-15: Example surface mapping results for the dipping reflectors projection algorithm; (a) y-z mapping; (b) x-z mapping; (c) x-y-z surface mapping sample

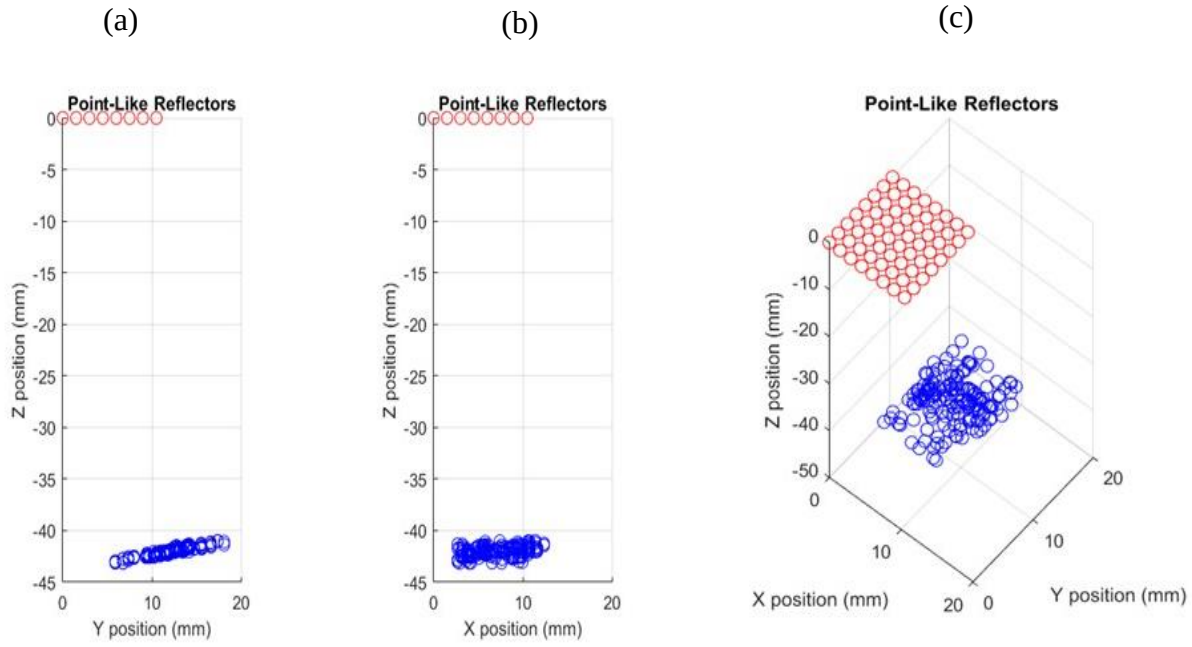

Figure 6-16: Example surface mapping results for the point-like reflectors projection algorithm; (a) y-z mapping; (b) x-z mapping. (c) x-y-z surface mapping sample

The point-like reflector algorithm did not produce a satisfactorily accurate surface map (see Figure 6-16). According to the illustrated results, the computed surface points would be a long way (> 20mm) from their expected approximate positions. Instabilities in the temporal domain were also observed. Given that this test was performed in laboratory conditions with stationary sample and probe, this algorithm was deemed unsuitable for surface mapping in this application. In contrast, the dipping reflector algorithm exhibited better performance in terms of mapping the curvature of the sample map (see Figure 6-15). It was still slightly unstable in the temporal domain. Potential improvements to the algorithm could be implemented to provide a number of ultrasonic acquisitions in order to average out some of the noise. Given that acquisition time was important for this application, this avenue was not pursued. The vertical projection algorithm proved to be very stable during the experiments (see Figure 6-14). Given that these were performed in ideal conditions, and the fact that conditions in the field are likely to be more challenging, the vertical projection algorithm was chosen as the surface-mapping technique.

6.7 Experimental testing – chain inspection

6.7.1 Experimental setup

The FMC software used in this research was designed by TWI Ltd. [142] with the use of the CUDA parallel programming model. The CPU and GPU architecture used in this software are discussed in [126] [125]. As mentioned previously, the intention of this research was to check the feasibility of using FMC/phased array to inspect the chain crown region when it is in air and in water (as an application novelty). In air, inspection can be identified as a challenging task compared to underwater, *i.e.* an additional coupling medium for underwater ultrasound inspection is not required. When considering in-air inspection, using water as a couplant for automated NDT is a common industrial approach. Most in-air industrial applications that use water as a couplant inspect pipes, tubes, plates etc. (hollow, tube-like or thin structures). Due to the significant curvature of the mooring chain (*i.e.* ≈ 66.5mm radius) and the great inspection depth (*i.e.* outer surface to the inner surface ≈ 133mm), a custom-built water coupling mechanism was needed with the following specifications: 1) it should be capable of being placed on the chain surface; 2) the wedge should be able to provide a sufficient water path between the chain surface and probe (*i.e.* 40mm); 3) the wedge should be able to be used as an attachment during the automation process; 4) the wedge should always place the probe signal perpendicular to the surface. As discussed earlier, phased array is a common NDT tool in relation to robotics

or automation, *i.e.* phased array is capable of covering an area under the probe due to its electronic beam-steering capability. Minimising the probe placement points on the chain surface was considered as an advantage because ensuring a discreet inspection can ease the automation process, *i.e.* if a continuous reading is required, the probe needs to move/drag along the chain surface, and discreet inspection is similar to spot inspection. Therefore, a submergible 2D phased-array probe with the specifications in Table 6-2 was selected.

Table 6-2: Phased-array probe specifications

Characteristics/parameters	**Value/acceptance criteria**
Centre frequency (-6dB)	5 ± 0.5MHz
Bandwidth (-6dB)	≥ 60%
Pulse length (-20dB)	≤ 0.8µs
Sensitivity homogeneity	± 3dB
Geometrical shape	2D array
Number of channels	64
Elementary pitch	1.5mm
Elements interspace	0.1mm
Elevation	1.5mm

6.7.2 Wedge design

A specification study was carried out to understand the physical parameters of the wedge. Unlike pipe inspection, the thickness of a mooring chain is significantly high (~ 133–134mm chain thickness in this study). It was necessary to understand the thickness of the water path in order to reduce/avoid front wall reflection.

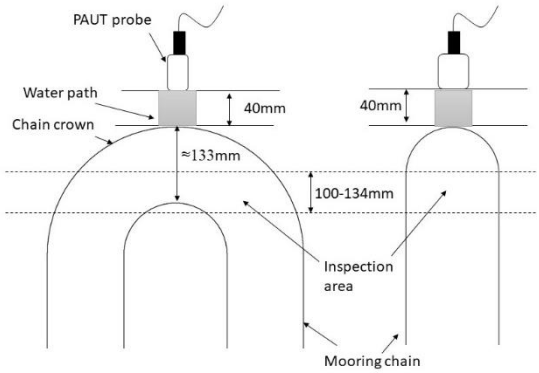

Figure 6-17: NDT probe holder/wedge design

As explained previously, cracks are commonly found in the interlink contact zone of the chain link (see Figure 6-7). Therefore, a 100–134mm thickness range was selected for inspection (see Figure 6-17). According to Eq 6-16, a water path of 40mm was obtained. This study aimed to automate in-air NDT inspection of mooring chains using a robot arm (the design of the robotic manipulator is discussed later in this chapter). Therefore, a wedge attachment with the end effector of the robotic manipulator was considered during the design.

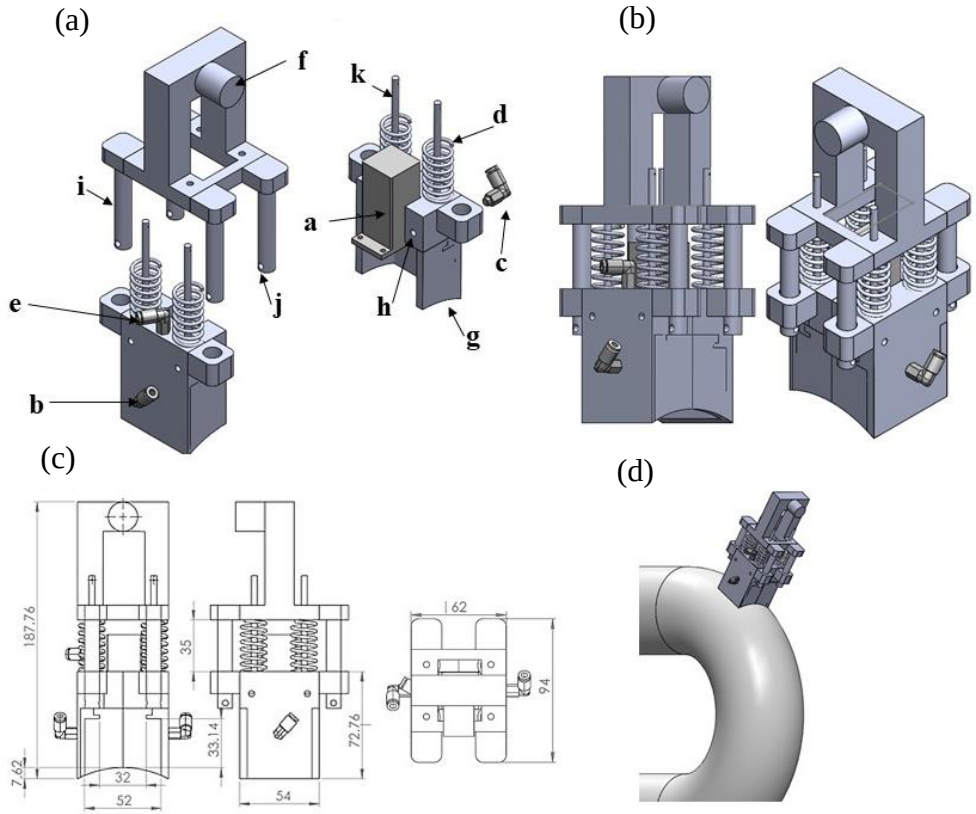

Figure 6-18: (a) Exploded view of the wedge design; (b) 3D CAD model; (c) 2D schematic; (d) probe holder placement on the chain surface

Figure 6-18(a) illustrates the main components of the probe holder/continuous water supply wedge, *i.e.* a – NDT probe, b – water inlet 1, c – water inlet 2, d – spring, e – excess water outlet, f – robotic manipulator mount, g – curved edge, h – wedge tightening (clamping) screw holes, i – carbon fibre wedge-holding bars, j – locking nut, and k – spring guiding bars. Moreover, the wedge was designed to hold the water path during the inspection. Water bubbles in the water pocket could disrupt the sound path. Therefore, two continuous water supplies were added to the design with an overflow outlet to avoid any water bubbles, as illustrated in the figure, *i.e.* if a water bubble started to form underneath the probe, the signals might not transmit. Due to the rough and robust surface nature of

mooring chains, a marine-grade silicon layer was proposed for the contact surface of the wedge (as the wedge–chain contact layer). Surface adaptation of the silicon gasket was considered in order to reduce the water leakage (water leakage from the chain–wedge contact surface), *i.e.* the compression capability of the silicon gasket was proposed to act as a water seal. The curved face of the wedge was introduced to reduce the thickness of the gasket and increase the adaptability to the chain curvature. Moreover, the curvature of the wedge was designed according to the chain's surface curvature (see Figure 6-18(d)). Using an automated manipulator for chain inspection was one of the main purposes of this study. Therefore, a passive complaint mechanism (spring mechanism) was added between the robotic manipulator mount and the end of the wedge. The force created by the compression of springs allowed the silicon gasket to settle on the chain surface and the passive compliance corrected small nominal deviations of the wedge, *i.e.* at a given point, it is essential to maintain the position of the probe nominal to the inspection surface.

6.7.3 Automated manipulator

A feasibility study for the use of phased array with a robotic arm to obtain NDT results (in the chain crown area) was the primary concern of this chapter. As mentioned previously, with the use of phased array, discreet inspection can be carried out along the chain surface. However, a pre-planned discreet placing of the probe must be made in order to conduct a full crown inspection, *i.e.* a raster scan along the chain crown. When considering ultrasound probe locations (on a mooring chain crown), as explained in [119], it is significant that a raster scan along the chain crown is needed for better investigation (as illustrated in Figure 6-19). The gap between the two scanning points must be determined according to the scanning requirement, *i.e.* closer gaps between two spot scans can ensure a comprehensive result. Scanning across the chain surface was limited due to the orthogonal chain link. A sample single-chain piece was used in this experiment, but an orthogonal chain link is always presented in in-situ chain environments.

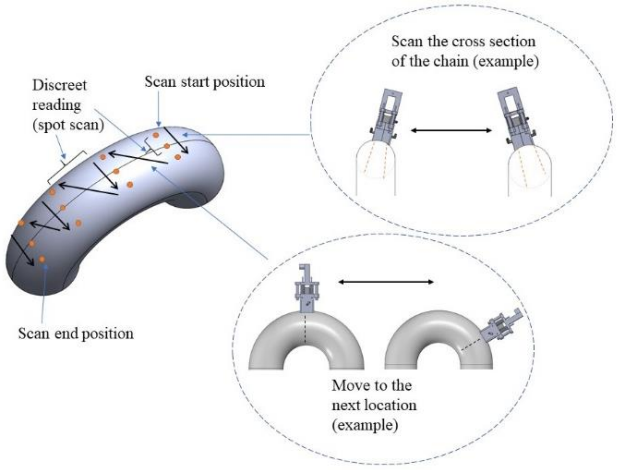

Figure 6-19: Proposed mooring chain scanning steps (for an automated manipulator)

The automated/robotic manipulator design was carried out according to the wedge placing requirements. When considering the wedge orientation (see Figure 6-20), 5DOF can be observed, *i.e.* to scan the cross-section, translations around the z axis and the y axis, and rotation around the x axis is needed (see Figure 6-20(a)). For a scan along the crown of the chain, translations in the x axis and the y axis, and rotation along the z axis are needed, as illustrated in Figure 6-20(b). In summary, three translations (along x, y, and z) and two rotations (around x and z) are needed for chain crown raster investigation. When considering the geometrical features of the manipulator requirements, x, y, and z translations can be modelled with a Cartesian (gantry-type) manipulator that has a two-axis wrist that carries the tool frame (wedge). After considering the requirements, a robotic manipulator, illustrated in Figure 6-21, was proposed, where L1–L8 are mechanical attachment clearances, d1, d2, and d3 are the linear axis variables in the z, x, and y directions, respectively, and Ø1 and Ø2 are the rotary axis variables in the z axis and x axis, respectively.

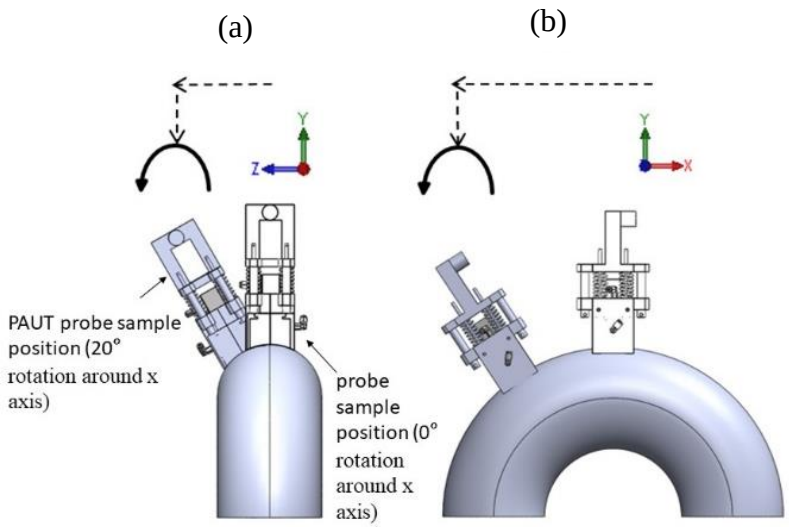

Figure 6-20: (a) Chain cross-section scan requirements; (b) chain scan along the crown requirements

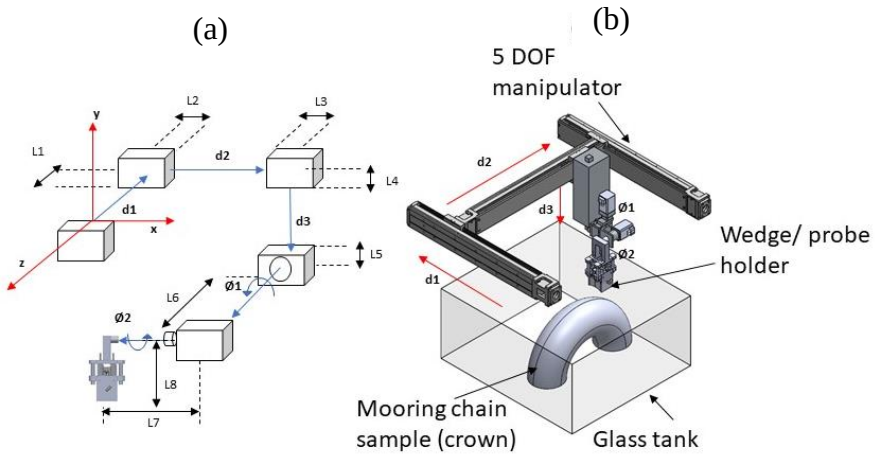

Figure 6-21: (a) Schematic of the proposed manipulator; (b) CAD model of the proposed manipulator

6.7.4 Prototype of the experimental setup

It was necessary to select an appropriate set of springs to provide a suitable force (illustrated in Figure 6-18(a)). Therefore, a simple experiment was carried out, as illustrated in Figure 6-22. The mooring chain sample was placed on material testing equipment that had a static load cell. Then, a perpendicular force was added to the wedge (sample wedge without the manipulator attachment), as illustrated by the red arrow in the figure (*i.e.* incremental force was applied to the wedge). Once the NDT results were clear, the corresponding force was recorded. The experiment was repeated ten times and the average reading was considered (ten readings for each place). The wedge was moved along the chain surface and the readings were recorded. According to the experimental results, 8N–13N force should be supplied by the springs, *i.e.* the applied force deforms the silicon gasket to make the wedge on the chain surface watertight. Four compression springs (0.72N/mm each) were added to the system to provide the required force. A 13N force was obtained by compressing each spring by ≈ 4.6mm.

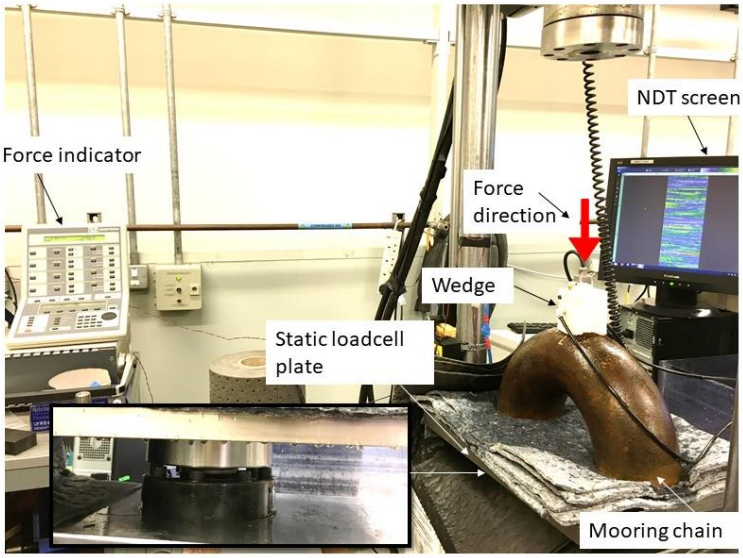

Figure 6-22: Spring force requirement test rig

To test the proposed 'continuous water supply wedge', a rapid prototype model was built, as illustrated in Figure 6-23. To place the PAUT probe, the water pocket area of the wedge was split into two main parts, as illustrated in Figure 6-23(a). The pocket was closed and tightened after placing the probe on the holding edges. The manipulator attachment was built as a separate module (see Figure 6-23(b)), then inserted into the wedge with the use of carbon fibre rods – locking nuts, as illustrated in Figure 6-23(c). Finally, the springs and the silicon gasket, illustrated in Figure 6-23(d), were added to the system.

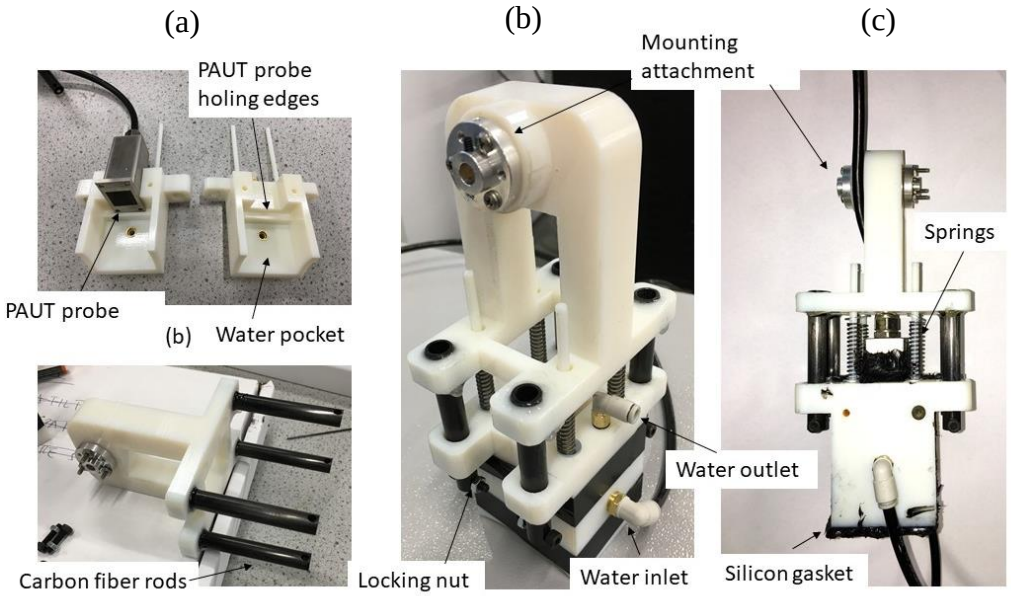

Figure 6-23: Prototype of the continuous water supply wedge; (a) water pocket and PAUT probe; (b) manipulator attachment; (c) and (d) prototyped wedge

The automated manipulator proposed in Figure 6-21 was prototyped and the wedge was attached, as illustrated in Figure 6-24. The x, y, and z linear axes were made with linear slider actuators – lead screw model (see Figure 6-23(d)), and each axis was driven with a DC 24V stepper motor. Hard rubber stoppers and magnetic limit switches were added to the linear axis to prevent slider collisions during the experiments.

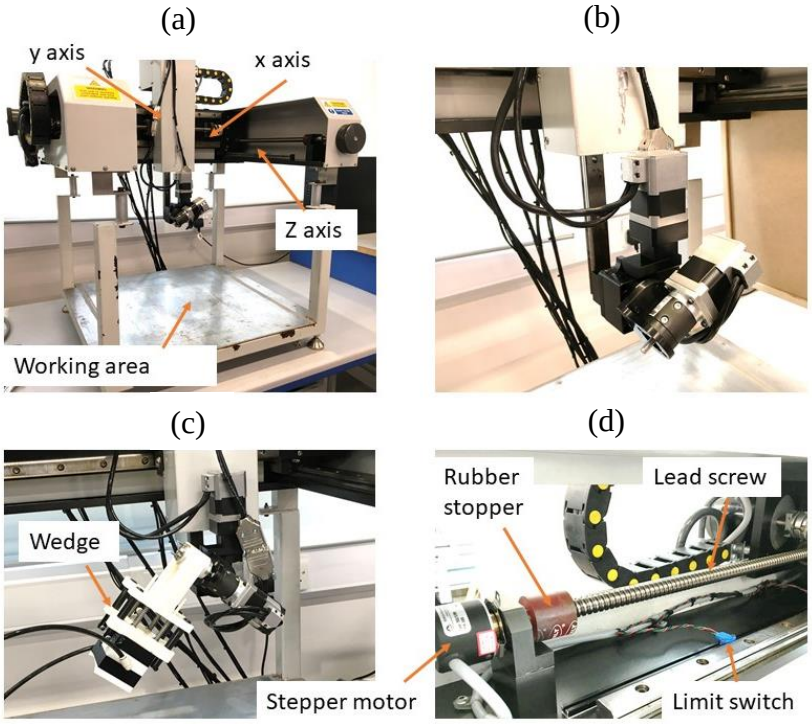

Figure 6-24: Automated 5DOF manipulator; (a) five-axis manipulator test rig; (b) two rotary axis closer view; (c) wedge attachment; (d) axis components

The experimental setup illustrated in Figure 6-25(a) was created according to the block diagram illustrated in Figure 6-25(b). As discussed previously (see Figure 6-18(a)), two water inputs were added to the wedge at the prototyping stage. Therefore, two IP 68 12V DC water pumps (300l/h each) were attached to the wedge with the use of a pneumatic push-fit connection. A five-axis controller was programmed using GalilTools™ [143] and this was connected to the controller via an ethernet connection. Similarly, the PAUT array was controlled by a MicroPulse™ array controller [144] and relevant commands were generated on a sperate processing unit (TWI PAUT processing unit/software CRYSTAL™ [142]). In this experiment, control of the NDT system and the manipulator system was carried out separately, *i.e.* no feedback data/signals were exchanged between systems.

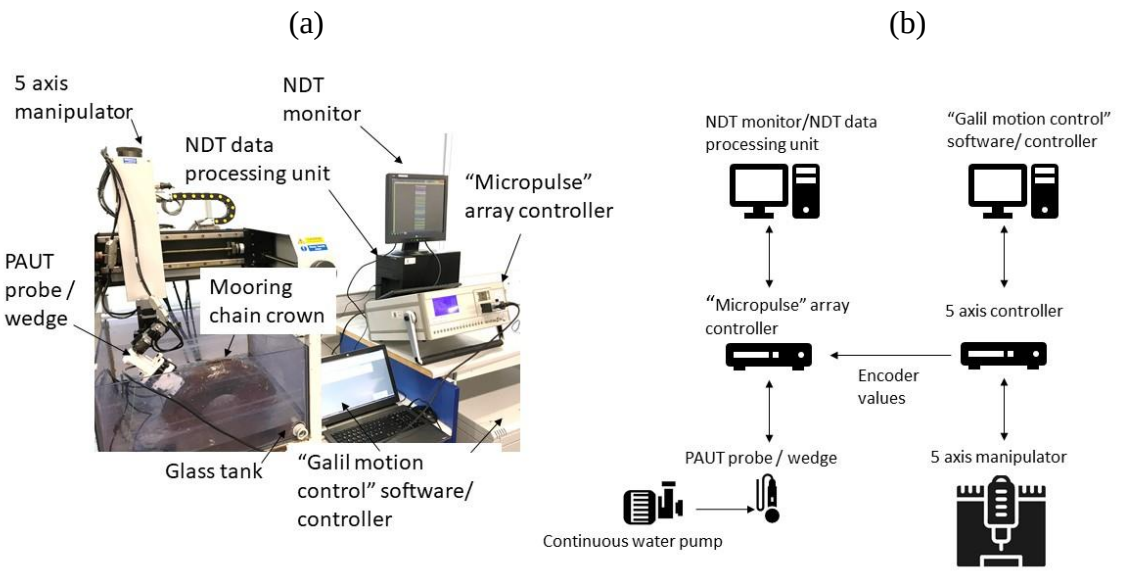

Figure 6-25: (a) Physical experimental setup; (b) experimental setup block diagram

As illustrated in Figure 6-25(b), GalilTools motion control software was used to programme the inspection path proposed in Figure 6-19. To execute the inspection, the tool frame (the PAUT probe and the wedge) was moved along the chain surface and the encoder readings of the five axes were recorded. The distances/angles for the two example inspection points are illustrated in Figure 6-26: Figure 6-26(a–b) illustrates the axis variations at two inspection points along the chain and Figure 6-26(c–d) shows the axis variation during the cross-section inspection. In Figure 6-26, the A, C, and B axes represent the x, y, and z Cartesian axes (in Figure 6-21), respectively. Rotation along the x axis is represented by the D axis and rotation around z is represented by the E axis. Moreover, each inspection point was represented by five encoder values (*i.e.* three distances, two angles) and the values were stored in the control software to execute the inspection path. As mentioned previously, air bubbles in the water chamber prevents a clear result. Therefore, a 15s delay was introduced before reading the data from the NDT display.

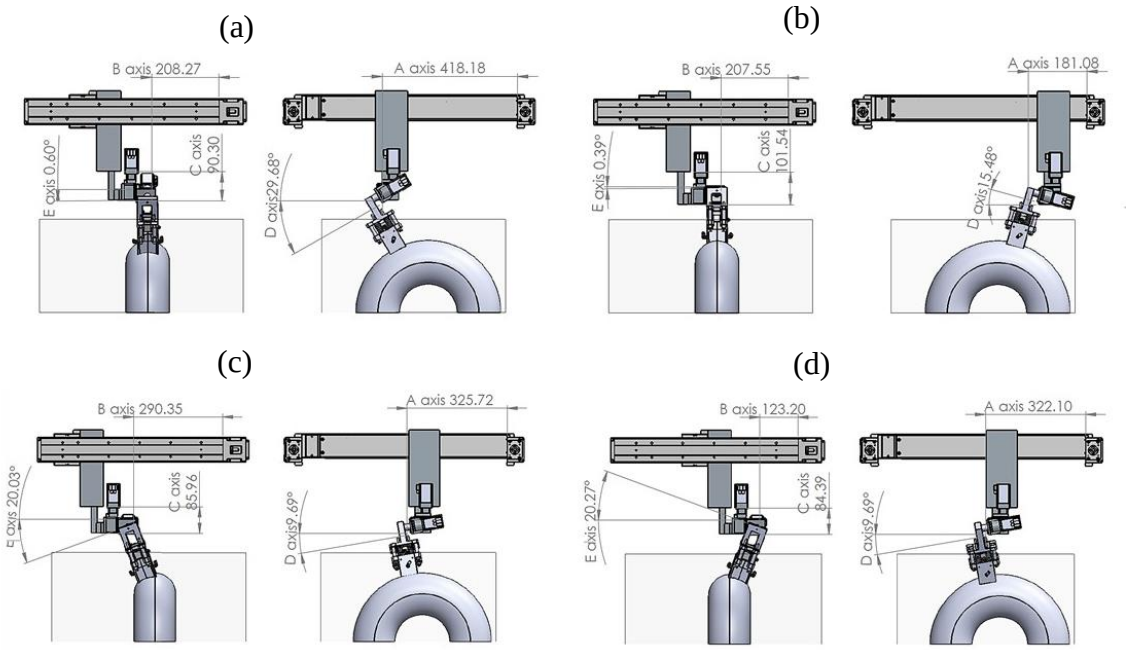

Figure 6-26: Inspection point examples; (a) inspection along the chain crown point example point 1; (b) inspection along the chain crown point example point 2; (c) inspection across the chain cross-section example 1; (d) inspection across the chain cross-section example 2.

6.8 Experimental results

The automated experimental setup proposed in Figure 6-25 was built in order to test the FMC phased-array inspection. A chain crown with a diameter of ≈ 133mm was used in this experiment. Four defects (*i.e.* drill hole/flat bottom) were introduced to the inner surface of the chain, as illustrated in Figure 6-27. Defects 1 and 3 were placed perpendicular, and 2 and 4 were placed 20° from the perpendicular position, as illustrated in Figure 6-27(b). Defects with a ≈ 5mm diameter were introduced, and the defect lengths are discussed with the results.

The phased-array inspection was carried out via the outer surface of the crown by placing the continuous water supply wedge using the automated manipulator. The phased-array FMC results were obtained using the TWI CRYSTAL^{TM} software [142]. A raster scan, proposed in Figure 6-26, was carried out with the automated 5DOF manipulator, as illustrated in Figure 6-28: Figure 6-28(a) illustrates examples of the cross-section inspection and Figure 6-28(b) illustrates inspections along the chain crown.

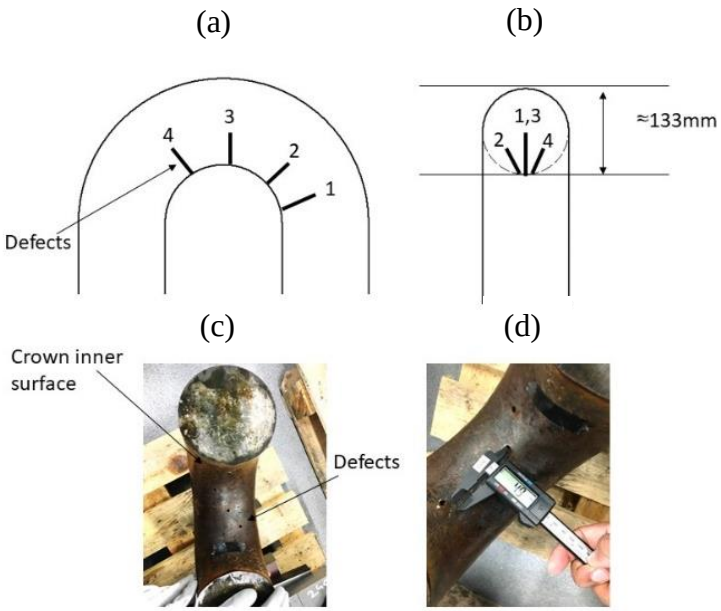

Figure 6-27: (a) Drill hole defects in chain crown (side view); (b) drill hole defects in chain crown (cross-sectional view); (c) defects image; (d) defect hole diameter (sample)

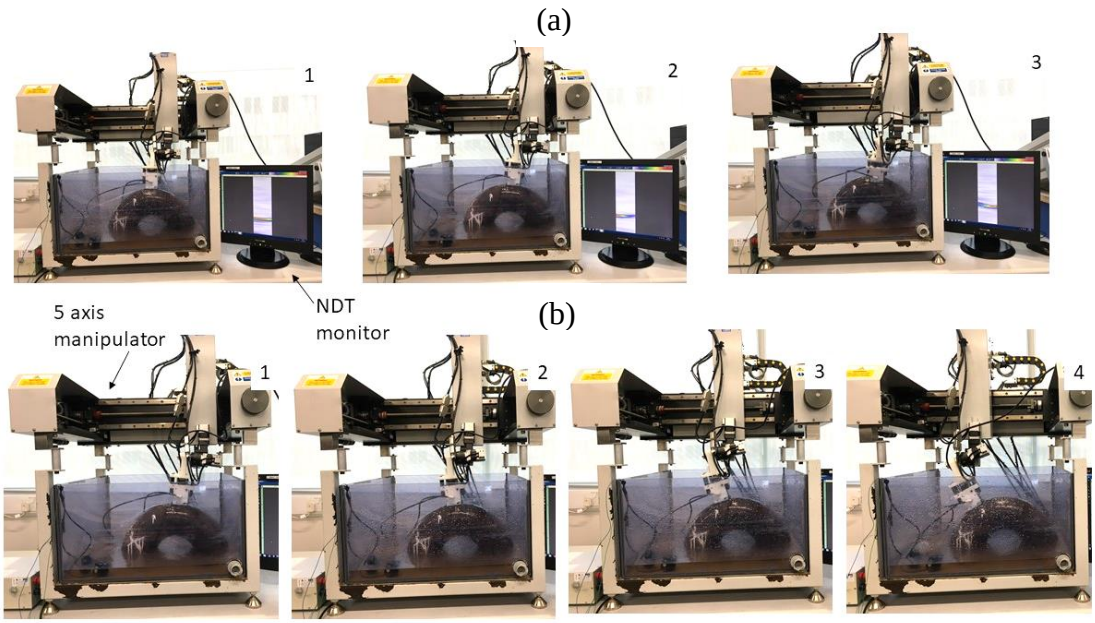

Figure 6-28: (a) Inspection example – cross-section of the chain; (b) inspection example – across the chain crown surface

According to the mooring chain inspection standards, it is crucial to check the material losses in chain interlink contact zone; therefore, the back-wall thickness was investigated, as illustrated in Figure 6-29(a). The recorded FMC images of the defects (see Figure 6-27) are illustrated in Figure 6-29(b–e), *i.e.* the back wall of the chain (inner crown surface) and the defect height are presented. With the proposed NDT imaging technique, the depth of the defect could be measured and the distances between the top of the defect and the back wall are shown in the images. The results presented in Figure 6-29 were recorded during the in-air inspection, and the defect depth results were compared (see Figure 6-30) with the underwater inspection results (taken without the wedge) and measured depth values (mechanical measurement using a calliper).

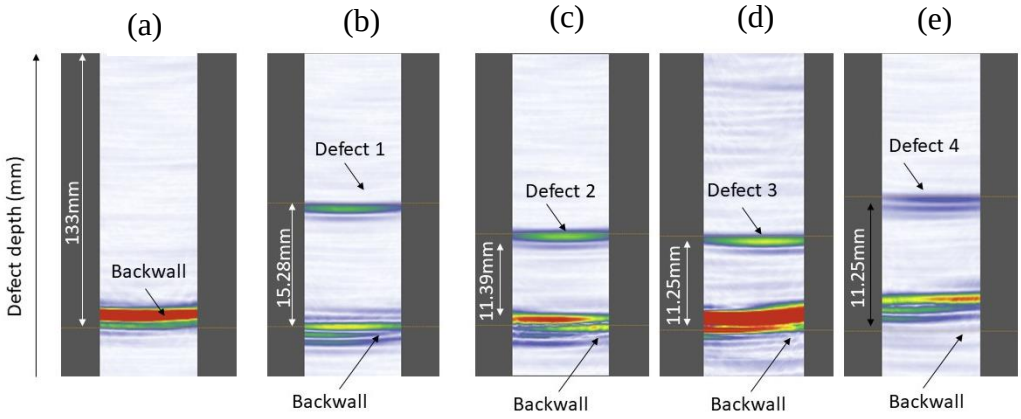

Figure 6-29: (a) Sample back wall (no defect); (b) defect 1 scan results; (c) defect 2 scan results; (d) defect 3 scan results; (e) defect 4 scan results

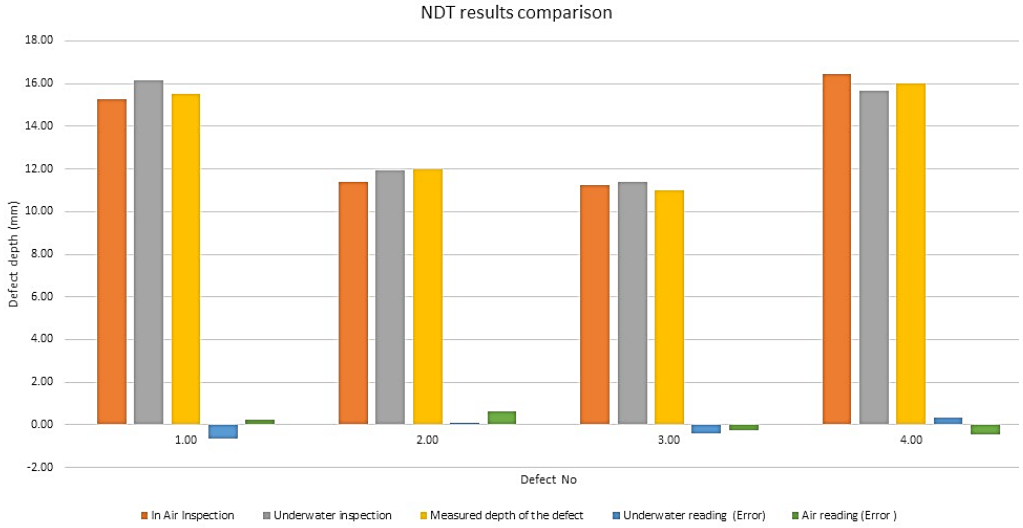

Figure 6-30: NDT results comparison

According to the comparison illustrated in Figure 6-30, it is significant that the proposed technique was capable of identifying a defect (illustrated in Figure 6-27(c)). Defect sizing was not a part of this study. However, the depth of the defect (height between the top of the defect and the back wall of the chain) could be measured with the presented technique. The recorded in-air results (with the use of the continuous water supply wedge) and the measured depth results (mechanical measurement) had a less error variation and the maximum variation was 0.61mm (≈ 5% difference). When considering the underwater results and the mechanical depth reading of the defect, it is possible to conclude that the proposed technique is able to operate both in air and underwater. Due to the amphibious nature of mooring chains, it was essential to develop a technique that could be automated and capable of operating in air and underwater. Moreover, the proposed technique could be used to evaluate material losses in the chain by measuring the through thickness of the chain diameter, as illustrated in Figure 6-29(a). If there is a material loss, the back-wall reading should be less than the expected value.

6.9 Visual inspection proposed technique

According to the mooring chain in-situ inspection standards, it is essential to obtain an image of the chain (during inspection). Therefore, a teleoperated camera was proposed for the climbing robot, described in Chapter 5. A teleoperated mechanism was proposed so that the operator could direct/focus the camera according to the inspection necessity. Visual inspection has been discussed in various robotic applications, *i.e.* a climbing robot with visual inspection [145], an underwater robot with visual inspection [146] etc. To demonstrate the principle of visual inspection, a camera mechanism was added to the climbing robot, as illustrated in Figure 6-31(a). The pan/tilt operation of the visual inspection system was controlled using LabVIEW (see Figure 6-31(b)). The images taken during the laboratory experiments are illustrated in Figure 6-31(d). These images were obtained in laboratory conditions, *i.e.* in air, under excellent ambient lighting.

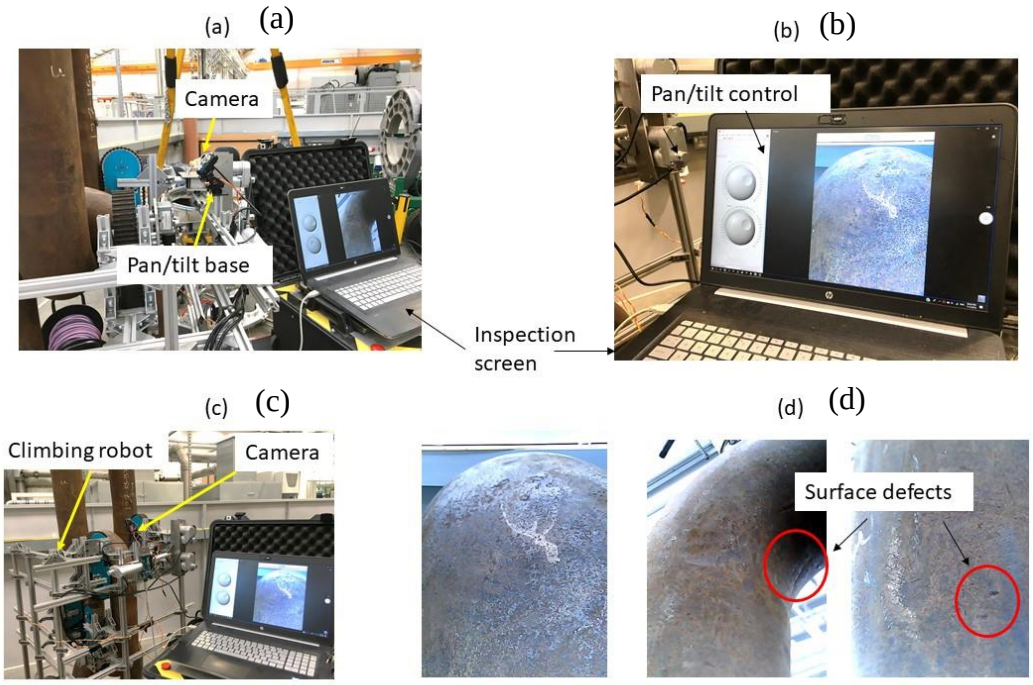

Figure 6-31: (a) Pan and tilt system with camera; (b) camera module control screen; (c) visual inspection module with robot; (d) sample images from visual inspection

6.10 Chapter summary

Mooring chain inspection is crucial when considering the integrity management of floating production units. However, only a few automated attempts have been tested due to the in-situ mooring chain complexities, *i.e.* difficult to reach, harsh environmental conditions etc. The use of sophisticated integrity management techniques, such as ultrasound inspection, guided-wave inspection etc., were comparatively less due to the lack of reachability. The weld area of the chain can be seen as the most studied inspection area. However, with new studies, the chain crown has become a crucial section that must be inspected for cracks, defects, material losses, and corrosion. Chain crown inspection is challenging due to the limited access and complicated geometry. The aim of this study was to investigate a technique that could be used in air and underwater for chain crown inspection. The automation of mooring chain integrity management was the main interest of this research; therefore, the inspection technique was selected carefully, *i.e.* automation capability was considered during the selection process.

Ultrasound inspection was selected due to the inspection depth, amphibious nature, and automated capability. Phased-array ultrasound was considered in order to ease the automation, *i.e.* discreet inspection capability is obtained with phased array. Mooring chain integrity assessment with phased array is still in its infancy due to the operational

complexity and geometrical features of the chain. Therefore, a feasibility study of novel NDT application was carried out. The FMC data acquisition technique was used in the interest of enhancing the quality of the NDT images. Mooring integrity inspection must be conducted both in air and underwater. Therefore, a continuous water supply wedge was designed to provide an underwater coupling environment in air. A five-axis automated manipulator was designed to simulate the automated inspection capability. The proposed phased-array automated inspection mechanism was tested with simulated defects, *e.g.* drill-hole-type defects. The NDT results were obtained during the in-air automated inspection and the defects were recorded. Finally, a pan/tilt camera mechanism was proposed for the magnetic adhesion tracked-wheel crawler as a conceptual idea of visual inspection, *i.e.* visual inspection is considered an inspection requirement in the standards.

In this study, a novel application of FMC/phased array was proposed for chain crown inspection and a laboratory experiment was carried out using an automated manipulator. According to the obtained results, the proposed automation-friendly technique is suitable for chain inspection.

Chapter 7: Conclusions and recommendations for future work

7.1 Conclusions

7.1.1 Research Summary

Integrity assessment of offshore floating platforms needs to be addressed by providing in-situ physical access to the mooring systems as the removal and transportation of chain links for inspection/repair is not practical. Most reliable integrity assessment methods, such as ultrasound testing, guided-wave inspection, mechanical measurements etc., require physical access to the chain to assess the structural health in in-situ conditions. Trained NDT divers and ROV inspections are the most common industrial mooring inspection methods. These methods raise health and safety concerns and diver inspection is very hazardous when inspecting a chain in the splash zone area. Using ROVs is expensive and access to the chain is limited. Removing and replacing mooring chains for inspection is a costly and unreliable method due to harsh operational conditions. Introducing an automated or teleoperated platform that can carry suitable NDT tools along in-service chain lines will help to enhance the integrity management of mooring chains in in-situ conditions. The development of chain-climbing robots is still in its infancy due to the complicated climbing structure presented by mooring chains. The current state-of-the-art automated systems are designed to investigate only the weld seam of a chain link. At TWI Cambridge, research was carried out to understand the stresses between mooring chain links and potential fatigue damage. In the previous automated studies, the primary concern was to investigate the weld seam of the chain. According to recent findings, chain crown inspection is also identified as crucial. The research presented in this thesis has achieved significant advances towards offshore mooring integrity management by introducing a novel climbing technique and a novel automated chain inspection application.

A summary of the thesis, an introduction to the subject, industrial needs, the contribution to the knowledge, and the organisation of this thesis were documented in Chapter 1. Chapter 2 familiarised the reader with the state-of-the-art chain-climbing techniques, design requirements, commonly used climbing techniques, and adhesion principles.

Chapter 3 was the first technical chapter of this thesis. The design of the lightweight, L-shaped tracked-wheel robot that could be placed easily around a mooring chain was discussed in this chapter. The robot adheres to a chain using a permanent magnet system. Permanent magnetic adhesion was selected due to the mooring chain's physical conditions and the in-situ environment. The neodymium permanent magnet (*i.e.* N 52) adhesion

module was optimised using the FEA software COMSOL Multiphysics to obtain the required adhesion force (*i.e.* 219.16N per unit). Structural analysis was conducted, and designs were created using CAD software (Autodesk Inventor, SolidWorks) and FEA software (COMSOL) to develop a robust structure. As discussed in Chapter 4, a lightweight (*i.e.* ≈ 20kg), fast-moving mooring-chain-climbing robot system that can be quickly deployed and retrieved was prototyped. Moreover, validation of the neodymium permanent magnet adhesion system was conducted. Finally, the robot system was tested in a laboratory on a three-link chain segment to study its climbing capability and stability. The permanent magnet adhesion crawler robot developed can climb mooring chains at a speed of 42cm/minute with a pay load of 50N (see Figure 7-1). **In conclusion, the feasibility of using a crawler with an orthogonal arrangement of tracked wheels to climb vertically aligned mooring chains has been established (*i.e.* the first approach to using permanent magnetic adhesion tracked wheels to climb mooring chains).**

(a) (b)

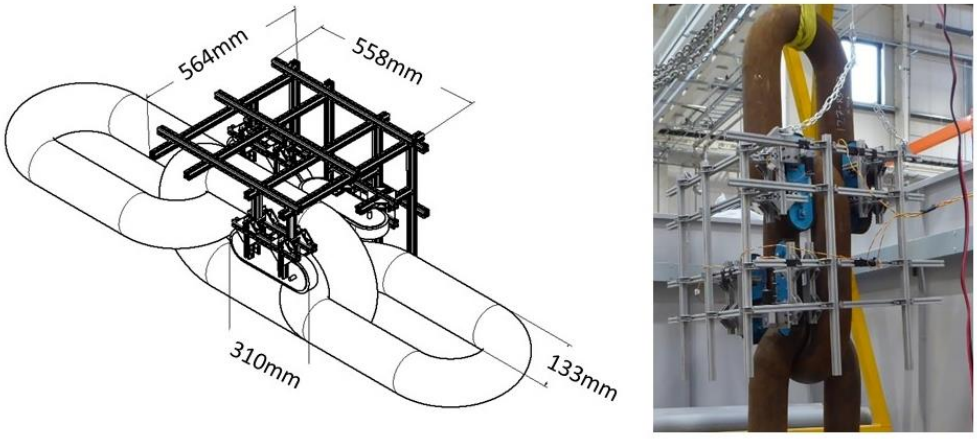

Figure 7-1: (a) Design of the first magnetic adhesion tracked-wheel crawler for chain climbing; (b) prototype of the crawler ***[D1]***

The first version of the climbing robot was unable to demonstrate climbing when a misalignment was present in the chain. Chapter 5 discussed the upgrade to the previously designed magnetic adhesion tracked-wheel mooring-chain-climbing robot (the robot discussed in Chapters 3 and 4) to address the misalignment issues of operational mooring chains. Two types of misalignment (chain twist and chain tilt) were studied and a mathematical model of a robot leg was proposed. Then, the proposed model was modified

according to the mechanical needs of the climbing robot. The prototyped robot leg was introduced to a single tracked-wheel module of the previous robot and experimental studies were carried out. The complete robot system was tested on a three-link mooring chain segment to study the climbing capability. For this study, 5–17° of link twist and 1–5° link tilt misalignments were introduced to the chain link and the robot was able to adapt the tracked-wheel unit by using the newly added Cartesian robot leg. The misalignment detection of the proposed robot was conducted by manual measurement and a numerical feasibility study was conducted to improve the robot by ensuring autonomous misalignment detection capabilities. Finally, a laboratory experiment was performed to validate the numerical modelling results. **As a result of this study, the idea of a legged magnetic adhesion tracked-wheel robotic platform that can eliminate concerns relating to misaligned mooring-chain-climbing has been established (see Figure 7-2).**

(a) (b) (c)

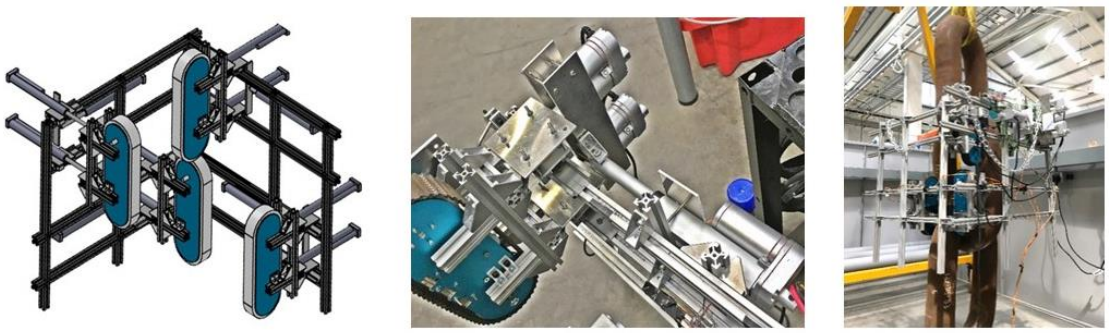

Figure 7-2: (a) Design of the adaptable legged chain-climbing robot; (b) prototype of a leg; (c) prototype of the robot

An amphibious automated NDT technique that can be used to assess the structural health of mooring chains was discussed in Chapter 6. The FMC technique was adapted according to the mooring chain's curved surface. In order to adapt, three surface-mapping techniques were evaluated in this research and a suitable technique was selected. In-service ultrasound inspection of the chain crown is not a state-of-the-art inspection procedure due to operational difficulty. Ultrasound inspection of the chain weld area is mandatory and is standard practice; however, according to recent investigations, the chain crown has also been identified as a crucial area for inspection. Ultrasound inspection was selected due to the inspection depth, amphibious nature, and automated capability. Phased-array ultrasound was considered in order to ease the automation, *i.e.* discreet inspection

capability is obtained with phased array. Mooring chain integrity assessment with phased array is still in its infancy due to the in-field operational complexities and geometrical features of the chain. Therefore, the research in this chapter was carried out as a feasibility study of a novel NDT application. The FMC data-acquisition technique was used in the interest of enhancing the quality of the NDT images. A continuous water supply wedge was designed to provide a marine coupling environment in air. A five-axis automated manipulator was designed to simulate the automated inspection capability. The proposed phased-array automated inspection mechanism was tested with simulated defects, *i.e.* drilled-hole-type defects. In this study, a novel application of FMC/phased array was demonstrated for chain crown inspection and laboratory experiments were carried out with the use of an automated manipulator**. According to the results, the proposed**

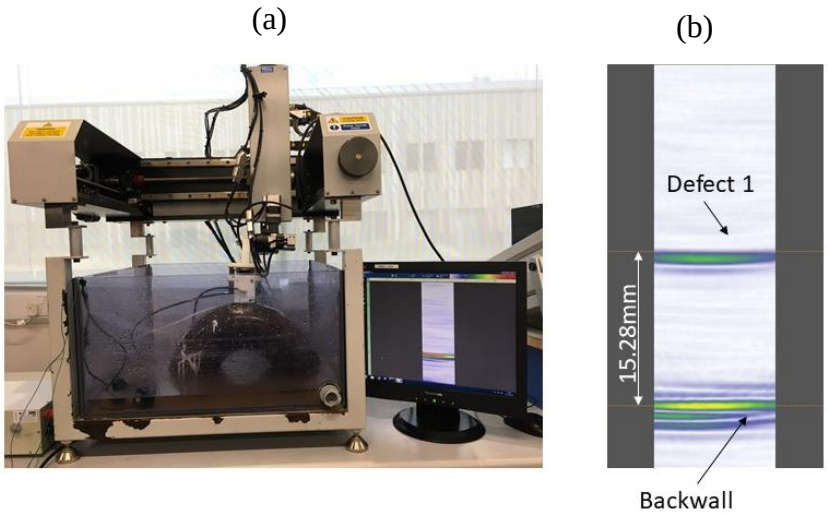

Figure 7-3: (a) Design of the automated inspection test rig; (b) sample FMC test results

automation-friendly technique is suitable for chain crown ultrasound inspection (see Figure 7-3).

The research presented in this thesis aimed to enhance the automated capability of offshore mooring integrity assessment. From this thesis, a significant amount of knowledge has been added to the field of automated mooring chain climbing and automated mooring chain inspection. However, further studies and improvements are required to enhance the performance and quality of the proposed techniques.

7.1.2 Research Conclusion

The focus of this research was to mitigate the challenges set out by the traditional mooring inspection techniques. Two research gaps were identified in the beginning of this research. (*i.e.* requirement of a mooring chain climbing platform and automated mooring chain crown inspection). Therefore, two main aims were considered. 1) development of a light weight, fast, easily deployable chain climbing robot which is applicable for both air and underwater. 2) development of an automated chain crown inspection mechanism which is applicable for the use of both air and underwater.

The first goal of the research was achieved by developing a magnetic adhesion orthogonal tracked wheel climber. The robot was tested in a laboratory environment. A straight chain links was used in this experiment and the concept was proofed. An adaptable Cartesian mechanism was developed in order to cope up with misalignments. As a result of that, a light weight, fast moving robotic platform was developed and presented.

The second aim was achieved by developing an automated chain crown inspection mechanism. Phased array inspection mechanism along with the FMC data acquisition techniques were used for this inspection. A continuous water supply wedge and a 5DOF robotic manipulator were used in order to demonstrate the concept. With the above-mentioned experiment, a successful technique was presented for chain crown inspection.

In conclusion, the research which was presented in this thesis was able to enhance the integrity management of mooring chains by introducing a new robotic chain climbing platform and a crown inspection method.

7.2 Further work

7.2.1 Vertically aligned chain-climbing robot

A straight mooring chain was used for part of this research. In practice, chains may have a catenary curvature. The current robot design should be modified to overcome misalignments in chain links that are caused by the catenary curvature. Future work should aim to introduce an active control mechanism that can correct the robot when it starts to slip due to mooring chain surface issues, change its path due to external forces, or climb links that are twisted relative to each other. Both the in-air and underwater sections of a mooring chain need to be inspected. Therefore, the robot should be able to travel

underwater. It will be necessary to marinise the motors and controllers and set up underwater laboratory trials.

7.2.2 Adaptable chain-climbing robot

A single leg was modelled and added to the robot to simulate misalignment. However, the introduction of multi-legged robotic locomotion will be the main improvement based on this study (see Figure 7-2(a)). The robot adhesion module was capable of carrying the modified leg (due to the additional adhesion capability). However, in order to prototype the fully functional system, a higher adhesion force is required. A significant improvement to the adhesion force could be achieved with longer tracked-wheel units and extended magnet modules (as illustrated in Figure 7-4).

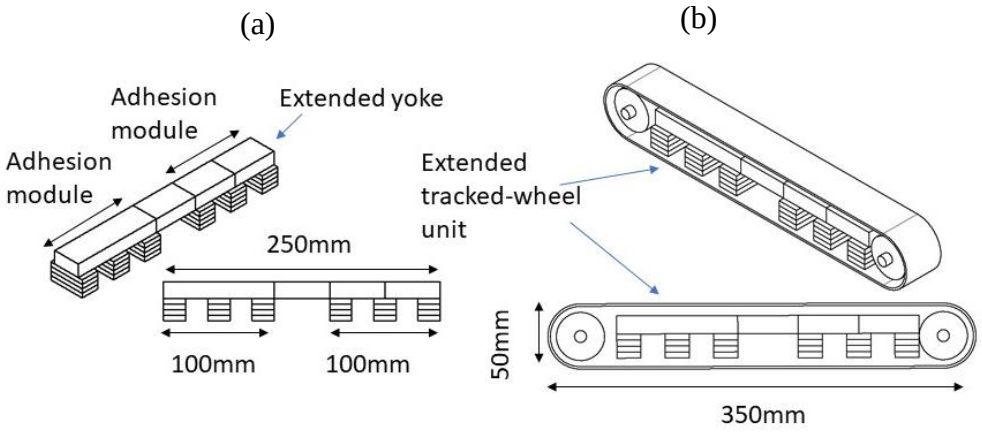

Figure 7-4: (a) Extended adhesion module; (b) extended tracked-wheel unit

A stationary simulation was conducted in COMSOL Multiphysics with the use of the MFNC module as a feasibility study for the extended idea. A free tetrahedral mesh was created with a maximum element size of 10mm and a minimum element size of 0.1mm. The data presented in Table 3-3 was used in the numerical modelling. The CAD model in Figure 7-5(a) was designed and a simulation was carried out by moving the positions along the chain. A ≈ 1,000N force was produced by the extended magnet (N52, neodymium) arrangement (see Figure 7-5(b). With these results, it is possible to conclude that the extended tracked-wheel idea will enable additional payload capacity for further development, *i.e.* the payload capacity depends on the industrial design and component of the robot.

(a) (b)

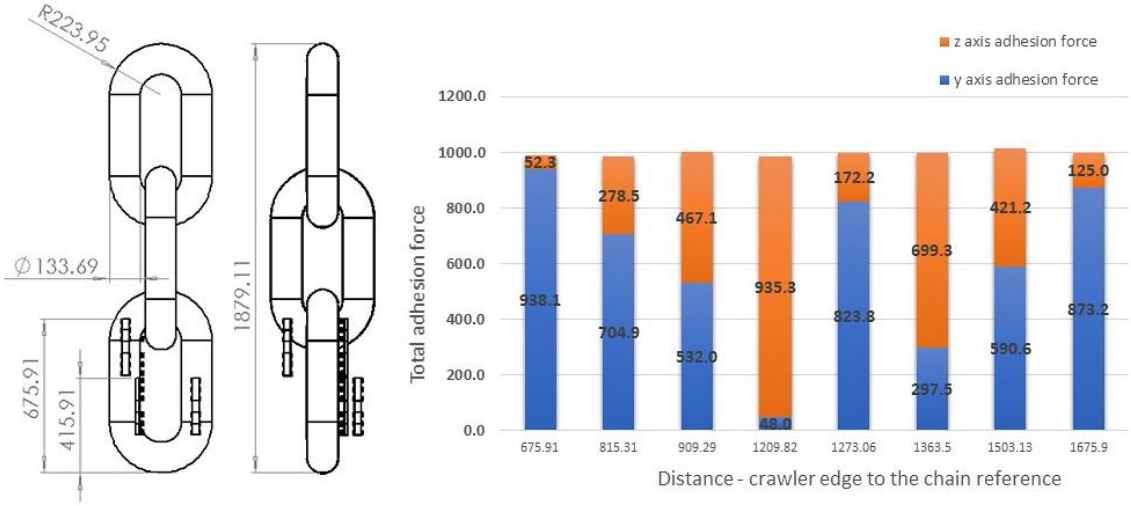

Figure 7-5: (a) COMSOL layout – simulation reference position (2D schematic); (b) recorded total adhesion force

In the current robot, misalignment angles were added to the system manually. A feasibility study was conducted with the use of ultrasound to detect misalignment, as discussed at the end of Chapter 5. Further work should be carried out to automate the misalignment angle detection system and integrate with the climbing robot.

7.2.3 Automated inspection mechanism

The research presented in Chapter 6 was conducted as a feasibility study, and further work should be carried out to develop a fully functional industrial chain inspection mechanism. Currently, defects are displayed, but a comprehensive defect-identification algorithm (*i.e.* cracks, corrosion, holes etc.) needs to be implemented. A phased-array controller and the NDT system were used under laboratory conditions; therefore, the physical size should be minimised for integration with a climbing robot. The robotic manipulator prototyped in the research was designed for laboratory-based experiments (*i.e.* heavy stand, not suitable for in-situ mooring conditions); therefore, it should be upgraded (*i.e.* axis marinisation and ruggedisation) and miniaturised to be mounted on a climbing robot. The chain geometry was known in this research; however, in real applications, the geometry may differ. Therefore, an automated chain crown shape detection mechanism needs to be implemented. The experiments were carried out to evaluate the structural health condition of the crown, but the proposed technique could be evolved to investigate both the crown

and the weld at the same time. A single system that can inspect both the crown and the weld will help to enhance the industrial capabilities. When the size and weight of the NDT module is reduced as an extension of this work, it can be placed on the robot as illustrated in Figure 7-6 (b). However, other non-contact NDT techniques (*i.e.* laser distance measurement, high-quality imaging techniques etc., can be mounted as illustrated in Figure 7-6(a).

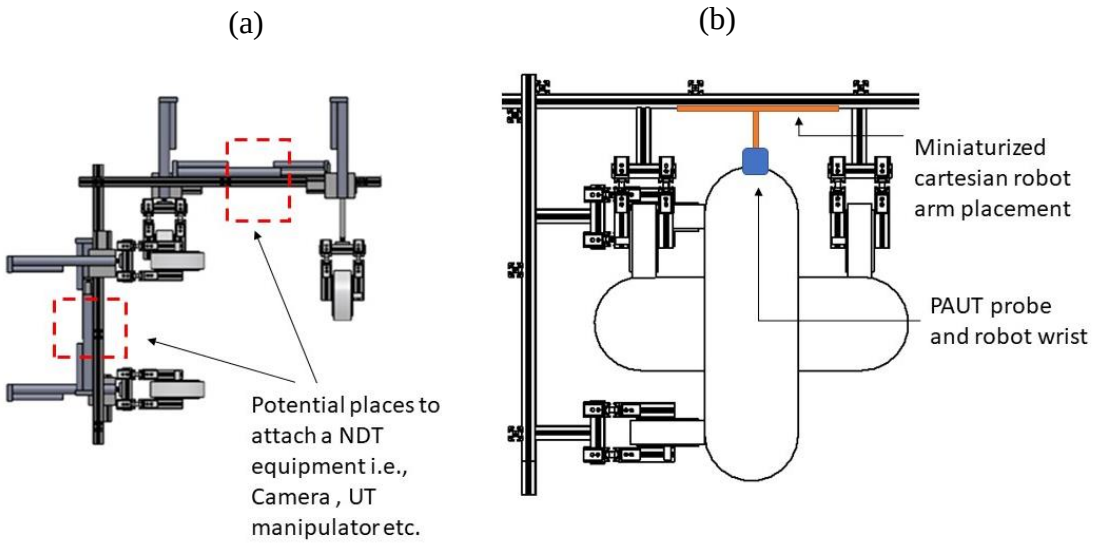

Figure 7-6: (a) Potential places to attach NDT equipment; (b) automated FMC manipulator placement

7.2.4 Industrial robotic system (as a product)

As mentioned in this thesis, mooring chain climbing is an industry-related task. Therefore, further work should be carried out to enhance the safety of the robot, *i.e.* according to the subsea FPSO safety regulations and codes of practice. A sophisticated user interface should be implemented in order to ease the robot's control. A sample control architecture is presented in Figure 7-7 and a sample operation concept is presented in Figure 7-8 for future development. An underwater umbilical power supply mechanism that adheres to the FPSO subsea practices should be added.

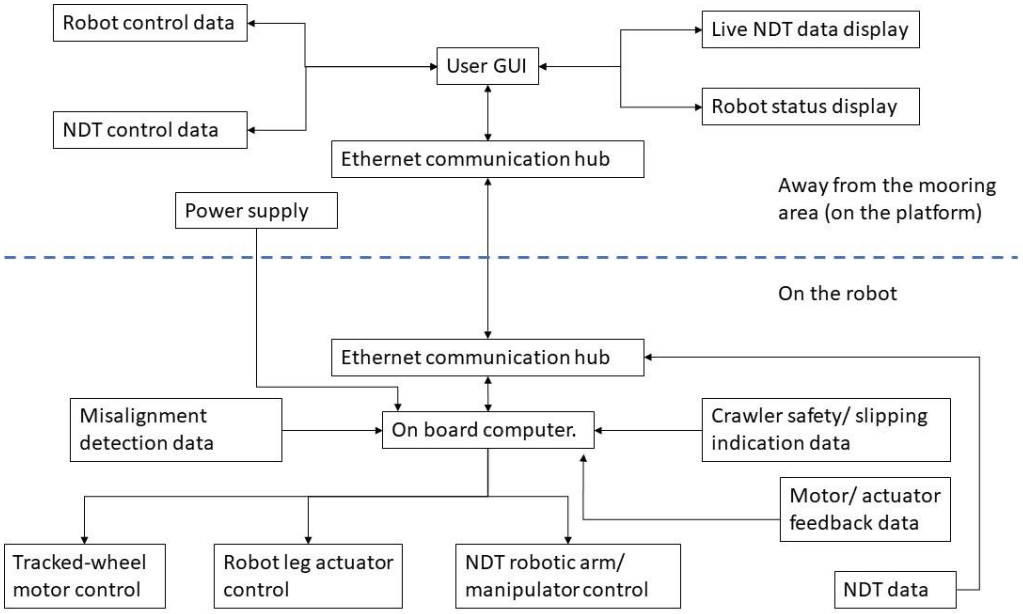

Figure 7-7: Proposed control architecture for an industrial mooring chain-climbing robot

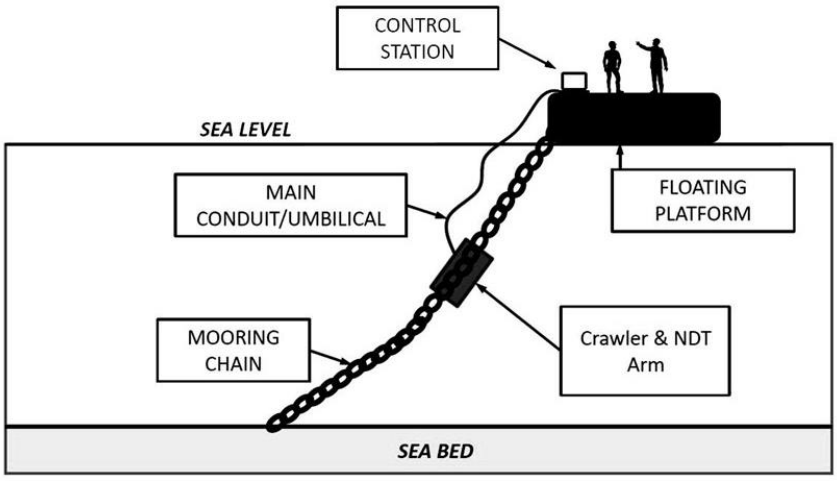

Figure 7-8: Proposed operational configuration of the chain-climbing robot

Chapter 8: References

[1] R. B. Gordon, M. G. Brown, E. M. Allen and DNV GL, "Mooring Integrity Management: A State-of-the-Art Review," in *Offshore Technology Conference*, Houston, Texas, 2014.

[2] P. Elman, . J. Bramande, . E. Elletson and K. Pinheiro, "Reducing Uncertainty Through the Use of Mooring Line Monitoring," in *Offshore Technology Conference*, Rio de Janeiro, Brazil, 2013.

[3] Kai-tung Ma, H. Shu, S. Philip and D. Arun , "A Historical Review on Integrity Issues of Permanent Mooring Systems," in *Offshore Technology Conference*, Houston, Texas, 2013.

[4] Á. Angulo, G. Edwards, S. Soua and T.-H. Gan, "Mooring Integrity Management: Novel Approaches Towards In Situ Monitoring," in *Structural Health Monitoring - Measurement Methods and Practical Applications*, Intechopen, 2017, pp. 87-108.

[5] Noble Denton Europe Limited, "Floating production system -JIP FPS mooring integrity," Health And Safety Executive, Aberdeen, 2016.

[6] A.-r.-p. 21, "in-service Inspection of mooring hardwear for floating strectures.," American Pertroleum Institute, 2008.

[7] I. Perez and B. Philippe, "Prediction of Residual Stresses in Mooring Chains and its Impact on Fatigue Life," in *ASME 2017 36th International Conference on Ocean, Offshore and Arctic Engineering*, 2017.

[8] P. Bastid and S. Simon, "Numerical Analysis of Contact Stresses Between Mooring Chain Links and Potential Consequences for Fatigue Damage," in *ASME 2013 32nd International Conference on Ocean, Offshore and Arctic Engineering*, Nantes, France, 2013.

[9] M. O. F. Howlader, "Development of a Wall Climbing Robot and Ground Penetrating Radar System for Non-Destructive Testing of Vertical Safety Critical

Concrete Structures," PhD thesis -London South Bank University , London , 2016.

[10] L. L. Menegaldo, M. Santos, G. Ferreira, R. Siqueira and L. Moscato, "SIRUS: A mobile robot for Floating Production Storage and Offloading (FPSO) ship hull inspection," in *10th IEEE International Workshop on Advanced Motion Control*, Trento, Italy, 2008.

[11] S. Jianzhong, B. Bryan, T. Sattar, Mondal, Shyamal and Brenner, Alina, "Development of a climbing robot for inspection of long weld lines," *Industrial Robot: An International Journal,* vol. 35, no. 3, pp. 217-223, 2008.

[12] Schempf, Hagen, Chemel, Brian and Everett, Nathan, "Neptune: above-ground storage tank inspection robot system," *IEEE Robotics & Automation Magazine,* vol. 2, no. 2, pp. 9-15, 1995.

[13] Sattar, Tariq , Leon Rodriguez and Bridge, Bryan, "Climbing ring robot for inspection of offshore wind turbines," *Industrial Robot: An International Journal,* vol. 36, no. 4, pp. 326-330, 2009.

[14] a. Kaur, B. Ma, M. Corsar, T. Sattar, A. Clarke, C. Forrest and I. Nicholson, "Risesure: Automated develpement of digital radiography for subsea inspection of flexible risers," in *IEEE 23rd International Conference on Emerging Technologies and Factory Automation*, Torino, Italy , 2018.

[15] Berns, K, Hillenbrand, C and Luksch, T, "Climbing robots for commercial applications--a survey," in *Proceedings of the 6th International Conference on Climbing and Walking Robots CLAWAR*, 2003.

[16] M. Armada, P. Santos, M. Jimenez and M. Prieto, "Application of Clawar Machines," *International Journal of Robotics Research,* vol. 22, no. 3, pp. 251-259, 2003.

[17] G. EDWARDS, "Periodic Report Summary - MOORINSPECT (Development of an Advanced Medium Range Ultrasonic Technique for Mooring Chains

Inspection in Water),” 29 05 2014. [Online]. Available: http://cordis.europa.eu/result/rcn/62360_en.html. [Accessed 20 September 2015].

[18] G. Edwards, T. Sattar, S. Kokkorikos, A. Garcia and C. Patton, “www.moorinspect.eu,” 2013. [Online]. Available: http://www.moorinspect.eu/publications/NDT2012MoorInspect_latest.pdf. [Accessed 21 December 2015].

[19] A. G. Ruiz, T. P. Sattar, . C. M. Sanz and B. S. Rodriguez-Filloy, “Inspection of floating platform mooring chain with a climbing robot,” in *17th International Conference on Climbing and Walking Robots and the Support Technologies for Mobile Machines*, Poznań, Poland, 2014.

[20] I. UK, “MoorInspect,” MoorInspect, [Online]. Available: http://www.innotecuk.com/moorinspect/#tabs2. [Accessed 1 12 2015].

[21] “Autonomous Robotic System for the Inspection of Mooring Chains that,” Project consortium.

[22] P. Weiss, F. Andritsos, F. Schom and A. Fidani, “Innovative Robotic Solutions for the Survey and Certification of Ships and Mobile Offshore Units,” in *COMPIT,* Siguenza, Spain, 2004.

[23] G. Alonso, F. Plaza, B. Carrillo, G. Ares and C. C. Suarez, “Automated Off-shore studless chain inspection system,” in *16th WCNDT 2004 - World Conference on NDT,* Montreal, Canada, 2004.

[24] . W. Stephen and T. L. , “Autonomous Robotic System for the Inspection of Mooring Chains that Tether Offshore Oil and Gas Structures to the Ocean Floor,” 14 March 2008. [Online]. Available: http://cordis.europa.eu/docs/publications/1216/121625181-6_en.pdf. [Accessed 10 December 2015].

[25] Hernandez, A, Altuzarra, O, Petuya, V , Pinto, Ch and Amezua, E, “A robot for non-destructive testing weld inspection of offshore mooring chains,” *International Journal of Advanced Robotic Systems,* vol. 15, no. 3, 2018.

[26] J. Flaig, “Tarzan-like inspection bot could protect lives and assets for oil and gas industry,” 04 May 2018. [Online]. Available: https://www.imeche.org/news/news-article/tarzan-like-inspection-bot-could-protect-lives-and-assets-for-oil-and-gas-industry. [Accessed 06 Sept 2018].

[27] “Robotic Inspection of Mooring Chains in Air and Water (RIMCAW),” EPSRC, 31 03 2018. [Online]. Available: http://gow.epsrc.ac.uk/NGBOViewGrant.aspx?GrantRef=EP/R00546X/1. [Accessed 08 08 2018].

[28] A. D. Hall, Welaptega Marine Limited and . G. M. Lethbridge, “Digital Imaging for Subsea Operations: Innovative ROV Tooling and Image Analysis Combinations for Mooring Chain Assessments Yield Cost Savings and Operational Confidence for Offshore Operators,” Aberdeen, Scotland, 1999.

[29] Welapetage, “http://www.welaptega.com/,” Welapetage, 2017. [Online]. Available: http://www.welaptega.com/services/subseameasurement/. [Accessed 25 06 2018].

[30] M. Yoshie and T. Toshinari , “Field test of a practical test model of maintenance examination system for mooring facilities and additional installation of chain grasping frame in the vehicle,” in *Underwater Technology Symposium (UT), IEEE International*, Tokyo, Japan, 2013.

[31] B. Philippe and . S. D. Simon , “Numerical Analysis of Contact Stresses Between Mooring Chain Links and Potential Consequences for Fatigue Damage,” in *ASME 2013 32nd International Conference on Ocean, Offshore and Arctic Engineering*, Nantes, France, 2013.

[32] E. Priscilla , B. Joseph and E. Edward and P. Karina, “Reducing Uncertainty Through The Use Of Mooring Line Monitoring,” in *Offshore Technology Conference*, Rio de Janeiro, Brazi, 2013.

[33] I Hobbs, RE and L Ridge, IM, “Torque in Mooring Chain. Part 1: Background and Theory,” *Journel of strain Analysis for Engineering Design,* vol. 40, no. 7, pp. 703-713, 2005.

[34] T. Moan, “Safety management of deep water station-keeping systems,” *Journal of Marine Science and Application,* vol. 8, no. 2, p. 83–92, 2009.

[35] A. L. Yaghin and . R. E. Melchers, “Long-term inter-link wear of model mooring chains,” *Marine Structures,* vol. 44, p. 61–84, 2015.

[36] R. E. Melchers, T. Moan and Z. Gao, “Corrosion of working chains continuously immersed in seawater,” *Journal of Marine Science and Technology,* vol. 12, no. 2, p. 102–110, 2007.

[37] J. Rosen, A. E. Potts and R. E. Melchers, “MIC and pitting corrosion on field recovered mooring chain links,” in *Australasian Corrosion Association,* 2014.

[38] Wei, Terence E and Quinn, Roger D and Ritzmann, Roy E, “A CLAWAR that benefits from abstracted cockroach locomotion principles,” in *Climbing and Walking Robots,* Springer, 2005, pp. 849--857.

[39] H. Chen , W. Sheng , Ning Xi and Jindong Tan, “Motion Control of a Micro Biped Robot for Nondestructive Structure Inspection,” *IEEE International Conference on Robotics and Automation,* pp. 478-483, 18-22 April 2005.

[40] Na Shun Bu He , Rong Liu, Wei Wang , Hao Yang and Xu Dong Wang, “A mini multi-joint wall climbing robot based on the vibrating suction method,” *Robotics and Biomimetics, 2007. ROBIO 2007. IEEE International Conference on,* pp. 1861 - 1865, 15-18 December 2007.

[41] A. Asbeck, S. Dastoor, A. Parness, L. Fullerton , N. Esparza, . D. Soto, . B. Heyneman and M. Cutkosky, “Climbing rough vertical surfaces with hierarchical directional adhesion,” in *Robotics and Automation, 2009. ICRA '09. IEEE International Conference* , Kobe, 2009.

[42] A. Sintov, T. Avramovich and A. Shapiro, “Design and motion planning of an autonomous climbing robot with claws,” *Robotics and Autonomous Systems,* vol. 59, no. 11, p. 1008–1019, 2011.

[43] W. Guo, . M. Zhong, Man-tian Li and Y. Li, "Design of a six legged wall-climbing robot," in *2008 IEEE Workshop on Advanced robotics and Its Social Impacts*, Taipei, 2008.

[44] G. Carlos, P. Manuel and A. Manuel and De Santos, P Gonzalez, "A six-legged climbing robot for high payloads," in *Control Applications, 1998. Proceedings of the 1998 IEEE International Conference*, Trieste, 1998.

[45] B. Paolo ,H.Michael , Li, Yasong and M. Carlo, "Optimal Gait for Bioinspired Climbing Robots Using Dry Adhesion ： A Quasi-Static Investigation," *Journal of bionics engineering,* vol. 10, no. 1, pp. 1-11, 2013.

[46] J. Xiao, H. Wang and N. Xi, "Intelligent control for wall climbing robot," in *Chinese Control and Decision Conference*, Guilin, 2009.

[47] L. P. Kalra, J. Gu and M. Meng, "A Wall Climbing Robot for Oil Tank Inspection," in *2006 IEEE International Conference on Robotics and Biomimetics*, Kunming, 2006.

[48] Z. Yi , . Y. Gong, Z. Wang and X. Wang, "Development of a wall climbing robot for ship rust removal," in *International Conference on Mechatronics and Automation,* Changchun, 2009.

[49] F. Rochat, P. Schoeneich, O. Truong-dat Nguyen and F. Mondada, "MINIATURE MAGNETIC CATERPILLAR CLIMBING ROBOT WITH PLANE TRANSITION ABILITY," *Robotica,* vol. 29, pp. 1075-1081, 2011.

[50] G. Lee, K. Seo, . S. Lee , J. Park , H. Kim , J. Kim and T. Seo, "Compliant track-wheeled climbing robot with transitioning ability and high-payload capacity," in *Robotics and Biomimetics (ROBIO), 2011 IEEE International Conference*, Karon Beach, Phuket, 2011.

[51] J. Shao, Xiaofeng Li, C. Zong , W. Guo, . Y. Bai , F. Dai and X. Gao, "A wall-climbing robot with gecko features," in *IEEE International Conference on Mechatronics and Automation*, Chengdu, 2012.

[52] F. Tache , W. Fischer, R. Siegwart, . R. Moser and . F. Mondada, "Compact magnetic wheeled robot with high mobility for inspecting complex shaped pipe structures," in *IEEE/RSJ International Conference on Intelligent Robots and Systems*, San Diego, CA, 2007.

[53] W. Fischer, G. Caprari , R. Siegwart and R. Moser, "Compact magnetic wheeled robot for inspecting complex shaped structures in generator housings and similar environments," in *IEEE/RSJ International Conference on Intelligent Robots and Systems*, St. Louis, MO, 2009.

[54] M. Eich and T. Vögele, "Design and control of a lightweight magnetic climbing robot for vessel inspection," in *Control & Automation (MED), 2011 19th Mediterranean Conference*, Corfu, 2011.

[55] M. Tavakoli, C. Viegas, L. Marques, P. J. Norberto and A. Aníbal T. de , "OmniClimbers: Omni-directional magnetic wheeled climbing robots for inspection of ferromagnetic structures," *Robotics and Autonomous Systems*, vol. 61, no. 9, p. 997–1007, 2013.

[56] X. Tang, . D. Zhang, Z. Li and . J. Chen , "An Omni-directional Wall-climbing Microrobot with Magnetic Wheels Directly Integrated with Electromagnetic Micromotors," *International Journal of Advanced Robotic Systems*, vol. 9, 2012.

[57] N. R. R. A. Tunwattana N, "Design of an underwater positioning sensor for crawling ship hull maintenance robots," *Proceedings of the Institution of Mechanical Engineers Part M: Journal of Engineering for the Maritime Environment*, vol. 224, no. 2, pp. 115-125, 2010.

[58] M. Wu, G. Pan, T. Zhang, . S. Chen, . F. Zhuang and Z. Yan-zheng, "Design and Optimal Research of a Non-Contact Adjustable Magnetic Adhesion Mechanism for a Wall-Climbing Welding Robot," *International Journal of Advanced Robotic Systems*, vol. 4, pp. 515-522, 2012.

[59] C. H. ,. K. B. D. Schmidt, "Omnidirectional locomotion and traction control of the wheel-driven, wall-climbing robot, Cromsci," *Robotica*, vol. 29, no. 7, pp. 991-1003, 2011.

[60] J. Li , X. Gao , . N. Fan, K. Li and Z. Jiang, "BIT Climber: A centrifugal impeller-based wall climbing robot," in *International Conference on Mechatronics and Automation , IEEE*, Changchun, 2009.

[61] Luk, BL and White, TS and Cooke, DS and Hewer, ND and Hazel, G and Chen,s,, "Climbing Service Robot for Duct Inspection and Maintenance Applications in a Nuclear Reactor," in *Proceedings of the 32nd ISR(International Symposium on Robotics)*, 2001.

[62] Z.Houxiang , L. Rong and Z. Guanghua and Z. Jianwei, "A Novel Autonomous Climbing Robot for Cleaning an Elliptic Half-Shell," in *Mobile Robots: towards New Applications*, 2006.

[63] J. Shang, T. Sattar , S. Chen and B. Bridge, "Design of a climbing robot for inspecting aircraft wings and fuselage,," *Industrial Robot: An International Journal*, vol. 34, no. 6, pp. 495 - 502, 2007.

[64] Z. Houxiang , Z. Jianwei and Z. Guanghua, "Effective pneumatic scheme and control strategy of a climbing robot for class wall cleaning on high-rise buildings," *International Journal of Advanced Robotic Systems,* vol. 3, no. 2, pp. 183-190, 2006.

[65] T. W. C. H. H. S. C. B.L. Luk, "Climbing Service Robot for Duct Inspection and Maintenance Applications in a Nuclear Reactor," in *Proceedings of the 32nd ISR(International Symposium on Robotics)*, 2001.

[66] Gradetsky, VG and Knyazkov, MM, "Multi-functional wall climbing robot," in *Adaptive Mobile Robotics*, World Scientific, 2012, pp. 807-812.

[67] S. Jianzhong ,S. Tariq , C. Shuwo and B. Bryan, "Design of a climbing robot for inspecting aircraft wings and fuselage," *Industrial Robot: the international journal of robotics research and application,* vol. 34, no. 6, pp. 495-502, 2007.

[68] Z. Houxiang, L. Rong , Z. Guanghua and Z. Jianwei, "A Novel Autonomous Climbing Robot for Cleaning an Elliptic Half-shell," *INTECH Open Access Publisher.,* 2006.

[69] D. S. A. Faina, A. Deibe, F. Lopez-Pena, R. J. Duro and X. Fernandez, "Development of a climbing robot for grit blasting operations in shipyards," in *Robotics and Automation, 2009. ICRA '09. IEEE International Conference* , Kobe, 2009.

[70] Tso, SK and Feng, TONG, "Robot Assisted Wall Inspection for Improved Maintenance of High-Rise Buildings," in *International Symposium on Automation and Robotics in Construction*, Eindhoven, 2003.

[71] W. Wei ,T. Boyan, Z. Houxiang and Z. Guanghua, "Robotic cleaning system for glass facade of high-rise airport control tower," *Industrial Robot: An International Journal*, vol. 37, no. 5, pp. 469-478, 2010.

[72] Q. Zhi-yuan, Z. Yan-zheng and Fu, Zhuang, "Development of wall-climbing robots with sliding suction cups," in *Intelligent Robots and Systems, 2006 IEEE/RSJ International Conference on*, IEEE, 2006.

[73] L. Domenico and M. Giovanni, "A modular approach for the design of the Alicia3 climbing robot for industrial inspection," *Industrial Robot: An International Journal*, vol. 31, no. 2, pp. 148-158, 2004.

[74] B. Filippo, B. Carlo, L. Domenico and M. Giovanni, "Structure and model identification of a vortex-based suction cup," in *Advances In Mobile Robotics*, World Scientific, 2008, pp. 303-310.

[75] Elkmann, N and Kunst, D and Krueger, T and Lucke, M and Bhme, T and Felsch, T and Strze, T,, "SIRIUSc: Facade Cleaning Robot for A High-Rise Building in Munich, Germany," in *Climbing and Walking Robots*, Springer, 2005, pp. 1033-1040.

[76] Y. Zhao , Z. Fu, Q. Cao and Y. Wang , "Development and applications of wall-climbing robots with a single suction cup," *Robotica*, vol. 22, no. 6, pp. 643-648, 2004.

[77] S. Wu , L. Wu and T. Liu, “Design of a sliding wall climbing robot with a novel negative adsorption device,” in *Ubiquitous Robots and Ambient Intelligence (URAI), 2011 8th International Conference* , Incheon, 2011.

[78] Y. Fu, . Z. Li , . H. Yang and S. Wang, “Development of a wall climbing robot with wheel-leg hybrid locomotion mechanism,” in *Robotics and Biomimetics, 2007. ROBIO 2007. IEEE International Conference* , Sanya, 2007.

[79] Z.-h. Wang, G.-j. Bao, L.-b. Zhang and Q.-h. Yang, “Development and control of flexible pneumatic wall-climbing robot,” *Journal of Central South University of Technology*, vol. 16, pp. 961-970, 2009.

[80] P. Saboori , W. Morris, J. Xiao and A. Sadegh, “Aerodynamic analysis of City-Climber robots,” in *Robotics and Biomimetics, 2007. ROBIO 2007. IEEE International Conference*, Sanya, 2007.

[81] M. Wang, Y. Qi , . W. Jiang, . S. Li, . H. Cheng and J. Bao, “Research on omni-directional moving adsorption mechanism and its application in wall-climbing robot,” in *IEEE Third International Conference on Information Science and Technology (ICIST)*, Yangzhou, 2013.

[82] A. Houssam , A. Anani and K. Ivan, “New concept of in-water surface cleaning robot,” in *IEEE International Conference on Mechatronics and Automation*, Takamatsu, 2013.

[83] X. G. Daijun Xu, X. Wu, N. Fan, K. Li and K. Kikuchi, “Suction Ability Analyses of a Novel Wall Climbing Robot,” in *IEEE International Conference on Robotics and Biomimetics*, Kunming, 2006.

[84] M. Elliott, W. Morris , A. Calle and J. Xiao, “City-Climbers at Work,” in *IEEE International Conference on Robotics and Automation*, Roma, 2007.

[85] Y. Yoshida and S. Ma, “A wall-climbing robot without any active suction mechanisms,” in *Robotics and Biomimetics (ROBIO), 2011 IEEE International Conference*, Karon Beach, Phuket, 2011.

[86] R. L. Na Shun Bu He, W. Wang, H. Yang and X. D. Wang, "A mini multi-joint wall climbing robot based on the vibrating suction method," in *Robotics and Biomimetics, 2007. ROBIO 2007. IEEE International Conference*, Sanya, 2007.

[87] W. W. ,. H. Z. Kun Wang, "The Mechanical Properties of a Wall-Climbing Caterpillar Robot: Analysis and Experiment," *International Journal of Advanced Robotic Systems*, vol. 10, 2013.

[88] Q. Hong, R. Liu and Y. Qu, "Principle and application of Underwater Vibration Suction Method," in *Robotics and Biomimetics (ROBIO), 2009 IEEE International Conference*, Guilin, 2009.

[89] T. G. H. Z. J. Z. a. Z. J. Daoguo Yang, "Analysis and Experiments on Pulse Vibrating Suction Method for Wall Climbing Robot," *Advanced Materials Research*, Vols. 201-203, pp. 1837-1844, 2011.

[90] W. Minghui , P. Gen , Z. Tao , C. Shanben , Z. Fu and Yan-zheng, Zhao, "Design and Optimal Research of a Non-Contact Adjustable Magnetic Adhesion Mechanism for a Wall-Climbing Welding Robot," *International Journal of Advanced Robotic Systems*, vol. 10, no. 63, 2013.

[91] M. O. f. Howlader and T. P. Sattar, "Development of Magnetic Adhesion Based Climbing Robot for Non-Destructive Testing," in *Computer Science and Electronic Engineering Conference (CEEC)*, University of Essex, UK, 2015.

[92] W. Shen , J. Gu and Y. Shen, "Permanent Magnetic System Design for the Wall-climbing Robot," in *Conference on Mechatronics & Automation*, Niagara Falls, Canada, July 2005.

[93] M. O. F. Howlader and T. P. Sattar, "Development of magnetic adhesion based climbing robot for non-destructive testing," in *Computer Science and Electronic Engineering Conference (CEEC)*, 2015.

[94] Bi, Zhiqiang , G. Yisheng , C. Shizhong , Z. Haifei and Z. Hong, "A miniature biped wall-climbing robot for inspection of magnetic metal surfaces," in *Robotics*

and Biomimetics (ROBIO), 2012 IEEE International Conference, Guangzhou, China, 2012.

[95] S. Park , H. D. Jeong and . Z. S. Lim, "Design of a mobile robot system for automatic integrity evaluation of large size reservoirs and pipelines in industrial fields," in *Intelligent Robots and Systems, 2003. (IROS 2003). Proceedings. 2003 IEEE/RSJ International Conference* , 2003.

[96] F. Wolfgang , C. Gilles , S. Roland and M. Roland, "Compact magnetic wheeled robot for inspecting complex shaped structures in generator housings and similar environments," in *IEEE/RSJ International Conference on Intelligent Robots and Systems*, St. Louis, MO, 2009.

[97] W. Minghui, P. Gen, Z. Tao, C. Shanben, Z. Fu and Yan-zheng, Zhao, "Design and Optimization of Variable Magnetic Force Wheel for Wall-Climbing Robot," *International Journal of Advanced Robotic Systems*, vol. 4, pp. 515 - 522, 2012.

[98] J. Shang, B. Bridge, T. Sattar, S. Mondal and A. Brenner, "Development of a climbing robot for inspection of long weld lines," *Industrial Robot: An International Journal,* vol. 35, no. 3, pp. 217-223, 2008.

[99] A. Teodor, A. Manuel and P. Manuel and U. Mauricio, "Concerning a technique for increasing stability of climbing robots," *Journal of Intelligent and Robotic Systems*, vol. 27, pp. 195-209, 2000.

[100] M. Carlo and S. Metin, "A Biomimetic Climbing Robot Based on the Gecko," *Journal of Bionic Engineering*, vol. 3, no. 3, pp. 115-125, 2006.

[101] S. D. Alan Asbeck, A. Parness, L. Fullerton, N. Esparza, D. Soto, B. Heyneman and M. Cutkosky, "Climbing rough vertical surfaces with hierarchical directional adhesion," in *Robotics and Automation, 2009. ICRA '09. IEEE International Conference*, Kobe, 2009.

[102] Krahn, J , Liu, Y , Sadeghi, A and Menon, C, "A tailless timing belt climbing platform utilizing dry adhesives with mushroomcaps," *Smart Materials and Structures,* vol. 20, no. 11, p. 115021, 2011.

[103] . T. Seo and M. Sitti, "Under-actuated tank-like climbing robot with various transitioning capabilities," in *Robotics and Automation (ICRA), 2011 IEEE International Conference,* Shanghai, 2011.

[104] Y. Liu , S. Sun, . X. Wu and T. Mei, "A leg-wheel wall-climbing robot utilizing bio-inspired spine feet," in *IEEE International Conference on Robotics and Biomimetics (ROBIO),* Shenzhen, 2013.

[105] C. Kute , M. p. Murphy, . Y. Mengüç and M. Sitti, "Adhesion recovery and passive peeling in a wall climbing robot using adhesives," in *Robotics and Automation (ICRA), 2010 IEEE International Conference,* Anchorage, AK, 2010.

[106] T. C. W. Kathryn A. Daltorio, G. D. Wile, L. R. Palmer, A. A. Malek, M. R. Ahmad, L. Southard, S. N. Gorb, R. E. Ritzmann and R. D. Quinn, "A body joint improves vertical to horizontal transitions of a wall-climbing robot," in *Robotics and Automation, 2008. ICRA 2008. IEEE International Conference*, Pasadena, CA, 2008.

[107] B. Paolo , H. Michael A , Li, Yasong and M. Carlo, "Optimal Gait for Bioinspired Climbing Robots Using Dry Adhesion: A Quasi-Static Investigation," *Journal of Bionic Engineering,* vol. 10, no. 1, pp. 1-11, 2013.

[108] R. Chen , R. Liu and H. Shen, "Design of a double-tracked wall climbing robot based on electrostatic adhesion mechanism," in *IEEE Workshop on Advanced Robotics and its Social Impacts,* Tokyo, 2013.

[109] R. Chen, "A Gecko-Inspired Electroadhesive Wall-Climbing Robot," *IEEE Potentials,* vol. 34, no. 2, pp. 15 - 19, 2015.

[110] F. I. Marc Osswald, "Design and control of a climbing robot based on hot melt adhesion," *Robotics and Autonomous Systems,* vol. 61, no. 6, p. 616–625, 2013.

[111] A. Sintov, T. Avramovich and A. Shapiro, "Design and motion planning of an autonomous climbing robot with claws," *Robotics and Autonomous Systems,* vol. 59, no. 11, p. 1008–1019, 2011.

[112] B. Carlos, G. Antonio and J. Alberto, "Climbing Robots' Mobility for Inspection and Maintenance of 3D Complex Environments," *Autonomous Robots,* vol. 18, no. 2, p. 157–169, 2005.

[113] M. Kai-tung, A. Duggal, P. Smedley, D. L'Hostis and S. Hongbo, "A Historical review on Integrity issues of permanent mooring systems," in *Houston , Texas*, Offshore Technology Conference, 2013.

[114] F. 4. Magnets, "40 x 20 x 5mm thick Ultra High Performance N52 Grade Neodymium Magnet - 15.1kg Pull," First 4 Magnets , [Online]. Available: https://www.first4magnets.com/rectangular-magnets-c35/40-x-20-x-5mm-thick-ultra-high-performance-n52-grade-neodymium-magnet-15-1kg-pull-p3794#ps_1-1837. [Accessed 25 June 2018].

[115] G. R. Edwards, S. Kokkorikos, A. Garcia, C. Patton and T. Sattar, "Moorinspect," [Online]. Available: http://www.bindt.org/downloads/ndt2012_3c1.pdf. [Accessed 08 06 2018].

[116] J. L. García, E. García, C. M. Suárez, . D. Blanco and . N. Beltrán, "Automated Off-shore studless chain inspection system," in *16th WCNDT - World Conference on NDT*, Montreal, Canada, 2004.

[117] S. Williams , "cordis.europa.eu," 14 March 2008. [Online]. Available: http://cordis.europa.eu/docs/publications/1216/121625181-6_en.pdf. [Accessed 10 December 2015].

[118] S. O. S. Ltd, "subsea-laser-mooring-chain-scans," Savante Offshore Services Ltd, 2017. [Online]. Available: https://www.savante.co.uk/subsea-laser-mooring-chain-scans/. [Accessed 08 06 2018].

[119] J. Rudlin, "Multi-channel ultrasonic inspection of a mooring chain for fatigue cracks," in *European Conference on Non-Destructive Testing*, Prague, Czech Republic, 2014.

[120] DNV, " DNV-OS-E303. Offshore Mooring Chain," 2013.

[121] A. r. p. 21, “in-service Inspection of mooring hardwear for floating strectures.,” American Pertroleum Institute , 2008.

[122] F. Campbell, “Inspection Methods—Overview and Comparison,” in *Inspection of Metals—Understanding the Basics,* ASM International, 2013, pp. 1-20.

[123] L. Cartz, “Quality Control and NDT,” in *Nondestructive Testing,* ASM International, 1995, pp. 1-13.

[124] H. Caroline, D. Bruce and W. Paul D, “Post-processing of the full matrix of ultrasonic transmit--receive array data for non-destructive evaluation,” *NDT & e International,* vol. 38, no. 8, pp. 701-711, 2005.

[125] . M. Sutcliffe, . M. Weston, B. Dutton, . P. Charlton and . K. Donne,, “Real-time full matrix capture for ultrasonic non-destructive testing with acceleration of post-processing through graphic hardware,” *Ndt & E International,* vol. 51, pp. 16--23, 2012.

[126] S. Mark, W. Miles , D. Ben , C. Ian and D. Kelvin, “Real-time full matrix capture with auto-focusing of known geometry through dual layered media,” in *Proceedings of the NDT 2012 Conference in British Institute of Nondestructive Testing,* 2012.

[127] J. Krautkramer and K. Herbert, Ultrasonic testing of materials, Springer Science & Business Media, 2013.

[128] J. L. Rose, Ultrasonic guided waves in solid media, Cambridge university press, 2014.

[129] J. Drury, “NDT FUNDAMENTALS: Ultrasonics, Part 1. Basic principles of sound,” *INSIGHT-WIGSTON THEN NORTHAMPTON,* vol. 46, no. 11, pp. 650-652, 2004.

[130] . S. Cochran, “Ultrasonics Part 12. Fundamentals of ultrasonic phased arrays,” *Insight-Non-Destructive Testing and Condition Monitoring,* vol. 48, no. 4, pp. 212-217, 2006.

[131] R. J. Mailloux, "Phased Array Theory and Technology," *Proceedings of the IEEE,* vol. 70, no. 3, pp. 246-290, 1982.

[132] Olympus, "Phased Array Tutorial," Olympus, [Online]. Available: https://www.olympus-ims.com/en/ndt-tutorials/phased-array/. [Accessed 08 08 2018].

[133] R. Tech, Introduction to Phased Array Ultrasonic Technology Applications, R/D Tech, 2004.

[134] F. Chengguang, C. Mihai, P. Mengchun and D. Bruce W, "A comparison between ultrasonic array beamforming and super resolution imaging algorithms for non-destructive evaluation," *Ultrasonics,* vol. 54, no. 7, pp. 1842-1850, 2014.

[135] H. Caroline, D. Bruce W and W. Paul D, "Post-processing of the full matrix of ultrasonic transmit--receive array data for non-destructive evaluation," *NDT & e International,* vol. 38, no. 8, pp. 701-711, 2005.

[136] . M. Sutcliffe, M. Weston, . B. Dutton, . I. Cooper and K. Donne, "Real-time full matrix capture with auto-focussing of known geometry through dual layered media," in *Proceedings of the NDT 2012 Conference in British Institute of Nondestructive Testing*, 2012.

[137] TWI Ltd, "Full Matrix Capture," [Online]. Available: https://www.twi-global.com/capabilities/integrity-management/non-destructive-testing/ndt-techniques/full-matrix-capture/. [Accessed 8 8 2018].

[138] L. Farr and C. Nageswaran, "TWI report 31331/1/17: Deliverable D4 -PAUT system," Project consortium internal report, 2017.

[139] R. E. Sheriff and L. P. Geldart, Exploration seismology, Cambridge: Cambridge university press, 1995.

[140] OLYMPUS, "HydroFORM/RexoFORM," OLYMPUS, [Online]. Available: https://www.olympus-ims.com/en/corrosion-solutions/hydroform-rexoform/#!cms[tab]=%2Fcorrosion-solutions%2Fcorrosion-mapping%2Fhydroform. [Accessed 23 08 2018].

[141] C. Mineo, J. Riise, S. G. Pierce, P. I. Nicholson and I. Cooper , "Robotic path planning for non-destructive testing through RoboNDT," in *54th BINDT Annual Conference,* 2015.

[142] TWI Ltd, "Advanced ultrasonic full matrix capture inspection software launched," TWI Ltd, 19 09 2016. [Online]. Available: https://www.twi-global.com/news-events/news/2016-09-advanced-ultrasonic-full-matrix-capture-inspection-software-launched/. [Accessed 14 08 2018].

[143] Galil, "GalilTools," Galil Motion Control , [Online]. Available: http://www.galilmc.com/downloads/software/galiltools. [Accessed 16 08 2018].

[144] P. NDT, "MicroPulse FMC," Peak NDT, [Online]. Available: https://www.peakndt.com/products/micropulse-fmc/. [Accessed 16 08 2018].

[145] Inuktun, "NanoMag™," Inuktun , [Online]. Available: http://inuktun.com/en/products/onsite-standard-products/nanomag-miniature-magnetic-crawler/. [Accessed 12 08 2018].

[146] M. F. Santos, M. O. Brito and C. Neves, "Development of an underwater riser inspection robot," *Industrial Robot: An International Journal,* vol. 40, no. 4, pp. 402-411, 2013.

[147] B. Siciliano, L. Sciavicco, L. Villani and G. Oriolo, "Introduction," in *Robotics: Modelling, planning and control*, London, Springer-verlag London Limited, 2009, pp. 1-34.

[148] M. W. Spong, S. Hutchison and M. Vidyasagar, Robot Dynamics and Control, Wiley, 2005.

[149] . J. M. Selig, "Active versus passive transformations in robotics," *IEEE Robotics & Automation Magazine,* vol. 13, no. 1, pp. 79-84, 2006.

[150] A. L. Yaghin and R. E. Melchers, "Long-term inter-link wear of model mooring chain," *Marine Structures,* vol. 44, pp. 61-84, 2015.

[151] K. Hwang, K. Dongmok , Y. Hojoon , L. Kyouhee , S. Kunchan and C. Doyoung and K. Jongwon, "Development of a wall-climbing robot using a tracked wheel

mechanism," *Journal of Mechanical Science and Technology,* vol. 22, no. 8, p. 1490–1498, 2008.

[152] A., Manuel , P. Akinfiev, T and F., Roemi and de Santos, P Gonzlez , Garcia, E Montes, H Nabulsi, S Ponticelli, R and Sarria, J, "On the design and development of climbing and walking robots for the maritime industries," *Journal of Maritime Research,* vol. 2, no. 1, pp. 9-32, 2005.

[153] L. Domenico and M. Giovanni, "The Alicia/sup 3/ climbing robot: a three-module robot for automatic wall inspection," *IEEE Robotics \& Automation Magazine*, vol. 13, no. 1, pp. 42-50, 2006.

[154] K. Pakpoom, K. Kazuto, K. Masaru, H. Mitsuhiro, M. Yasushi and A. Tatsuo, "A new close-loop control method for an inspection robot equipped with electropermanent-magnets," *Journal of Robotics and Mechatronics,* vol. 28, no. 2, pp. 185-193, 2016.

[155] Welapetage, "http://www.welaptega.com/," Welapetage, [Online]. Available: http://www.welaptega.com/services/subseameasurement/. [Accessed 25 06 2016].

[156] C. Rendón-Conde and E. Heredia-Zavoni b, "Reliability assessment of mooring lines for floating structures considering statistical parameter uncertainties," *Applied Ocean Research,* vol. 52, pp. 295-308, 2015.

Chapter 9. Appendix

9.0 Background of robotic manipulators

9.1 Robotic manipulators

To develop a robotic manipulator, a sequence of rigid bodies, commonly known as 'links', is interconnected by joints. A robotic manipulator consists of three main features: an 'arm', which is used for mobility; a 'wrist', which enables dexterity; and an 'end effector', which performs the task [147]. The end effector carries the pre-attached tool/equipment required to perform the task (final goal of the manipulator). The arm part of the manipulator is designed according to the geometrical reaching properties (*i.e.* moving to a given position in a specified space). The required agility to conduct the task is provided by the wrist operation. Typically, the degree of freedom (DOF) of a manipulator is determined by the number of joints. For example, a manipulator that has three independent degrees of movements for positioning and three independent movements for orientation is able to reach an object kept in any arbitrary position (in 3D space). The workspace of a manipulator is the volume covered by the end of the effector (while the manipulator executes every possible motion/path). The geometry of the workspace depends highly on the mechanical constraints of the joints and links. For example, theoretically, a revolute joint is capable of rotating a full 360°, but due to mechanical complexities and design constraints, it may be less than that. The 'reachable workspace' consists of all locations (points) that a robot manipulator can reach, whereas the 'dextrous workspace' accounts for all points that the manipulator can cover with arbitrary orientations of the end effector [148].

First, the three joints of the manipulator were considered in order to be classified kinematically, with the wrist described separately. According to the usual practice of classification, the majority of manipulators fall into following geometric types: the cylindrical manipulator (RPP type), the spherical manipulator/SCARA manipulator (RRP type), the Cartesian manipulator (PPP type), the elbow manipulator (articulated) (RRR type), where R is a revolute joint and P is a prismatic joint. Commonly used geometric manipulator types and their workspaces are illustrated in Figure 9-1. When assigning a manipulator for a given task, the power source (*i.e.* the method of joints are actuated), method of control (*i.e.* how complicated the control architecture should be), application area (*i.e.* integrity and reliability of the actuated joints with respect to the working environment), and geometry (*i.e.* suitable kinematic structure to achieve the task) should be considered [148]. Moreover, when a manipulator has to work in a given environment,

additional physical design constraints should be considered. For example, if the manipulator has to work in an in-situ environment or as part of a robot, then weight, strength, and power consumption are also added as design constraints. The commonly used symbolic representation of joints is illustrated in Figure 9-2.

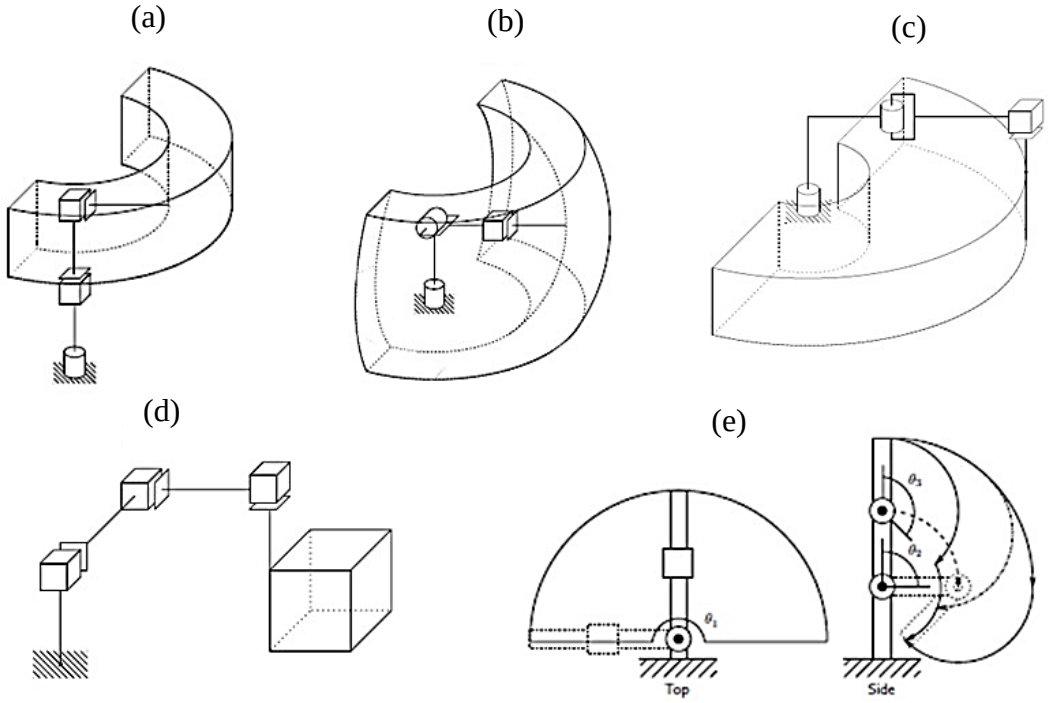

Figure 9-1(a): Geometric types of commonly used robotic manipulator and their workspaces; (a) cylindrical manipulator; (b) spherical manipulator; (c) SCARA manipulator; (d) Cartesian manipulator; (e) elbow manipulator (articulated) [148]

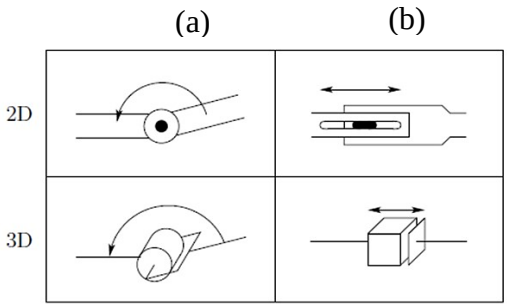

Figure 9-2: Commonly used symbolic representation of joints; (a) revolute joint; (b) prismatic joint [148]

9.2 Rigid body transformations

In robotic design, it is essential to keep track of a rigid body to understand its behaviour with respect to a known location in 3D space. Two main mathematical models are

presented in the literature to keep track of rigid body motion [149], *i.e.* the passive transformation approach and the active transformation approach. In the passive transformation technique, an embedded coordinate frame is given to the rigid body and its position and orientation are calculated by using the coordinate transformation from the world frame to the rigid body frame (*i.e.* to the embedded coordinate frame on the body). When the geometrical features of the manipulator/robot are complicated (*i.e.* several bodies involved in the motion and the bodies carry different coordinate frames), assigning different body frames for each body is not convenient [149]. However, the active body transformation technique is developed with a single fixed-coordinate frame. The position and orientation of a rigid body are specified by the transformation, which moves the body from its home position to its current position. A summary of active rigid body transformation is presented below. (*i.e. a* comprehensive study is presented in [149])

In common practice, an arbitrary point (p) in a 3D coordinate system is expressed as a 3 × 1 column vector:

$$p = \begin{bmatrix} x \\ y \\ z \end{bmatrix} \qquad \textit{Eq 9-1}$$

When point p is subjected to a rotation around an axis, the effect of such a rotation on point p is expressed as below:

$$p' = R(\emptyset)p \qquad \textit{Eq 9-2}$$

where $\emptyset$ represents the angle of rotation (rotation angle around the selected axis) and R is the corresponding rotation matrix.

Rotation around the x, y, and z axis can be expressed as $R_x(\emptyset)$, $R_y(\emptyset)$, and $R_z(\emptyset)$, respectively. In a given Cartesian coordinate system, rotation matrices are expressed as follows:

$$R_x(\emptyset) = \begin{pmatrix} 1 & 0 & 0 \\ 0 & cos\emptyset & -sin\emptyset \\ 0 & sin\emptyset & cos\emptyset \end{pmatrix} \qquad \textit{Eq 9-3}$$

$$R_y(Ø) = \begin{pmatrix} cosØ & 0 & sinØ \\ 0 & 1 & 0 \\ -sinØ & 0 & cosØ \end{pmatrix}$$

Eq 9-4

$$R_z(Ø) = \begin{pmatrix} cosØ & -sinØ & 0 \\ sinØ & cosØ & 0 \\ 0 & 0 & 1 \end{pmatrix}$$

Eq 9-5

Similar to a rotation, the vector addition can be used to model a translation in 3D space. If the translation is a vector t, the resulting effect on point p due to the translation is expressed below, where p is the new point after the translation:

$$p' = p + t$$

Eq 9-6

Using a 4 × 4 matrix system to combine rotation and translation is common practice in robotics. Therefore, the abovementioned translation and rotation can be modelled as follows, where M is the transformation matrix. This notation is often called homogeneous transformation:

$$M = \begin{bmatrix} R(Ø) & t \\ 0 & 1 \end{bmatrix}$$

Eq 9-7

According to the above homogeneous transformation, a point that has coordinates (x, y, z) is expressed as a four-dimensional column vector (4 × 1):

$$\tilde{p} = \begin{bmatrix} x \\ y \\ z \\ 1 \end{bmatrix} = \begin{bmatrix} p \\ 1 \end{bmatrix}$$

Eq 9-8

Therefore, the combined effect of rigid body transformation can be expressed as a matrix product:

$$\tilde{p}' = M\tilde{p} = \begin{bmatrix} R(Ø)p + t \\ 1 \end{bmatrix}$$

Eq 9-9

To compute a transformation matrix of a rotation about a general line in a given 3D space, a conjugation is used. When R (3 × 3) is a rotation matrix and its rotation axis lies in the direction of the line and p (p =(x, y, z)^{T}) is a position vector on the line, as illustrated in Figure 5-2, the 4 × 4 matrix can be written as fl (previously studied in the literature [149]):

$$A(\emptyset) = \begin{bmatrix} I & p \\ 0 & 1 \end{bmatrix} \begin{bmatrix} R & 0 \\ 0 & 1 \end{bmatrix} \begin{bmatrix} I & -p \\ 0 & 1 \end{bmatrix} = \begin{bmatrix} R & (I-R)p \\ 0 & 1 \end{bmatrix} \qquad \textit{Eq 9-10}$$

where *I* is an identity matrix (3 × 3).

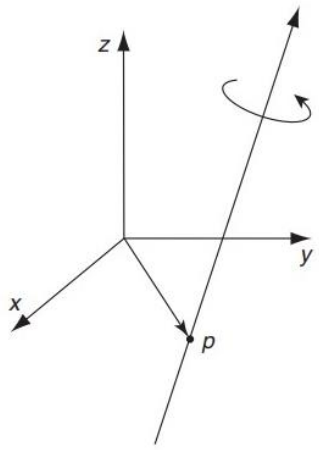

Figure 9-3: Schematic of a rotation around an arbitrary axis

The End.